Les eaux modales de l'Océan Austral

Jean-Baptiste Sallée

UNIVERSITÉ TOULOUSE III - PAUL SABATIER

Ecole Doctorale des Sciences de l'Univers, de l'Environnement et de l'Espace

Formation Doctorale Océan, Atmosphère et Environnement

-oOOo-

THESE

pour obtenir le titre de

DOCTEUR DE L'UNIVERSITE TOULOUSE III

Discipline : **Océanographie Physique**

présentée par

Jean-Baptiste Sallée

Les eaux modales de l'Océan Austral

Thèse soutenue le 5 Novembre 2007 devant le jury composé de :

Président du jury	Nick Hall	LEGOS, Toulouse
Rapporteurs	Gilles Reverdin	LOCEAN, Paris
	Gurvan Madec	LOCEAN, Paris
Examinateurs	Kevin Speer	FSU, Floride, USA
	Anne-Marie Treguier	LPO, Brest
Directrice de thèse	Rosemary Morrow	LEGOS, Toulouse

Laboratoire d'**E**tudes en **G**éophysique et **O**céanographie **S**patiales
UMR5566-CNRS/UPS/CNES, Observatoire Midi-Pyrénées,
14 Av. Edouard Belin, 31400 Toulouse, France

Remerciements

J'adresse mes tout premiers remerciements à Rosemary avec qui j'ai eu la chance de pouvoir travailler au cours de mon DEA. Merci de m'avoir fait confiance et de m'avoir offert l'opportunité de continuer mes recherches de DEA à travers cette thèse. Je te remercie tout particulièrement pour le soutien permanent que tu m'as apporté au cours de ces trois dernières années. Mais aussi, et ça va de pair, pour tes immenses qualités pédagogiques et pour ton inépuisable bonne humeur. Tout en travaillant intensément et sérieusement, tu m'as appris qu'il est possible (nécessaire ?) de ne jamais négliger les week-end, les vacances et les pauses café (ou thé ; n'oublions pas quand même qu'elle est Australienne !). Merci de m'avoir soutenu dans les différentes collaborations que nous avons mises en place, et de m'avoir donné la chance d'aller voir la vie avec "la tête à l'envers" chez nos amis les manchots. Merci enfin pour ton inimitable accent "Austwalienne". Merci Rosemary pour cette thèse ! Tu m'as fait aimer la recherche et j'espère continuer nos collaborations dans le futur !

Quand je me suis lancé, 3 mois avant le début de ma thèse, dans un stage océanographique en Floride, j'avais comme premier objectif de découvrir la campagne Redneck et d'aller manger des "bbq ribs" avec des conducteurs de "Hummer". Mais je suis tombé sur Kevin et Nico. Nous avons commencé un travail très intéressant dans une ambiance excellente. Finalement, me voilà encore aujourd'hui, trois ans après, à échanger des dizaines d'emails par jour avec Kevin pour finir des études en cours ! En effet, notre collaboration s'est poursuivie tout au long de ce travail de thèse. Je voudrais tout particulièrement remercier Kevin pour sa patience et ses impressionnantes qualités de scientifique. Merci de m'avoir dirigé dans ma compréhension des phénomènes océanographiques. Merci de m'avoir appris à ne jamais m'arrêter dans la remise en question et merci pour ton incessante curiosité sur le fonctionnement de l'Océan. J'espère sincèrement que nous continuerons à travailler ensemble ! Je tiens également à te remercier Nico pour les premières recherches que j'ai débutées avec toi, mais aussi pour VWFS, Cabos, pour m'avoir fait découvrir les ribs de Woodville, le smoked mullet et l'esprit Redneck ! Finalement, je profite d'être dans le paragraphe outre-Atlantique pour remercier Sophie, Emilie et Jérémie pour l'accueil si sympathique qu'ils m'ont offert à plusieurs reprises pendant ces trois dernières années. Merci à toi Jérémie pour m'avoir appris à fabriquer des épées, à faire du canoé, et à construire des bateaux de pirate.

Je suis également très reconnaissant envers Gilles Reverdin et Gurvan Madec qui ont accepté d'être les rapporteurs de cette thèse, et dont j'ai apprécié les remarques judicieuses. Merci aussi à Anne-Marie Tréguier et Nick Hall qui ont aimablement accepté de faire partie de mon jury.

Merci également à toutes les personnes avec qui j'ai collaboré pendant cette thèse. Fabienne Gaillard, merci pour le temps passé avec moi, même si nous n'avons pas pu finaliser nos projets. Steve Rintoul et Helen Phillips, merci pour votre accueil à Hobart pendant 2 mois. Rick Lumpkin, merci pour ton ouverture d'esprit et ta disponibilité. J'espère que l'on continuera à travailler ensemble.

Je voudrais finalement adresser mes remerciements à l'ensemble de l'équipe OLVAC pour la bonne ambiance qui y règne, et les réunions d'équipe arrosées, ainsi qu'à la secte des Algeco et de l'extension. Je ne pourrais oublier de remercier mes co-bureau Anne-Charlotte et Christelle qui ont dû endurer les allers et venus incessantes des chèvres de ce laboratoire.

Merci aux foubes et fouines pour les relectures et pour leur soutien face à la mafia chinoise toujours prête à tout pour choper un résultat ! Merci aussi au Mexicain, à qui seul je dois mon titre de Dr.

Rebêêrciements

Bêêêrci à toute la bande des rocambolesques du LEGOS ! Bêêêêêêêêêêrci Boubou pour tes imitations fabuleuses de Yo, ta feuille et ton accent Anglais ! Bêêêêrcie à Paté, Tempête et Momo pour m'avoir ramené à la raison au moment où je renonçais à la dernière bière au Champagne ! Bêêêrci à Yoyo pour ses soupirs et ses grattages de tête convulsifs, enchaînés de grosses goulées de coca ! Bêêêêêerci à Momo pour être la plus grosse chèvre que j'ai rencontrée jusqu'à ce jour. Bêêêêrrci aux parents de Ju pour avoir créé l'Homme au cerveau de poule le plus drôle de Provence ! Lado je rebêêêrcie ton coiffeur d'avoir alimenté plus d'une fois nos discussions ! Bêêêrci Marielle de ne jamais être à court de pastis et bêêêrci pour tes apéros improvisés ! Anne-Charlote bêêêêêêêrci de m'avoir supporté dans ton bureau pendant 2 ans ! Bess, bêêrci d'être le caprin qui a mis bas la plus belle des filles qui soit ! Bêêêêrci d'être le hippie le plus grand amateur de ice ludge (Sonia, dans 14 ans on aura à se parler... j'ai des photos pour toi !)

huuuuuuu choooooooo Bêêêêêêêêêhhhh Bêêêêêêêêêhhh uuhhhhhhhhh HUMMMMMMM. HUMMMM Jamon HUMMMM Jamon, c'est les Rambla de Barcelona ! ! HUMM uuuu choooo ! !

Bêêêêêrci Guitou pour être un guitou ! Le guitou c'est un guitou, le guitou c'est un guitou ! ! Bêêêêêêêêêêrci Alix, bêêêêêêrci de m'avoir fait découvrir les gauffres nutella chantilly de la plage centrale d'Hossegor ! Claire, bêêêrci de me motiver pour venir aux réunions d'équipe chaque semaine ! Bêêêêerci Maria de m'avoir appris que tous les Espagnols n'avaient pas des gros morceaux de Jamon accrochés dans leurs salons ! Pepette, bêêêêrci pour tes crises de nerf et bêêêêreci de calmer Elvis lorsqu'il s'en prend à moi ! Bêêêrci Guitou pour ton adoration des gros seins, pour les parties de pétanques à la prairie des filtres et pour ton style claquette/short inégalable !

Chooooooooo huuuuuuu choooooooo Bêêêêêêêêêhhhh uuhhhhhhhhh ! Bêêêêê uuuuuuuuuuuuu chooo ! ! ! Bamonitos en la caille ! Bamonitos por el Jamon ! HUMMMMM ! Chooooooooo huuuuuuuuuuuuu

Bêêêêêêêrci Guts et Cha pour avoir découvert avec moi les plus grosses bouses que le cinéma occidental ait créé ! Bêêêrci pour P2, pour les tours dans les bois, et le suivi de MétéoFrance-montagne.fr quotidien ! Bêêêêrci finalement pour votre douce musique, que vous m'avez appris à apprécier ! Bêêêêêrci Christelle de m'avoir accepté dans ton bureau et pour les week end à St Trop ! Bêêêêêêrci Renaud alias le Gangsta' pour ta surhumaine motiv' de planchiste ! Bêêêêêrci Mathilde pour ta cool attitude ! Bêêêêci Gilbert LAVAL de m'avoir affiché sur google comme un galérien de l'océanographie ! Enfoiré ! Finalement, Bêrci à l'équipe des jeunes qui s'annonce comme une bonne relève ! Bêêrci à la coloc ! Enfin... Bêêrci Boutch et Bill, Vinz et Pedro !

HUMMMM ! Chooooooooo huuuuuuuu bêêêêêêêêêhh huuuuuuuu chooooooo Bêêêêêêêêêhhhh ! Huuuuuuuu Chooooooooo huuuuuu bêêêêêêêêêhh HUUUMMMM ! ! ! ! ! huuuuuuuuuuuu Chooooooooo huuuuuuuuuu Chooooo !

Bêêêrci à toi Spada de manager une équipe de feu qui nous régale tous les jours !

Bêêêrci Paté pour nos discussions politiques d'ivrognes ! Bêêêêrci Boubou de savoir rendre ton Kebab quand il le faut ! Mais aussi pour les ballades à Arnaud B. ! Bêêêêêrci Yoyo pour les lancés de jambes les plus hauts du monde et pour les apéros au Quartier ! Bêêêrci Tempète d'être un sergent et pour ton mémorable : "Chui pas un embusqueur !" Beeerci Momo pour ta naïveté et ton naturel : "moi j'ai presque pas bu de bière !" Bêêêêrci Ju d'assumer ton ridicule veston jaune de vélo qui nous fait tant rire ! Bêêêrci au Champagne et aux ADLboisson de m'avoir fait rencontrer la plus belle des marinières !

Activité scientifique pendant la thèse

Articles de rang A

Sallée, J.B. ; Wienders, N. ; Morrow, R. and Speer, K. *Formation of Subantarctic mode water in the Southeastern Indian Ocean*, Ocean Dynamics, 2006 , 56 , 525-542

Sallée, J.B. ; Morrow, R. and Speer, K. *Southern Ocean fronts and their variability to climate modes*, Journ. of Climate, 2007, in press

Morrow, R. ; Valladeau, G. and Sallée, J.B. *Observed subsurface signature of Southern Ocean decadal sea level rise* Prog. Oceanogr., 2007 , in press

Sallée, J.B. ; Morrow, R. ; Speer, K. and Lumpkin, R. *An estimate of Lagragian eddy statistics and diffusion in the mixed layer of the Southern Ocean*, submitted to Journ. of Marine Res., 2007

Sallée, J.B ; Morrow, R. ; Speer, K. *Subantarctic Mode Water formation around the circumpolar belt : the role of eddy diffusion*, submitted to Geophys. Res. Let., 2007

Boutin, J. ; Merlivat, L. ; Hénocq, C. and Sallée, J.B. *Air-sea CO_2 flux variability in frontal region of the Southern Ocean from CARIOCA drifters*, submitted to Limnol. and Ocean., 2007

Autres publications

Sallée, J.B. and Morrow, R. *Salinity calibration for the Southern Ocean ARGO data*. Coriolis newsletter, 3, july 2006.

Speer, K. ; N. Wienders ; J.B. Sallée ; R. Morrow, 2005. *Surface Layer heat Flux Variability in the SouthEastern Indian Ocean*. Clivar Exchanges, No. 35, 36-37.

Speer, K. ; N. Wienders ; J.B. Sallée ; R. Morrow, 2005. *Circulation of Subantarctic Mode Water in the Indian Southern Ocean from ARGO and ALACE floats*. Clivar Exchanges, No. 35, 53-55.

Sallée J.B. and Morrow R. *Delayed mode salinity quality control of Southern Ocean ARGO floats*. Legos technical report, Toulouse, 2007.

Voyage océanographique

Lanceur de XBT à bord de l'Astrolabe, entre la Tasmanie et la Terre-Adélie dans le cadre du programme SURVOSTRAL. Décembre 2005.

Communications scientifiques

EGU, Vienne, mai 2005 - poster
AGU, Hawaii, Fevrier 2006 - poster

Réunion ARGO-France, Brest, mai 2006 - présentation orale
GMMC, Toulouse, Décembre 2006 - présentation orale
Séminaire au Csiro, invité par S.Rintoul, Hobart, Australie ; Fevrier 2006 - présentation orale
Séminaire à l'université de Floride, invité par K.Speer, Tallahassee, USA ; Fevrier 2007 - présentation orale

Collaborations à l'étranger

3 mois à l'université de Floride, Tallahassee, USA, dans le cadre d'une collaboration avec K.Speer et N.Wienders. Juillet-Septembre, 2004
2 mois au Csiro à Hobart, Australie, dans le cadre d'une collaboration avec S.Rintoul et H.Phillips. Janvier-Fevrier, 2006
2 mois à l'université de Floride, Tallahassee, USA, dans le cadre d'une collaboration avec K.Speer. Janvier-Fevrier, 2007

Enseignement

2 ans de monitorat à l'université Paul Sabatier, soit 127 heures équivalent TD d'enseignement en physique, mathématiques et informatique, niveau licence.

abstract

Subantarctic mode water (SAMW) are formed in the Southern Ocean in the deep winter mixed layers north of the Subantarctic front. They influence the climate at interannual and decadal scales and play a fundamental role in the ventilation of Southern Hemisphere thermocline. We study the details of SAMW formation using the recent deployment of ARGO profiling floats and GDP surface drifters, which provide an excellent space-time coverage of the Southern Ocean upper ocean processes. Since the beginning of the ARGO international program, the number of vertical hydrographic profiles in the Southern Ocean have increased considerably so that nowadays we have a comparable number of profiles to decades of hydrographic ship data. Based on this dataset, we found that the dominant forcing for SAMW formation in winter in the Southern Indian Ocean was due to air-sea and Ekman fluxes. We found a rapid transition to thicker surface mixed layers in the central South Indian Ocean, at about 70°E, associated with a reversal of the horizontal eddy heat diffusion in the surface layer and the meridional expansion of the ACC as it rounds the Kerguelen Plateau. These effects are ultimately related to the bathymetry of the region, leading to the seat of formation in the region southwest of Australia.

SAMW formation is tightly linked to the Southern Ocean dynamics and position of the main polar fronts. A second study concerned the ACC circulation and frontal variability. In this study we mixed in-situ and altimeter data to monitor the position of the two main fronts of the ACC during the period 1993-2005. Then, we related their movements to the two main atmospheric climate modes of the Southern Hemisphere, the Southern Annular Mode (SAM) and the El-Nino Southern Oscillation (ENSO). We found that although the fronts are steered by the bathymetry, which sets their mean pathway at first order, in flat-bottom areas the fronts are subject to large meandering due to mesoscale activity and atmospheric forcing.

In parallel, we developed a new estimate of the circumpolar distribution of eddy diffusion in the Southern Ocean. Diffusion has almost never been studied in the Southern Ocean with in-situ data. We analysed up to 10 years of surface drifter trajectories and applied a statistical analysis previously developed in other oceans. We mapped a climatological eddy diffusion coefficient and derived an altimetric parametrization of the coefficient for easy use by the modeling community and for future studies on the interannual evolution of eddy diffusion. This study shows that the Southern Ocean is highly diffusive north of the ACC core, with several spots of very strong diffusion : the Agulhas Retroflection, the Campbell Plateau region, and the Brazil Current region.

These results lead us to a circumpolar analysis of the SAMW formation, and to a representaion of the link between Southern Ocean dynamics and SAMW formation. The constant increase in hydrological profiles in the Southern Ocean via the ARGO program allowed us to have a better spatial representation of the regions of SAMW formation. We found that eddy heat diffusion play a substantial role in the local heat balance. South of the western boundary currents and north of the SAF, the eddy heat diffusion is positive and counterbalances the cooling of the mixed layer by winter Ekman and air-sea fluxes. Specifically, it reduces the mixed layer destabilisation north of the SAF in the Western Indian Ocean downstream of the Agulhas Retroflection and in the Western Pacific downstream of Campbell Plateau.

Résumé

Les eaux modales Subantarctiques (SAMW) sont formées dans la profonde couche de mélange au nord du front Subantarctique (SAF) dans l'Océan Austral. Elles influencent le climat à des échelles décennales et inter-annuelles et jouent un rôle fondamental dans la ventilation de la thermocline de l'Océan Austral. Nous étudions la formation des SAMW en nous fondant sur les récents flotteurs profilants ARGO et sur les dériveurs de surface GDP. Ces jeux de données fournissent une très bonne couverture spatio-temporelle des processus à l'oeuvre dans les couches supérieures de l'Océan Austral. Depuis le lancement du programme international ARGO, le nombre de profils hydrographiques a augmenté de façon considérable dans l'Océan Austral. Une analyse de ces données a montré que les flux air-mer et les flux d'Ekman sont les forçages dominants dans la formation des SAMW. Nous avons trouvé une transition rapide, autour de 70 °E, des couches de mélange peu profondes en amont vers des couches de mélange très profondes en aval. Cette transition est associée à un changement de signe de la diffusion tourbillonnaire horizontale dans les couches de surface, et à l'extension méridionale de l'ACC lorsqu'il passe autour du plateau de Kerguelen. Ces effets sont directement liés à la bathymétrie et laissent place à une région de formation des SAMW au Sud-Ouest de l'Australie.

La formation des SAMW est intimement liée à la dynamique océanique Australe et à la position des principaux fronts polaires. Une deuxième étude concerne la circulation de l'ACC et la variabilité frontale. Dans cette étude, nous avons tiré parti de la complémentarité des données in situ et altimétriques afin de suivre l'évolution des deux principaux fronts de l'ACC pendant la période 1993-2005. Nous avons comparé leurs mouvements avec les deux principaux modes de variabilité atmosphérique de l'Hémisphère Sud, le mode annulaire Austral (SAM) et l'Oscillation Australe El-Niño (ENSO). La position moyenne des fronts est déterminée avant tout par les fonds océaniques. Cependant, nous avons trouvé que dans les régions à fond plat, les fronts forment de grands méandres dus à l'activité tourbillonnaire et aux forçages atmosphériques.

En parallèle, nous avons développé une nouvelle estimation de la distribution circumpolaire de la diffusion dans l'Océan Austral. La diffusion n'a presque jamais été étudiée à partir de données in situ dans cet océan. Nous avons calculé une estimation du coefficient de diffusion tourbillonnaire à partir d'une analyse statistique de dix années de trajectoires de dériveurs de surface. Nous avons cartographié ce coefficient dans l'Océan Austral, puis nous l'avons paramétré à partir de données altimétriques pour pouvoir en étudier l'évolution inter-annuelle et en faciliter l'utilisation dans le futur. Cette étude montre que l'Océan Austral est fortement diffusif au nord de l'ACC, et particulièrement près des courants de bord Ouest, c'est à dire dans la Rétroflexion des Aiguilles, dans la région du plateau de Campbell, et dans le courant de Brésil-Malouines.

Ces résultats nous ont menés à une analyse circumpolaire de la formation des SAMW, et à une meilleure conception du lien entre la dynamique océanique Australe et la formation des SAMW. La croissance constante des données hydrologiques du programme ARGO dans l'Océan Austral nous a également permis de mieux représenter la répartition des régions de formation des SAMW. Nous avons trouvé que la diffusion tourbillonnaire joue un rôle majeur dans les budgets de chaleur locaux. Au Sud des courants de bord Ouest, et au nord du SAF, la diffusion tourbillonnaire apporte de la chaleur, équilibrant et même dominant les refroidissements hivernaux dus aux flux d'Ekman et aux flux air-mer. Elle réduit en particulier la déstabilisation de la couche de mélange au nord du SAF dans l'Ouest du bassin Indien, en aval de la Rétroflexion des Aiguilles, et dans l'Ouest du bassin Pacifique, en aval du Plateau de Campbell.

Table des matières

Introduction

Contrairement aux autres océans du globe qui sont tous limités par des terres, l'Océan Austral est le seul à encerclé un continent. Cet "anneau" océanique représente environ 20 % de la surface océanique mondiale, et peut être vu comme une ceinture circumpolaire qui établit la plus grande connexion existante entre les trois principaux océans, l'Océan Atlantique, l'Océan Indien, et l'Océan Pacifique. Cet océan est animé d'un fort courant : le Courant Circumpolaire Antarctique (ACC), qui circule autour du continent Antarctique d'Ouest en Est sur une distance d'à peu près 21000 km, et transporte approximativement 130 millions de mètres cubes d'eau chaque seconde (Cunningham et al., 2003 ; Rintoul et al., 2001). Le Courant Circumpolaire Antarctique isole les eaux stratifiées de la thermocline subtropicale au Nord des eaux homogènes polaires au Sud. Les conditions climatiques extrêmes qui siègent dans les régions Australes font de cet océan une région clef pour la formation et la transformation de masses d'eaux aux caractéristiques particulières (Speer et al., 2000 ; Sloyan et Rintoul, 2000). Une autre spécificité de l'Océan Austral réside dans le fait que, reliant les principaux bassins océaniques, il permet la mise en place d'une circulation thermohaline globale.

Considéré sur la verticale, L'Océan Austral peut se diviser schématiquement en trois zones distinctes. En premier lieu on trouve la couche superficielle et sa couche de mélange qui sont en interaction constante avec l'atmosphère. Ensuite on rencontre les masses d'eau de profondeur intermédiaire. Elles sont associées à une boucle de circulation "supérieure" qui forment les eaux Antarctiques intermédiaires (AAIW) et Subantarctiques (SAMW) puis les exportent vers le nord (Sloyan et Rintoul, 2001a et 2001b ; Speer et al., 2000). Une fois formées, ces eaux sont isolées de tout forçage extérieurs, et gardent très longtemps en mémoire les caractéristiques qu'elles ont acquises lors de leur formation en surface. Enfin sous ces masses d'eau évolue une deuxième boucle de circulation, dite "profonde". Celle-ci est associée à la formation et à l'export des eaux abyssales (AABW) autour de l'Antarctique, ainsi qu'à la modification dans l'Océan Austral des eaux profondes en provenance de l'Hémisphère Nord (NADW). Ces boucles de circulation sont de la première importance dans la mise en place de la circulations thermohaline globale qui redistribuent à l'échelle planétaire les caractéristiques hydrologiques et notamment la chaleur. Les fortes interactions entre air, mer et glace dans l'Océan Austral sont les moteurs de ces boucles de circulation et de la circulation thermohaline plus généralement (Sloyan et Rintoul, 2001 ; Speer et al., 2000). Lorsque la couche de mélange océanique s'approfondit suffisamment, elle perfore la thermocline saisonnière et fonctionne alors comme une "cheminée" qui rend possible le transfert d'anomalies océaniques et climatiques de l'océan superficiel vers l'océan intérieur. Les masses d'eau de profondeur intermédiaire (eaux Antarctiques intermédiaires et modales subantarctiques) prennent leurs caractéristiques en surface dans la couche de mélange océanique, puis après subduction, sont exportées dans l'ensemble de l'océan mondial et ventilent la thermocline subtropicale sur des échelles de temps décennales (McCartney, 1982).

Les masses d'eau profondes sont formées par interactions énergétiques complexes entre glaces, air et mer à la surface océanique puis plongent ensuite pour alimenter le renouvellement des eaux abyssales (Gordon et al., 1993 ; Gordon, 1998 ; Jones et al., 1990 ; Rintoul, 1998).

Les eaux modales subantarctiques (SAMW) et les eaux antarctiques intermédiaires (AAIW) font partie des masses d'eau de profondeur intermédiaire, qui se trouvent directement sous la thermocline saisonnière. Elles sont formées au nord de l'ACC et jouent un rôle fondamental dans la ventilation de la thermocline de l'Hémisphère Sud (Wong et al., 1999 ; Hanawa et Talley, 2000). Au cours de leurs trajets et recirculations, ces eaux froides, peu salées et riches en oxygène sont modifiées et exportées soit vers les tropiques, soit dans l'Océan Austral où elles sont transportées vers l'Est par l'ACC. Elles sont un indicateur très pertinent de la variation temporelle des conditions océaniques et par conséquent des conditions climatiques (Wong et al., 1999 ; Sabine et al., 2004 ; Metzl et al., 1999 ; Sarmiento et al., 2004). La variation des propriétés, de la distribution et de la circulation des eaux modales est le reflet des changements des interactions air-mer de l'hiver, et du transport océanique de chaleur dans la zone de formation. Une variation spatiale de ces propriétés peut aussi refléter des processus de mélange pendant la recirculation, dus à une l'activité tourbillonnaire, ou à des ondes internes, ou encore à des phénomènes à plus petite échelle. Par ailleurs, ces mêmes masses d'eau constituent un chemin privilégié pour le piégeage du CO2 et le transport associé du carbone d'origine anthropique (Metzl et al., 1995 et 1999 ; Takahashi et al., 2002). La connaissance de ces eaux et la compréhension des mécanismes qui les fondent ainsi que du rôle exact qui est le leur est ainsi l'une des quatre priorités majeures du groupe CLIVAR (CLImate VARiability and predictability) " Southern Ocean ".

Bien que l'on ait reconnu le rôle important de ces masses d'eau dans l'évolution du climat mondial, leurs caractéristiques restent mal connues. Nous ne connaissons pas avec précision, par exemple, ni leurs régions et processus de formation, ni le cours exact de leur circulation, ni la manière dont leurs propriétés physiques, - température, salinité, quantité de CO2 transportée -, sont modifiées pendant leur parcours. Ce que l'on sait actuellement, c'est représenter ces transferts à grande échelle de façon simplifiée via des modèles de circulation générale océanique (England, 1993 ; Guilyardi et Madec, 1999) . Mais, alors que l'on avance souvent le rôle des tourbillons pour expliquer la transformation des eaux modales "jeunes" en des eaux plus âgées, ceux-ci trouvent en général peu de place dans les modèles actuels. L'Océan Austral souffre d'un manque cruel d'observation in situ. Ainsi la majorité des études antérieures sur les mécanismes de formation et de modification des masses d'eau SAMW et AAIW se sont appuyées sur des modèles numériques (Speer et al., 1995 ; Ribbe, 1999 ; Rintoul et England, 2002). Nous essayerons dans cette étude de mieux comprendre ces processus en nous limitant le plus possible aux informations contenues dans les données de l'océan recueillies in situ.

Bien que l'Hémisphère Sud souffre d'une pauvreté de données en matière d'observations in situ, le développement récent de grands projets internationaux comme le programme ARGO permet désormais une étude détaillée de la dynamique océanique des régions Australes. Le programme international ARGO a été mis en place dans tous les océans du monde dans le cadre d'un système de prévision de l'état des océans. Ce programme ARGO vise à développer et à généraliser la mise à l'eau de nouveaux flotteurs profilants Lagrangiens. Ceux-ci transmettent tous les dix jours par satellite leurs relevés de température et de salinité entre 0 et 2000 mètres de profondeur. L'objectif initial de ARGO de trois mille flotteurs dérivant dans l'ensemble des océans du monde est aujourd'hui en passe d'être atteint.

Ainsi, la quantité de profils de température et de salinité de la base de données ARGO recueillie en moins de cinq ans dans l'Océan Austral est aujourd'hui comparable à des dizaines d'années de profils collectés lors de missions océanographiques par bateau. L'Océan Austral est par ailleurs parsemé d'une grande quantité de dériveurs de surface permettant pour la première fois d'étudier la dynamique océanique des premiers mètres de l'océan à grande échelle et pendant toutes les saisons. Les données des flotteurs ARGO et des dériveurs de surface représentent une réelle avancée dans l'étude des eaux intermédiaires Antarctiques et des eaux modales Subantarctiques. En effet, ces instruments de mesure échantillonnent des données toute l'année, notamment en hiver lorsque ces masses d'eau se forment, alors que les données historiques provenant des bateaux sont très rares pendant la saison hivernale dans l'Océan Austral. Cependant, les profils de température et de salinité rassemblés dans le cadre du programme international WOCE (World Ocean Circulation Experiment) sont tout de même une source considérable d'observations de la colonne d'eau des océans. Ce programme, lancé en 1990 et réunissant une trentaine de pays a pour but de mesurer une fois pour toutes la structure 3-D de l'océan avec des profils hydrologiques de bonne qualité. Si les données récentes des dériveurs de surface et des profileurs ARGO nous apportent une information inestimable pour l'observation des variations spatio-temporelles de l'Océan Austral, notre étude s'est également fortement appuyée sur les données du programme WOCE pour établir correctement l'état moyen de l'océan.

Le présent travail de thèse a consisté à comprendre et à documenter les processus physiques de formation des SAMW autour de la ceinture circumpolaire Antarctique en exploitant au maximum toutes les observations de l'Océan Austral, en les confrontant et en profitant de leur éventuelle complémentarité. Afin d'aller au-delà d'une description qualitative des propriétés des SAMW, nous sommes passés par des étapes intermédiaires afin de préciser la relation entre les SAMW et la dynamique océanique Australe. Ainsi, nous avons ajouté aux études directes de la formation des SAMW, l'analyse des problèmes que posent la variabilité de la circulation de l'ACC et l'importance de la diffusion tourbillonnaire sur la formation de ces masses d'eau.

Ce manuscrit a été organisé en cinq parties : un état de l'art de la physique océanique de l'Océan Austral (chapitre 1) précède l'exposition des quatre grands chantiers qui ont fait l'objet du travail de ces trois dernières années. En nous appuyant sur un bilan de chaleur à une échelle régionale dans la zone de formation des SAMW de l'Océan Indien Sud-Est, nous avons mis à jour les forçages directs ou indirects intervenant de façon notable dans le renouvellement de cette masse d'eau (chapitre 2). Nous avons en particulier pu remarquer que les SAMW avaient un lien étroit avec la circulation de l'ACC, et spécialement avec le front Subantarctique. Nous avons également trouvé que la diffusion tourbillonnaire avait un impact local important sur la répartition des zones de formation des SAMW. Il nous a donc été nécessaire de prendre du recul sur la formation des SAMW afin de parvenir à mieux définir chacun des deux axes que constituent, d'une part la circulation de l'ACC et d'autre part la diffusion tourbillonnaire. Nous nous sommes efforcés à mener une enquête détaillée sur la définition des fronts de l'ACC. Nous avons voulu savoir comment ces fronts, qui traduisent la circulation de l'ACC, varient en temps et en espace. Aidés de données satellitales confrontées à des données de la colonne d'eau de l'océan, nous avons développé une technique de suivi des fronts qui nous a permis d'étudier leur réponse à des variabilités atmosphériques (chapitre 3). En parallèle, nous avons concentré nos efforts pour tenter d'apporter une nouvelle estimation de la diffusion tourbillonnaire méso-échelle dans l'Océan Austral. En nous basant sur des données de dériveurs de surface, nous avons calculé une nouvelle estimation statistique du coefficient de diffusion tourbillonnaire. Nous avons également fait ressortir les principaux facteurs physiques contribuant

à la diffusion (chapitre 4). La synthèse de ces trois premières études nous a permis d'aborder l'analyse circumpolaire des SAMW. Un bilan de chaleur des couches de mélange hivernales a mis en évidence les deux forçages dominants pour la destabilisation de la couche de mélange en hiver : le flux air-mer et le flux d'Ekman. Mais, bien que la répartition circumpolaire de ces forçages soit assez homogène, nous observons une inhomogénéité spatiale de la répartition des couches de mélange hivernales profondes. Nous avons fait ressortir deux endroits clefs où le volume de SAMW formé change brutalement : le bassin Ouest Pacifique et le bassin central Indien. C'est là, dans ces deux sites, que la circulation de l'ACC interagit avec les courants de bords Ouest. Ceci implique un inversement du signe de la diffusion tourbillonnaire qui a des conséquences locales de première importance sur les SAMW (chapitre 5). Pour clore ce travail, nous présenterons quelques conclusions préliminaires montrant en quoi ces nouveaux résultats nous ont amenés à modifier notre représentation de la circulation méridienne dans l'Océan Austral et de quelle manière. Ces réflexions nous conduiront à évoquer notre idée du lien plus général de la diffusion tourbillonaire avec la cellule méridienne et la circulation thermohaline globale.

Chapitre 1

Etat de l'art

Sa position géographique très éloignée des terres parcourues par les principaux grands explorateurs, son environnement hostile et ses conditions océanique et climatique extrêmes, ont durablement tenu l'Océan Austral à distance de la recherche scientifique. Si depuis très longtemps, les hommes avaient imaginé que des terres Australes devaient bien exister pour contrebalancer le poids des terres septentrionales, l'existence d'un océan annulaire au "Sud" n'a été mise au jour qu'au début du XVIème siècle. C'est l'époque où Magellan prit la mer à la tête d'une flotte de cinq bateaux et de deux cent soixante cinq hommes dans le but de rejoindre les îles des épices (les Moluques) sans empiéter sur le domaine Portugais. Cette mission permit en l'an 1520 la découverte du détroit qui porte son nom. Il fit le tour du monde par la voie maritime, mettant en évidence l'existence d'un océan circumpolaire. Les premières expéditions dans l'Océan Austral ont succédé à cette découverte : Francis Drake en 1578, Abel Tasman en 1642, Halley en 1700, Kerguelen-Tremarac en 1772, Cook en 1772, Weddell en 1823, etc.

L'océanographie Antarctique fait ses premiers pas à la fin du XIXème siècle, lors des campagnes du navire Anglais "Challenger" en 1873, et le "Belgica", celui du Belge Adrien de Gerlache, en 1897. Ces expéditions océanographiques s'intéressaient en particulier aux températures de l'eau de surface et de l'eau profonde mais aussi à la circulation des courants. L'équipe menée par de Guerlache a réalisé la première expédition à but uniquement scientifique et le premier hivernage sur le continent Antarctique.

Mais la connaissance de l'hydrologie de l'océan Austral débute vraiment à partir des travaux d'océanographes Anglais. Ceux-ci, de 1925 à 1939, ont recueilli des données physiques et biologiques de l'océan Austral en vue d'établir, sur des observations précises, la réglementation et le contrôle international de la chasse aux grands cétacés. Un accord international confia la responsabilité de ces recherches en 1923 à un organisme Britanique, le "Discovery Committee". Les résultats de ces observations hydrologiques conduites pour la plupart à bord du "Discovery I" et du "Discovery II" ont été exposés par G.E.R. Deacon dans trois importants articles (1933, 1937a et 1937b).

D'autres observations hydrologiques systématiques ont également été effectuées à cette période par des océanographes de diverses nationalités : les Allemands à bord du "Meteor" (Wurst, Defant, Bohnecke, Watternberg, etc.), les Norvégiens sur le "Norvegia" et le "Brategg" (Mossby, Middtun et Natvig), les Australiens aux commandes du "Discovery I", et les Francais sur le "Commandant Charcot".

Les recherches sur l'Océan Austral se sont ensuite largement développées à partir des années 1960. L'Année Géophysique Internationale (AGI) en 1957 a contribué à multiplier les efforts de la communauté scientifique et a notamment débouché sur la réalisation de cinquante-deux voyages du navire Américain Eltanin entre 1962 et 1972. Ces missions sont à l'origine de la publication d'un atlas de l'Océan Austral qui réunit des cartes des principales propriétés hydrologiques (température, salinité et oxygène) à différentes profondeurs. Le développement de modèles numériques depuis les année 1980 a beaucoup aidé à comprendre la physique de l'Océan Austral. L'amélioration des moyens de calcul et de stockage informatique que l'on connaît depuis une vingtaine d'années permet des analyses quadridimensionnelles de plus en plus réalistes.

Par ailleurs, le programme international WOCE (World Ocean Circulation Experiment) lancé en 1990 a favorisé la mise à l'eau d'un nombre considérable d'instruments de mesure océanographique. Ce programme a largement contribué à augmenter le nombre de mesures in situ dans les océans. Cependant, l'Océan Austral est une région particulièrement hostile qu'échantillonnent très peu de navires océanographiques, et que pratiquement aucun ne se risque à explorer en hiver. Aussi manque-t-on d'une bonne couverture spatio-temporelle d'observation in situ dans cet Océan. La mise en place du programme international ARGO en 1999 a en partie résolu ce problème de sous-échantillonage in situ de l'Océan Austral. Aujourd'hui, en 2007, l'objectif initial de 3000 flotteurs dans les océans du globe est pratiquement atteint. Le nombre de profils effectués dans l'Océan Austral durant les cinq dernières années est sans précédent et dépasse notablement le nombre de profils historiques effectués auparavant. La couverture spatiale et saisonnière de ces nouveaux profils est beaucoup plus équitable car les flotteurs échantillonnent toute l'année et sont bien répartis , loin des côtes, dans le milieu des gyres. Cependant, ces données méritent d'être utilisées avec circonspection car, comme tout capteur physique, les capteurs des flotteurs ARGO sont sujets à des dérives et des décalages. En règle générale, un capteur est calibré avant et après une série de mesures destinées à repérer un éventuel problème. Mais, les capteurs des flotteurs ARGO, une fois lâchés dans l'océan, ne peuvent plus être étalonnés. Il est donc nécessaire d'être méfiant face à ces données. La communauté ARGO a insisté sur ce point dès le lancement du programme (ARGO Science Team, 2000). Alors que les capteurs de pression et de température peuvent être considérés comme fiables en général[1], les capteurs de salinité sont susceptibles de connaître des dérives et décalages significatifs. Même si des méthodes pour détecter et éventuellement corriger de tels ennuis ont été développées ces dernières années (Wong et al, 2003 ; Boehme et Send, 2005), les problèmes posés par les flotteurs de l'Océan Austral sont restés sans solution. Le peu de données historiques de référence et les forts gradients de propriétés hydrologiques associés à au Courant Circumpolaire Antarctique (ACC) limitent les performances des méthodes élaborées avant tout dans l'Océan Atlantique et l'Océan Pacifique. Dans un souci de fiabilité de nos résultats, et d'aide au développement de cette "révolution" en terme de données océanographiques de l'Océan Austral, nous avons mis en oeuvre une adaptation des précédentes méthodes de correction des données de salinité ARGO, en prenant en compte les problèmes spécifiques de l'Océan Austal. Cette méthode est présentée en Annexe 1. Elle a été appliquée aux flotteurs français du programme FLOSTRAL (Sallée et Morrow, 2006). Cette méthode a également été présentée par A.Wong (coordinatrice ARGO-delayed mode pour les Etats-Unis) et C.Coatanoan (coordinatrice ARGO-delayed mode pour la France) dans le cadre de la deuxième réunion ARGO, correction en temps différé (King et Sudheer, 2006).

[1] il a récemment été découvert que toute une série de flotteurs ARGO présentent des problèmes de capteur de pression mais ce problème est dû à un défaut de construction et non à un problème intervenu après la mise à l'eau

De nos jours, l'Océan Antarctique fait l'objet de toutes les attentions. Son rôle fondamental dans la "machine climatique" ne fait plus de doute. De plus en plus nombreux sont les pays qui s'impliquent ou se sont impliqués dans les recherches sur cet océan si particulier. Le programme international CLIVAR, qui a pour objectifs la compréhension du climat et sa prévision, accorde à l'Océan Austral tout un pan de son programme. Celui-ci insiste sur la nécessité de comprendre la formation et la circulation des masses d'eau formées dans l'Océan Austral. L'année 2007 a été déclarée année polaire internationale sous l'influence du Conseil des Sciences International (ICSU) et de l'Organisation Mondiale de la Météorologie (WMO). Ceci atteste une nouvelle fois de l'importance donné aux pôles de notre planète et donne à nouveau l'occasion de rappeler le rôle fondamental que jouent ces lieux hostiles et reculés pour le climat mondial. Ce travail de thèse s'inscrit dans la continuité du développement d'une connaissance de l'Océan Austral engagée il y a quelques centaines d'années et qui s'est considérablement accélérée depuis une décennie grâce à la mise en place de grand projets internationaux. Avant d'entrer dans le détail de la recherche exposée dans cet ouvrage, nous commencerons par introduire dans un bref résumé ce que l'on sait actuellement du principal courant de l'Océan Austral, le Courant Circumplaire Antarctique et de sa structure en front hydrologique. Nous présenterons également l'état des connaissances portant sur les eaux modales Subantarctiques, masse d'eau qui sera placée au centre de nos préoccupations tout au long de cet ouvrage.

1.1 Le Courant Circumpolaire Antarctique

1.1.1 L'ACC dans un système océanique global

Le continent Antarctique est l'unique région du globe encerclée par un courant qui ne rencontre jamais dans sa course l'obstacle d'un continent. Ceci confère à l'Océan Austral une circulation proche de la circulation atmosphérique, sans comparaison avec tous les autres bassins océaniques. Cette structure circumpolaire fait de l'Océan Austral une "clef de voûte" de la complexe circulation thermohaline parcourant les océans du globe (voir Figure 1.1). La structure verticale de l'Océan Austral présente elle aussi une particularité : dans les eaux Antarctiques, les masses volumiques varient très peu avec la profondeur, comparativement aux régions tropicales ou subtropicales. Les isopycnes y sont beaucoup plus verticales que dans n'importe quelle autre région du monde. Ainsi, les forces de gradient de pression sont redistribuées de façon nettement plus équitable sur la verticale, et les courants, au lieu d'être restreints aux quelques premières centaines de mètres sur la verticale, s'étendent très profondément. Il est ainsi plus aisé de comprendre comment le courant circumpolaire Antarctique transporte une telle masse d'eau. Il déplace un volume d'eau sur plus de 2000 mètres de profondeur avec des vitesses de surface comparables à celles des autres courants du globe. Son débit atteint des valeurs moyennes de 134 Sv à travers le passage de Drake, au Sud du Cap Horn (Whitworth, 1983 ; Whitworth et Peterson, 1985) et de 150 Sv au Sud de la Tasmanie (Phillips et Rintoul, 2000 ; Rintouls et Sokolov, 2001), soit plus de cent fois celui de l'ensemble des fleuves du monde (équivalent à à peu près 1 Sv).

La forme annulaire du courant et la liaison qu'il crée entre les principaux bassins océaniques du globe permettent la mise en place d'une circulation thermohaline à grande échelle à travers les océans du globe (voir Figure 1.1), dominant les redistributions globales de chaleur, de salinité, de nutriments, et de biens d'autres propriétés influençant le climat à des échelles interannuelles (Gordon, 2001). D'autre

part, des anomalies climatiques formées dans un bassin particulier peuvent être transportées vers de très lointaines partie du globe et y produire des effets. (White et Peterson, 1996 ; White, 2000).

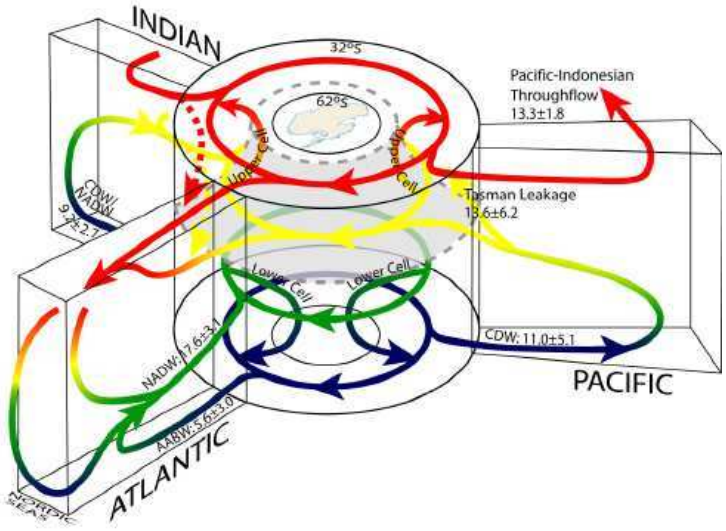

FIG. 1.1 – Schéma 3-D de la circulation thermohaline globale (de Lumpkin et Speer, 2007)

1.1.2 Dynamique, thermodynamique et rôle des tourbillons

La dynamique de l'Océan Austral interagit fortement avec la circulation atmosphérique, surtout en réponse aux forts vents d'Ouest des quarantièmes hurlants et des cinquantièmes rugissants (Baker, 1982 ; Warren et al., 1996 ; Hughes et al., 1999 ; Gille et al., 2001 ; Dong et al., 2006). Les théories classiques de la circulation de Sverdrup ne peuvent pas être appliquées à un courant non limité par des frontières zonales. La dynamique de l'ACC a ainsi été depuis longtemps sujette à des discussions théoriques. Bien plus que dans n'importe quel autre océan, les flux turbulents tourbillonnaires jouent un rôle central dans la balance thermodynamique et dynamique de l'Océan Austral.

L'ACC contribue à isoler le continent Antarctique des eaux chaudes subtropicales. Le fait que le courant géostrophique tourne en boucle sur lui-même de façon quasi-zonale implique qu'il n'y a aucun écoulement géostrophique méridional net, et contribue en quelque sorte à conserver l'état glacial du continent Antarctique (Rintoul et al., 2001). Un transport de chaleur existe néanmoins entre le nord et le sud de l'ACC, mais celui-ci est pris en charge principalement par le transport tourbillonnaire dans les premiers 2000 mètres (Rintoul et al., 2001). Le transport tourbillonnaire, induit principalement par des instabilité baroclines qui transforment l'énergie potentielle contenue dans l'ACC en énergie cinétique, joue un rôle fondamental dans la balance dynamique et thermodynamique de l'ACC (McWilliams et al., 1978 ; Marshall et Shutts, 1981 ; Johnson et Bryden, 1989 ; Gille, 1997 ; Phillips et Rintoul, 2000 ; etc.).

L'Océan Austral est le seul océan à être dépourvu de barrière continentale zonale. Ainsi les théories classiques de circulation à grande échelle ne sont pas applicables dans cet océan (Sverdrup, 1947 ; Hughes,

2002). En particulier, il n'existe pas de fort courant méridional à ces latitudes. Les forts vents d'Ouest de l'hémisphère Sud induisent des écoulements d'eau de surface vers le Nord par transport d'Ekman. La question qui s'est posée très tôt aux océanographes a donc été celle de savoir quelle force zonale était susceptible de contrebalancer la tension de vent zonale. Il s'avère qu'au niveau des dorsales océaniques de grande taille (de profondeur inférieure à 2000 mètres), cette quantité de mouvement introduite par le vent en surface est équilibrée par des pertes de quantité de mouvement par "form drag". Lorsque l'ACC qui s'écoule vers l'Est passe au dessus d'une dorsale d'extension méridionale, l'amont de la dorsale est caractérisé par de fortes pressions alors que l'aval l'est par de faibles pressions. Ceci s'explique par le fait que le courant a tendance à s'orienter vers le Nord lorsque la colonne d'eau s'amincit (ou a contrario vers le Sud lorsque celle-ci s'épaissit) par conservation de vorticité potentielle. Le gradient de pression zonale ainsi installé sous le niveau de la dorsale (à peu près 2000 mètres en général dans l'Océan Austral) se traduit par géostrophie en un transport de masse net vers le Sud qui équilibre le transport d'Ekman de surface vers le Nord. Le transfert de quantité de mouvement sur la colonne d'eau entre la source en surface et le puits au fond est assuré par les flux tourbillonnaires verticaux (Munk et Palmen, 1951 ; Bryden et Heath, 1985 ; Olbers, 1998 ; Johnson et Bryden, 1989 ; Treguier et McWilliams, 1990 ; Döös et Webb, 1994 ; Morrow et al., 1994 ; Phillips et Rintoul, 2000 ; Rintoul et al, 2001)

L'absence de courant méridien important à ces latitudes a aussi des conséquences sur le bilan thermodynamique. L'équilibre nécessaire des pertes de chaleur dans les régions polaires doit donc être assuré par un processus différent de celui qui est à l'oeuvre dans les autres océans. Le budget de chaleur à grande échelle de la zone au Sud de l'ACC implique nécessairement un fort flux de chaleur tourbillonnaire vers le Sud à travers le courant (de Szoeke et Levine, 1981). Les observations numériques le confirment en montrant un transport de chaleur de 0.3-0.7 PW à la traversée de l'ACC (Gordon et Owens, 1987 ; Keffer et Holloway, 1988). Ce flux de chaleur est principalement assuré par les tourbillons océaniques (Bryden, 1979 ; de Szoeke et Levine, 1981 ; Speer et al., 2000). A partir d'études locales extrapolées à la ceinture circumpolaire, on arrive en première approximation à fermer le budget de chaleur grâce aux flux tourbillonnaires (Bryden, 1979 ; Nowlin et al., 1985 ; Bryden and Heath, 1985 ; Johnson et Bryden, 1989 ; Phillips et Rintoul, 2000 ; Rintoul et al., 2001).

Si les effets tourbillonnaires sur les propriétés hydrologiques sont souvent étudiés en terme de transport de chaleur, il est bon de rappeler qu'il ont une conséquence sur tous les traceurs hydrologiques. Ils produisent notamment un effet démontré et non négligeable sur le transport de sel (Keffer et Holloway, 1988 ; Stammer, 1998 ; Morrow et al., 2003). L'étude du transport du sel et de sa diffusion pourrait apporter une aide substantielle à l'analyse des caractéristiques des masses d'eau SAMW et AAIW. Les mesures croissantes de salinité des océans à partir des données ARGO ouvrent la voie à des études plus précises dans ce domaine. De plus, le développement du programme de mesure satellitale de salinité de surface SMOS, qui est encore aujourd'hui en préparation, permet d'espérer dans un futur proche un important développement de nos connaissances dans ce domaine.

Si les tourbillons jouent un rôle important dans le transfert de quantité de mouvement et dans le transport de chaleur et de sel, ils sont aussi déterminants dans les processus de mélange et de diffusion de ces traceurs. L'axe de l'ACC, en particulier, est associé à une forte activité tourbillonnaire qui a été précédemment observée par altimétrie (Chelton et al., 1990 ; Morrow et al., 1994), ainsi que par le biais des flotteurs de surface (Daniault et Ménard, 1985 ; Zhou et al., 2002 ; Zhurbas et Oh, 2004). Ainsi, deux particules lâchées au même instant dans l'océan dans des zones très proches l'une de l'autre peuvent être animées de trajectoires très différentes. Ce phénomène traduit la turbulence de l'océan

de même que la dispersion et la diffusion des particules associées. Les tourbillons de moyenne échelle ont été reconnus comme jouant un rôle important dans la diffusion (Stammer, 1998). Ils provoquent un mélange des caractéristiques hydrologiques le long de surfaces isopycnes. Cette diffusion tourbillonnaire est une composante encore mal connue de l'écoulement horizontal. Elle est pourtant fondamentale et sa connaissance faciliterait la compréhension approfondie des mécanismes qui contrôlent le transport de propriétés hydrologiques, biologiques et chimiques par les instabilités baroclines. La diffusion réunit des phénomènes beaucoup trop complexes pour pouvoir être écrite de façon mathématique. Il a été reconnu depuis longtemps que ces phénomènes nécessitaient une description statistique et donc un grand nombre de données. Or le manque de données in situ dans l'Océan Austral a jusqu'ici empêché toute tentative de mesure in situ de ses effets. La diffusion tourbillonnaire est paramétrée dans les modèles numériques, mais ces paramètres n'ont pratiquement jamais été confrontées à des mesures réelles de la diffusion à grande échelle. On considère pourtant la diffusion tourbillonnaire comme un possible régulateur de la tendance au réchauffement observé dans l'Océan Austral (Hogg et Blundell, 2007). Une partie de cette thèse est consacrée à une meilleure description de la diffusion tourbillonaire dans l'Océan Austral (Chapitre 4).

1.1.3 Circulation horizontale et notion de front

L'ACC n'est pas un grand fleuve s'écoulant en un bloc cohérent, mais peut être schématisé sous la forme d'une association de plusieurs fronts circumpolaires. Ces fronts correspondent d'une part à la frontière entre des masses d'eau de caractéristiques hydrologiques différentes, d'autre part aux puissants jets océaniques composant l'ACC (Orsi et al., 1995). Ce que l'on appelle courant circumpolaire est en effet la juxtaposition de très intenses et profonds "filaments de courants" pouvant se joindre à certains endroits pour former de plus forts courants, se dissocier en d'autres points, ou encore s'intensifier ou s'affaiblir (Hughes et Ash, 2001 ; Sokolov et Rintoul, 2002). On nomme fronts ces forts jets océaniques. Les deux principaux fronts de l'ACC sont le front Subantarctique (SAF) et le front Polaire (PF), représentés schématiquement en Figure 1.2. Ces fronts représentent aussi une barrière hydrologique séparant au Nord et au Sud de chacun d'entre eux des masses d'eau aux caractéristiques distinctes. Les fronts sont classiquement définis par leurs caractéristiques en sub-surface (Orsi et al., 1995 ; Belkin et Gordon, 1996). Cependant, à cause de la difficulté à recueillir des données de la colonne d'eau, les fronts définis de cette manière sont toujours considérés sous un angle climatologique. Une série de nouvelles définitions frontales basées sur des produits satellitaux a récemment vu le jour (Moore et al., 1999 ; Sokolov et Rintoul, 2002 ; Dong et al., 2006 ; Sokolov et Rintoul, 2007). Le grand avantage de ces définitions est qu'elles permettent d'aborder la variabilité frontale. Une partie de cette thèse aborde ce sujet de définition frontale et de sa variabilité temporelle et spatiale (Chapitre 3).

Comme nous l'avons mentionné plus haut, l'ACC est un courant très profond se répartissant sur une grande partie de la colonne d'eau. Ceci fait de l'Océan Austral un océan quasi-barotrope, très influencé par les fonds sous-marins. La bathymétrie a un rôle très important dans la dynamique de l'Océan Austral. Les fronts de l'ACC sont notamment conduits en premier ordre par les grosses structures bathymétriques (voir entre autres Gordon et al., 1978 ; Chelton et al., 1990 ; Gille, 1994 ; Moore et al., 1999 ; Sokolov et Rintoul, 2006 ; Dong et al., 2006). Figure 1.2 montre à quel point les positions du PF et du SAF sont dépendantes de la péninsule Antarctique et de la pointe du continent Sud Américain, du plateau de Kerguelen, du plateau de Campbell, ou encore de la zone de fracture de la dorsale du Pacifique. Au nord du fort courant circumpolaire, la circulation est dominée par les gyres subtropicaux anticycloniques

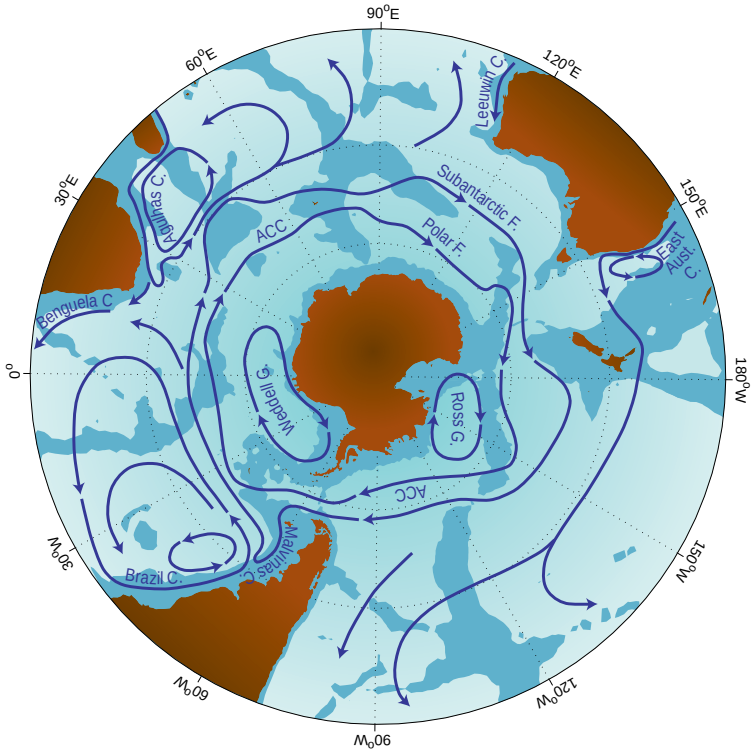

FIG. 1.2 – Carte schématique des courants principaux de l'hémisphère Sud, au Sud de 20°S. Les profondeurs inférieures à 3500 mètres sont colorées en bleu plus foncé. Les deux fronts les plus puissants de l'ACC sont indiqués : le PF et le SAF. Les autres abréviations sont F pour front, C pour courant, et G pour gyre. (de Rintoul et al., 2001)

et leurs forts courants de bord Ouest : courant du Brésil, des Malouines, des Aiguilles et du Sud-Est Australien (voir Figure 1.2). Ces gyres profonds pilotés par une dynamique de Sverdrup, permettent l'exportation vers les tropiques des masses d'eau formées dans l'ACC dans la partie Est des bassins, ainsi que l'advection d'eau chaude et salée subtropicale vers le courant circumpolaire à travers les courants de bord ouest.

1.1.4 Circulation verticale

La circulation horizontale annulaire de l'ACC est associée à une circulation verticale méridionale plus complexe. La Figure 1.3 en propose une vue schématique. Elle est très largement dominée par les flux air-mer, et surtout les vents de surface et les transports d'Ekman associés, qui provoquent des divergences, des convergences, et forcent la plongée ou la remontée des eaux (Speer et al., 2000). Cette circulation est liée à la formation de masses d'eau et à la ventilation des océans du globe (voir Figure 1.1). Les masses d'eau exportées vers les tropiques depuis l'Océan Austral, dans les couches intermédiaires et abyssales, contribuent à la remontée et à un renouvellement des eaux profondes des océans. Schématiquement, les eaux profondes Nord Atlantiques (NADW) remontent à la surface au Sud de l'ACC, sont advectées au Nord par les courants d'Ekman, puis pénètrent à nouveau dans l'océan en formant les eaux intermédiaires Antarctiques et modales Subantarctiques (voir Figure 1.3 ; Sverdrup et al., 1942 ; Speer et al., 2000). Une autre partie des NADW qui remontent à la surface est transformée en eaux abyssales de fond (AABW) puis plonge le long du continent Antarctique. La transformation et formation de masses d'eaux dans l'Océan Austral permet l'existence d'une intense circulation thermohaline à l'échelle planétaire et renouvelle les eaux des océans du globe (voir Figure 1.1). Cette circulation est animée par les intenses interactions entre air, mer et glace dans l'Océan Austral (Rintoul et al., 2001).

Bien que le rôle de cette circulation et de l'Océan Austral sur le climat soit reconnus depuis des dizaines d'années, les études précises des chemins de circulation et de la quantité d'eau exportée ne sont que très récentes. L'un des objectif de cette thèse est de mieux comprendre la formation des masses d'eau modales subantartiques (SAMW) qui naissent en hiver austral au nord du front Subantarctique de l'ACC.

1.2 Masses d'eau associées au fronts de l'ACC

Les masses d'eaux de profondeurs intermédiaires de l'Océan Austral ont été depuis longtemps reconnues comme essentielles à la ventilation de la thermocline des gyres subtropicaux (McCartney, 1982). Elles sont également considérées comme des indices potentiels de changement climatique. Les deux principales masses d'eaux de profondeur intermédiaire sont les eaux modales Subantarctique (SAMW) et les eaux intermédiaires Antarctique (AAIW). Des observations de changement en température et en salinité des eaux de profondeur intermédiaire (SAMW, AAIW) donnent à penser que la couche supérieure de la circulation thermohaline pourrait déjà répondre à de sensibles baisses de salinité polaire (Bindoff et Church, 1992 ; Bindoff et McDougall, 2000 ; Johnson et Orsi, 1997 ; Wong et al., 1999 ; Rintoul, 2007). Des changements de propriétés des AAIW et SAMW pourraient rétro-agir sur les cycles hydrologiques et la capacité de stockage de chaleur des gyres subtropicaux (Gordon, 1991). L'étude de la formation et de la circulation de ces masses d'eau a été reconnue comme nécessaire à la compréhension du climat et à sa prévision.

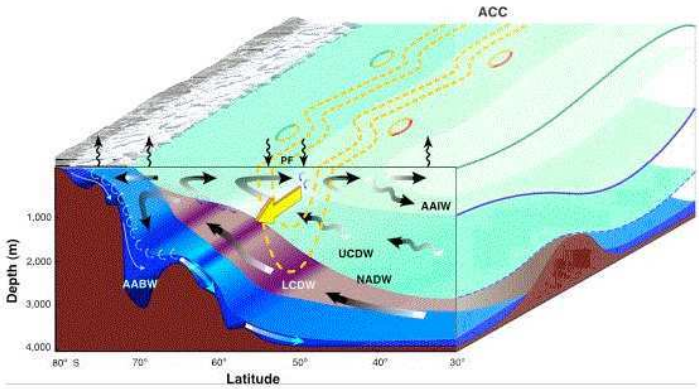

FIG. 1.3 – Vue schématique de la circulation méridionale dans l'Océan Austral. Une cellule supérieure est formée par les courants d'Ekman en surface vers le Nord et fermée par un transport tourbillonnaire vers le Sud dans la couche des UCDW. Une cellule inférieure est constituée par la formation des denses AABW le long du continent Antarctique. AAIW : eau intermédiaire Antarctique ; UCDW : eau profonde circumpolaire supérieure ; NADW : eau profonde de l'Atlantique Nord ; LCDW : eau profonde circumpolaire inférieure ; AABW : eau Antarctique de fond (de S.Rintoul inspiré de Speer et al., 2000)

1.2.1 Les eaux modales Subantarctiques (SAMW)

Masuzawa (1969) a été le premier à parler d'eau modale. Il a défini l'eau modale subtropicale en référence à une couche de température de 16-18 degrés Celsius dans le Nord Ouest du gyre subtropical du Pacifique Nord. Ce terme d'eau modale a été étendu à l'épaisse couche d'eau de subsurface au Nord du front subantarctique de l'ACC par McCartney (1977). Puis McCartney and Talley (1982) ont appliqué le terme d'eau modale subpolaire à l'épaisse couche d'eau de subsurface du gyre subpolaire Nord Atlantique. Le terme d'eau modale est désormais générique pour désigner une couche d'eau de caractéristique hydrologique (température, salinité et densité) homogène verticalement et recouvrant une grande zone géographique. Pour distinguer les eaux modales les unes des autres, on a ajouté des qualificatifs liés aux sources. Des eaux modales ont été repérées dans chacun des océans (voir Figure 1.4a) et leur région de formation est toujours située à proximité d'un courant ou d'un front. Il s'avère qu'elles se trouvent toujours du côté chaud du courant ou du front, et sont formées dans la couche de mélange profonde en hiver. Ainsi a-t-on nommé eaux modales Subantactiques (SAMW) les eaux qui se forment au nord du front Subantarctique.

Les eaux modales représentent un gros volume comparé aux masses d'eau environnantes, ce qui leur confère une importance d'autant plus grande en terme d'impact climatique. Elles naissent dans les régions de très profonde couche de mélange hivernal et une fois subductées dans l'intérieur de la colonne d'eau, elles se caractérisent par une homogénéité verticale de leurs propriétés telles que leurs caractéristiques hydrologiques, ou encore par un minimum de vorticité potentielle (PV). Les eaux modales, sous l'angle du minimum de vorticité potentielle sont un très bon traceur de la ventilation subtropicale, aussi intéressantes que les traceurs chimiques.

Les eaux modales Subantarctiques sont produites dans l'épaisse couche de mélange hivernal se développant au Nord du SAF (McCartney, 1977). Cette masse d'eau subducte dans l'océan intérieur à travers cette épaisse couche de mélange qui crée une sorte d'ouverture entre la surface et l'océan intérieur, à travers la thermocline saisonnière. Elle est ensuite advectée vers le Nord et recircule dans les gyres subtropicaux. Cette advection conduit à la formation d'une épaisse couche fortement chargée en oxygène qui persiste même au delà des tropiques (McCarthy et Talley, 1999), servant ainsi à ventiler l'océan de subsurface (McCartney, 1982 ; Hanawa et Talley, 2001). Au lieu de recirculer vers le Nord, une portion des SAMW est advectée vers l'Est par l'ACC où elle est refroidie et devient ainsi plus dense (Hanawa et Talley, 2001).

Plusieurs études récentes ont montré l'importance des SAMW dans le système climatique, soit directement à travers des anomalies de température, de salinité ou de contenu en CO_2 de cette couche d'eau (Wong et al, 1999 ; Sabine et al, 2004), soit indirectement par des contrôles physiques et biologiques de flux de CO_2 à travers les SAMW (Sarmiento et Orr, 1991 ; Caldeira et Duffy, 2000 ; Sarmiento et al., 2004 ; Metzl et al., 1999).

Une compréhension approfondie de la formation et de la circulation de ces eaux, et en particulier des processus déterminant leurs propriétés hydrologiques et biologiques, est nécessaire pour répondre aux questions fondamentales sur le carbone, le cycle des nutriments et de la circulation thermohaline dans un contexte de changement climatique. L'Organisation Internationale sur la Variabilité du Climat et sa Prédiction (CLIVAR) en fait d'ailleurs un de ses objectifs principaux.

1.2.2 Les eaux intermédiaires antarctiques (AAIW)

L'eau intermédiaire Antarctique (AAIW) est une couche d'eau peu salée s'étendant directement sous la couche des SAMW. Le mécanisme de formation des eaux antarctiques intermédiaires reste encore mal connu et débattu. Soit elles sont issues d'un mélange à travers le front polaire en différentes régions le long du courant circumpolaire et en particulier dans le Sud Ouest de l'Atlantique (McCartney, 1977 ; Talley, 1996 ; England et al., 1993), près de la côte d'Amérique du Sud. Soit elles résultent de la densification et du radoucissement des eaux modales subantarctiques, intervenant tout au long du trajet circumpolaire depuis le bassin Atlantique (Sverdrup et al., 1942 ; Sorensen et al., 2001) (voir Figure 1.4b).

On trouve des AAIW dans tous les secteurs de l'Océan Austral au nord du PF (Figure 1.4b). Ces eaux sont caractérisées par un minimum de salinité. Leurs caractéristiques en température/salinité ont déjà été largement documentées dans plusieurs études (Deacon, 1933 ; Piola et Georgi, 1982). Des changements de grande échelle des propriétés de ces eaux ont été mis en évidence selon qu'elles appartiennent à tel ou tel océan. Ainsi, elles sont plus chaudes et salées dans l'océan Indien Sud et plus douces et froides dans l'Atlantique Sud. Après leur formation, on sait qu'elles sont transportées vers l'Est par le courant circumpolaire et s'étendent vers le Nord depuis le PF à des profondeurs intermédiaires autour de 800-1000 mètres, en dessous de la thermocline subtropicale et des eaux modales, à une densité potentielle avoisinant 27.1-27.3 $kg.m^{-3}$ (Molinelli, 1981 ; Piola et Georgi, 1982). Les AAIW se différencient clairement des SAMW par leur faible taux d'oxygène et un maximum en PV (McCartney, 1977).

Les AAIW pénètrent dans chacun des trois océans de l'hémisphère Nord (Atlantique : Wust, 1935 et Taft, 1963 ; Pacifique : Reid, 1965 et Tsuchiya, 1991 ; Indien : Taft, 1963). Elles ont été observées très au nord, jusqu'à 30°N dans l'océan Atlantique Nord (Pickard et Emery, 1990 ; Talley, 1996)

Le nombre croissant des études portant sur cette masse d'eau est en adéquation avec l'importance que la communauté scientifique lui confère dans la balance globale du transport de chaleur et de sel dans l'océan (Piola et Geogi, 1982 ; England et al., 1993 ; Johnson et Orsi, 1997 ; Wong et al., 1999). La connaissance de la variabilité des propriétés des AAIW, tout comme celle des SAMW, est fondamentale pour la compréhension à long terme d'un changement climatique.

1.3 Forçage climatique de l'hémisphère Sud.

Le moteur principal de la dynamique de l'Océan Austral, tant du point de vue de la circulation horizontale que de celui de la circulation verticale méridienne, essentielle dans la circulation globale thermohaline, est l'interaction entre l'océan, l'atmosphère et les glaces de mer. Le mode climatique dominant de l'Hémisphère Sud est le "Southern Annular Mode (SAM)". Ce mode de variabilité du climat a une structure annulaire. Il consiste en un bipôle de pression atmosphérique (défini en général à partir de la surface 700 Hpa) avec un pôle de basse pression centré sur le continent Antarctique et un pôle circumpolaire de haute pression autour des latitudes -50°S lors d'un épisode positif (Thompson et Wallace, 2000). Une telle variabilité atmosphérique implique, lors d'un épisode positif, une contraction des vents dominants de l'Hémisphère Sud sur un axe plus au Sud. Le SAM a des conséquences dans un nombre considérable de domaines dans l'Hémisphère Sud. Cette variabilité pourrait en particulier avoir un impact sur le chenal moyen des cyclones, sur le taux des précipitations en Australie, sur la variabilité de la fonte

des glaces en Antarctique ou encore sur le transport de l'ACC (Hall et Visbeck, 2002 ; Sen Gupta et England, 2006 ; Yuan, 2004). Le SAM doit son existence à une interaction entre l'écoulement moyen et tourbillonnaire atmosphérique dans le chenal des trajectoires des tempêtes de l'hémisphère Sud (Thompson et Wallace, 2000). Il est aujourd'hui clair que le SAM a suivi une tendance croissante ces 50 dernières années (Thompson et Wallace, 2000 ; Thompson et Salomon, 2002 ; Marshall, 2003). Cette tendance a été attribuée dans certaines études à une influence de l'activité humaine, soit du fait des changements de l'ozone stratosphérique (Thompson et Salomon, 2002 ; Gillett et Thompson, 2003 ; Arblaster et Meehl, 2006), soit par le biais d'une augmentation de l'effet de serre (Fyfe et al., 1999 ; Kushner et al., 2001 ; Cai et al., 2003). D'autres études ont plutôt proposé l'hypothèse que ce changement n'était dû qu'à des variabilités naturelles (Marshall et al., 2004). Cette question est encore ouverte aux débats scientifiques, mais il est avéré que le nombre d'événements positifs du SAM tend à augmenter sur des échelles de temps décennales depuis les années 1950 et que ceci a un impact sur le climat de l'hémisphère Sud. Le SAM aurait un impact sur la circulation océanique Australe. Un événement positif du SAM pourrait par exemple contracter légèrement la circulation océanique plus au Sud et en renforcer l'intensité (Hall et Visbeck, 2002 ; Sen Gupta et England, 2006). D'autre part, cet indice pourrait avoir un impact sur la profondeur de la couche de mélange au Nord de l'ACC, et avoir ainsi un impact indirect sur la biologie dans l'Océan Austral (Lovenduski et Gruber, 2005).

Le mode climatique du Pacifique tropical ENSO (El-Niño Southern Oscillation) a, lui aussi, une forte influence sur les hautes latitudes de l'Hémisphère Sud. Un lien atmosphérique est créé par l'onde de Rossby sur des échelles de temps très courtes entre le Pacifique tropical et les zones extratropicales du Pacifique (Karoly, 1989). Ce mode influence la circulation atmosphérique mais aussi la distribution de glace de mer dans le Pacifique Sud et le Sud-Ouest Atlantique (Renwick, 2002 ; Kwok et Comiso, 2002 ; Yuan, 2004). Il a été montré qu'il pourrait exister des corrélations entre ce mode et le SAM (L'Heureux et Thompson, 2004). Ces corrélations semblent être plus importantes pendant la saison estivale. Cependant ces relations entre indices climatiques sont encore peu comprises.

Ces dernières 10 années, la communauté scientifique a beacoup parlé de l'onde circumpolaire Antarctique (ACW) qui a été décrite pour la première fois par White et Petterson (1996). Il s'agit d'une propagation d'Ouest en Est d'anomalies en température à la surface de la mer, en pression à la surface océanique, en étendue des glaces de mer et en tension méridienne de vent. Cette onde a une amplitude maximum entre 50-60°S et est associée au nombre d'onde 2. La période apparente de cette onde circumpolaire est d'environ 4 ans. L'ACW peut avoir des conséquences climatiques importantes(White et Cherry, 1998 ; White, 2000). La compréhension de l'origine de cette onde reste au coeur des débats scientifiques (Peterson et White, 1998 ; Qiu et Jin, 1997 ; Goodman et Marshall, 1999 ; Weisse et al., 1999). Son existence a cependant été récemment de plus en plus remise en cause (Connoley, 2002 ; Visbeck et Hall, 2004). Elle avait en effet une signature claire entre les années 1985 et 1994, mais sa régularité et son intensité sont nettement moins marquées après cette période. La tendance dans la communauté scientifique depuis la fin des années 1990 est de privilégier l'étude du mode annulaire de l'Hémispère Sud (SAM) qui semble finalement avoir un impact plus dominant dans l'Hémisphère Sud que l'ACW.

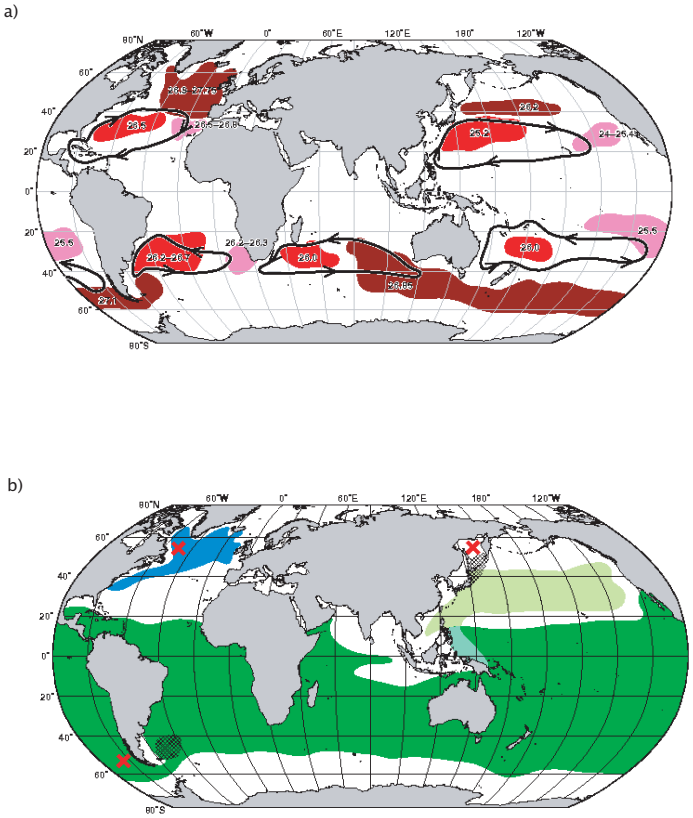

FIG. 1.4 – **(a)** Distribution des eaux modales dans les océans (Talley, 1999). Les zones rouges montrent les eaux modales subtropicales (STMW) associées aux courants de bord Ouest. Les zones roses indiquent les eaux modales de type Est et les zone brunes désignent les eaux modales subtropicale et subpolaire, notamment les eaux modales subantarctiques (SAMW). Les densités potentielles approximatives sont indiquées. Les boucles avec des flèches montrent leur recirculation dans chaque gyre subtropical.**(b)** Distribution des eaux intermédiaires dans les océans (Talley, 1999). L'endroit de formation de chacun des trois types d'eaux intermédiaires est marqué par un X. Les régions d'important mélange proches des sources de ventilation qui affectent fortement les caractéristiques de ces eaux sont hachurées.

Chapitre 2

Formation des SAMW dans l'océan Indien Sud-Est

Depuis les premières études sur les eaux modales Subantarctiques, nous savons que ces eaux se forment en hiver Austral dans l'épaisse couche de mélange au Nord du front Subantarctique (McCartney, 1977). Ces eaux subductent ensuite dans l'océan intérieur en conservant durablement leurs propriétés hydrologiques acquises en surface. Cette masse d'eau est très épaisse sur la verticale et très étendue horizontalement sous la thermocline. Elle représente ainsi un volume considérable d'eau, qui a une forte influence sur le système climatique (Sarmiento et Orr, 1991 ; Caldeira et Duffy, 2000 ; Sarmiento et al., 2004 ; Metzl et al., 1999). Ces impacts climatiques sont en partie modulés par les propriétés hydrologiques de la masse d'eau. Aussi est-il de la première importance, dans un contexte d'étude du climat, de comprendre quels sont les processus qui entrent en jeu dans la détermination des propriétés hydrologiques des SAMW dans leur zone de formation (Sarmiento et al., 2004). Cette problématique revient à comprendre quels sont les phénomènes physiques qui provoquent la déstabilisation de la couche de mélange hivernale au Nord du SAF en hiver austral et qui vont ainsi forcer la formation des SAMW.

Plusieurs études se sont déjà penchées sur ces questions. Mais à cause du grand manque de données in situ dont souffre l'Océan Austral, les travaux consacrés aux phénomènes de formation des SAMW à une échelle régionale ont été limités au calcul de certaines composantes du forçage ou à des études numériques basées sur des modèles ou des analyses dimensionnelles (Speer et al., 1995 ; Ribbe, 1999 ; Rintoul et England, 2002). Jamais ces résultats n'ont été confrontés à l'évolution réelle de la colonne d'eau.

Le but que nous nous sommes fixés dans le premier volet de cette thèse est de tenter de lever les incertitudes à ce sujet en étudiant l'évolution de la couche de mélange d'un point de vue temporel à partir de données in situ. Forts du nouveau jeu de données ARGO, nous avons suffisamment de matériel recueilli in situ pour effectuer un bilan de chaleur à grande échelle de la couche de mélange dans la zone de formation des SAMW. Cette étude porte sur la zone du Sud-Est de l'Océan Indien qui est une très large région de formation des SAMW (McCartney, 1982). Cette région présente l'interêt de rassemblé des couches de mélange extrêmement profondes (approximativement 600 mètres), et une bonne répartition de données in situ ARGO, données dont une partie est issue du programme FLOSTRAL.

Notre principale motivation était de vérifier avec des données in situ les résultats de la plupart des études précédentes. Ceux-ci avancent que seuls les flux de chaleur air-mer aidés du transport d'Ekman peuvent expliquer la variation du contenu de chaleur de la couche de mélange. Nous voulions également comprendre pourquoi la déstabilisation de la couche de mélange n'apparaît que dans l'Est du bassin Sud-Indien, alors que l'Ouest et l'Est du bassin sont soumis à des forçages air/mer et d'Ekman d'intensités comparables. Pour répondre à ces questions nous nous sommes intéressés à l'évolution de la stabilité et du contenu de chaleur de la couche de mélange pendant les années 2003 et 2004, pendant lesquelles nous avions suffisamment de données ARGO. Les résultats de cette étude ont abouti à la publication d'un article en décembre 2006 dans le journal *Ocean Dynamics* dont la version finale fait l'objet du paragraphe suivant.

2.1 Formation of subantarctic mode water in the Southeastern Indian Ocean (Sallée J.B. , Wienders N. , Morrow R., et Speer K., 2006)

abstract : Subantarctic Mode Water is the name given to the relatively deep surface mixed layers found directly north of the Subantarctic Front in the Southern Ocean, and their extension into the thermocline as weakly stratified or low potential vorticity water masses. The objective of this study is to begin an investigation into the mechanisms controlling SAMW formation, through a heat budget calculation. ARGO profiling floats provide estimates of temperature and salinity typically in the upper 2000 meters, and the horizontal velocity at various parking depths. These data are used to estimate terms in the mode water heat budget ; in addition, mode water circulation is determined with ARGO data and earlier ALACE float data, and climatological hydrography. We find a rapid transition to thicker layers in the central South Indian Ocean, at about 70^oS, associated with a reversal of the horizontal eddy heat diffusion in the surface layer and the meridional expansion of the ACC as it rounds the Kerguelen Plateau. These effects are ultimately related to the bathymetry of the region, leading to the seat of formation in the region southwest of Australia. Upstream of this region, the dominant terms in the heat budget are the air-sea flux, eddy diffusion, and Ekman heat transport, all of roughly equal importance. Within the formation area, the Ekman contribution dominates and leads to an downstream evolution of mode water properties.

2.1.1 Introduction

Mode water is the name given to an ocean layer with physical properties (temperature, salinity) that are nearly homogeneous vertically and horizontally, covering an extended area in a given basin (e.g. Hanawa and Talley, 2001), and thus occupying a relatively large volume compared to other water types. Mode waters can be identified by relatively deep surface mixed layers, or, within the water column, by a pycnostad on a density-depth plot, or by a minimum of large-scale potential vorticity. They are one of the primary results of air-sea interaction (Speer et al., 1995), and serve to ventilate the interior of the upper ocean as they spread within gyres and boundary currents (McCartney, 1982 ; Hanawa and Talley, 2001).

In the Southern Ocean, Subantarctic Mode Water (SAMW) is formed when winter cooling leads to convection and the formation of a deep mixed layer just north of the Subantarctic Front (SAF) (McCartney, 1977). In the Indian Ocean, as in the Atlantic and Pacific Oceans, SAMW then enters the thermocline by advection and diffusion ("spreading") where it becomes part of central waters, and contributes to ventilating the thermocline. Oxygen rich layers thus formed may persist to the tropics (McCartney, 1982). These waters progress in density (and decreasing temperature) from west to east culminating in the formation of Antarctic Intermediate Water in the southeast South Pacific Ocean.

Recently, the role of the SAMW in the climate system has been brought to light, both directly, via observed changes in the temperature, salinity, and CO2 of mode water thought to be related to climate change (e.g. Wong et al., 1999, Sabine et al., 2004), and indirectly, by the physical and biological controls on CO2 fluxes into and out of this water mass (Sarmiento and Orr, 1991 ; Caldeira and Duffy,

2000 ; Sarmiento et al., 2004 ; Metzl et al., 1999). We need to understand the formation mechanisms for SAMW, in particular which processes set their hydrological and biogeochemical properties, in order to answer fundamental question about the carbon and nutrient cycles and the evolution of these cycles in the context of climate change.

Talley's (1999) map of mixed layer oxygen saturation shows an onset of higher oxygen in the southern Indian Ocean, at about 70° E, which supports the idea that the southeast Indian Ocean is a dominant source region of mode water ; McCarthy and Talley (1999 ; see also Keffer, 1985) show a low potential vorticity (PV) pool at 26.8 sigma-theta centered near 90 E ,40 S, which is generated by relatively deep winter mixed layers, that spreads into the subtropical Indian Ocean. The low PV pool also extends in a narrow tongue eastward south of Australia, a pattern which becomes more pronounced at slightly greater density.

Karstensen and Quadfasel (2002) examined the subduction of water into the south Indian Ocean thermocline owing to the horizontal circulation and to Ekman pumping, showing a roughly equal partition between the two components. Mode water formation by air-sea fluxes was estimated and shown to be comparable to net subduction rates. The rough agreement between geostrophic, Ekman, and buoyancy-driven fluxes suggested to them that eddy contributions are unimportant overall. Based on silica concentrations at the base of the mixed layer they suggested that transport across the SAF was a significant source of mode water.

The northward spreading of mode water into the subtropical gyre is presumably due to northward advection, itself a partial result of the fluxes that create mode water. Stramma (1992) showed that southeast of Africa the Subtropical Front (STF) is associated with a geostrophic transport of some 60 Sv (1 Sv = $10^6 m^3.s^{-1}$), and that this transport is reduced to less than 10 Sv as Australia is approached (Figure 2.3). South of Australia the strength of the STF decreases further, reaching negligible magnitude near 130 E (Schodlock et al., 1997). The cooling and densification of the water between the STF and SAF across the southern Indian Ocean is associated with the development of northward thermal wind, thus gradually carrying away water from the northern side of the ACC and into the subtropical gyre.

The question arises concerning the mechanism for the cooling and densification : are air-sea fluxes consistent with this evolution or are other processes acting ? According to the NCEP reanalysis, the annual average air-sea flux tends to heat the surface of the ocean in the region between the Polar Front and STF, but if the Ekman heat transport (defined below) is taken into account, the net effect is broad cooling (Fig. 1). Ribbe (1999) has shown in idealized contexts how the Ekman transport can modify the T, S characteristics of water in the Southern Ocean ; Rintoul and England (2002) estimated a dominant contribution of Ekman heat advection to observed variability in SAMW characteristics south of Australia, and suggested that Ekman fluxes might partly explain a gradual cooling and freshening across the Indian and Pacific Oceans. Speer et al. (1995) also inferred a strong Ekman contribution to SAMW formation. Our principal goal is to evaluate the contribution of the different terms of the mode water heat budget in the south Indian Ocean using a variety of data sources, but principally ARGO and satellite data. Previous studies did not have access to heat content on the space and time scales of the seasonal development of mode water and could not directly relate fluxes to changes in mode water properties.

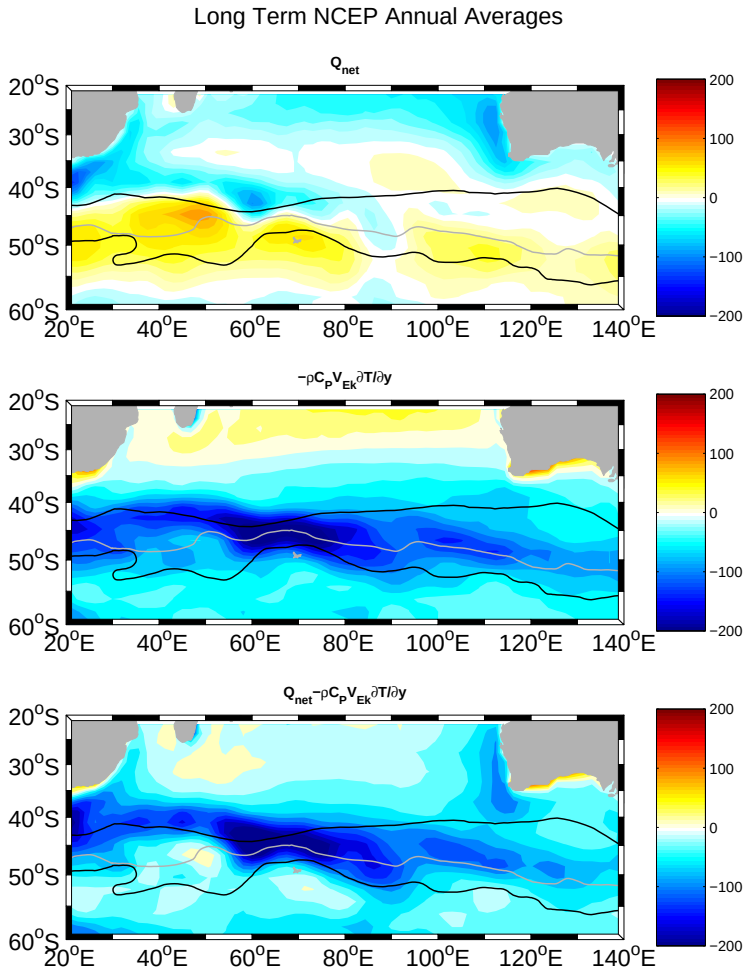

FIG. 2.1 – Climatological average of net heat flux (upper), Ekman heat transport (middle), and their sum (lower), averaged over the entire NCEP record (1948-2005). Contours show the position of the STF, SAF (gray) and PF from Orsi et al. (1995).

2.1.2 Circulation of the southern Indian Ocean

To consider the dynamics of SAMW in the southeast Indian sector, we begin with a discussion of the general upper ocean circulation of the southern Indian Ocean, as summarised in the schematic of Figure 2.2. SAMW forms in the deep winter mixed layers in the Subantarctic Zone (SAZ), north of the Subantarctic Front (SAF) and south of the Subtropical Front (STF). Downstream of the Kerguelen Plateau near 80°E, the main fronts diverge; the STF moves northward, whereas the main branch of the SAF follows the northern flank of the Southeast Indian Ridge (Sandwell and Zhang, 1989) (Figure 2). This is the region of deepest winter mixed layers described by Talley (1999), McCarthy and Talley (1999).

Fine (1993) divided Indian Ocean SAMW into three density ranges : 26.65-26.7σ_θ, which dominates in the southwestern region, 26.7-26.8σ_θ, which dominates in the central region, and 26.8-26.85σ_θ, which dominates in the south-eastern region. These divisions are presumably related to circulation, influenced by the warm, salty Agulhas Return waters upstream, which are continually cooled, freshened and densified by the northward Ekman advection of Antarctic Surface waters along its path (Rintoul and England, 2002)(see Figure 2.2), and by other processus such as air-sea fluxes and eddy mixing. The identification of different mode water density horizons seems to imply distinct formation areas and possibly different forcing mechanisms.

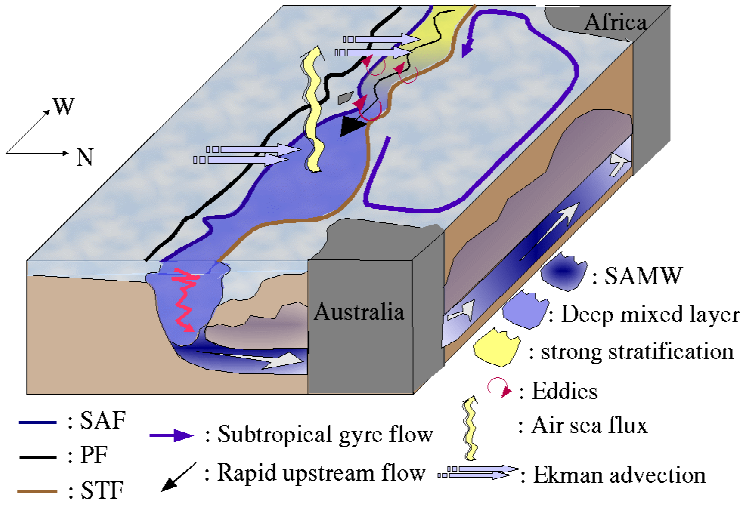

FIG. 2.2 – Schematic of SAMW formation showing the main forcing mechanisms and the relation between the circulation and the region of deep winter mixed layers.

Figure 2.3 shows a climatological average of velocities at 400 meter depth deduced from an objective analysis of ARGO and PALACE floats in the Southern Indian Ocean (cf. Appendix 1). The meandering Agulhas Return Current is centred around 40°S with velocities greater than $40cm.s^{-1}$ at 400 m depth. In this analysis, the Antarctic Circumpolar Current (ACC) bifurcates upstream of the Crozet Plateau (55°E) at 40°S, the northern branch merging with the Agulhas Return Current, and the southern branch continuing eastward. Further downstream, this eastward branch bifurcates again between the Crozet Plateau and the Kerguelen Plateau (80°E) (Figure 2.3). The main southerly branch continues eastward

across the plateau, merging with flow downstream of the plateau. This circulation pattern is also indicated by the SVP drifters (not shown). The merging of ACC and Agulhas waters upstream of the two plateaux points to preferred regions of water mass mixing.

The bathymetry clearly has a direct impact on the circulation in this region, creating large permanent meanders of the Agulhas Return Current and the ACC, and limiting the latitudinal excursions of the hydrological fronts (see Figure 2.3). North of the ACC distinct interior recirculation regimes exist related to bathymetry that may set the primary mode water divisions. Within the ACC, the Crozet Plateau and the Kerguelen plateau, strongly control the frontal positions in the south Indian Ocean, and the SAF and the STF converge north of these plateaux (Figures 2 and 3). In the southeastern sector downstream of the Kerguelen Plateau, these two fronts diverge, giving rise to a large area of reduced flow (Figure 2.3) where the SAMW forms.

Finally, strong eddy activity is associated with instabilities of the main currents described above. The Agulhas Current System to the west has the highest eddy kinetic energy (EKE) of the global ocean, and EKE maximums are located along the main axes of the meandering Agulhas Return Current and the ACC (Le Traon and Morrow, 2001). Eddy mixing can be important in the diffusion of tracers (Davis, 1991), and in the transport of properties across the SAF (Karstensen and Quadfasel, 2002).

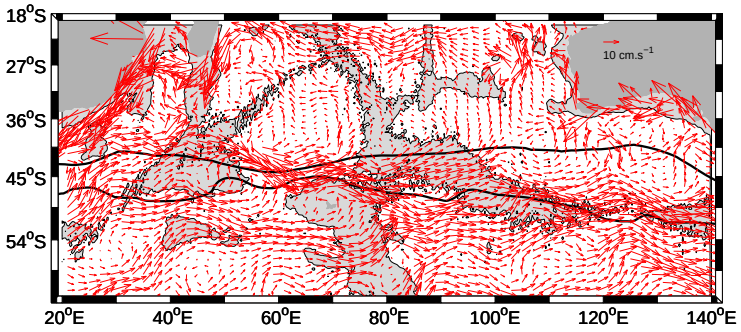

FIG. 2.3 – Averaged velocities at 400 meter depth deduced from an objective analysis of ARGO and PALACE floats in the southern Indian Ocean (cf. Appendix III). Bathymetry less than 3500 meters depth is shaded gray. Solid lines indicate the STF (north) and the SAF (south) from Orsi et al. (1995).

In the following analysis, we will consider how these different dynamics and forcing mechanisms influence the surface heat budget in the region of SAMW formation downstream of the Kerguelen Plateau. We start by the heat budget since we have good surface temperature fields which allow us to accurately calculate the spatial-temporal evolution of the temperature gradients. Unfortunately, accurate surface salinity measurements are not available on the same space and time scales to estimate a similar surface salinity budget, but we will address the role of salinity in the discussion.

2.1.3 Data

Profiling floats

The vertical structure of the ocean is obtained in this study using the ARGO dataset. The ARGO float program has seeded all of the world's ocean for several years in particular the Southern Ocean which

historically is poorly sampled. Good data coverage in the southern Indian Ocean started in late 2002, and this study focuses on the years 2003 and 2004. These data were collected and made freely available by the International Argo Project and the national programmes that contribute to it[1]. We only used profiles which pass the ARGO real-time quality control, containing information on their position, date, T and S profiles, with their first measurement point shallower than 20 meters. According to Wong et al. (2003) the accuracy of the Argo salinity data in the Southern Indian Ocean is better than 0.01 psu, which in our case is sufficient for defining the mixed layer characteristics. PALACE data (Davis, 2005) were combined with ARGO floats to compute the mean flow in the Southern Indian Ocean (cf Appendix I).

Air-sea fluxes and winds

For the heat budget calculation, we will compare different surface forcing fields. We use the monthly NCEP reanalysis on a 2°grid to estimate the air-sea heat flux. These data are made available by the NOAA-CIRES Climate Diagnostic Center[2]. Two different wind products will be used : monthly averaged winds computed from the NCEP reanalysis, and higher-resolution monthly Quickscat gridded winds on a 0.5 °grid, available on the IFREMER Cersat (French Satellite Processing and Archiving Facility) website[3].

Sea-surface temperature

We also use two different Sea Surface Temperature fields. Monthly Reynolds SST on a 1°grid are used in the climatological analyses, distributed by the NOAA-CIRES Climate Diagnostic Center. For the higher-resolution analysis we use a global satellite SST product (0.25°x0.25°) computed by a combination of two satellites : TMI and AMSR, made available by Remote Sensing Systems[4].

Surface Drifter

Satellite-tracked surface drifter data are used to compute a parameterisation of the lateral eddy diffusion coefficient. This dataset is part of the Global Drifter Program/Surface Velocity Program and spans the period 1995-2005 in the Southern Indian Ocean. The drifters are equipped with a holey sock drogue at 15 m depth to reduce their surface wind drag. Their positions are determined by ARGOS. The data are received, processed and distributed by the Atlantic Oceanographic and Meterological Laboratory (AOML, Miami) [5]

2.1.4 Surface mixed layer properties

The availability of ARGO profile data allows us for the first time to map the evolution of the surface mixed layer properties over large portions of the Indian Ocean, and to resolve the seasonal variations.

Figure 2.4 shows the summer and winter mixed layer depths observed by ARGO profiles during 2003-2004 in the South Indian Ocean. The location of the deep winter convection downstream of the Kerguelen Plateau is clearly illustrated. Figure 2.5 shows the mixed layer temperature, salinity, and potential density versus longitude between the STF and the Polar Front for all the ARGO profiles during 2003-2004. The properties show a distinct emergence of 2 branches : a colder, fresher branch of water south of the SAF, and a warmer, saltier branch of water north of the SAF. These branches have

[1] www.ifremer.fr/coriolis/cdc/argo.htm and www.argo.ucsd.edu
[2] http ://www.cdc.noaa.gov/
[3] http ://www.ifremer.fr/cersat/
[4] http ://www.ssmi.com/
[5] http ://www.aoml.noaa.gov/

relatively shallow winter depths ($\leq$ 200m) upstream of 70°E ; downstream the deep mixed layers (large dots ; Figure 5) occur in the main mode water formation area.

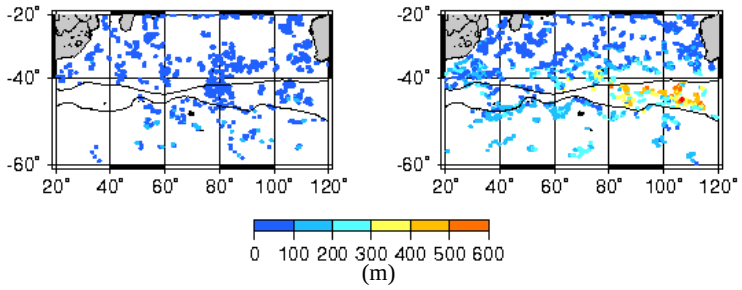

FIG. 2.4 – Mixed layer depth computed from ARGO profiles during 2003 and 2004. The base of the mixed layer is found using a density difference criterion of 0.03 $kg.m^{-3}$ (cf. Appendix 1). Solid lines mark the STF (north) and the SAF (south) from Orsi et al. (1995). **Upper-left panel :** Summer profiles (January, February, March). **upper-right panel :** Winter profiles (July, August, September). **lower panels :** zoom on the deep winter 2003 (left) and 2004 (right) profiles found in the main formation area, defined by the region between 70°E and 140°E and between the SAF and STF (Nagata et al., 1988).

The existence of the branches reflects the frontal structure of the region with strong gradients at the surface across the SAF, but also indicates the evolution of these water masses to a common mode water by lateral exchange. Some of this exchange is accomplished by Ekman transport, and some arises due to lateral eddy mixing. The density of the mode water increases to the east, by a combination of temperature and salinity effects.

A T-S diagram (Figure 2.6) of the deeper mixed layers south of 30°S (and greater than 200m depth) shows the SAMW (near 9°C, 34.6 ppt, sigma 26.8 ; see Figure 2.5) in relation to neighboring winter mixed layers across the entire ACC. Some very dense mixed layers occur at the southern limits of the ARGO data near 60°S, with temperature below 3°C and salinity below 34 ppt. At the warm, salty limit are the mode waters of the subtropical gyre in the western Indian Ocean (sigma 26.5 - 26.7). The deepest mixed layers are found between this wide range of T and S in a relatively narrow density range, 26.7 - 26.9. Thus, near density-compensation occurs in the mode water across an extraordinarily large range of T and S, and again points to lateral processes as sources of heat and salt.

In the following sections we will consider certain characteristics of the surface mixed layer in the formation region of SAMW in the southeast Indian Ocean. Our study region lies north of the SAF and south of the STF, downstream of Kerguelen Plateau at 70°E and extending eastward to 140°E. The front positions are defined from the vertical ARGO profiles, since precise horizontal subsurface gradients are not available. The SAF is defined using the Nagata et al. (1988) definition, as the isotherm 7°C at 100 m. The STF also follows Nagata et al. (1988), and is defined as the isotherm 11°C at 150 m.

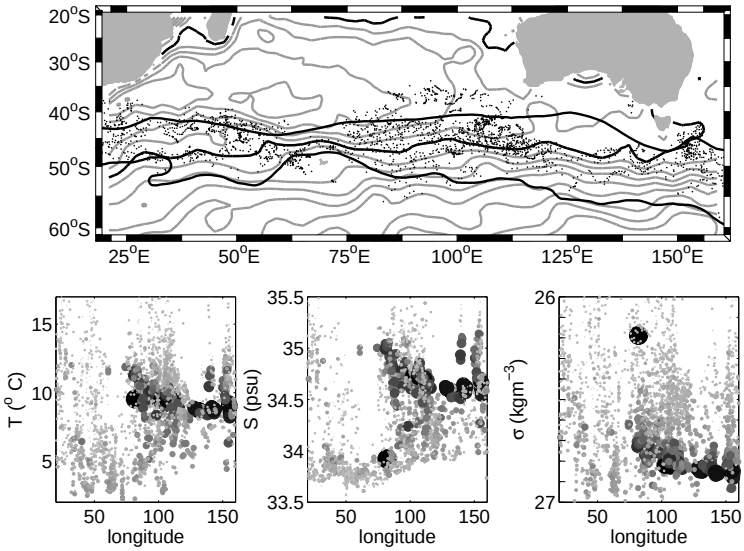

FIG. 2.5 – **Upper panel :** Position of all ARGO profiles between the Polar Front and the STF (as defined by the properties of each individual profile). Streamfunction derived from an objective analysis of float positions (Appendix I) is in gray contours. Solid lines indicate the STF (north) and the SAF (south) from Orsi et al. (1995). **Lower panel :** Temperature, salinity, and potential density for each profile displayed as a function of longitude, with symbol size corresponding to mixed layer depth. The evolution of properties along and between the fronts shows a convergence of values on either side of the SAF to form progressively denser mode waters.

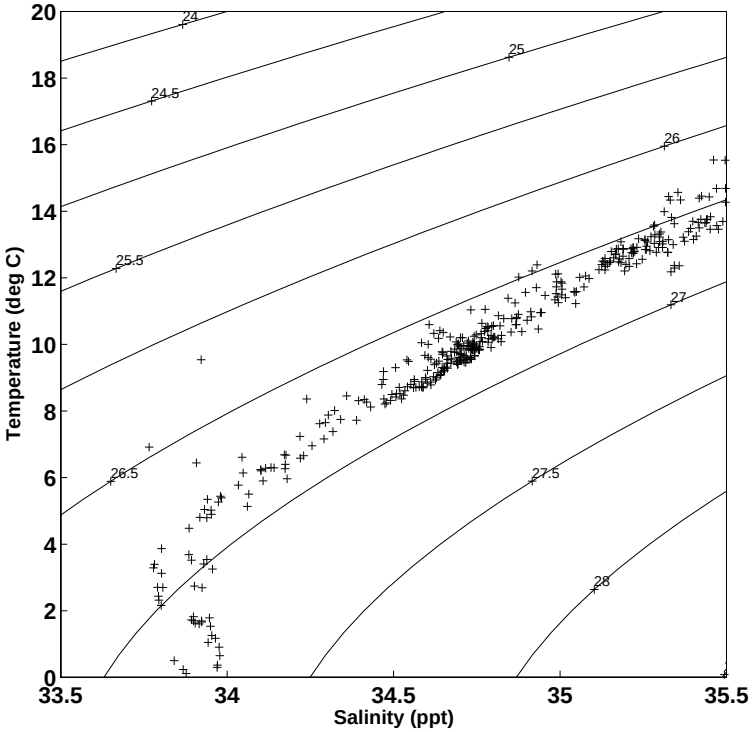

FIG. 2.6 – Temperature-salinity diagram for mixed layers (values at mid-depth within the layer) greater than 200m thick, from all ARGO data between 30 S - 60 S. Potential density overlaid. SAMW in longitudes 70-120 E is concentrated between 8-10 C and 34.4 - 34. 9 ppt, and 26.7 sigma. Relatively deep mixed layers also exist at neighboring T,S values outside this range ; the distinction between mode waters is not absolute, either in T,S space or geographically.

2.1.5 Stability at the base of the mixed layer

The mixed layer in the formation region creates the dynamic link between the atmospheric forcing and subsurface mode water layer. Before we start an analysis of the forcing terms for the mixed layer, we will first consider the stability at the base of the mixed layer. Is the base of the mixed layer strongly or weakly stratified throughout the different seasons, and is this stability dominated by a strong thermocline or halocline ?

The stability of a water column is characterized by the Brunt-Vaïsala coefficient N defined by : $N^2 = \frac{g}{\rho}.\frac{\partial \rho}{\partial z}$. The column is stable if and only if N is positive. The base of the mixed layer is defined using a 0.03 density difference criteria (see Appendix II). Figure 2.7 shows the evolution of the stability, calculated over a 10 m depth interval at the base of the mixed layer, using the available ARGO floats in the formation region. The strong seasonal cycle remains positive, i.e., the base of the mixed layer is always stable. However, the stability at the base of the mixed layer is weak in winter, indicating that it is close to the threshold allowing deeper convection.
A more interesting view comes from splitting this stability calculation into its thermal and haline parts.

The vertical density gradient can be written as a first approximation (Gill, 1982) :

$$\frac{1}{\rho}.\frac{\partial \rho}{\partial z} = -\alpha.\frac{\partial T}{\partial z} + \beta\frac{\partial S}{\partial z}$$

$$\text{where : } \alpha = \frac{1}{\rho}.\frac{\partial \rho}{\partial T} \text{ et } \beta = \frac{1}{\rho}.\frac{\partial \rho}{\partial S}$$

The role of the thermal and haline stratification on the stability at the base of the mixed layer is represented by the two terms : $N_T = -g.\alpha.\frac{\partial T}{\partial z}$ (thermal stability) and $N_S = g.\beta.\frac{\partial S}{\partial z}$ (haline stability).

The thermal stratification is dominant at the base of the mixed layer for most of the seasonal cycle (Figure 2.7). The exception is during early winter, when the base of the mixed layer is strongly destabilised by cooling (the thermal stability term becomes negative in June-July) and the stability is maintained by the haline component (fresher). In late winter (August to October), positive thermal stability at the base of the mixed layer is reestablished and now it is the haline component which tends to destabilises the water column (saltier). We note that during winter the two terms tend to compensate, that is, the thermal destabilisation is compensated by a freshening, and vice versa.

An analysis of the heat budget equation in the mixed layer of the formation region will give us a clearer idea of the seasonal evolution of the forcing terms, and their relation to this observed mixed layer destabilisation. It is also clear that the salinity terms will play an important role in late winter. To start, we consider the heat budget equation.

2.1.6 Heat budget equation in the mixed layer

For the vertically averaged surface layer, the heat budget can be written :

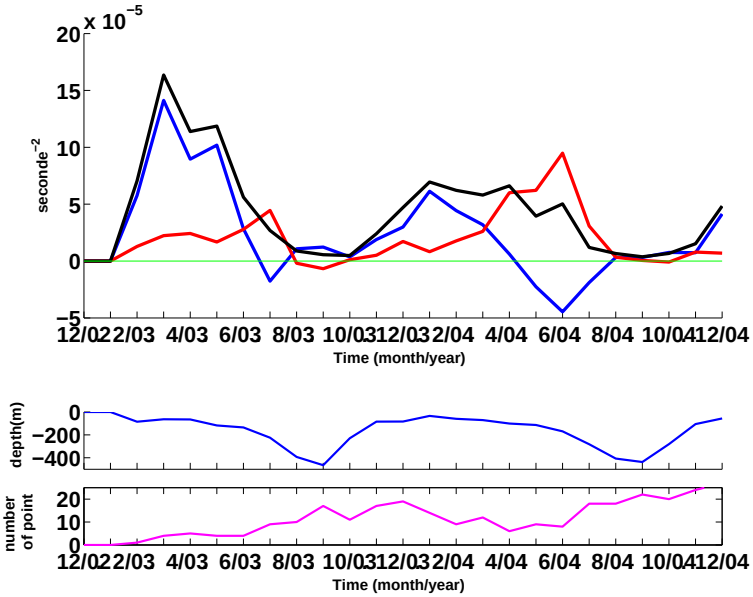

FIG. 2.7 – **upper panel :** monthly average of the stability (s^{-2}) at the base of the mixed layer computed from the 2003 and 2004 ARGO profiles in the SAMW formation region. The black line represents the stability at the base of the mixed layer, i.e, the evolution of the Brunt-Väisala coefficient. Red line is the haline component of the stability at the base of the mixed layer, i.e, $N_S = \beta.\frac{\partial S}{\partial z}$. Blue line is the thermal component. **middle panel :** monthly averaged mixed layer depth (in meters) computed from the same data. **lower panel :** monthly number of points used in the mixed layer stability calculation.

$$h(\frac{\partial T}{\partial t} + \mathbf{v}.\nabla T + \overline{v'.\nabla T'}) + \Delta T w_e + \nabla . \int_{-h}^{0} \hat{v}\hat{T} dz = \frac{Q_o}{\rho C_p} \tag{2.1}$$

(e.g. Stevenson and Niiler, 1983 ; Qui, 2000), where h is the layer thickness, T the mean (low-passed in time/space) temperature, v the mean horizontal velocity vector, primes denote variability about the mean state, ΔT the temperature jump at the base of the layer, w_e the entrainement velocity, $\hat{T}$ and $\hat{v}$ represent deviations from the vertical average, and Q_o is the net heat flux at the ocean surface. The heat flux across the base of the layer due to shortwave radiative penetration is assumed small for the deep winter mixed layers considered here, and the diffusive flux of heat at the base of the layer is neglected. The role of vertical temperature deviations within the surface layer associated with small vertical density variation were considered, but found to be small in all instances in this region, hence are also neglected.

Previous studies suggest that Ekman advection and air sea fluxes are dominant terms in destabilizing the winter water column to create the strong and deep convection observed (Ribbe, 1999 ; Rintoul and England, 2002). These studies were based on numerical model outputs or dimensional analysis ; here, we estimate these terms from the available in-situ data. The balance

$$h.\frac{\partial T}{\partial t} = \frac{Q_{net}}{\rho C_p} - V_E.\frac{\partial T}{\partial y} \tag{2.2}$$

agrees with the simplified model of MacCready and Quay (2001) for the heat balance in the ACC. We will consider this simple balance first.

The temperature evolution and mixed layer depths are calculated from the ARGO data. A critical term in the heat budget equation is h, the depth of the mixed layer. We carried out numerous tests to decide which criterion would be the most appropriate in the present case (Appendix II). The method retained was to use a 0.03 density difference threshold for the determination of the mixed layer depth.

The temperature evolution is calculated for each ARGO float within the formation region, as described in Appendix III. For the calculation, we use pairs of float profiles separated by 30 days (3 float cycles) which remain in our zone, and the temperature is integrated down to the deepest mixed layer depth occurring for the two profiles. Thus the mixed layer depth for our calculation is not fixed, but varies in space and time. The heat content variation for each individual float is obtained using those two profiles.

The forcing terms are interpolated onto each ARGO float position and then averaged over the same 30 day period. In other words, considering 4 consecutive float profiles, Ekman advection and air sea flux are interpolated (in time and space) onto the first, the second and the third profile and then averaged to form the monthly mean, and the monthly heat content variation is computed between the first and the fourth profile (3 float cycles).

Comparing climatological and realistic Ekman forcing

We used two different techniques to compute the Ekman term. The first uses classical climatological data sets : NCEP monthly winds and Reynolds monthly SST climatology. We find that the magnitude of the Ekman term is small compared to the analytical predictions (Rintoul and England, 2002). For the second Ekman calculation, we use higher-resolution Quickscat satellite scatterometry winds and satellite

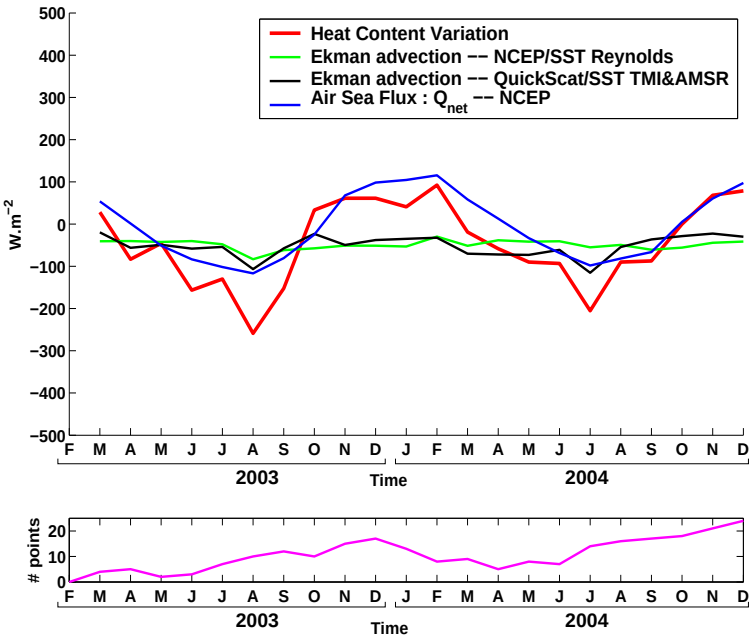

FIG. 2.8 – **upper panel :** Monthly averaged simplified heat budget terms ($W.m^{-2}$) for 2003-2004 in the SAMW formation area. Red line : heat content variation computed from the ARGO profiles in the formation area. Blue line : NCEP air-sea heat fluxes. Green line : Ekman advection calculated using the Reynolds optimal interpolated SST in association with the NCEP winds. Black line : Ekman advection from the combination of satellite TMI/AMSR SST, and satellite Quickscat winds. **lower panel :** number of points used in the monthly heat content calculation.

SST fields from TMI/AMSR. The result is surprising : during winter 2003, realistic forcing increases the Ekman component by 30 percent, from -80 to -110 $W.m^{-2}$, while in winter 2004 it increases by more than 50 percent from -60 to -130 $W.m^{-2}$ (see Figure 2.8). The annual mean increases by 10 percent (from -49.35 $W.m^{-2}$ to -54 $W.m^{-2}$).
The main reason for this difference is that the Reynolds SST is much too smooth at these latitudes ; there is little ship SST data and considerable cloud cover which blocks the satellite AVHRR measurements, and so the Reynolds SST reverts to the climatological mean. In contrast, the microwave TMI/AMSR traverses the clouds, and provides mesoscale SST coverage which is highly correlated with altimetric observations (not shown). For instance, we frequently observe frontal movements of the SAF associated with meanders or eddy spawning which are detected by TMI/AMSR but not observed by Reynolds SST. Having strong SST gradients which are correctly positioned and not too smooth impacts directly on the Ekman advection calculation (Figure 2.9). This also impacts on the temporal evolution : the high-resolution Ekman forcing has a strong seasonal cycle while the Reynolds-NCEP Ekman calculation is weaker, with a smaller difference between the two calculations for the annual mean. If we spatially average the two product over a large enough region, we get comparable results (not shown), suggesting that the large-scale forcing is well represented. In the following section we chose to work with the satellite Ekman heat flux based on Quickscat winds and TMI AMSR SST, providing a better local estimate of the Ekman forcing around the individual ARGO floats.

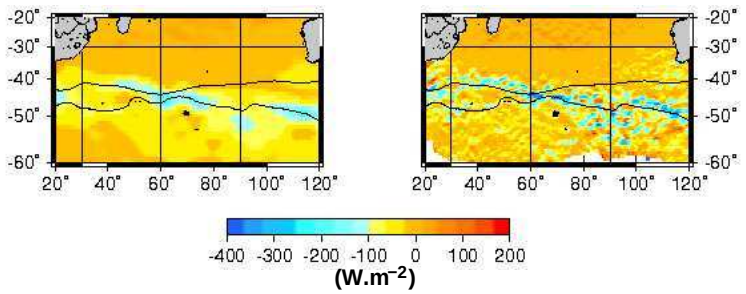

FIG. 2.9 – Mean meridonal Ekman advection in August 2003 in the Southern Indian Ocean, computed from NCEP reanalysed winds and Reynolds SST (left), and from the combination of Quickscat winds and TMI/AMSR SST (right).

Comparison of the forcing terms

The monthly averages of the different forcing terms are shown in Figure 2.8. The annual heating and cooling cycle from the air-sea flux Q is largely responsible for the variations in mixed layer heat content. Very strong cooling is observed in winter in the mixed layer, with mean values of over 200 $W.m^{-2}$ heat loss. Half of this heat loss is due to air-sea fluxes (-100 $W.m^{-2}$ heat loss on average in winter), and the increased Ekman fluxes in winter also contribute to cooling the mixed layer (by -100 $W.m^{-2}$).

Figure 2.10 shows the two sides of Equation 5.1, as the sum of the air sea fluxes and the Ekman forcing versus the heat content variation, and their associated error bars. The two curves coincide almost throughout the two year period, validating our technique and the use of the ARGO data set to calculate

the heat content variations. Within the error margin, the sum of the two forcing terms is enough to close the heat budget for this SAMW formation region. We note that this closure is improved by using the high-resolution Ekman term, which increases the forcing term by 30-50 % in winter.

The standard deviation of the ARGO heat content evolution is large compared to the forcing terms. This raises the question of whether these monthly averages are representative of all of the floats in our formation region, particularly when we consider that the winter standard deviation of the heat content variation ranges from 0 to -500 $W.m^{-2}$. In the following section we will investigate whether the Ekman advection and the air sea flux are always sufficient to explain the heat content variation in the mixed layer, or whether, for some float conditions, the neglected terms in the simple balance (Equation 5.1) become important.

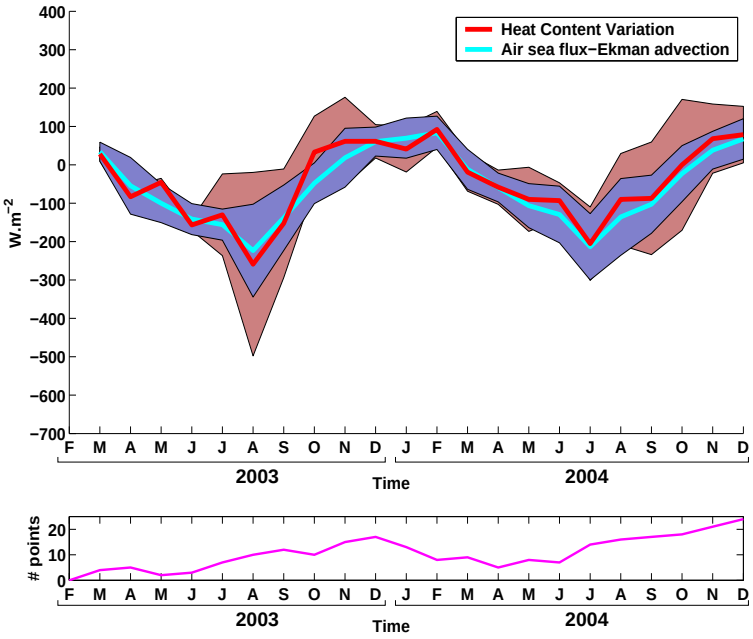

FIG. 2.10 – **upper panel :** Heat balance ($W.m^{-2}$) for 2003-2004 in the SAMW formation area. Red line shows the monthly average of the heat content variation computed from the ARGO profiles in the formation area for the years 2003 and 2004. Light blue line is the sum of the high-resolution Ekman advection and air-sea heat fluxes computed around each ARGO profile. Red and blue shading represent the standard deviation for the monthly heat content variation and the forcing contributions, respectively. **lower panel :** Number of points used in the monthly heat content calculation.

Wintertime heat content

Here we consider the detailed heat budget for all of the ARGO float pairs available during the winter 2003 where we found a maximum of heat content variation rms. Figure 2.11 (top panel) shows the two sides of the heat budget (Equation 5.1) for all float pairs in our zone, before making the monthly average. There is a good agreement between the two curves, however certain float pairs show large differences : for example, profiles 2, 3, 4 and 5 diverge away from the range of the forcing terms. All of these

float pairs are moving in strong SST gradient meanders and may be caught in the energetic eddy and meander propagation north of the front (bottom pannel).

Profile pairs 4 and 5 show a large cooling of the surface layer (down to 500 m depth), whereas Profiles 2 and 3 shows warming at depth. Although these float pairs are located north of the Subantarctic Front following the Nagata et al. (1988) definition, they are clearly influenced by the frontal dynamics, and part of the observed cooling may be due to cross-frontal exchange with the cooler Polar Frontal Zone water masses. For these cases, the difference in the two heat budget curves is not simply due to increased Ekman transport of cooler, fresher surface waters, but may be influenced by geostrophic or eddy advection terms over greater depth.

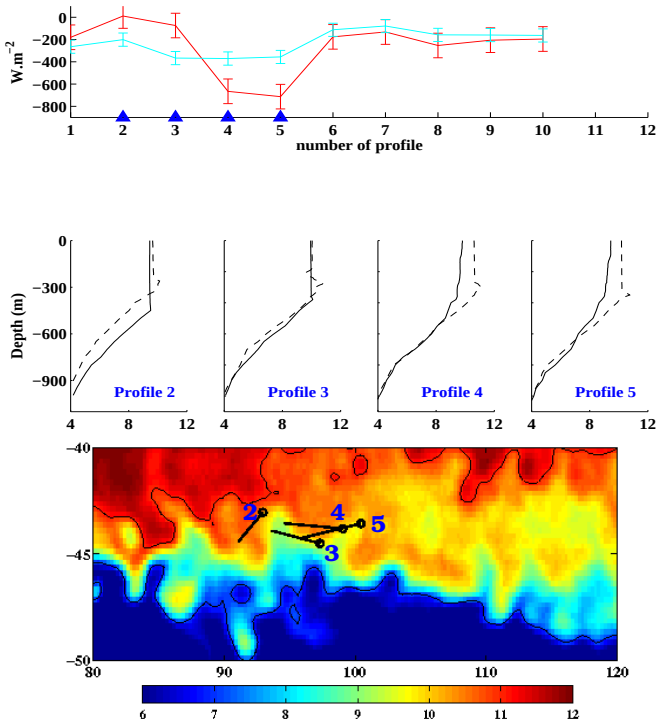

FIG. 2.11 – Details of the individual winter heat budget terms included in the August 2003 monthly average. **upper panels :** the ARGO heat content variation (red line) and the associated forcing contributions (Ekman advection + air-sea fluxes) (light blue line) which were used in the monthly average presented in Figure 2.10. Error bars are the 2003/2004 rms of heat content variation (red) and forcing contribution (light blue). **middle panel :** Pairs of profiles where we found a large difference between heat content variation and forcing contribution. The dashed profile is one month before the solid profile. The difference between them is the heat content in the mixed layer. **lower panel :** geographical position of previous profiles. The circle denotes the profile correponding to the solid line. Colour contours of SST for 15 August 2003 are shown. Black curves are the 7 and 11 degree Celcius coutours.

This focus on the 2003 winter case highlights two important features. For most of the float pairs which remain in a fairly homogeneous subantarctic water mass, the simple balance of air-sea heating plus meridional Ekman flux is sufficient to explain the heat content variation over a one month period, even during winter. However, certain float pairs that are situated close to the SAF or its meanders can exhibit large heat content variations which are not explained by this simple balance, suggesting that the floats may also move across eddies and meanders of the mean flow. These cases can have a large impact on our monthly averages - without the four extreme cases in winter 2003, the average heat content evolution would be around -190 Wm^{-2}, rather that the observed -260 Wm^{-2}. We know that the float sampling is not completely random - Lagrangian floats tend to converge towards the more energetic regions (Davis, 1991), and are especially influenced by the deep-reaching meanders and eddies of the SAF. So these extreme cases will be more numerous in our ARGO data than if we had made a homogeneous Eulerian sample of the formation region. On the other hand, these cross-frontal exchanges are also a key mechanism in bringing deep cool, fresh layers into the formation region.

Role of the eddy diffusion term

We suspect that eddy fluxes (due to mesoscale eddies or meanders of the front) may be important close to the energetic SAF for the heat balance equation. To investigate this further, we replace the missing $h.\overline{v'\nabla T'}$ term from Equation 2.1 by a simple Laplacian form to parameterize the eddy heat diffusion, $K_h.\nabla^2 T$. We have computed a climatological average of the lateral eddy diffusion coefficient K_h in 5°by 5°bins following Davis (1991) (see also Oh and Zhurbas, 2000) [6], using the available surface drifter data from 1995 to 2005 over the Indian Ocean. Mean eddy heat diffusion in $W.m^{-3}$ is then calculated using the relation : $\rho.C_p.K_h.\nabla^2 < T >$; here $< T >$ is the mean SST derived from 3 years of high-resolution TMI-AMSR data.

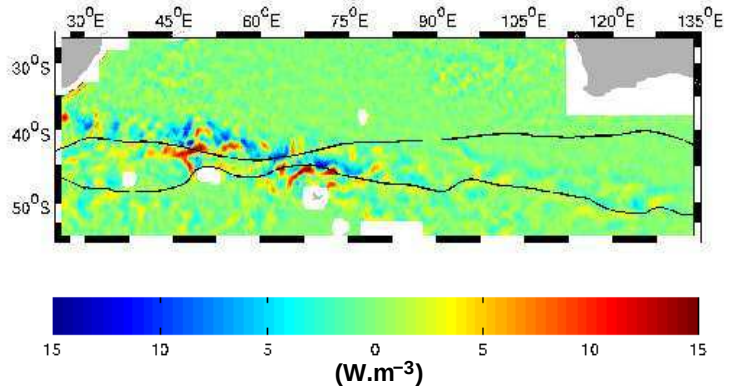

FIG. 2.12 – Lateral surface eddy heat flux in the Southern Indian Ocean (in $W.m^{-3}$) from surface drifter and averaged TMI/AMSR SST. Solid lines indicate the STF (north) and the SAF (south) from Orsi et al. (1995).

[6] The eddy diffusion coefficient has been computed using the single particle diffusivity tensor relation described by Davis (1991) : $k_{jk}(\mathbf{x} =< v'_j(t_0|\mathbf{x},t_0)d'_k(t_0-t|\mathbf{x},t_0) >$, where v' and d' are the departures from the lagrangian mean velocity and displacement,respectively ; t_0 is the initial time and the brackets indicate averaging over the ensemble of the particles ; the notation $a(t|\mathbf{x_0},t_0)$ represents the value of a at time t of a particle passing through $\mathbf{x_0}$ at time t_0.

This surface eddy heat flux estimate based on surface drifter data (Figure 2.12) is consistent with the Gille (2003b) results, and indicates that the maximum eddy heat diffusion occurs upstream of the Crozet Plateau and Kerguelen Plateau, where the STF and the SAF converge between 60-70°E.

In the region of SAMW formation downstream of Kerguelen, the eddy heat diffusion is weaker. This confirms our results from the previous section, where we saw only a few cases in the monthly average which were influenced by mesoscale eddies and possible stronger eddy diffusion. Karstensen and Quadfasel (2002) also proposed that eddy fluxes were not important for the generation and subduction of mode water since air-sea flux based estimates agreed with kinematic models. However, their results were by construction averaged over all of the density outcrop area, that is, averaged over longitude too, which tends to average out the eddy flux. Our results indicate that eddy heat diffusion is also weak in the seat of SAMW formation. However, there is substantial variation of eddy diffusion along the fronts, and importantly, just upstream of Kerguelen Plateau. We will now consider how the along path variations in mixed layer properties and eddy diffusion may control the location of mode water formation.

2.1.7 Longitudinal variation of mixed layer properties

Here we consider the circulation around the Crozet and Kerguelen Plateaux in more detail. Figure 3 showed that branches of the ACC bifurcate to the north, and merge with the Agulhas Return Current near Crozet Island at 50°E, and upstream and downstream of the Kerguelen Plateau. Near 60°E and 75°E. These branches appear to be topographically controlled and bring cold, fresh Antarctic water from the south of the SAF in contact with the warm, salty subtropical water asssociated with the Agulhas Return current.

To illustrate how the water column is modified in these merging areas, we will examine the along-stream properties of a composite of two ARGO floats (WM0 No. 1900042 and 1900164) which remained north of the SAF and sampled from upstream of the Crozet Plateau to downstream of Kerguelen (Figure 2.13). The first float (WM0 No. 1900164) drifted from 40 to 83°E during September 2004 to September 2005, while the second float (WM0 No. 1900042) drifted downstream from December 2004 to September 2005. Hence, this composite permits an analysis of the longitudinal evolution of the water column during three seasonal cycles.

To identify the intense mixing region we have divided the composite track into three parts : profiles from upstream of Crozet are in red, from 55°E to 80°E are in blue, and profiles from the mode water formation area downstream are in light blue. In addition to this composite, we also show profiles from south of the SAF (black star ; Figure 2.13). We will also consider the longitudinal evolution of the forcing terms in the simplified heat equation 5.1, including an extra climatological eddy diffusion term. The annual mean forcing terms are averaged between the SAF and the STF (as defined by Orsi et al., 1995) in 10 degrees longitude bins (Figure 2.14).

1. Upstream of Crozet (red profiles) there is a strong vertical stratification below the surface mixed layer, with PV $\geq 50.10^{-9}(m.s)^{-1}$ (Figure 2.14b). During winter, the mixed layer deepens to 200 m depth with a density of 26.8 $kg.m^{-3}$ which is within the mode water density class. However, it appears that the strong vertical density gradient beneath the mixed layer prevents deeper convection in winter. Furthermore, although the lateral eddy heat fluxes are strong in this region (Figure 12),

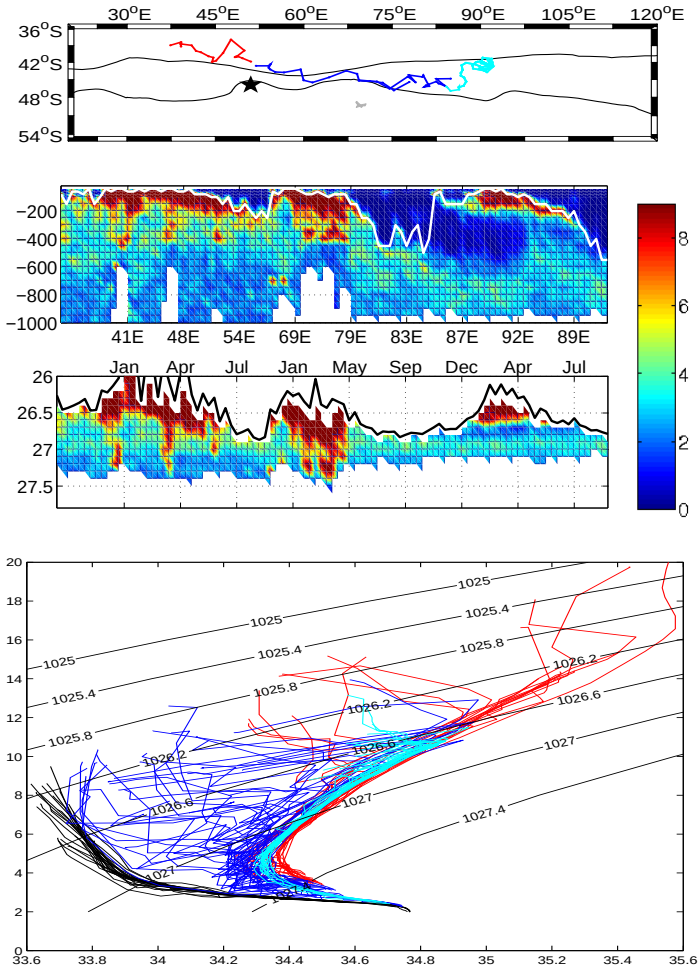

FIG. 2.13 – Vertical structure analasys upstream and downstream of the Kerguelen Plateau from a composite of 2 ARGO float (WM0 No. 1900042 and No. 1900164). **a)** Position map of the profiles analysed. Colors are linked with the temperature/salinity plot (lower pannel). The black star corresponds to the region were we picked the profiles from the South of the SAF in the Temperature/Salinity analysis. **b)** Temporal evolution of the Potential vorticity ($(m.s)^{-1}$) profiles along the float trajectory. The horizontal axis is time in "month/year" ; vertical axis represents depth in meters. **c)** Three region have been chosen to illustrate the evolution of the temperature (upper) and density (lower) profiles from west to east. Temperature in °C, Density in $kg.m^{-3}$. Colors are linked to the postion map ; blak profiles correspond to the blak star region in the position map.

the climatological eddy heat diffusion is positive between the fronts (Figure 2.14), inducing an annual mean diffusive warming, which opposes the net Ekman cooling.

2. Between the Crozet and Kerguelen Plateaux (blue profiles), we observe a sharp reversal of the eddy heat diffusion term (see Figure 2.14) which becomes strongly negative. In this region the annual mean Ekman and eddy diffusion terms both contribute to cool the mixed layer. Although the eddy heat diffusion term is a climatological parameterization, we can see the impact of the eddy mixing in the individual profiles which show strong interleaving from the surface down to the deep water density class ($\geq 27.4 kg.m^{-3}$) ; (Figure 2.13c). The blue profiles show a tendency towards density-compensating interleaving between water masses from south of the SAF (black profiles) and from the northern branch (red profiles).We note that the stratification at 27.2 $kg.m^{-3}$ is associated with the salinity minimum linked to intermediate water, which appears to be modified and freshened by the increased mixing in this region (see temperature/salinty plot ; Figure 2.13c).
3. Downstream of Kerguelen, the fronts separate and the circulation slows. We know from Figures 2.5 and 2.13 that the surface mixed layer properties converge towards a more homogeneous density, which is fresher and cooler than upstream. Figure 2.13c) also suggests that the mode and intermediate water masses (light blue profiles) have tighter T-S curves, and tend to be cooler and fresher than the upstream profiles (red).

   Strong Ekman advection also extends to 58°S, potentially bringing much fresher and colder water into the formation area, and contributing to the large winter Ekman fluxes observed here. As we have seen, eddy heat diffusion is weak (Figure 2.14). However, the combination of strong lateral mixing upstream, and the slower circulation leaves more time for water masses to undergo the cooling, as shown for the our composite (Figure 2.13).

Consider a schematic of the temporal evolution of a classical profile in the SAMW formation region during autumn/early winter (see Figure 2.15), which is similar to our observed ARGO profiles. During autumn, the water column is weakly stratified, due to the upstream eddy mixing, with the remnants of the summer heating at the surface. In early winter (June), increased Ekman advection brings more cool, fresh surface water which deepens and mixes due to the increased atmospheric cooling, but leaves a lens of warm saltier water just below the mixed layer. This spreading of cool fresh water across the SAF with a warmer and saltier subsurface is also observed at other sections farther east (Gordon and Molinelli, 1982 ; Rintoul and Trull, 2001).

As winter progresses, Ekman advection and the atmosphere cooling both increase to the point where a strong vertical circulation is induced just north of the front. The strong convection is sufficient to erode the weakened warm and salty lens, deepening the thermocline, leading to the deep winter mixed layers observed (see Figure 2.15).

2.1.8 Summary and discussion

This study has used ARGO float data to estimate the heat balance in the surface mixed layer in the region of SAMW formation in the southeast Indian Ocean. We have been able to observe the full seasonal cycle over a two year period, and our in-situ data confirms previous modelling and climatological studies which find that air-sea fluxes plus Ekman fluxes dominate the surface heat budget (Ribbe, 1999 ;

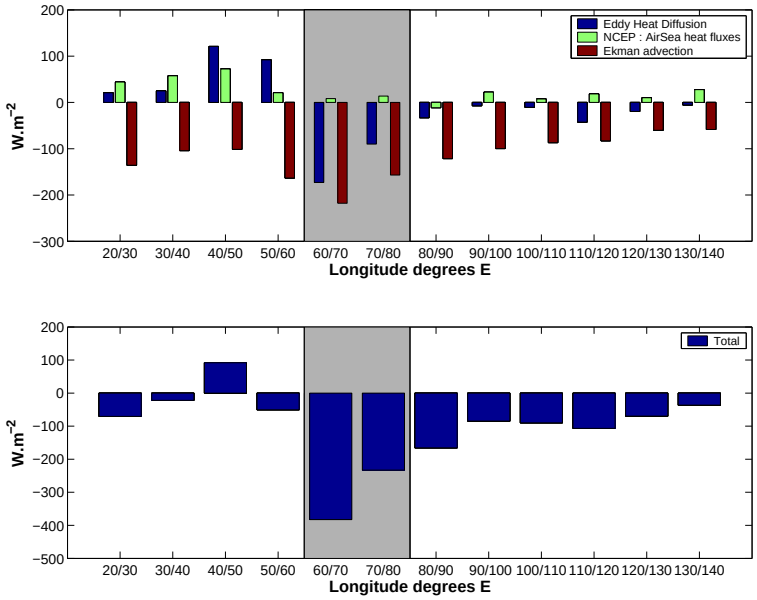

FIG. 2.14 – Longitudinal evolution of the annual mean heat budget forcing contributions averaged between the STF and SAF (fronts defined by Orsi et al., 1995). Ekman advection and air-sea fluxes are computed from long-term NCEP averages; eddy heat diffusion is computed as described in section 6.4 from surface drifter and satellite SST data. Gray shading indicates the Kerguelen Plateau region.

Rintoul and England, 2002; Speer et al., 1995). In the southeast Indian Ocean we have quantified that the seasonal cycle of air-sea fluxes dominates the seasonal heat content variations in the mixed layer. Ekman fluxes continually cool the mixed layer, with an increased amplitude in winter of roughly -100 Wm^{-2}.

One of the interesting results from this ARGO float analysis is how the subantarctic water masses evolve from west to east along the ACC axis, and the role of "upstream conditioning" on the formation of the deep winter mixed layers. Figure 2.5 clearly shows how the wide range of water mass properties upstream converges after the Kerguelen Plateau, leading to deeper mixed layers which are cooler, fresher and denser towards the east. Ekman forcing may be the dominant forcing downstream of Kerguelen, yet this term is as strong upstream of Kerguelen Plateau and the mixed layer remains at 100 m depth. It is the reversal of the eddy diffusion term upstream of Kerguelen which appears to be a key factor in destratifying the base of the mixed layer, and allowing the deeper winter mixed layers to develop downstream. This sudden strong cooling observed in the eddy heat diffusion parametrisation is linked to the energetic eddy field, and the strong cross-frontal interleaving observed in the ARGO profiles occurs at the convergence of the fronts upstream of Kerguelen.

Although SAMW forms at many locations along the SAF (Hanawa and Talley, 2001), the southeast Indian Ocean has the largest region with the deepest winter mixed layers, and is a dominant source of SAMW. The particular combination of conditions upstream, illustrated in the schematic of Figure 2.2, may make the formation process in the Indian Ocean more effective than elsewhere : a convergence of two strong dynamical fronts with an energetic eddy field around a large bathymetric barrier, the strong sudden cooling due to the eddy diffusion term, the circumpolar maximum in mean wind forcing and

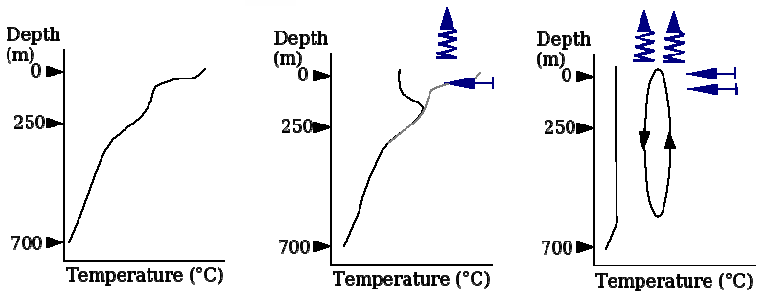

Month	May	June	July
Ekman intensity	-	+	++
Air Sea Fluxes	-	+	++

FIG. 2.15 – Schematic of the temporal evolution of a temperature profile during autumn/early winter in the region of SAMW formation. In autumn (left panel) the temperature profile is well stratified. As winter begins (middle panel), stronger Ekman advection of cold and fresh water reduces the temperature of the surface layer. A lens of warm and salty water remains just below the Ekman layer. As winter progresses (right panel), the Ekman advection and air sea cooling increase, destabilising the surface layer and eroding the subsurface lens to create a deep mixed layer.

Ekman heat transport. Downstream, the air-sea fluxes and Ekman transport are sufficient to explain the observed heat budget, but the deep mixed layers are present evidently because of the upstream conditions.

We have not included explicitly eddy diffusion or geostrophic advection in our downstream heat budget calculation, although we noted in section 6.3 that these terms may be locally important for float pairs which are entrained in meanders of the SAF. We did estimate the diffusion and advection terms based on the available datasets. Eddy heat diffusion was calculated from surface drifter data and temperature fields ; horizontal advection was calculated from altimetric data and temperature fields. However, when attempting to resolve fields dominated by strong mesoscale eddies, large errors were introduced, whenever any of the components (e.g. currents and temperature) were slightly offset from one another in space and time. Close to the energetic SAF with strong currents and strong temperature gradients, we often have random values of order 1000 Wm^{-2} but the net balance of terms is not calculated coherently. The large errors involved in the calculation led us to abandon the technique. The Ekman advection term, based on a larger scale forcing, is less affected by any spatio-temporal offsets in the two forcing components.

We have also seen from the stability analysis and the ARGO profiles that the haline component is important for the process of SAMW formation. The thermal destabilisation at the base of the mixed layer is compensated by the fresh haline stratification (see Figure 2.15). At present, we cannot calculate an accurate salt budget in the mixed layer due to the lack of high-resolution sea surface salinity data (equivalent to the satellite SST fields). However, the loss of salt and heat observed at the surface on the ARGO profiles is consistent with an Ekman advection from the South of cold and fresh water. Precipitation is thought to be of secondary importance compared to the Ekman contribution.

The sea surface salinity data are sparse, and spatial gradients are poorly resolved in the Southern Ocean by the climatological averages of SSS (Chaigneau and Morrow, 2002), although this situation will be improved as more ARGO floats are deployed. Satellite salinity measurements will be available in the future from missions such as SMOS or Aquarius, but are not expected to be accurate at high latitudes (low temperatures) nor available at mesoscale resolution.

Acknowledgements

The ARGO data were collected and made freely available by the International Argo Project and the national programmes that contribute to it. (www.argo.ucsd.edu, argo.jcommops.org). Argo is a pilot programme of the Global Ocean Observing System. This study was supported by the French PATOM and Coriolis programmes, and by NSF grants OCE 0336697 and OCE 0117618 to KS.

2.1.9 Appendix I : objective analysis of the float displacements

We obtained 8849 velocity components from the ARGO database and 11667 from the ALACE/PALACE database. We deduced from them the velocities at 400m by adding the climatological shear between their drifting depth and 400m. The velocities were averaged into 2°longitude by 1°latitude bins. Values formed by at least 5 data points are retained.

We mapped the velocity field and a stream function from the ARGO data in the Southern Indian Ocean using an objective analysis following Gille (2003a). We seek an estimate $\hat{\psi}$ of the true streamfunction ψ using the key relation :

$$\hat{\psi} = P\,(A + \epsilon I)^{-1}\,\phi \tag{2.3}$$

with :

$$P = \langle \phi, \psi \rangle \tag{2.4}$$

$$A = \langle \phi, \phi^T \rangle \tag{2.5}$$

where $\langle . \rangle$ is a scalar product, and ϕ is a column vector containing all of the u and v measurements : $\phi = [u_1, u_2, ...u_n, v_1, v_2, ...v_n]$. A is the covariance matrix of the measurement. We add an error ϵ to its diagonal which represents the effective increase in autocovariance due to measurement noise. This simplification assumes that the measurement noise is independent between two different positions and between u and v at the same position.

As shown by Gille and Kelly (1996), in the Southern Ocean we can apply a Gaussian correlation function in space. Gille (2003a) shows that an isotropic decorrelation scale of 495 km gives the best results for an objective analysis in the Southern Ocean. In this study we chose an isotropic decorrelation scale of 400 km.

The mean 10-day current velocities estimated from ARGO data at the parking depth contain errors, mainly due to the float drift at the surface. Furthermore, the float drift during the descent and ascent phase is also unknown. A study on the error in the drifting velocity at the float parking depth by Ichikawa et al. (2002) estimates this error to be between 10 to 25 percent. To be sure to overestimate this error we chose 50 percent error level for the float velocities.

2.1.10 Appendix II : Definition of the mixed layer depth

Accurate estimation of the mixed layer depth is a crucial part of the heat budget calculation. According to Thomson and Fine (2003) the threshold method with a finite difference criterion better approximates the "true" mixed layer depth, compared to the integral and regression methods. Experimental studies (see Brainerd and Gregg, 1995) also find that the mixed layer depth based on a difference criterion is more stable since the gradient criterion method requires high-resolution profiles which resolve the sharp vertical gradients. High-resolution in-situ profiles are not always available, and ARGO profiles with a 10-20 m vertical resolution in the mixed layer cannot resolve sharp vertical gradients.

We chose to use a difference criterion method. The usual parameters used with this method are temperature and density ; temperature is normally used when there is no equivalent salinity profiles. Most ARGO floats offer temperature and salinity profiles. We examined three different methods to find the mixed layer depth :

- a temperature difference criterion with a threshold 0.1° C ; $\Delta T \leq 0.1°$ C ,
- a density difference criterion with a threshold 0.01 $kg.m^{-3}$; $\Delta\sigma \leq 0.01\ kg.m^{-3}$,
- a density difference criterion with a threshold 0.03 $kg.m^{-3}$; $\Delta\sigma \leq 0.03\ kg.m^{-3}$

The first measurement closest to the surface was chosen as the reference for each profile if this measurement is in the range from 0 to 10m. If not the profile is rejected.

Consider first the difference between the two density criteria : $\Delta\sigma \leq 0.01$ and $\Delta\sigma \leq 0.03$. The results obtained by these two criteria are similar over most of the southern Indian Ocean (not shown). Nevertheless, some 3 % of the profiles reveal mixed layer depths which vary by more than 50 %. When these exceptional profiles are examined, the 0.03 threshold is consistently associated with the mixed layer that we seek (i.e., the mixed layer depth for monthly averaged applications).

In the southern Indian Ocean, there are big differences in the mixed layer depth depending on whether we use the temperature or the density criteria. In order to visually highlight these differences, we calculated the average of the mixed depth layer in bins (2° latitude by 4° longitude) for each criteria and then mapped the differences. Figure 2.16 shows the difference between the method $\Delta T \leq 0.1$ and $\Delta\sigma \leq 0.03$.
South of the SAF, the $\Delta T \leq 0.1$ criteria shows a mixed layer depth far deeper than the density criteria ; here there are small vertical temperature gradients but a strong halocline near the surface separating the fresh Antarctic Surface Waters from the saltier deep waters. In the region of mode water formation east of the Kerguelen Plateau between 80 and 120 East the temperature criterion is shallower than the density criterion where the surface T-S compensates. Figure 2.16 also shows selected profiles in these two areas where the there is a maximum depth difference between the two methods ($\Delta Depth > 100m$). Clearly in both areas the density difference method is much better in identifying the mixed layer depth. For the following work, we will apply the 0.03 density criteria to find the mixed layer depth.

2.1.11 Appendix III : Detailed heat budget calculations

Ekman Heat Transport

For the advective term of the heat budget equation (2.1), $\mathbf{v}$ the horizontal mean velocity can be decomposed into the Ekman and geostrophic components as $\mathbf{v} = \mathbf{v_E} + \mathbf{v_g}$.

The Ekman heat transport correspond to :

$$\int \mathbf{v}_E . \rho C_p \nabla T dz$$

integrated over the mixed layer. Here

$$\mathbf{v}_E . \nabla T$$

can be written :

$$\mathbf{v}_E . \nabla T = u_E \frac{\partial T}{\partial x} + v_E \frac{\partial T}{\partial y} + w_E \frac{\partial T}{\partial z}$$

Assuming that the Ekman layer is included in the mixed layer, ρC_p has no dependency with the vertical and within the mixed layer $\frac{\partial T}{\partial z} = 0$. Thus :

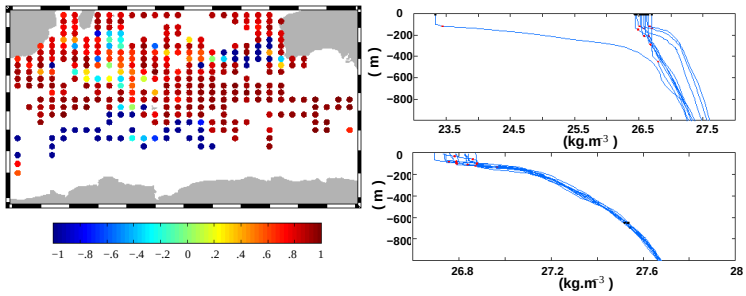

FIG. 2.16 – Left pannel : Normalized Depth differences of the mixed layer depth identified by the $\Delta\sigma \leq 0.03$ and the $\Delta T \leq 0.1$ criteria. A negative difference occurs when the $\Delta T \leq 0.1$ criteria is shallower than the $\Delta\sigma \leq 0.03$ criteria. Right pannel : selected density profiles in the region of mode water formation (upper) and south of the SAF (lower) which show large mixed layer depth differences using the density or temperature criteria. The red points correspond to the $\Delta\sigma \leq 0.03$ criterion and the black points to the $\Delta T \leq 0.1$ criterion.

$$\int_{EL} \mathbf{v}_E.\rho C_p \nabla T dz = \rho C_p (U_E \frac{\partial T}{\partial x} + V_E \frac{\partial T}{\partial y})$$

In the Southern Indian Ocean, the Ekman transport is mainly northward (positive) with regard to the strong westerly winds, and ∇T is dominated by the strong (positive) meridional temperature gradient. So we expect $V_E \frac{\partial T}{\partial y}$ to be much greater than $U_E \frac{\partial T}{\partial x}$. Consequently the Ekman induced heat flux can be approximated by $\rho C_P V_E \frac{\partial T}{\partial y}$. We note from this equation than a positive Ekman heat transport (as in our case) will induce a negative temperature tendency, or cooling. In other words a positive Ekman heat transport can induce a negative effective Ekman heat flux at the base of the Ekman layer.

Heat Content variations from ARGO **floats**

The heat content variation is calculated for each ARGO float within the formation region, using pairs of float profiles separated by 30 days (3 float cycles) which remain in our zone. The temperature is integrated down to the deepest mixed layer depth which occurs for the two profiles.

Since the floats do not sample identically the water column, every profile has been vertically interpolated onto a regular 10db grid. The shallowest value of each profile has also been extended to the surface.

Several techniques were applied to evaluate the heat content variation. A first possibility was to calculate a mean temperature profile for every month, which was used to calculate a mean mixed layer depth and thus a mean heat content. This method shows a poor ability to represent the cycleXS of the wintertime enhanced convection and was not retained. Instead we adopted a second method where all of the 30 day heat content variations available for the different floats were binned to form the monthly average.

For each 30 day heat content calculation, the forcing terms (Ekman and air sea fluxes) are interpolated onto the 10-day float positions and then averaged over the 30 days. In other words, considering 4 profiles from the same float, Ekman advection and air sea fluxes are interpolated onto the first, the second and the third profile, and then averaged, and the heat content variation is computed between the first and the fourth profile. The average of the forcing terms, and the variation of the heat content are stored with the date of the fourth profile. The monthly averages shown in Figures Figures 2.8 and 2.10 are the average of all float pairs within the formation region whose fourth profile occurs during the given month.

One problem encountered with this calculation concerns the lagrangian behaviour of our floats. The heat budget calculation assumes a local change of the mixed layer in the same location, but for our calculation the floats move between two samples. The movement of the float from one water mass to another introduces a change of heat content due to the float's advection. To assure that the floats remain in the same local area and water masses and to reduce this "relative advection", we developed a series of tests.

1. First, we elimated pairs of profiles when their difference in SST (considering time and position) was 1 °C greater than the local change of SST (at the last profile position) during the same period. This reduces the effects of floats close to the SAF crossing large SST gradients due to meanders or eddies.
2. We also added a deep density criteria. If the difference between the density at 1000m is greater than 0.1 $kg.m^{-3}$ we consider that the float doesn't sample the same water mass.
3. We also calculated the monthly rms of the forcing terms and of the ARGO heat content variation. We then removed the individual ARGO profiles whose value plus one rms lay outside the range of the forcing terms plus one rms. We visually checked that this criteria removed most profiles crossing the SAF.

The net effect of these tests was to eliminate 36 % of data pairs.

Chapitre 3

Les fronts de l'ACC et leur variabilité

L'étude sur la formation des SAMW qui a fait l'objet du précédent chapitre nous mène à considérer de façon plus approfondie les fronts de l'ACC. Nous avons montré avec des données in situ de l'océan que la formation des SAMW dans la zone du Sud-Est Indien peut être expliquée à grande échelle uniquement avec les deux termes de flux de chaleur air-mer et de transport de chaleur d'Ekman. Nous avons également montré que cette formation apparaît juste au Nord du front Subantarctique moyen tel qu'il a été défini par Orsi et al. (1995). Enfin, nous avons défendu la thèse selon laquelle la diffusion tourbillonaire, qui n'a qu'un rôle "direct" négligeable à grande échelle dans la zone de formation, prend une grande importance "indirecte" pour pré-conditionner la colonne d'eau ou pour empêcher la déstabilisation dans l'Ouest du bassin Sud-Indien.

Une part non négligeable de nos conclusions porte sur l'importance du rôle, dans la formation des SAMW, du fort courant circumpolaire Antarctique et de la dynamique tourbillonnaire associée. Ces résultats nous ont ainsi suggéré une étude détaillée des fronts de l'ACC, afin de mieux les définir et d'en étudier leur éventuelle variabilité.

Qu'est ce qu'un front ? Comme nous l'avons vu en section 1.1, les fronts sont définis comme des frontières entre des masses d'eau aux caractéristiques hydrologiques différentes ou comme de puissants jets océaniques. Mais ces deux définitions, hydrologique et dynamique, correspondent-elles aux mêmes fronts ? Est-il justifié de croire que les fronts sont continus tout autour de la ceinture circumpolaire ? Le tracé des fronts a été établi historiquement à partir de données in situ à certains point clés de la ceinture circumpolaire, puis a été lissé et relié entre ces points clés. Ne pourrait-on pas imaginer des portions de fronts se séparant puis se reliant à d'autres endroits, des portions du SAF moins intenses, avec une quasi disparition du front et un autre front qui prendrait le relais ? Pourrait-on aussi concevoir une variabilité similaire dans le temps ? Si ces hypothèses s'avéraient réelles, ceci aurait évidemment des conséquences de première importance pour la formation et les caractéristiques des SAMW, formées au Nord du SAF.

Aussi le deuxième volet de cette thèse a-t-il concentré nos efforts pour trouver une définition des fronts de l'ACC en nous servant au maximum des observations de l'Océan Austral. En nous positionnant

dans la continuité des récentes évolutions de la définition des fronts, nous avons développé une nouvelle définition du SAF et du PF en nous basant sur des données satellitales de hauteur de mer et des données in situ de la colonne d'eau. Forts de cette définition, nous avons pu étudier avec précision la position moyenne des fronts ainsi que leur variabilité sur les treize ans de données disponibles (1993-2005). Nous avons ensuite analysé les forçages atmosphériques de cette variabilité, en particulier les forçages climatiques de l'Hémisphère Sud.

Les résultats de cette étude ont été exposés dans un article que nous avons soumis à la revue *Journal of Climate* en septembre 2006 et dont la version après révision est exposée dans la prochaine section.

Dans cette étude nous nous sommes focalisés sur la variabilité haute fréquence de la circulation de l'ACC le long de la ceinture circumpolaire. Dans ce type d'étude, il faut choisir entre enquêter sur un endroit précis de l'Océan où des mesures répétées de la colonne d'eau ont été effectuées, ou entreprendre une étude à plus grande échelle avec un nombre plus restreint de données de la colonne d'eau. Ces deux stratégies ont chacune leurs avantages et leurs inconvénients. C'est pourquoi nous avons décidé de mener parallèlement deux études, respectivement reliées à chacune des deux stratégies. Dans une étude connexe à celle présentée dans ce chapitre, nous avons étudié la variabilité des propriétés hydrologiques à basse fréquence en nous focalisant sur des sections répétées entre la Tasmanie et l'Antarctique (autour de la longitude 140°E) : la ligne SURVOSTRAL et la section WOCE SR3. Les objectifs premiers de cette étude étaient de comprendre les causes de la hausse du niveau de la mer observée dans la région pendant les treize dernières années, et d'analyser l'éventuelle tendance du mouvement des fronts à partir de données précises de la colonne d'eau. Cette étude a fait l'objet d'un article qui a été accepté pour publication dans le journal *Progress in Oceanography*. Cet article est présenté en Annexe 2. La seconde stratégie, qui fait l'objet de ce chapitre analyse le suivi des fronts sur toute la ceinture circumpolaire et leur déplacement forcé par des variabilités climatiques.

3.1 Response of the Antarctic Circumpolar Current to atmospheric variability (Sallée J.B., Speer K., and Morrow R. , 2007)

Abstract. Historical hydrographic profiles, combined with recent ARGO profiles, are used to obtain an estimate of the mean geostrophic circulation in the Southern Ocean. Thirteen years of altimetric sea level anomaly data are then added to reconstruct the time variable sea-level, and this new dataset is analyzed to identify and monitor the position of the two main fronts of the ACC during the period 1993-2005. We relate their movements to the two main atmospheric climate modes of the Southern Hemisphere, the Southern Annular Mode (SAM) and the El-Nino Southern Oscillation (ENSO). We find that although the fronts are steered by the bathymetry, which sets their mean pathway at first order, in flat-bottom areas the fronts are subject to large meandering due to mesoscale activity and atmospheric forcing. While the dominant mode of atmospheric variability in the Southern Hemisphere, SAM, is relatively symmetric, the oceanic response of the fronts is not, showing substantial regional differences. Around the circumpolar belt the fronts vary in latitude, exposing them to different Ekman transport anomalies induced by the SAM. Three typical scenarios occur in response to atmospheric forcing : poleward movement of the frontal structure in the Indian basin during positive SAM events, an equatorward movement in the Central Pacific, and an intensification without substantial meridional movement in the Indo-Pacific basin. The study also shows the geographical regions which are dominated by a SAM or ENSO response at low and high frequencies.

3.1.1 Introduction

Atmospheric studies in the Southern Hemisphere have shown a strong dominance of one particular mode of variability that accounts for most of the variance in sea level pressure (SLP) (Thompson and Wallace, 2002). The ringlike character of this mode (see Figure 3.1a) has given rise to the term "Southern Annular Mode" (SAM). There is a clear out-of-phase pressure relationship over the polar and subtropical regions. Thompson and Wallace (2002) showed that this ringlike pattern is associated with a typical zonal wind pattern. During positive SAM periods, the maximum wind stress is shifted to the south, and the westerly winds are reinforced around 60°S with easterly anomalies around 35°S. The Antarctic Circumpolar Current (ACC) is strongly wind forced, although whether or not its forcing is dominated by the wind stress or the wind stress curl remains controversial (e.g. Baker, 1982 ; Warren et al., 1996 ; Hughes et al., 1999 ; Gille et al., 2001 ; Dong et al., 2006). However, it may be expected to move in response to a changing SAM. Coupled model studies have suggested that a dominantly zonally symmetric response to the SAM exists in the Southern Ocean (Hall and Visbeck, 2002 ; Sen Gupta and England, 2006).

Other climate modes can also impact on the Southern Ocean circulation. The El Nino-Southern Oscillation (ENSO), defined by sea-surface temperature anomalies in the tropical Pacific latitudes, has a definite zonally asymmetric impact on the atmospheric circulation at extratropical latitudes. ENSO generates atmospheric Rossby waves which travel to high latitudes (Hoskins and Karoly, 1981 ; Turner, 2004). Karoly (1989) demonstrated that El-Nino (positive ENSO) events are associated with the generation of two large low pressure cells over South America and New-Zealand, and one high pressure cell over the central Pacific. This pattern, clearly shown by a regression of SLP on the ENSO index (see Figure 3.1c),

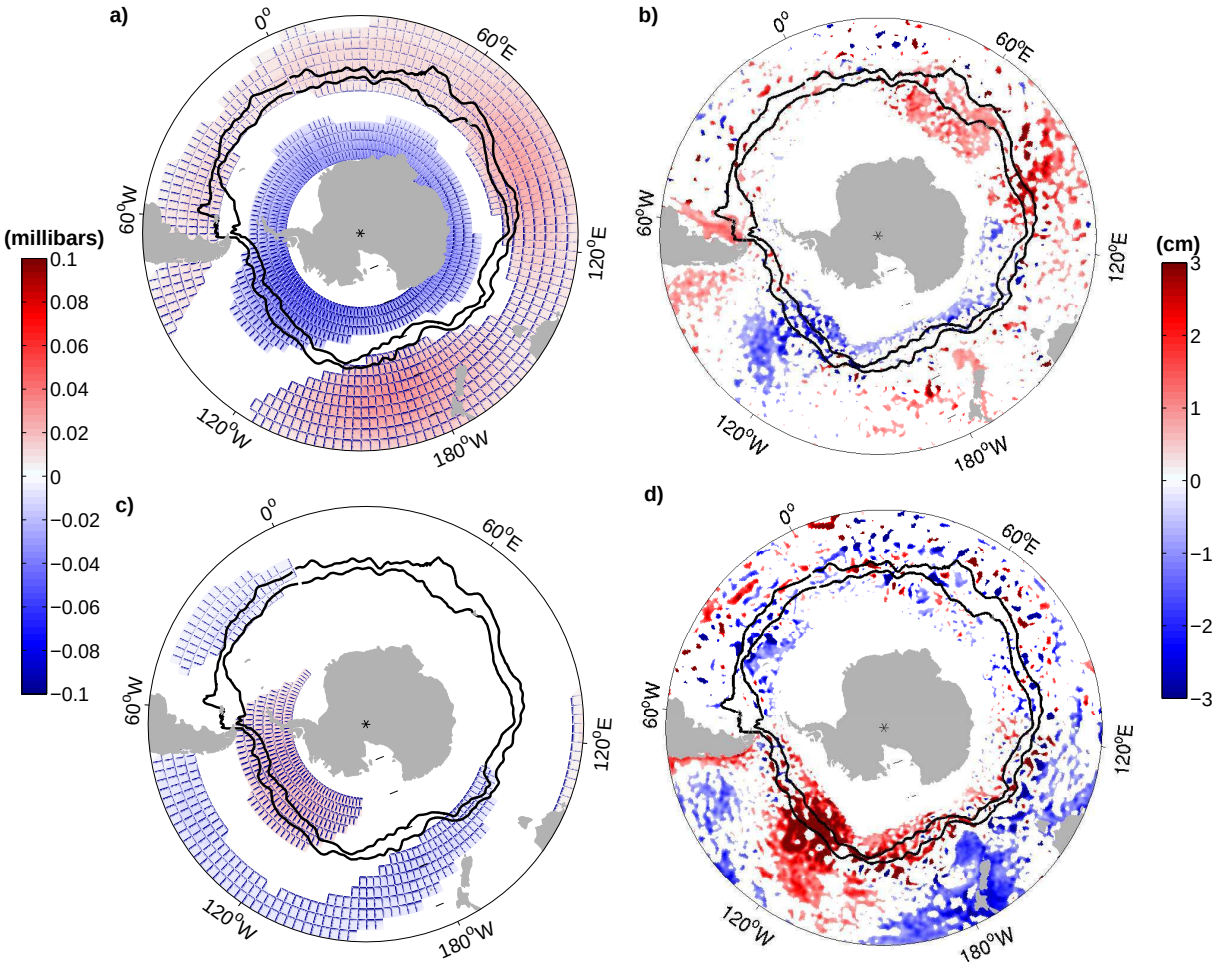

FIG. 3.1 – (a) SLP and (b) SLA regressed onto the SAM index for the period 1993-2005. (c) SLP and (d) SLA regressed onto the ENSO index for the period 1993-2005. Patterns below the 80 % significance limit are blanked. The black lines show the mean SAF and PF positions.

is known as the Pacific-South American Oscillation (PSA). This mode is centered on the Pacific Ocean and is associated with the second EOF mode of the SLP field in the Southern Hemisphere (SAM being the first mode).

With respect to the mean ocean circulation, the Southern Ocean is distinguished from all other oceans by the presence of a strong, eastward, circumpolar current, the Antarctic Circumpolar Current (ACC). The ACC connects the three major ocean basins (Atlantic, Pacific and Indian) and redistributes active and passive oceanic tracers such as heat, salt, and nutrients. Thus, anomalies created by atmospheric forcing in one basin can be carried around the globe affecting the global oceanic mass balance, ocean stratification, circulation and consequently heat transport and climate. The ACC is traditionally thought to be composed of a series of hydrographic fronts, associated with sloping isopycnals and relatively strong meridional property gradients. Several cores of strong horizontal gradients in potential temperature, salinity, and density, implying intense geostrophic currents, typically characterize the ACC fronts (Deacon, 1937; Nowlin et al, 1977; Orsi et al, 1995; Belkin and Gordon, 1996). These fronts separate regions with different water masses and more homogeneous oceanic properties.

The fronts are usually defined by simple criteria based on the interior hydrographic structure (e.g. Peterson and Stramma, 1991; Orsi et al., 1995; Belkin and Gordon, 1996). Recently, however, satellite data have provided a new set of frontal definitions based on gradients of sea-surface temperature (SST) or sea surface height (SSH) (Gille et al., 1994; Hughes and Ash, 2001; Sokolov and Rintoul, 2002; Sokolov and Rintoul, 2006; Dong et al., 2006). Interestingly, the two types of frontal definitions, based on interior hydrographic structure or on surface satellite data, show close agreement in regional comparisons (Sokolov and Rintoul, 2002; Sokolov and Rintoul, 2006; Dong et al., 2006). However, the satellite observations not only reveal the time variability of these fronts but also show that the ACC has a much more complex frontal structure than is evident from climatological hydrographic data.

Previous work on the ocean response to the different atmospheric modes has mainly been based on numerical modeling results (e.g. Hall and Visbeck, 2002; Sen Gupta and England, 2006). These numerical results are difficult to confirm with real ocean observations due to the lack of data from the mid- to high-latitudes in the Southern Ocean. Gridded altimetric sea level data offers relatively uniform spatial coverage at roughly 100km scales every week for more than 13 yrs, permitting studies of the lower frequency variability. In addition, as of 2006, the international Argo project has added more than 30,000 hydrographic profiles in the Southern Ocean, coarsely distributed in space, but evenly distributed in time, providing an unprecedented seasonal sampling of the subsurface ocean.

Based on these two databases, altimetry and Argo, we are now able have a better view of the Southern Ocean at the circumpolar scale. A first glance reveals that the ocean does not respond to the SAM atmospheric forcing as a purely zonal response. Figure 3.1b shows that the altimetric Sea Level Anomaly (SLA) regressed onto the SAM index between 1993 and 2005 has distinct regional differences, although the SAM shows an annular pattern during the same period (Figure 3.1a). In particular, in the Indian sector from 30-120°E, the sea level is anticorrelated with the surface pressure (Figure 3.1a and b). Sea level anomalies regressed onto the ENSO index are well correlated with surface pressure in the Pacific (Figure 3.1c and d). In other basins, the ENSO sea level response does not resemble the ENSO-related winds, but tends to be anticorrelated with the oceanic SAM response (Figure 3.1b and d).

In this paper we are interested in how changes in the large-scale atmospheric forcing can impact on the Southern Ocean circulation and fronts. For example, trends in the atmospheric circulation are thought to have modified the Pacific subtropical gyre (Roemmich et al., 2005 ; Qiu, 2002 ; Vivier et al., 2005). This study will consider the Southern Ocean response to the primary atmospheric modes. We will focus on the frontal zones since they will be associated with the strongest signals of variability in SST, intensity of the flow, and upwelling.

We will present a robust satellite-based definition of the two main dynamic fronts in the Southern Ocean : the Subantarctic Front (SAF) and the Polar Front (PF)(section 3.1.2). These two fronts carry up to 75 % of the total ACC transport south of Australia (Rintoul and Sokolov, 2001). In certain regions of the ACC, these fronts are strongly constrained by the bathymetry (Moore, et al., 1999 ; Dong et al., 2006) but elsewhere the frontal positions vary regionally in response to the main climate modes (ENSO and SAM ; section 3.1.3). In section 3.1.4 we will discuss the mechanisms which control the frontal movement for the different basins.

3.1.2 Data and methods

Data

Mean sea surface height

In this study, the vertical structure of the Southern Ocean is determined from the combination of two distinct datasets : the Argo database and the WOCE Southern Ocean Data Base (SODB).

The Argo international program has seeded all of the world's oceans since 1999 and is particularly important in the Southern Ocean which is historically poorly sampled. As of 2006, this database includes about 30,000 Southern Ocean profiles. These data were collected and made freely available by the International Argo Project and the national programs that contribute to it[1]. We only use profiles which have passed the Argo real-time quality control, containing information on their position, date, temperature (T) and salinity (S) profiles. Most Argo profiles sample T and S from the surface to 2000m depth every 10 days.

The SODB consists of about 93,000 hydrographic (bottle and CTD) stations south of 25°S. The primary source is the World Ocean Atlas 98 (WOA98) and its successor, World Ocean Database 2001 (WOD01), which have been augmented with the World Ocean Circulation Experiment (WOCE) observations and also with stations coming directly from investigators. Each station was individually quality controlled by comparison to nearby WOCE stations. This work of collection and quality control have been performed and made freely available (Orsi and Whitworth, 2005[2]).

The Argo project contributes about 30 % of the total number of Southern Ocean profiles, however it provides very important sampling. In fact, the two datasets are complementary in space and time. The first 5 years of ARGO sampling provides more profiles in the center of ocean basins, and during austral winter and spring, than decades of historical data (see Figure 3.2).

[1] http ://www.argo.ucsd.edu and http ://www.ifremer.fr/coriolis/cdc/argo.htm
[2] http ://woceSOatlas.tamu.edu

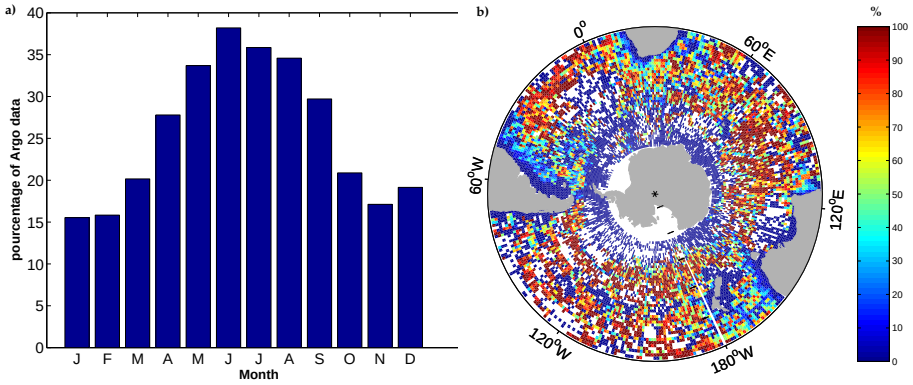

FIG. 3.2 – (a) Monthly and (b) spatial in one degree bins percentage of ARGO profiles in the combined ARGO-SODB database, gridded from one degree bins.

Our first goal was to establish the long term mean dynamic height field and geostrophic circulation of the Southern Ocean from the Argo and SODB hydrography. We selected the T-S profiles defined between 10 and 1500 m to produce a database of the surface dynamic height referenced to 1500m. This 1500 m reference level was chosen as the best compromise between the deepest possible level and including a maximum number of data profiles. In this database the percentage of Argo profiles is even more striking, providing 22,894 profiles (55 %) against 18,956 profiles (45 %) for the SODB. We computed mean dynamic height and geostrophic circulation maps using the Ridgway et al (2002) interpolation method.

Time variable sea surface height

In order to map the time variable dynamic height and monitor the frontal positions we have constructed 13 years of weekly maps of Sea Surface Height referenced to 1500m (SSH_{1500m}) from 1993 to 2005. Specifically, we add the mean dynamic height computed from the historical database (see section 3.1.2) to the weekly maps of altimetric sea level anomaly (SLA). The mapped SLA fields are provided by CLS/AVISO and are based on data from the available altimeter missions (Topex/POSEIDON, ERS-1 and ERS-2, GFO, ENVISAT, JASON). The mapping technique is described by LeTraon et al. (1998). Anomalies are calculated with respect to a 7-year mean (1992-1999) and are mapped onto a 1/3° grid in longitude and variable grid in latitude, ranging from approximately 1/20° at 80°S to 1/4° at 30°S. A discussion of the aliased high frequency errors is given by Morrow et al. (2003). The altimetry data resolves wavelengths greater than 150 km, with a temporal resolution of 20 days (Ducet et al., 2000). In the Southern Ocean where the groundtracks converge, we can resolve 100 km wavelengths. These weekly data are filtered to a one month interval to compare them to the monthly atmospheric indexes used in this study.

Climatic indexes

The monthly Southern Annular Mode Index and the El Nino-Southern Oscillation Index were obtained from the NOAA Climate Prediction Center web site[3] for the period 1979-2004. The SAM index is defined as the first principal component of monthly 700-hPa geopotential height anomalies from the

[3] www.cpc.ncep.noaa.gov

NCEP-NCAR reanalysis dataset. We use the Nino3.4 ENSO index. Its variations are based on SST anomalies averaged over the region spanning 5°N-5°S, 170-120°W.

Atmospheric data

To investigate the link between the atmospheric and oceanic dynamics, we use the monthly NCEP reanalysis of wind stress and sea level pressure (SLP) which are made available by the NOAA-CIRES Climate Diagnostic Center[4].

Definition of the Fronts in the ACC

Recently, new Southern Ocean frontal definitions have emerged based on satellite data (Gille et al., 1994 ; Hughes et Ash, 2001 ; Sokolov and Rintoul, 2002 ; Sokolov and Rintoul, 2006 ; Dong et al., 2006). Sokolov and Rintoul (2002) found that a judicious choice of SSH contour provided a good representation of the mean position of the main fronts south of Tasmania, and more recently developed an objective method to select the SSH contours representing different fronts (Sokolov and Rintoul, 2006). In the region between 100 and 180 °E they found a series of contour values which were relatively stable in time and space. They concluded that 10 branches are necessary to completely describe the ACC in this region. The primary frontal positions appear to agree well with the previous hydrographic-based definitions.

The strong advantage of the satellite definition is the potential for revealing the complexity and the variability of the fronts. Fronts merge, split, weaken, meander, etc., and this variability can be monitored with satellite data. In comparison, hydrographic data provide information on the vertical structure of the fronts. However, given that the in-situ data distribution is sparse, a description based on non-synoptic hydrographic data tends to mix together the different frontal states.

We chose to apply a similar SSH contour definition to describe the two most energetic fronts of the Southern Ocean, the Subantarctic Front and Polar Front (resp. SAF and PF). In the presence of time variations in intensity, splitting and merging of fronts, we cannot expect even the primary fronts to be uniquely defined or identified by a single contour or by any other quantity at every time. They can be ambiguous at certain times within their zone of strong amplitude variability. However, a single contour can be associated with the front in the sense that most of the time (for instance, 98 % in the case of the PF, see below) they would be located together based on a suite of traditional definitions. Since fronts are an association of filaments that merge, split, appear and disappear within the primary frontal zones (Hughes and Ash, 2001), the motion of a single contour does not necessarily always follow exactly the same filament of a given front. However, as we will see, it will often follow the filament with a strong SSH gradient.

Gradients of SSH or SST are a natural way to define a front. In order to exploit a SSH gradient definition one would have to find the location of the maximum gradients and define a curve going through these points. The choice of the contour value has to be carefully defined to match the subsurface data, as well as the position of the maximum SSH gradient.

The traditional definition of the Polar Front (PF) is the northern limit of the Antarctic Winter Water (AAWW) defined as the tongue of 2°C water at 200m (Orsi et al., 1995 ; Belkin and Gordon, 1996).

[4]http ://www.cdc.noaa.gov

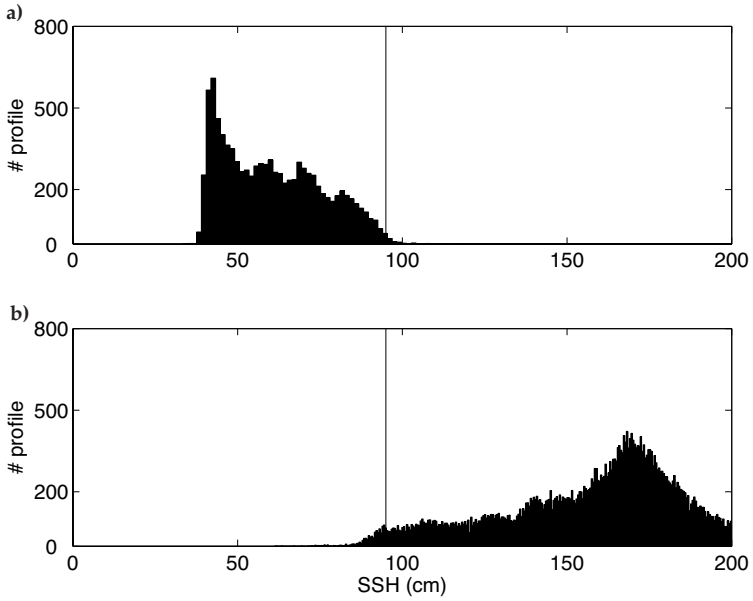

FIG. 3.3 – (a) Number of profiles sampled within the AAWW region as a function of the SSH_{1500} of the profile. (b) Number of profiles sampled outside the AAWW region as a fonction of the SSH_{1500} of the profile. The vertical line represents $SSH_{1500} = 0.95m$, our chosen PF contour.

Our choice of contour which defines this limit is $SSH_{1500m} = 0.95m$ which shows very good agreement with the subsurface definition of the AAWW tongue. Figure 3.3 shows the distribution of historical profiles (from SODB and ARGO) sampled during the altimetric period, with respect to the AAWW position. Virtually every profile with AAWW characteristics (T less than 2°C within the first 200m) has a SSH referenced to 1500m which is less than 0.95m (99.4 %). Conversely, almost every profile found north of the AAWW has a SSH referenced to 1500m greater than 0.95m (98 %). The contour SSH_{1500m}=0.95m was chosen as it maximizes these percentages.

The Subantarctic Front can be defined as the maximum in the meridional gradient of temperature, density, or potential vorticity (PV). Belkin and Gordon (1996) define the SAF as the maximum temperature gradient at 300m (T_{300m}). Unfortunately we cannot directly compare this definition with our altimetric definition because the sampling of historical profiles is sparse and we cannot accurately resolve the horizontal property gradients. Instead, we have extracted T_{300m} from profiles obtained during the altimetric period and calculated their distance from the $SSH_{1500m} = 1.20m$ contour for the same day. We observe that the $SSH_{1500m} = 1.20m$ contour coincides with the region where there is a sharp change in T_{300m} along the ACC pathway, and also agrees very well with the maximum in potential vorticity gradient along the $\sigma_\theta = 27kg.m^{-3}$ (see Figure 3.4). We tested different contour values and 1.20m was associated with the strongest gradients of T_{300m} and $PV_{27kg.m^{-3}}$.

Downstream of Drake Passage, the fronts cross the Falkland Ridge and make a loop to the north along the Argentina coast to join the Brazil Current (Orsi et al., 1995). The individual SSH contours do track this pathway quite well, but our mean and variability calculations use longitudinal bin averages which create a false mean position and exagerate the variability in the loop area. These statistical errors

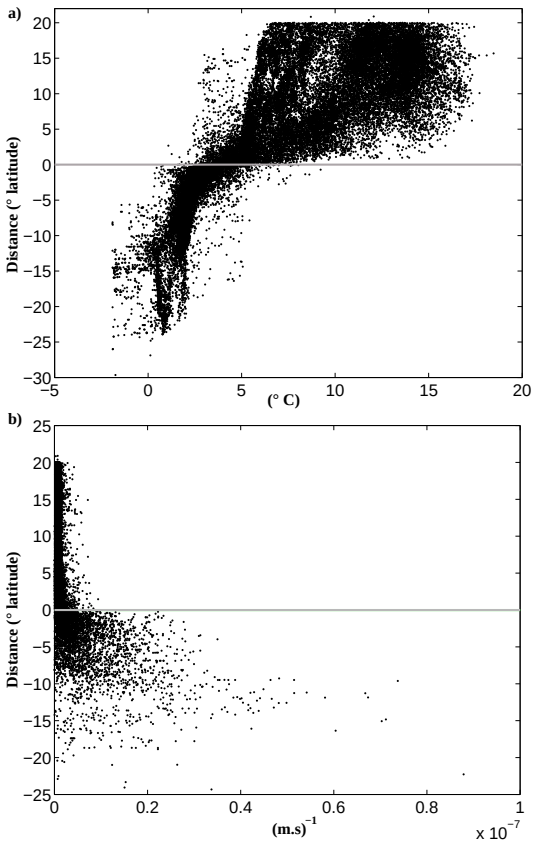

FIG. 3.4 – (a) Distance (in latitude) of SSH_{1500} from the 1.20m contour for each profile, plotted as a function of T_{300m}. (b) Distance of SSH_{1500} from the 1.20m contour as a function of the PV on $\sigma_{theta} = 27kg.m^{-3}$. Positive distance corresponds to a profile north of the contour ; negative distance corresponds to a profile south of the contour. The contour 1.20m is our chosen SAF contour.

are increased when the loop is not connected, for example when the jet path switches south of the Falkland Islands. For these reasons, this area from 290 °E to 310 °E will not be analyzed further in this study.

Figure 3.5 shows the mean position of the PF and SAF, as defined from the 0.95m and 1.20m contours of SSH_{1500m}, overlaid on the climatological SST and SSH gradients. Our chosen contours join the patches of strong gradients, which are characteristic of the intense jet. The exception is in the region 20-70°E where the strongest gradients are associated with the Agulhas Retroflection and its fronts. We have compared our frontal definition with the Sokolov and Rintoul (2006) fronts defined for the region 100-180 °E. Sokolov and Rintoul (2006) have different frontal contour values since they use a climatological steric height relative to 2500m. In order to include the Argo floats, our climatology is relative to 1500m, so we can't directly compare our contour values. However, we can compare the positions of our respective fronts. Our PF corresponds to their northern branch of the PF which is the most intense of their three PF branches. Our SAF corresponds to their southern branch of the SAF which is again their most intense branch. Thus, with our definition we have identified the most intense fronts of the ACC in the zone 100-180°E.

Our mean frontal positions agree globally with the mean position of Orsi et al. (1995) (see Figure 3.6). However, in some places large differences exist. For example, near the Kerguelen Plateau our method sometimes positions the PF to the south of Kerguelen Island and sometimes to the north. Orsi et al. (1995) located the PF farther north. Other studies have also positioned the PF clearly north of the Island (e.g. Gille, 1994; Belkin and Gordon, 1996; Dong et al., 2006). However, our position seems to be consistent with the results of Moore et al (1999), Kostianoy et al (2004) and Park et al (1998). Faced with this controversial positioning of the front in this region, we tested our front definition against the repeated OISO CTD sections for the three years from 1998 to 2001 (see Figure 3.7). Our PF is coherent with the subsurface AAWW tongue extension over these three summers, which gives us confidence that our PF contour is consistently following the primary PF location. The SAF is also coherent with the subsurface data.

It is also instructive to consider the time series of frontal movements at a given location. Figure 3.8a shows the time series of our SAF and PF contours, superimposed on the meridional SSH gradients at 255°E in the southeast Pacific. This deep-basin region with relatively weak mean gradients (Figure 3.5) is also a region where our mean fronts show different stationary meanders compared to the Orsi fronts (Figure 3.6). Figure 3.8a shows that both the PF and the SAF track coherent positive SSH gradient structures over time. Furthermore, there are clearly periods where the fronts split (e.g., around year 2002) and our chosen contour tends to follow the most intense branch. There are a few high frequency outliers, but these events are rare. In general, the varying position of the maximum SSH gradient is very well captured by our chosen 1.2 m and 0.95 m contours. The method provides one way to analyze the evolution of the complex frontal structure that is associated with the two primary fronts of the ACC.

It is not too surprising that fronts defined by the contour method are in good agreement with the subsurface hydrography. In the Southern Ocean, and particularly for the SAF, the baroclinicity extends to the sea floor. The geopotential height of the sea surface is approximately a streamline, and exhibits a tight empirical relationship with the hydrographic structure of the entire water column (Sun and Watts, 2001; Watts et al., 2001). Hence the maximum in SSH gradient (associated with the core of the internal jet) is associated with a particular hydrographic structure, and will be also associated with a particular

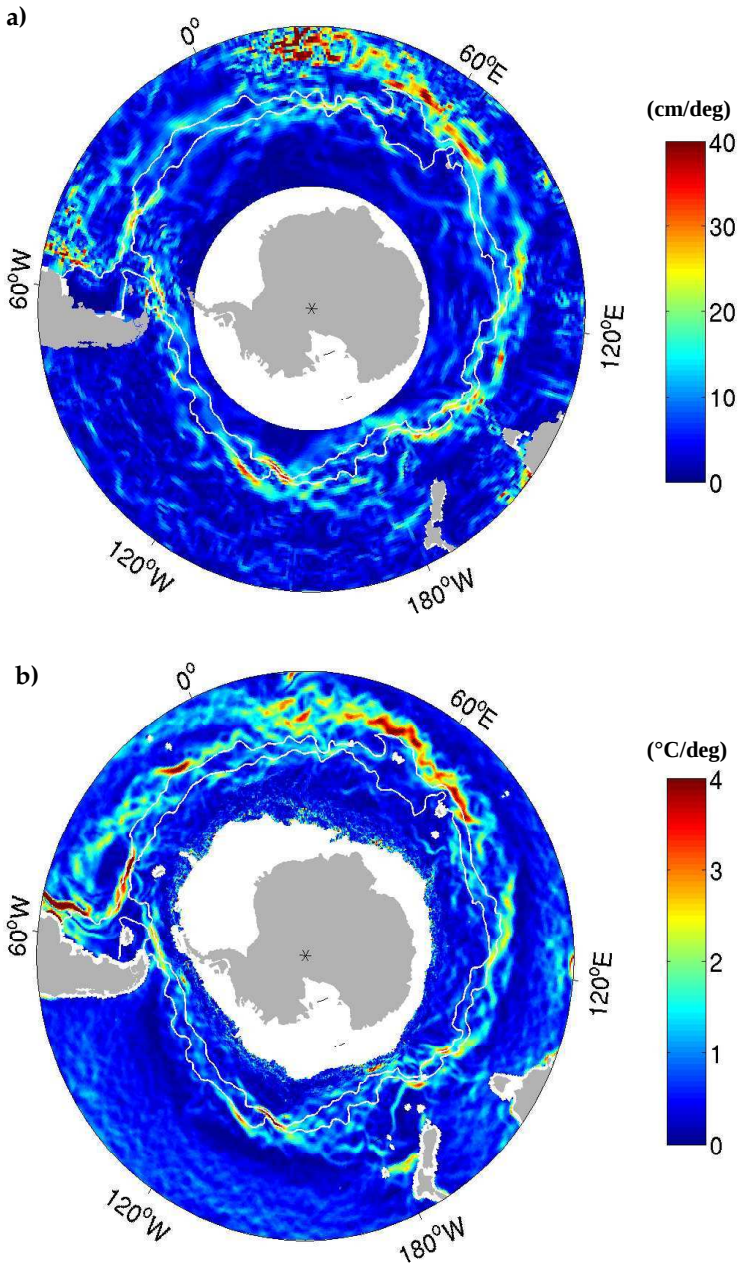

FIG. 3.5 – Mean (a) SSH gradient ; (b) SST gradient. White lines are the mean positions of SAF (north) and PF (south) from the climatological SSH field.

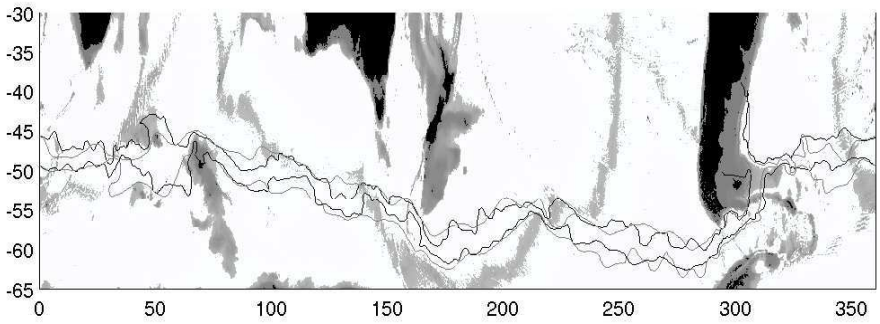

FIG. 3.6 – Mean PF (south) and SAF (north) positions from Orsi et al. (1995) (in gray) and our SSH contour method (in black), superimposed on the bathymetry shallower than 3000m.

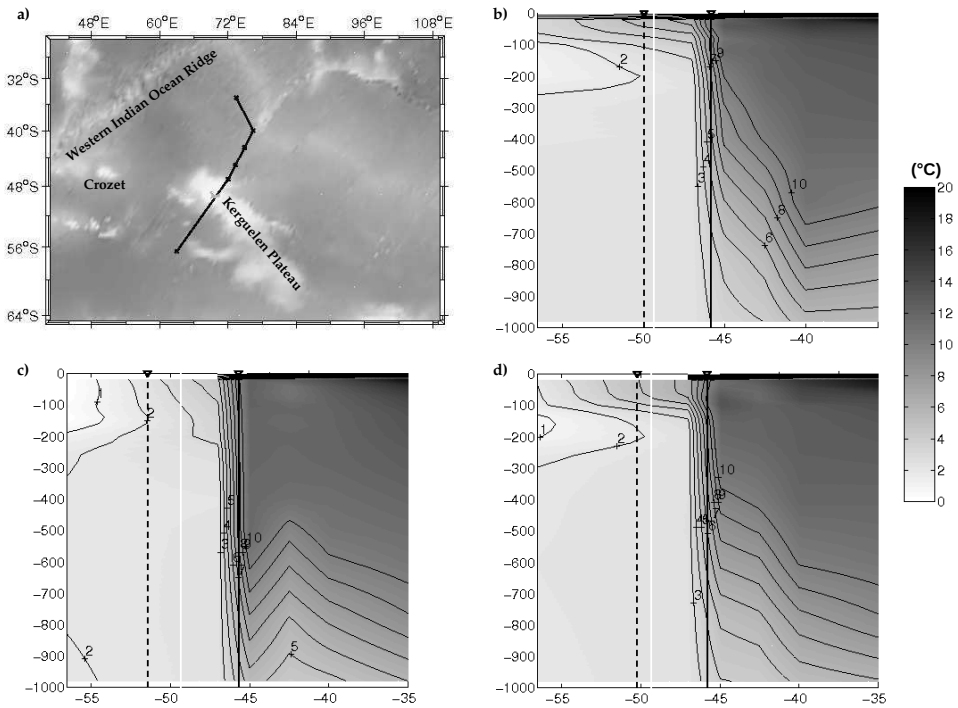

FIG. 3.7 – Vertical temperature sections from the repeated OISO sections in the Southern Indian Ocean from 1998 to 2001. (a) section positions ; Summer sections in (b) 97-98, (c) 98-99, and (d) 99-00. The vertical solid black line represents the position of the SAF found by the SSH contour method at the period of the cruise. The vertical dashed black line is the PF position found by the contour method, and the white line represents the position of Kerguelen Island.

SSH contour. This is why a SSH contour provides an accurate estimate of the position of the principal jet cores in the ACC, for the combined mean and mesoscale variability.

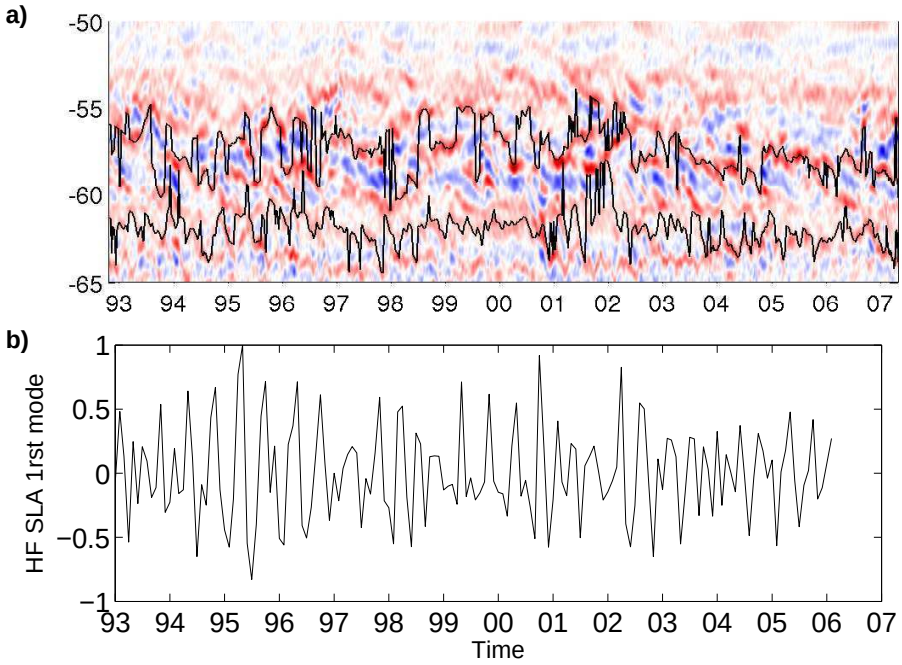

FIG. 3.8 – a) Hovmuller diagram of our SAF and PF contours, superimposed on the meridional SSH gradients at 255 °E in the southeast Pacific. Positive gradient values are shown in red and negative in blue. The x-axis is the time in year. b) Normalized time series of the first EOF of the large-scale high-frequency SLA mode. The spatial mode is similar to the high-frequency barotropic modes found in previous studies (e.g. Fukumori et al., 1998) and is maximum in the South East Pacific around 255°E. At 255°E this mode introduces maximum variations of +/- 1° latitude in the frontal position.

Errors in the frontal definition

This validation in different regions supports the notion that associating a SSH contour with a particular front is realistic and gives us confidence to continue with a study on frontal variability. However, we need to address the errors of this method. Note that the inverse barometer effect has already been corrected in the treatment of altimetric data (Ducet et al., 2000), hence does not represent an error on the contour position. The main errors can be induced by :

- the seasonal steric cycle,
- the trend in long term sea level rise,
- using a 1500 m level of no motion,
- the accuracy of the altimeter data,
- large-scale, high-frequency SSH variability.

We examine these in turn. Stammer (1997) estimated the seasonal steric cycle in the global ocean and found it to be less than 2cm in the Southern Ocean. Lombard et al. (2006) found an increasing trend in long term sea level of around 3 mm/year on average in the Southern Ocean from 1993 to 2003. Over a decade this gives a large-scale sea level rise of about 3cm, which tends to shift our frontal positions south over the same period.

Using a 1500m level of zero motion implies that we neglect the mean barotropic flow and the mean baroclinic flow below 1500m. In order to assess the impact of this assumption we compared our mean dynamic height field with the absolute mean dynamic height product developed by Rio et al. (2005). This latter product mixes satellite data from GRACE and altimetry with in-situ data from SVP drifters, ARGO profiles and ship-based hydrographic data. Their mean field includes both barotropic and baroclinic components and is in very good agreement with ours. The Rio et al. (2005) product uses a different reference density, and when using the Rio et al. (2005) mean SSH our PF corresponds to a 0.6m contour, and our SAF to a 1.0m contour. We find that both products show the same large scale patterns and large stationary meanders of the ACC. Using the 1500m level of zero motion will reduce the steric height amplitude and slightly reduce the intensity of the cross-frontal gradients. However, it does not affect the position of the mean dynamical structure of the ACC fronts. We note that the variable part of the barotropic and the deep baroclinic flow will be observed by altimetry. The Rio et al. (2005) product does not use in-situ profiles sampled after 2002. Given the substantial increase in the number of ARGO profiles in the Southern Ocean since 2002, we believe our mean field provides a better representation of the finer scale structure of the Southern Ocean.

The accuracy of the altimeter data is another source of error for our method. It includes many different kinds of errors (Ducet et al., 2000), and in particular the high frequency barotropic variability in the Southern Ocean, although this is partly corrected by the mapping technique (LeTraon et al., 1998). We estimate the altimetric sea level error to be less than 3 cm, based on Ducet et al. (2000).

Any kind of large scale sea level variation centered on the front, will add a bias which moves the SSH contour position without necessarily shifting the maximum in SSH gradient. This will induce an error in our front position, which will no longer be consistent with the core of the jet (or the maximum in SSH gradient). As we have seen above, the long term sea level trend is one large scale pattern that can induce such a problem. Another pattern is the large scale barotropic sea level response to atmospheric forcing which has a strong amplitude in the Southern Ocean. Coherent patterns of sea level variability with spatial scales of 1000km and timescales of 20 days to one year have been found in the Southern Indian and Southern Pacific basins (Fukumori et al, 1998 ; Webb and Cuevas, 2002 ; Fu, 2003). In order to assess the effect of such variability on our frontal movements we performed an EOF (Emprical Orthogonal Function) analysis on the SLA field filtered over these time and space scales. The first EOF mode has a similar pattern as that found by Fukumori et al. (1998). The EOF mode is revealed by spatial filtering the SLA field over areas much larger than the fronts (larger than 1000km), and is associated with 10 % of the variance. Without the spatial filtering, the variance of this apparent barotropic mode vanishes. The amplitude of this mode is approximately 4 cm in the most variable areas (South Indian and South Pacific basins). However, the frontal displacements associated with this EOF mode are weak around the circumpolar belt, with a circumpolar average of 0.1° +/- 0.2° for the SAF, and 0.15° +/- 0.2° for the PF. An exception is in the South Pacific where the barotropic mode is strong and can introduce frontal movements of up to 1° latitude. However, even here, our time series example at 255°E in the South Pacific shows that our frontal movements do follow the maximum SSH gradients (Figure 3.8a), and that these

frontal movements are not correlated (r=0.1 for both PF and SAF) with the first EOF (Figure 3.8b). This high frequency mode may be responsible for the high frequency noise in our contour positions but is not the dominant mechanism controlling the observed frontal movements.

All of these different contributions will induce movements in the SSH contour which do not represent a movement of the jet core, and are thus considered as errors of the method. The sum of these errors for the contour method is +/- 12cm, which corresponds to +/- 1.2°of error in the latitudinal position.

3.1.3 Frontal variability in the ACC

Overview of variability

The Polar and Subantarctic Front positions are subject to strong and spatially inhomogeneous variability. Topography constrains the frontal variability in the Southern Ocean as found in previous studies (e.g. Gordon et al, 1978; Chelton et al., 1990; Gille, 1994; Moore et al., 1999; Sokolov and Rintoul, 2006; Dong et al., 2006). Steep bottom slopes are associated with very weak variations of the front position, whereas flat bottom areas are subject to large movement of the fronts (Figures 3.9a and 3.10a). The variability of the jet intensity is shown on the panels (Figures 3.9b and 3.10b) which represent the frequency of occurrence of a particular SSH gradient at each longitude. Topography influences not only the front's position but also its intensity. Figures 3.9c and 3.10c show the depth of the bathymetry along the pathway of the fronts; the ACC must negotiate a number of large topographic barriers and the meridional deflection of the current influences its structure and variability.

Along the ACC pathway we can define three categories of flow for the SAF and the PF. These are merging, shoaling, and strong meandering in the wake or the lee of topographic obstacles.

Merging. When the flow is steered around major topographic structures but is not forced to pass over them, the two fronts converge, their spatial variability is reduced, and their intensity strongly increases (Figures 3.9 and 3.10). These major topographic features have stronger planetary vorticity (f/h) gradients which impose a stronger constraint on the flow, and induce the merging of the different branches of the ACC into fewer but more intense jets. This is observed at the Kerguelen Plateau for the SAF, around the bathymetry south of the Crozet Island at 40°E for the PF, around the Campbell Plateau at 170°E, and across the Eltanin Fracture Zone.

Shoaling. When a jet is constrained to pass over a shallow plateau or ridge, the intensity of the flow decreases and the front tends to move equatorward to compensate for its loss of potential vorticity. In most cases, fractures or valleys exist in the bathymetric structure, creating a fixed pathway for the flow. This explains the weak spatial variability observed. This occurs at the Western Indian Ocean Ridge, at the Crozet Plateau for the SAF, at the Kerguelen Plateau for the PF, at the South Eastern Indian Ridge, at the Macquarie Ridge, in the middle of the Eltanin Fracture Zone, between the two fractures, and above the South Atlantic Mid-Ocean Ridge (Figures 3.9 and 3.10). The drop in variability over shallow plateaux is well documented in numerical models (e.g. Treguier and Mc Williams, 1990) and altimetric studies (Sandwell and Zhang, 1989; Morrow et al., 1994). Wilkin and Morrow (1994) have also shown that kinetic energy above sharp topography is transferred from the turbulent (EKE) to the mean (MKE) component resulting in a more stable flow.

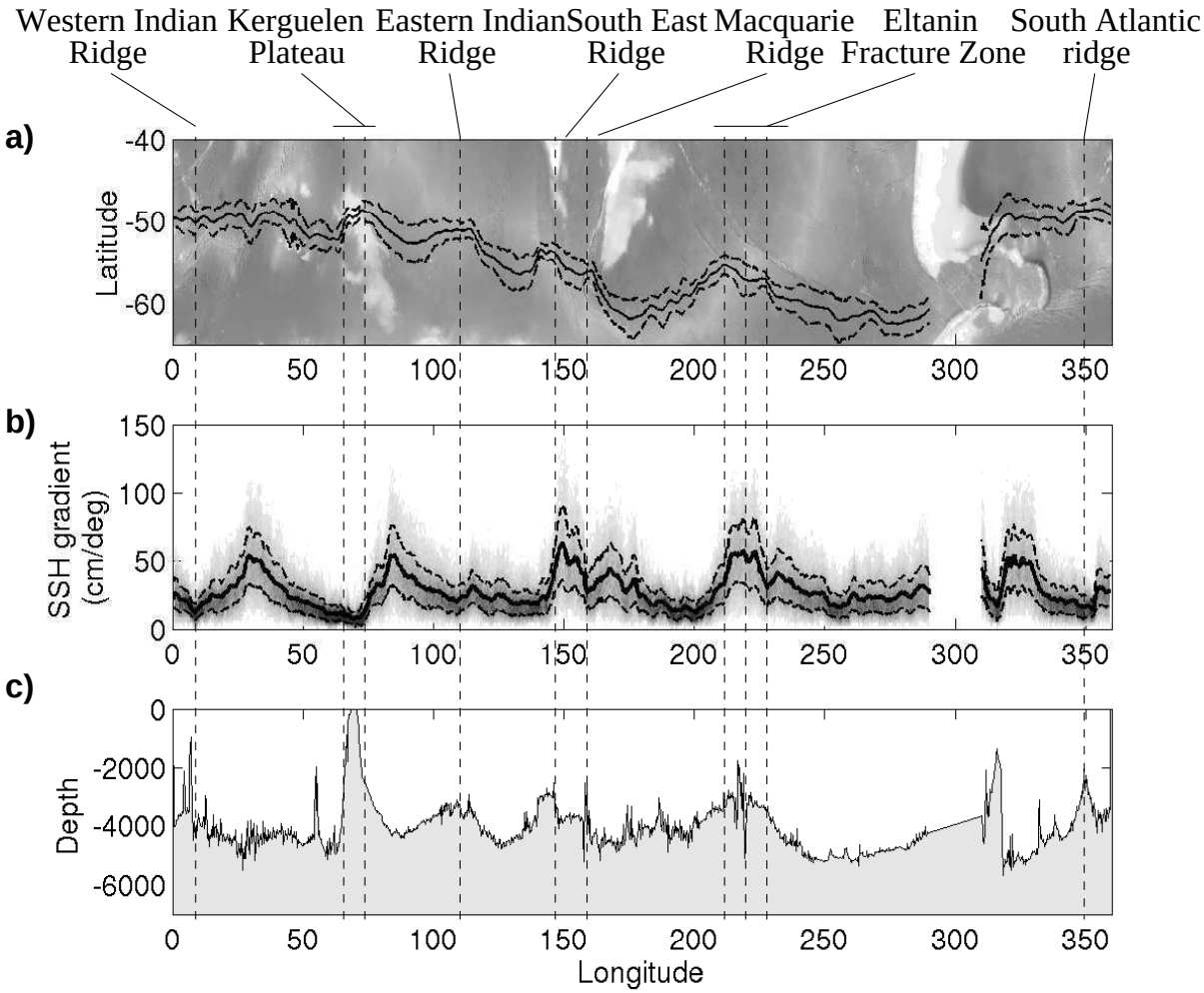

FIG. 3.9 – **panel (a) :** Map of bottom topography in the Southern Ocean with the mean PF position superimposed (solid line black), the dashed line represents the two standard deviation enveloppe around the mean PF position. **panel (b) :** The frequency of occurrence of SSH gradients at the PF position, as measure of the front intensity at each longitude. Colors range from black (often) to white (rare). Also marked are the mean SSH gradient at each longitude (solid black) and the two standard deviation limit (dashed line). **panel (c) :** Depth of the bathymetry along the mean PF pathway.

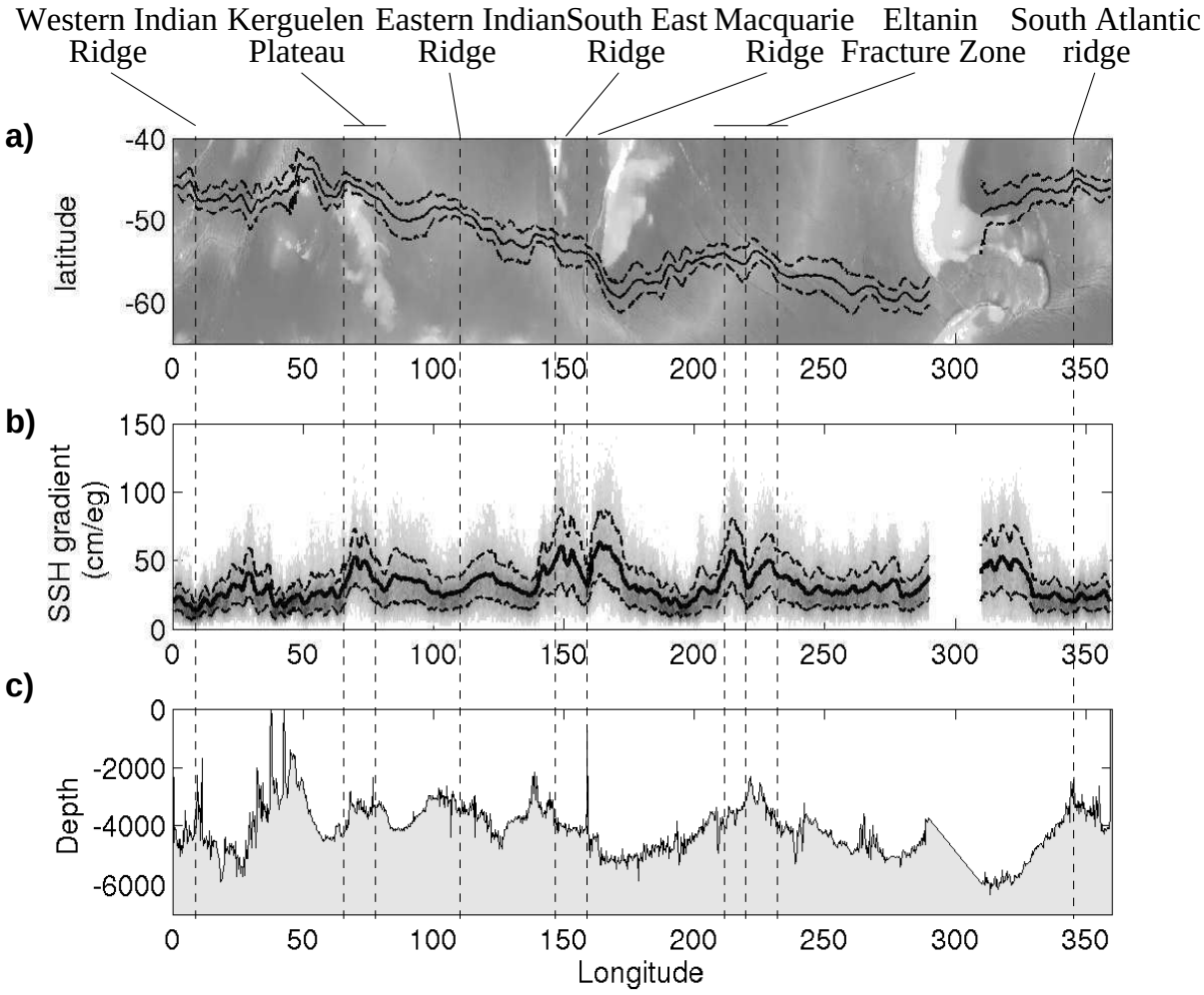

FIG. 3.10 – Same as Figure 3.9 for the SAF.

Lee effect. Downstream of strong topographical constraints, as f/h gradients become weaker, the current becomes much more variable in space and the fronts split. At least three areas show this behavior clearly : downstream of Kerguelen Plateau, downstream of the Campbell Plateau, and downstream of the Pacific mid-ocean ridge fracture zones. In these areas of variable current, the intensity remains strong. So although the jet's position is highly variable, with strong meanders, it is generally still a coherent jet.

In areas where the fronts are subject to strong spatial variability and can be shifted by a few degrees latitude from their mean pathway, we aim to establish whether or not their changing position is driven by atmospheric forcing. A direct local dynamical relation between front position and wind stress curl would be surprising since the ocean response is expected to be partly driven by the net integrated effect of forcing across a large region. Nevertheless, there may be a local correlation and we first investigate this possibility. A positive correlation is found between frontal and zero wind stress curl positions in the South Indian Basin and near Drake Passage (not shown). However, our results also show substantial longitudinal structure in the ocean response. A coherence analysis by Dong et al. (2006) suggests that meridional shifts of the PF correspond to meridional shifts of the wind field. Our regional variations differ from the results of Dong et al. (2006), probably because they focussed on a zonal mean of their local coherence results. As noted earlier, if a significant direct link exists between the structure of the atmospheric forcing and the ACC system of fronts, then we expect to find it mainly through the SAM and ENSO climate modes. The observed SLA response to the atmospheric SAM and ENSO forcing shows a distinct regional pattern (Figure 3.1b). Hence, we have divided the Southern Ocean into smaller basins to consider how the ACC fronts respond regionally to the atmospheric forcing.

Indian sector : 40-110 °E

Figures 3.9a and 3.10a have already shown the strong topographic influence of the Crozet Plateau and Kerguelen Plateau, constraining the flow in the Indian Basin. The SAF and PF show strong variability downstream (80/100°E) of the Kerguelen Plateau. Upstream of the plateau, the SAF is constrained by the Crozet Plateau but the PF shows a more variable position. In these regions of strong variability, a regression of the SAF (Figure 3.11a) and PF (Figure 3.12a) shows a clear anti-correlation between the front position and the SAM. The fronts are shifted to the south (north) during positive (negative) SAM events. For the SAF, this occurs downstream of Kerguelen Plateau between 80°E and 110°E. For the PF, it occurs upstream and downstream of the plateau, with no significant relationship as the front traverses the Kerguelen Plateau. No significant influence of ENSO is observed in the Indian sector.

Figures 3.11b,c and 3.12b,c show that the strong covariances around Kerguelen are dominated by the high frequency band (less than 3 months), with almost no significant covariance observed in the low frequency band (greater than one year). SAM explains up to 20% of the high frequency movement of the SAF and PF. Thus, in the Indian sector, it is mainly the high frequency positive SAM events which are associated with a southward meandering of the front, in line with the southward shift of the maximum wind stress.

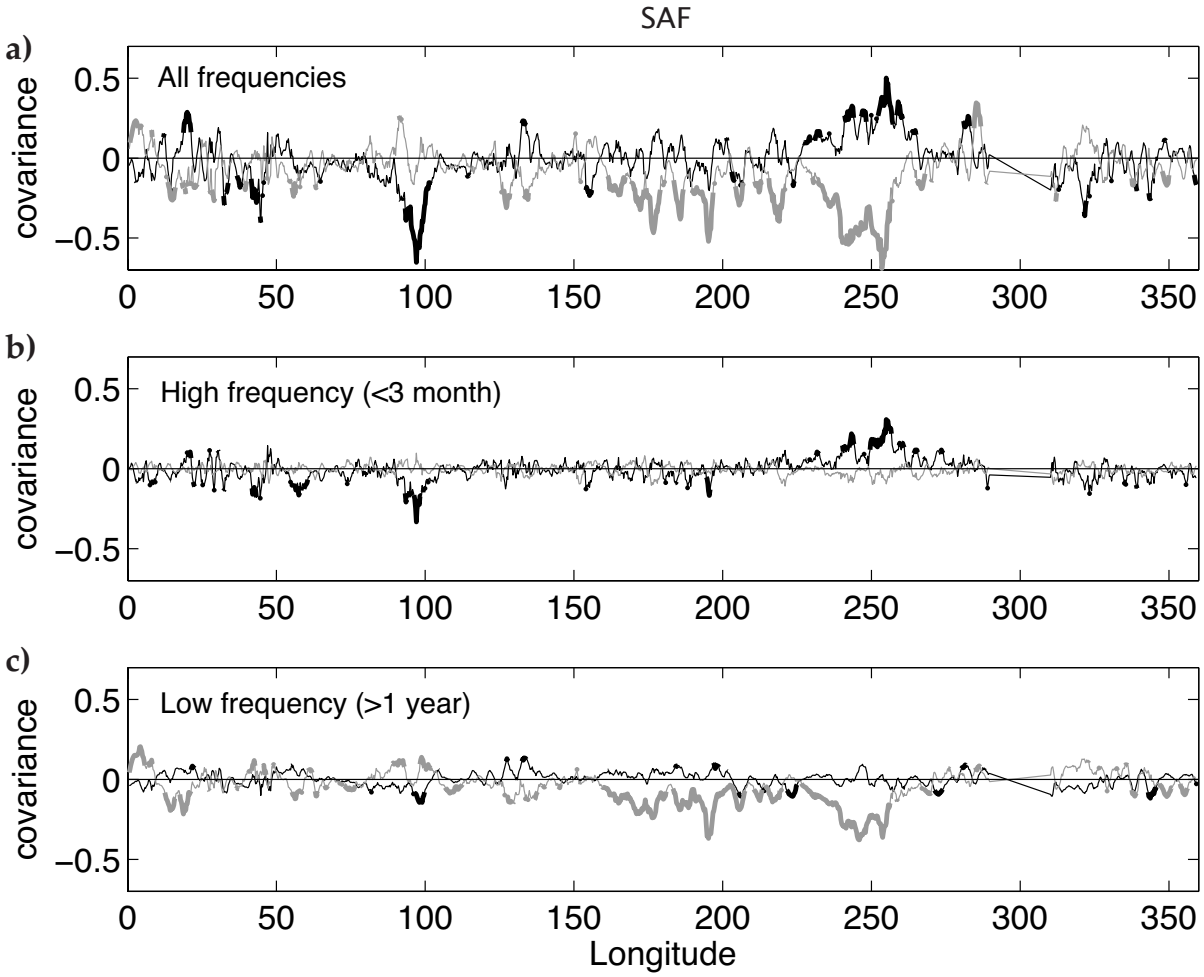

FIG. 3.11 – **panel (a) :** Covariance of the meridional position of the SAF with the SAM (black) or ENSO (gray) indexes as a function of longitude. Bold line shows values above the 95 % confidence level. **panel (b) :** Same as panel (a) but for the high frequency band (less than 3 months). **panel (c) :** Same as panel (a) but for the low frequency band (more than one year).

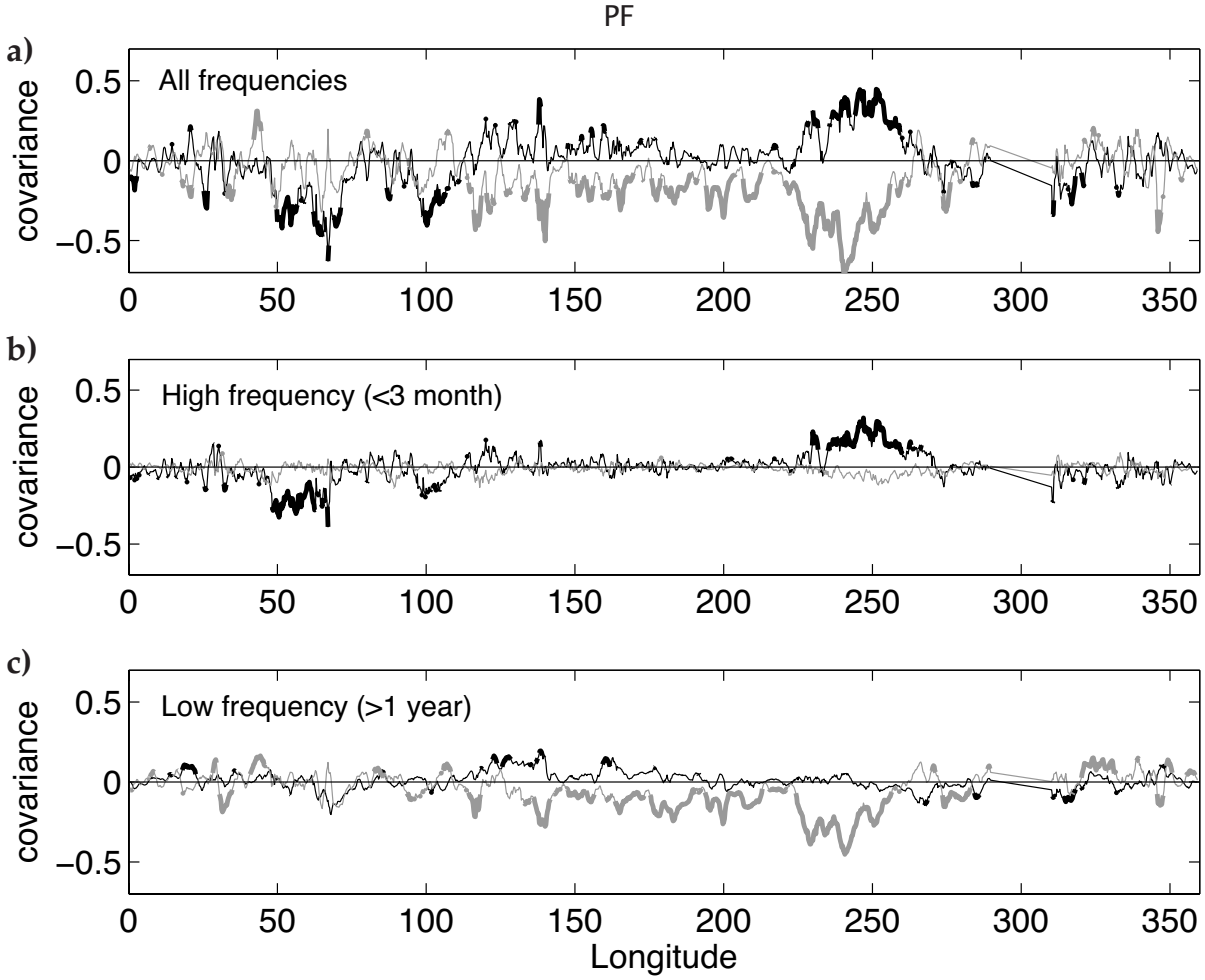

FIG. 3.12 – **panel (a) :** Covariance of the meridional position of the PF and the SAM (black) or ENSO (gray) indexes as a function of the longitude. Bold line shows a significance above the 95 % confidence level. **panel (b) :** Same as panel (a) but for the high frequency band of the signal (less than 3 months). **panel (c) :** Same as panel (a) but for the low frequency band of the signal (more than one year).

Indo-Pacific sector : 110-220°E

In the Indo-Pacific sector frontal movements are very different than those observed in the Indian basin. The regression of the front position on the indices shows that the high frequency frontal response is much weaker (Figures 3.11b and 3.12b). However, at low frequencies, a positive ENSO event is associated with a statistically significant southward movement of the fronts (especially for the Polar Front). The ENSO index explains up to 40 % of the low frequency movement of the fronts with a correlation of approximately -0.5. Positive SAM is associated with a weak northward frontal movement.

In this sector, negative ENSO events and positive SAM events are also associated with a southward anomaly of the zero stress curl position (not shown). For positive SAM events, the atmospheric circulation shows a southward shift in maximum winds or strengthened westerlies to the south as described by Thompson and Wallace (2002). Then, one might predict an associated southward intensification of the oceanic jet (as in Hall and Visbeck, 2002; Sen Gupta and England, 2006). However, we observe the opposite phenomena. The frontal movements are dominated by a lower frequency response, which is may be due to a nonlocal wind response.

Eastern Pacific sector : 220-290 °E

The eastern Pacific sector, downstream of the Pacific mid-ocean ridge, shows a strong response to both ENSO and SAM which is time dependent. There is a clear relation between the frontal movement and the ENSO index at low frequencies (Figures 3.11c and 3.12c). Positive ENSO events are associated with a poleward frontal displacement, and this index explains about 50 % of the low frequency frontal variability variance. However, these plots also depict a significant high frequency response of the fronts to the SAM forcing. Positive SAM events tend to push the fronts to the north, and SAM explains more than 20 % of the high frequency frontal variance. Interestingly, we have the same low frequency frontal response to ENSO in the Indo-Pacific and Central Pacific, with negative ENSO events leading to an equatorward movement of the fronts. However, the high frequency frontal response to positive SAM event is equatorward in the Eastern Pacific, whereas it is poleward around Kerguelen in the Indian sector. In the following section we will consider why this is so.

3.1.4 Mechanisms controlling the observed variability

The longitudinal structure of the ACC is controlled at first order by the bottom topography. However, in flat-bottom regions the position of the fronts is more variable and can be influenced by mesoscale activity or atmospheric forcing. We have shown in the previous section that the atmospheric variability of the Southern Ocean representing by the SAM and the ENSO climate modes can act to shift the ACC jet from its mean position, and that this variability is accentuated in flat-bottom areas. In addition, the ACC, steered by topography, experiences large meridional excursions and exposes itself to different Ekman regimes. Even if the wind variations were entirely zonal this effect would induce zonal asymmetry. Here we consider the circumpolar evolution of the response in relation to realistic Ekman pumping, and offer schematic models of the response in the different regions.

Previous studies have described a zonal ocean response to positive SAM events as follows (see e.g. Sen Gupta and England, 2006) : (i) the increase of westerly wind intensity around 60°S implies a northward Ekman transport anomaly, while the easterly wind intensification around 40°S creates a poleward Ekman anomaly. (ii) Ekman convergence occurs between these two areas causes increased downwelling around 45-55°S, and the divergence created South of 60°S (due to the Antarctic continent) causes increased upwelling near the continent. (iii) The 3-D Ekman circulation induces movement of the isopycnals and consequently a zonal barotropic current is created by geostrophic adjustment. This generates an intensification of the westward current to the south (around 60°S) and a deceleration of the current to the north (around 40°S).

Section 3.1.3 has shown that although both the SAM and ENSO climate modes influence the front position, each index generates a different response depending on frequency and location. The relationship between the front position and SAM is dominated by a high-frequency response (periods shorter than 3 months), whereas the frontal response to the ENSO forcing is at low frequency (periods greater than one year). In the Indo-Pacific and Central Pacific Ocean, a positive ENSO event is associated with a low frequency southward movement of the fronts. Figure 3.13b shows that such an event is associated with a decrease of the westerlies in the whole Indo-Pacific basin as noted by Karoly (1989). Investigating the mechanisms associated with this low frequency response would require a much longer observational time series than that is currently available with altimetry data, but could be investigated in the future. We note that the first mode of the detrended lowpass filtered SSH in the Southern Ocean is highly dominated by ENSO (not shown).

Hereafter we will focus on the mechanisms controlling the high frequency relationship between the SAM variability and frontal movements. A regression of the high frequency part of the zonal wind stress on the SAM index reveals a strong zonal pattern with an intensification of the westerlies (Figure 3.13a). However, when the fronts are superimposed, some regional differences appear. Although the wind anomaly pattern is quite zonal (Figure 3.13a), the relative position of the fronts with respect to the maximum in wind intensification introduces different regional oceanic responses.

To better understand the regional ocean response we propose three schematic descriptions of the frontal response to the high frequency Ekman transport anomalies.

The Indian-Atlantic case :

The SAM events tend to dominate the sea level response, and the maximum in northward Ekman transport intensification occurs south of the fronts. North of the fronts, we observe either a weaker northward anomaly of Ekman transport or a southward anomaly. The resulting Ekman convergence north of the intensification causes increased downwelling anomalies, both north and south of the fronts. In this region of the ocean the ACC flows at latitudes near 45°S, hence the Antarctic continent is ignored. The downwelling over the whole region north of the ACC can contribute to the positive SLA pattern observed in Figure 3.1b. The downwelling also increases the slope of the isopycnals causing a strong intensification of the flow and a baroclinic displacement of the upper front to the south, via geostrophic adjustment. This phenomenon has been observed previously in realistic coupled models, and is capable of shifting the circulation (Hall and Visbeck, 2002 ; Sen Gupta and England, 2006). This is summarized in the schematic in Figure 3.14a, which agrees with the observations of frontal movements described in sections 3.1.3, and in Figures 3.11b and 3.12b.

The Indo-Pacific case :

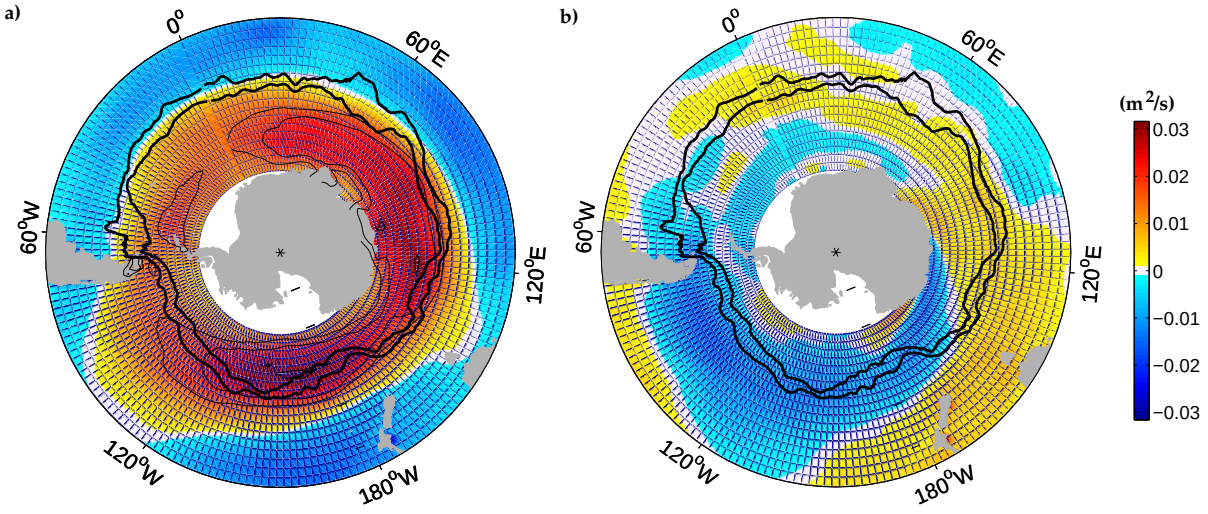

FIG. 3.13 – **panel (a) :** High frequency component (less than 3 months) of the meridional Ekman transport anomaly regressed onto the SAM index. **panel (b) :** Low frequency component (more than one year) of the meridional Ekman transport anomaly regressed onto the ENSO index (right).

A tongue of maximum equatorward Ekman transport intensification occurs in the Indo-Pacific region between 110°E and 140°W. The Campbell Plateau south of New-Zealand blocks the whole ACC system of fronts, steering them further south into the maximum equatorward Ekman transport anomaly. Ekman pumping anomalies are thus centered on the fronts. Divergence occurs to the south, whereas a convergence is induced to the north. In terms of sea level anomalies, the upwelling to the south of the fronts is associated with a negative SLA, and the downwelling to the north of the front with a positive SLA (Figure 3.1b). In the idealized case where the anomalous upwelling and downwelling are symmetric across the front, the front would remain in the same position but the slope of the isopycnals would increase, intensifying the near surface current. This scenario is summarized in Figure 3.14b and is consistent with the observed lack of high frequency frontal movements revealed in section 3.1.3, Figure 3.11b and Figure 3.12b.

The Pacific case :

In the Pacific, the SLP pattern associated with the SAM mode shows an equatorward extension of its low pressure cell in the Pacific, creating a large non-symmetric pattern in this area (220-300°E) (see Figure 3.1a). Around the circumpolar belt, this is the primary asymmetric of the low pressure pattern of SLP associated with SAM. Lachlan-Cope et al. (2001) explained the SLP response to the SAM asymmetry by demonstrating a sensitivity in the strength of this low pressure anomaly to the zonal asymmetry of the Antarctic landmass distribution. This induces a wind anomaly farther north than anywhere else in this region during positive SAM events. In addition, the topography forces the mean position of the fronts to pass farther south through the Pacific mid-ocean ridge fracture zones near 55°S and through Drake Passage (-55/-60°S), implying a mean position of the fronts farther south. Thus, in the Pacific, the maximum intensification of the northward Ekman transport occurs far to the north of the fronts.

Consequently, upwelling occurs over the whole region surrounding the fronts. This can explain the large northward extension of negative SLA (Figure 3.1b). The colder, fresher water and denser water being transported by the Ekman currents shifts the isopycnals to the north. This alteration of the isopycnal gradient will propagate to the interior by geostrophic adjustment. Again, this type of dynamical process has been previously observed in realistic coupled model in response to atmospheric variability (Hall and Visbeck, 2002 ; Sen Gupta and England, 2006). The schematic shown in Figure 3.14c summarizes this scenario and, again, is consistent with the description of the frontal movements shown in section 3.1.3, Figure 3.9b and Figure 3.10b.

The dynamical mechanisms explained by these simplified schematics focus on the processes that will act on the fronts and their associated vertical isopycnals. Our simple dynamical arguments are based on the varying strength of the regions of convergence/divergence of the surface and subsurface density field and follow on the same line as previous more complex and detailed coupled model studies on these issues (Hall and Visbeck, 2002 ; Sen Gupta and England, 2006).

The crux of our study is in revealing how the position of these zones of maximum convergence/divergence varies regionally with respect to the mean axis of the fronts. We note that these regional movements of the jet are qualitatively consistent with a simple zonal acceleration model forced by the typical wind pattern observed during positive SAM event (not shown). A more detailed analysis of the dynamics of these mechanisms is needed to complete this first observational approach, and will be investigated in the future using a realistic numerical model. Finally, we note that the impact of these atmospheric climate modes is not restricted to the frontal region. Figure 3.1b clearly shows that SAM has a large-scale impact on the ocean, whereas we have mainly focused on its forcing of the frontal stucture. The subsurface hydrographic evolution has been investigated at 140°E and shows a large-scale sea level response to SAM and ENSO over the same period (Morrow et al., 2007) as well as weak frontal shifts as described in the Indo-Pacific case.

3.1.5 Conclusion

The position and variability of the two main fronts of the ACC have been determined using a combination of altimetric and hydrographic data. Argo profiles are very important in the representation of the subsurface ocean. They provide more than 50 % of the total historical profiles deeper than 1500m which contribute to our finer resolution mean sea surface height field. We have extended the method developed by Sokolov and Rintoul (2002) for the region south of Australia to the circumpolar Southern Ocean, and we have identified the SAF and the PF with a particular SSH contour. Detailed comparisons of these front positions with hydrographic data support the identification of these two principal ACC fronts in this fashion. It is not clear that additional circumpolar fronts may be identified in this way. The great advantage of this method is to provide a robust way to monitor the frontal variability over the entire circumpolar path for more than 13 years.

Fronts are strongly steered by the topography. We found three typical frontal regimes : merging, shoaling and lee meandering, depending on their position relative to the bathymetry. Thus, topography influences the pathway of the fronts as seen in previous studies (e.g. Gordon et al, 1978 ; Chelton et al., 1990 ; Gille, 1994 ; Moore et al., 1999 ; Sokolov and Rintoul, 2006 ; Dong et al., 2006), but also influences

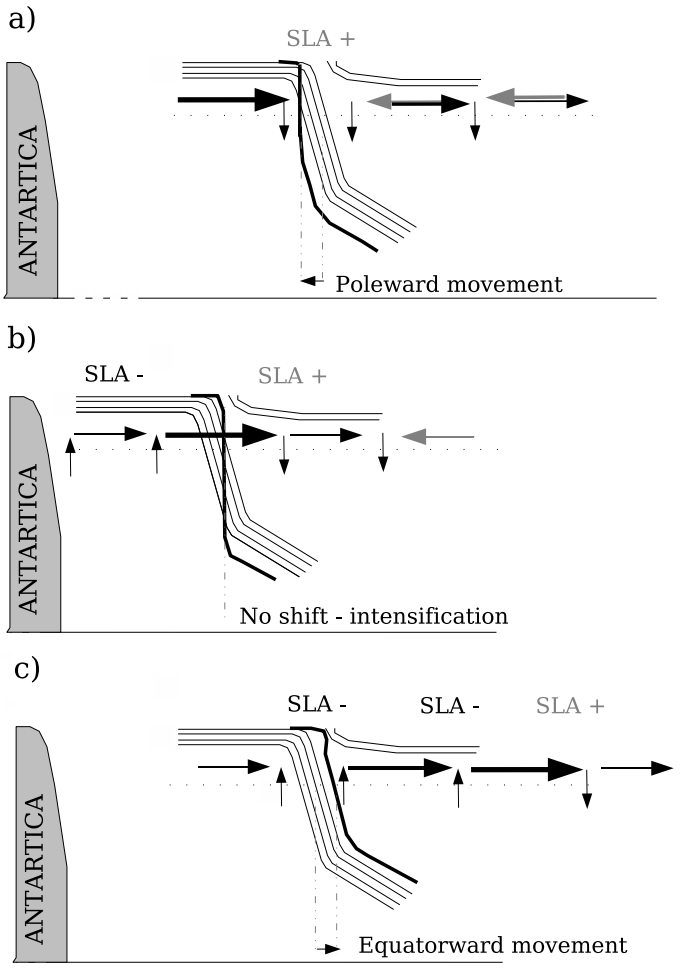

FIG. 3.14 – Schematic of the different scenarios observed in the Southern Ocean during positive SAM events for a) typical Indian Ocean case, b) Indo-Pacific case, and c) Central Pacific case. Black and gray arrows represent the Ekman transport anomaly. Their intensity is shown by the thickness of the line. Vertical black arrows show the vertical Ekman velocity anomaly. Thin black lines are the isopycnals in their mean frontal position, whereas the thick black vertical line represents the typical isopycnal response to the positive SAM event. The horizontal dotted line represents the base of the Ekman layer.

the mean intensity of the jet. In nearly flat-bottom areas fronts are especially subject to large meandering due to mesoscale activity and atmospheric forcing.

We have investigated the role of atmospheric forcing, considering the two most important modes of variability in the Southern Hemisphere, the SAM and ENSO. We found that both ENSO and SAM produce a substantial oceanic response but in different spectral windows. SAM tends to dominate the high frequency band (less than 3 months), whereas ENSO dominates the low frequency band (more than year), especially in the Pacific region. We note that there is still a weak low frequency SAM response in the Indo-Pacific. We found that although the SAM is the dominant mode of atmospheric variability in the Southern Hemisphere, and has a large degree of zonal symmetry, the high frequency oceanic response to this mode, including the movement of the ACC fronts, shows strong regional differences. This is partly because the fronts, steered by the topography, traverse different latitudes around the circumpolar belt and are exposed to different Ekman regimes.

Instead of a zonally uniform response of the ACC to the atmospheric forcing we have proposed three typical scenarios depending on which Ekman regime the fronts cross. For example, during positive SAM events, the response in the Indian Ocean is a poleward frontal movement, whereas in the Pacific the movement is equatorward. In the Indo-Pacific the fronts are intensified with no distinct meridional shift. These scenarios agree with the observed reaction of the fronts and are consistent with the observed SLA response to the atmospheric forcing. Note that these scenarios are based on a negative correlation between the temporal derivative of the SLA and the vertical Ekman velocity (i.e, upwelling is associated with a decrease of the SLA). We indeed observe this correlation with essentially no spatial pattern in the Southern Ocean (not shown).

The shifting of these ACC fronts in response to the climate mode forcing may invoke a local feedback onto the atmospheric circulation (Chelton et al., 2004), which warrants further investigations. In addition, the position of the SAF provides the natural southern boundary limiting the water mass properties of Subantarctic Mode Waters, formed in the deep winter mixed layers directly north of the fronts (e.g. Hanawa and Talley, 2001). These waters have been observed to freshen in recent decades. This freshening is thought to be due to the mean Ekman advection of fresher surface water from farther south (Wong, 1999 ; Aoki et al., 2005). Thus, cross-frontal exchange of cool, fresh water is important in setting their water mass characteristics, and frontal fluxes have been shown to be key in setting up the the deep mode water formation area in the South-Eastern Indian Ocean (Sallée et al., 2006). Whether or not the direct impact of atmospheric modes on SST and on air-sea fluxes over mode waters outweighs their indirect effect via anomalous advection or variable cross-frontal exchange is an important question to resolve.

Acknowledgments The Argo data were collected and made freely available by the International Argo Project and the national programs that contribute to it (http ://www.argo.ucsd.edu, http :// argo.jcommops.org). Argo is a pilot program of the Global Ocean Observing System. We thank the SURVOSTRAL/WOCE SR3 project for providing corrected section data south of Australia, and Nicolas Metzl for the OISO hydrographic data collected near the Kerguelen Island. KGS received support from NSF OCE-0336697 and the Laboratoire d' Etudes en Geophysique et Oceanographie Spatiale. Funding for this study comes from the French PATOM and TOSCA programs.

Chapitre 4

La diffusion tourbillonnaire dans l'Océan Austral

Le premier volet de cette thèse a montré l'importance pour la formation des SAMW de la dynamique frontale et de la dynamique tourbillonnaire associée. Nous nous sommes donc efforcés de mener une étude détaillée de la dynamique frontale dans le précédent chapitre. Nous avons notamment proposé une nouvelle définition des deux principaux fronts de l'ACC et étudié leur variabilité. Les nouvelles données de la colonne d'eau disponibles dans l'Océan Austral nous fournissent une représentation plus précise de la répartition des profondes couches de mélange hivernales dans l'Océan Austral. Au vu de ces données, il nous semble que les fortes déstabilisations hivernales de la couche mélange sont, au moins sur une partie de la ceinture circumpolaire, associées à la branche Nord du SAF (le SAF-N). Le SAF est la branche la plus intense du transport, mais dans le cadre d'une étude des SAMW, il nous semple opportun de nous interesser également au SAF-N. Comme pour les définitions des fronts SAF et PF que nous avons introduites au chapitre précédent, et en nous fondant sur l'analyse des branches de l'ACC de Sokolov et Rintoul (2007), nous associons au front SAF-N le contour $SH_{1500m} = 1.35m$. Le présent chapitre se propose de développer notre réflexion à partir de ces premiers résultats.

La diffusion tourbillonnaire n'a jamais fait l'objet de paramétrisation à grande échelle basée sur des données in situ de l'Océan Austral. Certains travaux se sont penchés sur la paramétrisation de la diffusion tourbillonnaire dans l'Océan Austral, mais soit ces études ont été des études locales (par exemple, Phillips et Rintoul, 2000), soit elles résultent d'analyses dimensionnelles (Stammer, 1998). Les premières sont difficiles à généraliser à l'ensemble du bassin, et les secondes dépendent de coefficients de proportionnalités difficiles à calibrer.

L'un des résultats remarquables qui ressort du premier volet de cette thèse concerne le rôle possible de la diffusion tourbillonnaire : nous avons pu montrer qu'elle peut avoir un rôle de pré-conditionnement de la colonne d'eau pour la formation des SAMW, ou encore qu'elle peut empêcher la formation de SAMW dans certains endroits de la ceinture circumpolaire. Au vu de ces résultats, il nous est apparu que si nous voulions mener une étude sérieuse de la formation des SAMW, il nous était nécessaire de parvenir à une compréhension et à une représentation plus satisfaisantes de la diffusion tourbillonnaire dans l'Océan Austral.

A partir des trajectoires des dériveurs de surface SVP nous avons calculé des coefficients de diffusion tourbillonnaire dans l'Océan Austral sur une grille régulière. Nous avons appliqué des équations décrivant la turbulence de manière statistique à ces données in situ en nombre croissant dans l'Océan Austral depuis 1995. Nous avons essayé de comprendre l'origine physique de la diffusion. Ainsi, nous avons simulé des trajectoires de dériveurs virtuels aux caractéristiques bien particulières et testé l'impact de ces caractéristiques sur nos résultats de diffusion. Cette étude a fait l'objet d'un article que nous avons soumis au journal *Journal of Marine Research* et dont voici le contenu.

4.1 An estimate of Lagrangian eddy statistics and diffusion in the mixed layer of the Southern Ocean (Sallée J.B., Speer K., Morrow R., and Lumpkin R., 2007)

Abstract. A statistical analysis of surface drifter observations is used to compute eddy length and time scales and eddy diffusion in the Southern Ocean. Eddy diffusion values of the order of 10^4 $m^2.s^{-1}$ are found in the energetic western boundary currents north of the Antarctic Circumpolar Current (ACC) and secondary peaks show up where the ACC negotiates topography. The diffusivity shows an increase from the Antarctic continent to the ACC, a stable plateau within the ACC and further increase north of the ACC dominated by the western boundary current regions. Diffusivity is also calculated from simulated trajectories based on altimetric geostrophic velocities, with and without mean flow, as well as with simulated trajectories based on Ekman currents. Ekman currents at the drogue depth (15m) have only a small impact whereas the geostrophic currents dominate the eddy diffusivity. The mean flow acts as a weak barrier to mixing and tends to reduce the eddy diffusion. Complementary statistical analyses confirm these results. The surface drifter eddy diffusion is used to test a simple parameterization based on satellite altimetric observations of eddy kinetic energy (EKE). For $EKE \geq 150cm^2.s^{-2}$: $\kappa = 1.35\sqrt{EKE}L_d$, where L_d is the first baroclinic Rossby radius. This parameterization holds in the energetic ACC, consistent with an eddy field in the "frozen field" regime, and fails over broader areas of weak eddy fields, where mixing is nevertheless fairly uniform and stable at about 1800 +/- 1000 $m^2.s^{-1}$.

4.1.1 Introduction

A knowledge of the mechanisms controlling the transport and mixing of mixed layer properties by mesoscale eddies is of primary importance to our understanding of the general circulation of the ocean. An accurate parameterization of the effect of these eddies on the large scale circulation is fundamental for climate models as well as for in-situ studies of dynamic processes. However, such parameterization are often poorly justified by observational data due to the difficulties in observing these effects. Eddies drive fluid particles in a complex evolution, straining and distorting the flow. It is difficult to describe mathematically all of the components of such an evolution, so it has long been accepted that a useful framework for eddy effects on the larger scale flow is a statistical one.

The calculation of the eddy diffusion coefficient based on Lagrangian data statistics was introduced by Taylor (1921) and summarized by Batchelor and Townsend (1953). In the context of ocean circulation, Davis (1991) discussed the application of Lagrangian observations (e.g. Owens, 1984) and treated the problem of data distribution (see review by LaCasce, 2007). To produce significant results, a statistical approach requires a substantial amount of Lagrangian data. In recent years, the steady increase in ocean subsurface floats and surface drifters has led to several studies applying the statistical formalism to ocean data, mainly in the Atlantic and Pacific Oceans (e.g. Lumpkin and Flament, 2001 ; Lumpkin et al., 2002 ; Bauer et al., 2002 ; Lascase and Bower, 2002 ; Oh et al., 2000 ; Zhurbas and Oh, 2003 ; Zhurbas and Oh, 2004). However, few attempts have been made to compute Lagrangian statistics in the Southern Ocean, because few observations existed.

Early work in the Southern Ocean was directed at the basic circulation and energetics of surface flow (Patterson, 1985). More recently, the advent of satellite altimetry has greatly improved our knowledge of the Southern Ocean surface eddy statistics (e.g. Stewart et al 1996). Keffer and Holloway (1988) and Stammer (1998) provided a global assessment of the eddy diffusion coefficient computed from an altimetric sea level product and based on scaling arguments. However these parameterizations are compromised by the fact that the diffusivity is scaled by an unknown multiplicative coefficient. Zhurbas and Oh (2004) used global surface drifter observations to estimate eddy diffusivity in the Pacific and Atlantic Ocean. They found patches of intense diffusivity in all the energetic western boundary currents and in the equatorial band. For the Southern Ocean in particular they found highly diffusive areas in the Brazil Current, and in the Atlantic portion of the Agulhas Retroflection.

Marshall et al. (2006) developed an eddy diffusion estimate in the Southern Ocean based on the spreading of a virtual tracer whose evolution is deduced from altimetric sea-surface height data. Their results are derived formally as averages on tracer coordinates, but could be displayed in geographical coordinates after some transformation. In interior and highly energetic areas (such as the Agulhas Retroflection or Brazil current), they show weaker values than previously found with in-situ Lagrangian analyses (Zhurbas and Oh, 2004), or compared to diffusion in other highly energetic currents, such as the Gulf Stream (Lumpkin et al, 2002) or the Kurushio (Zhurbas and Oh, 2004).

Although poorly known, eddy diffusion in the Southern Ocean has been shown to be of primary importance in climate studies. A recent study by Hogg et al. (2007) suggested that that eddy heat flux may contribute significantly to the observed warming of the Southern Ocean. In addition, eddy diffusion has been shown to be important in the local mixed layer heat budget and in reducing stratification in regions of the Subantarctic Mode Water (SAMW) formation in the Southern Ocean (Sallée et al., 2006). A better understanding and parameterization of surface eddy diffusion is important for upper ocean heat and salt budgets, and clearly fundamental for large-scale sea-surface temperature prediction and climate studies.

In this paper we estimate the eddy diffusion coefficient over the circumpolar Southern Ocean, based on the statistics of surface drifter displacements. We also attempt to understand operationally the dynamical origin of this coefficient, in terms of geostrophic and other accessible components of the flow. The statistical theory is briefly reviewed in section 2, while the data and the practical difficulties of applying the theory to in-situ data are presented in section 3. We present the results and a discussion in section 4.

4.1.2 Background

A statistical description of the ocean is often made in terms of single particle statistics, or absolute statistics, such as means, variances and dispersion (Freeland et al., 1975 ; Davis 1991). These statistics are based on the probability that a given particle of the flow is found at a particular position in space, and relate to the translation of a marked fluid.

Multiple particle statistics provide a complementary description of the flow, more directly related to the distortion of the flow by shear (Bennett, 1984 and 1987). LaCasce and Bower (2000) examined relative dispersion in the ocean, especially to determine the scales of the transition from anomalous to

regular dispersion. In this paper we will consider the relative dispersion of two particles in the description of the diffusivity in the Southern Ocean. Single and multiple particle statistics have been widely examined and described. Next, we present a summary of terms and notation following LaCasce (2007).

Single particles. We start with the probability density function, $Q = Q(X,t)$, a function of displacement X and time t. The assumption that Q is independent of geographic position is questionable but standard ; we will divide the domain into small geographic areas in which the flow is assumed to be homogeneous. The first moment of Q defines the mean displacement, $\overline{X}(t)$. The second moment is the dispersion, $\overline{X^2}(t)$. The absolute diffusivity $\kappa^{(1)}$ is defined as the time derivative of the second moment :

$$\kappa^{(1)} \equiv \frac{1}{2}\frac{d}{dt}\overline{X^2} \tag{4.1}$$

which in (well-sampled) homogeneous turbulence becomes a constant after several integral time scales.

Taylor (1921) showed that under stationary conditions the dispersion can be associated with an effective eddy diffusivity and can be written :

$$\kappa^{(1)} \equiv u_{rms}^2 \int_0^t R(\tau)d\tau, \tag{4.2}$$

where $u_{rms} = \sqrt{u'^2}$ is the characteristic eddy speed, u' is the fluctuating part of the velocity, and the velocity autocorrelation function, R, is :

$$R(\tau) = \lim_{T_m \to \infty} \frac{1}{u_{rms}^2 T_m} \int_0^{T_m} u'(t)u'(t+\tau)dt \tag{4.3}$$

Consequently, the dispersion can be written :

$$\overline{X^2}(t) = 2u_{rms}^2 \int_0^t (t-\tau)R(\tau)d\tau \tag{4.4}$$

The characteristic timescale of dispersion is the Lagrangian time scale : $T = \int_0^\infty Rd\tau$. This is the lag over which the motion of a particle remains strongly correlated with itself. This timescale may be converted to a distance called the Lagrangian eddy length scale, $L = u_{rms}T$. At short time scales, i.e. $t \ll T$, $R(t) \approx 1$, and the dispersion grows quadratically in time. At longer scales, when $t \gg T$, if the integral converges, then the diffusion grows linearly in time. Consequently, the diffusivity asymptotes to $\kappa_\infty^{(1)} = u_{rms}^2 T_L$ (Davis, 1982).

Multiple particles. Consider two particles at position x_1 and x_2. We define their reference position $x \equiv x_1$ and separation $y \equiv x_2 - x_1$. Let Q(x,y,t | x_0,y_0,t_0) be the probability that two particles, initially at x_0 with separation y_0, will move to x at time t with a separation y. As with the single particle statistics, we can define their relative dispersion by the second moment of Q, $\overline{Y^2}(t)$. Hence, the relative diffusion is defined as the temporal derivative of the relative dispersion :

$$\kappa^{(2)} \equiv \frac{1}{2}\frac{d}{dt}\overline{Y^2}. \tag{4.5}$$

When the separation is small, the relative dispersion grows quadratically. When the particle separation is large, the relative diffusion approaches twice the absolute diffusion : $\kappa_\infty^{(2)} = 2\kappa_\infty^{(1)}$ (LaCasce, 2007). Both single and multiple particle estimates are made in the following sections.

4.1.3 Data and Method

In the first part of this study we use satellite-tracked surface drifter data to derive an assessment of the absolute diffusivity and eddy length scales in the Southern Ocean. We also use altimetry to simulate drifter trajectories. The advantage of simulating drifter trajectories using altimetry is that we overcome the problems of the irregular distribution of real drifter data in the ocean. We also reduce the noise of the aliased small-scale phenomena in the drifter measurement (e.g. inertial waves). Altimetry also allows us to perform multiple particle calculations. Since drifter data are sparsely distributed in the ocean, it is nearly impossible to find a statistically sufficient number of drifters which are close enough together to perform this calculation. With simulated drifters we can release as many particles as we need, as close together as we want, within the resolution of the altimetry data. Finally we can estimate the role of the mean flow on the eddy diffusion by simulating drifters with and without a mean flow. We also assess the contribution of the Ekman component of the velocity to the eddy diffusion by simulating drifters advected only by the Ekman flow.

In this section we present the datasets we have used, the problems in applying the theory to each dataset, and the solutions we have chosen to resolve these problems.

Global Drifter Program drifters

We use satellite-tracked surface drifter data from the Global Drifter Program (GDP, Lumpkin and Pazos, 2007) to compute the Lagrangian statistical formulation presented previously. This dataset spans the period 1995-2005 in the Southern Ocean. The drifters are equipped with a holey sock drogue at 15 m depth to reduce their surface wind drag (Sybrandy and Niiler, 1991). The data are received, processed and distributed by the Atlantic Oceanographic and Meteorological Laboratory (AOML, Miami)[1]. Drifters operating at a duty cycle of 1/2 or less were excluded from our analysis. Drifters having lost their holey sock drogue were also dropped from our calculation for this study. Velocities $\mathbf{u}$ were calculated from 6-hourly interpolated positions (Hansen and Poulain, 1996) via a 12-hour centered difference. Residual velocities $\mathbf{u}' = \mathbf{u} - \mathbf{U}_s$ were calculated with respect to seasonal mean currents $\mathbf{U}_s$, the latter calculated from drifter observations at a resolution of 1° using the technique of Lumpkin and Garraffo (2005)[2] and mapped onto the 6-hourly positions via linear interpolation. The Lagrangian time series of residual speeds for each drifter was low-pass filtered to remove energy at periods smaller than two days, e.g., inertial and tidal oscillations, using a second order Butterworth filter. Trajectories shorter than six days were discarded.

Altimetry

In order to simulate drifters in the Southern Ocean we have constructed weekly maps of Sea Surface Height referenced to 1500m (SSH_{1500m}) from 1993 to 2005. Specifically, we add the mean dynamic height computed from a historical database relative to 1500m using ship and Argo float data (Sallée et al., 2007) to the weekly maps of altimetric sea level anomalies, SLA. The mapped SLA fields are provided by CLS/AVISO and are based on data from the available altimeter missions (Topex/POSEIDON, ERS-1

[1] http ://www.aoml.noaa.gov/phod/dac.html

[2] Mean currents available at http ://www.aoml.noaa.gov/phod/dac/drifter_climatology.html

and ERS-2, GFO, ENVISAT, JASON). The mapping technique is described by LeTraon et al. (1998). Anomalies are calculated with respect to a 7-year mean (1993-1999) and are mapped onto a 1/3° grid in longitude and variable grid in latitude, ranging from approximately 1/20° at 80°S to 1/4° at 30°S. A discussion of the aliased high frequency errors in the Southern Ocean is given by Morrow et al. (2003). The altimetry data resolves wavelengths greater than 150 km, with a temporal resolution of 20 days (Ducet et al., 2000). In the Southern Ocean where the groundtracks converge, we can resolve 100 km wavelengths.

Two kind of simulations have been performed. In the first case we released virtual drifters at the same time and position as the real drifters. In the second simulation, we released virtual drifters on a regular half degree grid over the whole Southern Ocean, from 30°S to 70°S. In this latter simulation we launched these virtual drifters in summer and in winter, to better represent the whole seasonal cycle of eddy energy. The simulations last one year, except for those virtual drifters which run aground at a coast. Simulations have been performed with and without mean flow. The mean flow was estimated from both climatological mean dynamic height relative to 1500m (ship and Argo float database) and from a mean sea surface of Rio et al. (2005). Both give similar results, but we prefer the climatological database since more Argo data are incorporated in the Southern Ocean, and smaller scales are resolved.

Pairs of virtual drifters were made from the simulation performed on the regular half degree grid. The pair of drifters were released on the same day and separated by half a degree. This separation ranged between 50 and 100km, small enough to resolve mesoscale dispersion, and at the limit of the altimetry-based flow resolution. However, this distance is at the upper boundary of the typical mesoscale size, so we expect the pairs of drifter to decorrelate quickly, and consequently we expect a rapid convergence of the relative dispersion.

Wind data

In order to simulate drifters advected only in the Ekman flow, we have constructed weekly maps of Ekman velocity at 15m, which is the depth of the drogued GDP drifters. We used the parametrization proposed by Van Meurs and Niiler (1997) to derived Ekman velocities at 15m from wind stress :

$$u_e + iv_e = B \exp^{i\theta}(\tau^x + i\tau^y) \tag{4.6}$$

where the amplitude $B \simeq 0.3 m.s^{-1}\ Pa^{-1}$ and θ is the turning angle relative to the wind direction : 55°to the left of the wind in the southern hemisphere at 15 m depth. Wind stress (τ^x, τ^y) is in Nm^{-2}. The value of the turning angle of 55° proposed by Van Meurs and Niiler (1997), has recently been tested by Sudre and Morrow (2007) with a denser drifter dataset, and they found a good visual fit with the in-situ data. The resulting Ekman currents at 15 m depth U_e (u_e,v_e) are :

$$u_e = B[\tau^x.\ \cos(\theta) - \tau^y.\ \sin(\theta)] \tag{4.7}$$

$$v_e = B[\tau^x.\ \sin(\theta) + \tau^y.\ \cos(\theta)] \tag{4.8}$$

We use the Quickscat Mean Wind Field (QSCAT MWF) gridded product for the wind stress (τ^x, τ^y). This global half degree resolution product provides daily and weekly wind stress fields, and is processed and distributed by the Centre ERS d'Archivage et de Traitement (CERSAT)[3]. We used the

[3]http ://www.ifremer.fr/cersat/en/documentation/manuals.htm

weekly maps available between July 1999 and March 2007 to simulate virtual drifters released at the same time and position as the real drifters.

Applying the theory to data

We aim to map the dispersion coefficient $\kappa_\infty^{(1)}$, as well as the typical Lagrangian eddy scales, T and L, in the Southern Ocean by applying the previously presented formulations to the surface drifters. This type of calculation requires a series of modifications and particular care. The main problem is averaging over sparsely distributed drifters. In most geophysical experiments, and especially in the present case with surface drifter data, the drifters are deployed at different locations and at different times. Under the conditions of stationary and homogeneous flow, averaging over an ensemble is still possible. But the oceanic flow is neither homogeneous nor stationary, and consequently the averaging has to be adapted. The following discussion presents some of the solutions we have chosen in this study.

Eulerian map. To solve the problem of homogeneity we have reduced the geographical area to be analyzed by dividing the total domain area into bins (Davis, 1991). The size of these bins has to be carefully adapted to the physical scales we are interested in, to assume homogeneity over each bin. Diffusivity is inherently non-local because it is defined as a correlation between a particle velocity at a particular location x_0 and the history of the velocity along the particle track. Choosing the portion of the track which best describes the conditions at x_0 is not obvious. We decided to adapt the size of the track portion to match the size of the Eulerian bins. Lagrangian scales were calculated from non-overlapping 90-day segments of the float trajectories and binned in 5° longitude by 1° latitude bins. The choice of these time and space scales is based of the typical size of an eddy loop along the trajectories. We expect these scales to be larger than the typical scale of energetic eddies but small enough to resolve substantial large-scale variability.

Separation of the mean velocity and the anomaly. In theory, the definition of a mean flow assumes a separation in time scales, or equivalently a gap in the velocity frequency spectrum. However, such a gap does not exist in the ocean. Instead the mean is calculated operationally for a particular time-scale, which is basically the duration of the experiment. Velocity Anomalies are then available at all scales shorter than the length of the experiment, which is of the order of 10 years for the GDP drifters in the Southern Ocean (between 1995 and 2005). However, as mentioned in section 4.1.3, a seasonal mean has been removed from the GDP drifters so the drifter mean is based on a seasonal evolution over 10 years. For the virtual drifters computed from altimetry velocities, we use a different 7-years altimetric mean from 1993 to 1999 (see section 4.1.3). An additional problem is to resolve the relevant eddy time scale, which needs to be separated from other time-scales in the residual velocity. For example, short time scales may be associated with inertial oscillations or wind effects, and longer time-scales with long term meandering of the jet, which are not captured by the mean flow. Previous Southern Ocean studies have shown that periods between 40h and 90 days account for most of the eddy signal (Nowlin et al, 1985 in Drake Passage; Phillips and Rintoul, 2000 south of Australia). In this study we chose to filter the residual velocity fields to remove periods less than 5 days and more than 90 days. This band-pass filtering applied to both the GDP and virtual drifters limits the error introduced by using a different mean definition for each dataset. The filtering also limits the dynamical range and constitutes a second operational definition of the dominant mesoscale flow scales responsible for diffusion. We found that band-passing

the velocity in this way improves the diffusivity convergence, consistent with studies by Bauer et al (2002).

Coordinates. In isotropic flow the choice of the coordinate system is irrelevant but it can be important in anisotropic flow. The ocean is not isotropic, due primarily to the beta effect which constrains the flow to be mainly zonal, but also because of bottom topographic constraints (LaCasce 2005). The Antarctic Circumpolar Current (ACC) is particularly subject to topographical constraints (Sinha and Richards, 1999). Many studies have shown that the ACC is strongly steered by the topography (eg. Moore et al., 1999; Dong et al., 2006; Sallée et al., 2007). Since our main interest is in cross-frontal eddy diffusion it is important to separate the along-stream and cross-stream components. For each bin we have calculated the principle axes of the current (eigenvalues of velocity covariance) and derived the eddy diffusivity in the major and minor axis directions. The minor axis diffusivity is retained as the "true" estimate of cross-ACC mixing. Figure 4.1 shows the EKE ellipses in the Southern Ocean from the drifter dataset, similar to those of Ducet et al. (2000) and Morrow et al. (1994). The principal axes of these ellipses are the principal axes of the currents.

Integration of the autocorrelation function. Auto-correlation functions were calculated using $T_m = 90$ days. The main difficulty of this calculation is that noise tends to dominate R for large lags. The diffusive time scale, T, which is based on the integration of R, will also be dominated by noise. Standard methods have been developed to reduce the noise problem. For example, R can be integrated up to a constant lag (see Speer et al., 1999) or up to the first zero crossing (e.g. Freeland et al., 1975; Poulain and Niiler, 1989).

In the Southern Ocean, both of these methods produce noisy fields. The former provides T_L values which are function of the constant lag, which is not desirable. The Southern Ocean is a very large and inhomogeneous area where the lag varies from one region to another, hence this method of constant lag is not satisfying. The "first zero crossing method" does adapt the lag to each geographical region. However, in regions with strong oscillatory motion, the zero crossing can be very short, inducing small values of T_L, although a longer integration could take into account the oscillations.

In this study, we have adapted a method developed by Garraffo et al. (2001). In the T_L calculation we fit an autocorrelation function of the form :

$$R^* = \cos\frac{\pi\tau}{2Td}e^{-(\tau/\tau_e)} \tag{4.9}$$

to the observed R. Td is the first zero crossing of R and the e-folding timescale τ_e is found by a least squares method. The autocorrelation function R is the average over the autocorrelation functions of all particles in each bin. Finally, we compute the exact integral of the R^* function to infinite lag to obtain the integral time scale T :

$$T = \int_0^\infty R^*(\tau)d\tau = \frac{\sqrt{\pi}}{2}\tau_e e^{-(\pi\tau_e/4Td)^2} \tag{4.10}$$

.

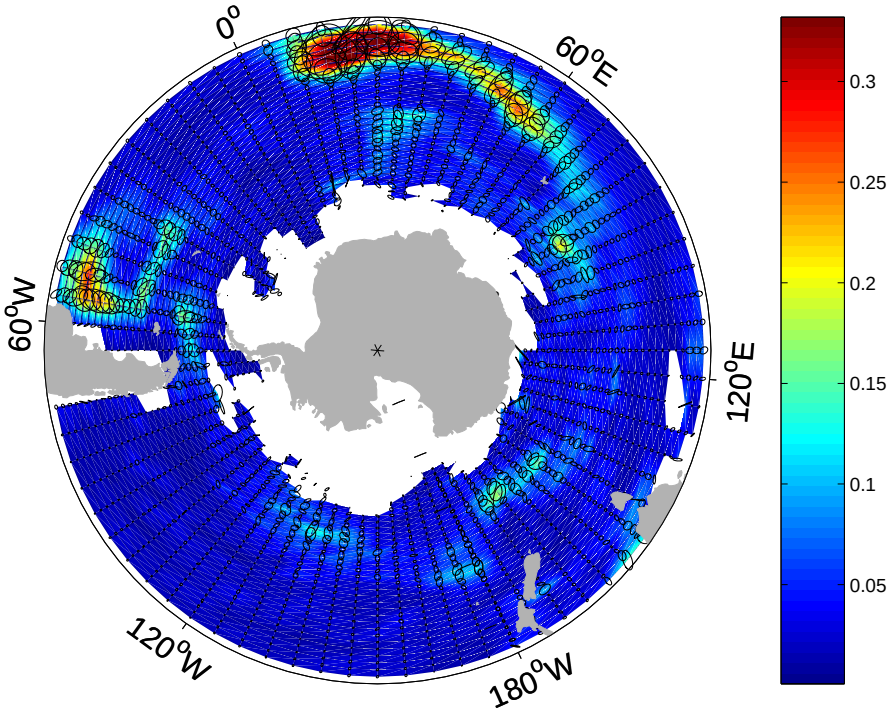

FIG. 4.1 – EKE (in $m^2.s^{-2}$) in the Southern Ocean from GDP drifter data. Ellipses of velocity covariances are superimposed in black.

4.1.4 Results

Eddy scales deduced by in-situ surface drifters

Figure 4.2 shows the eddy diffusivity κ calculated with equation 4.2, and the associated eddy time and length scales for the Southern Ocean. The largest values are found in the vicinity of the highly energetic currents, mainly near the western boundary currents. κ peaks in the Agulhas Retroflection north of the ACC, between 30 and 70°E, and in the southwestern Atlantic in the Brazil Current area. Secondary peaks are found along the ACC where it interacts with bathymetry at 30°E, 80°E, 170°E and 220°E, and finally west of New Zealand, near 190°E, 50°S (see Bryden and Heath, 1985). κ is much weaker in the eastern parts of all gyres and south of the ACC. Along the mean pathway of the ACC, κ tends to be weak. However we observe exceptions, where the flow passes over shallow bathymetry such as Western Indian Ocean Ridge (110°E), the Macquarie Ridge (150°E), the Central Pacific Fracture Zone (220°E), and the Falkland Plateau (320°E). Over these shallow bathymetries the eddy diffusivity tends to increase (Witter and Chelton, 1998).

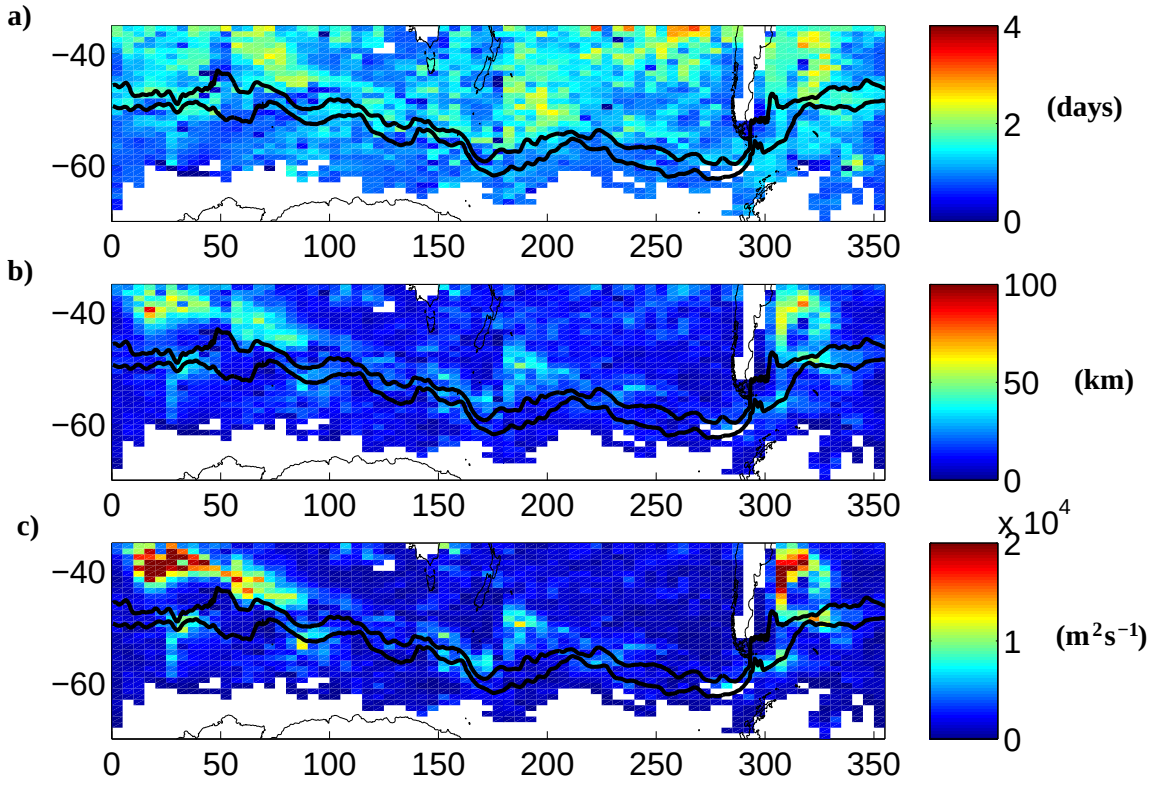

FIG. 4.2 – Cross-stream eddy scales in the Southern Ocean from GDP drifter data. Black lines are the mean SAF and PF from Sallee et al. (2007)**(a)** Lagrangian eddy time-scale in days. **(b)** Lagrangian eddy length-scale in km. **(c)** Eddy diffusivity coefficient in $m^2.s^{-1}$

This large scale pattern agrees well with previous studies calculating κ (e.g. Stammer, 1998 ; Davis, 2005 ; Zhurbas and Oh, 2004). However, we find slightly higher amplitudes in all of these regions (see Table 4.1). We note that Marshall et al. (2006) found much smaller values of surface diffusion. Their mapped estimates are one order of magnitude less than ours, although the pattern is similar. Our calculation is based on Lagrangian drifter statistics and gives information about the particle dispersion, whereas their study by construction produced circumpolar integrated measures of tracer transport and an inferred net diffusivity based on tracer gradient budgets in tracer coordinates. After averaging along streamlines we find values closer to theirs, within a factor of 2-5. This difference may be partly explained by their choice of parameters relating explicit mixing and effective mixing, and partly by the different circumpolar averaging procedure in tracer or streamline coordinates.

	Agulhas Retroflection	Brazil Current	Campbell Plateau	East of New Zealand
Stammer (1998)	1.10^4	1.10^4	1.10^4	-
Davis (2004)	$1.5 - 2.10^4$	-	$0.5 - 1.10^4$	$0.5 - 1.10^4$
Zhurbas and Oh (2004)	$2 - 3.10^4$	$1.5 - 2.10^4$	1.10^4	$0.6 - 0.8.10^4$
Rupolo (2007)	$2 - 3.10^4$	2.10^4	$1.5.10^4$	1.10^4
Our Study	$2 - 3.10^4$	2.10^4	$0.5 - 1.10^4$	1.10^4

TAB. 4.1 – Approximate values of the eddy diffusivity coefficient ($m^2.s^{-1}$) extracted from previous studies and compared to our present study. Stammer (1998) applied a 0.1 factor to his results to transform calculated surface values to a vertically averaged value ; we remove this factor and display the surface value for a more consistent comparison.

As mentioned earlier, our diffusion coefficients result from the average of an ensemble of autocorrelation functions from several particle trajectories. We can estimate the error of the diffusion coefficients by computing the standard deviation of the autocorrelation functions and propagating this in the integration of the diffusivity. This generates an error of approximatively 25%. This is a substantial error, but the general structure remains within the confidence limit.

Simulated experiments

As seen in section 4.1.3, we are confronted by several problems when applying the statistical formulation to real in-situ data. We will use the simulated experiments to assess the impact of these problems on our calculation. In situ GDP drifters are sparsely distributed in the ocean, and can converge around frontal regions. These sampling problems have been widely explored by Davis (1991). With the simulated experiments, we can perform statistics with different number of data in each bin and with data released at different times and locations. As described in section 4.1.3, we launched virtual drifters at every grid point, during summer and winter, and followed their trajectories during one year using altimetric-based currents. We note that these mapped altimetric velocities will have reduced noise and divergence from small scale processes and will mainly focus on the mesoscale eddy diffusion. In addition, since altimetric velocities are nearly non-divergent, we can quantify the error introduced by the divergent characteristics of the real ocean.

In a first experiment we launched virtual drifters at the same place and time as the real GDP drifters and computed the same calculation of eddy scales. We found very similar time, length and diffusion scales (not shown). The patterns are exactly the same and intensities are comparable. The simulated drifters are only advected by the geostrophic mean flow and the quasi-geostrophic mesoscale eddies captured by altimetry. The fact that there is such good agreement with the in-situ data suggests that the calculation presented in Figure 4.2 is dominated by mesoscale eddy activity and the mean flow, and that there is not significant aliasing of small-scale phenomena by the divergent flow of the real ocean. This exercise reveals that the geostrophic flow is the main contributor to the observed eddy diffusion.

In the second experiment we launched virtual drifters on a regular half degree grid, first in winter and then in summer and let them drift for one year. Once again, we found results in very good agreement with the real data estimates of eddy scales. Both the pattern and the intensity of the eddy scales are comparable. This shows that the irregular sampling of the real drifter dataset does not significantly affect our results.

In order to assess the role of the mean flow on the diffusion, we ran another simulation with no mean flow. In these new idealized experiments, the drifters evolved only with the anomaly of the geostrophic flow. Figure 4.3 shows that on average over the circumpolar belt, the real data and the simulated drifter calculation gives similar results. The general pattern revealed by an along stream average is : 1) an increase of the diffusion from Antarctica to the southern edge of the ACC strong jets (Polar Front, PF) ; 2) a plateau or even a slight northward decrease in diffusion across the very intense jets of the ACC (between the PF and the Subantarctic Front, SAF) ; 3) and an increase in the diffusion north of the ACC toward the highly diffusive western boundary current regions.

This pattern of weak eddy diffusivity in the jet and an increase to the equatorward side has been previously observed (Bower et al., 1985 ; Marshall et al., 2006). A strong PV gradient associated with the jet is thought to provide a barrier to the mixing. The association of a reduction in mixing in the core of the jet and an increase in the diffusion outside the strong flow is a frequently observed phenomena in fluids, as discussed in Marshall et al. (2006) and Shuckburgh and Haynes (2003).

Although this general pattern is observed in each of the different calculations we note some small but interesting differences : the increase of the diffusion south of the ACC has a weaker slope in the real data than in the simulated data, and the plateau across the ACC is slightly less intense. The reason may be related to the simulated mean flow. The mean flow we used is based on a dynamical topography referenced to 1500m (see section 4.1.3). Thus, although the axis of the jet is correctly located (see Sallée et al., 2007) its intensity is somewhat reduced compared to the real current. The effective "barrier" in the core of the strong jet is apparently reduced and the simulated diffusion appears greater in the vicinity of this jet. We note however, that the mean flow of Rio et al. (2005) produces similar results.

North of the ACC the real drifter diffusion and the virtual drifters launched at the same locations as the real data show a sharper increase in diffusion than the simulated drifters released on a idealized grid. Because virtual drifter simulation on a dense regular grid is very demanding in term of memory and calculation time, we only simulated them for one particular year (1993), although the other calculations represent averages over many years (1993-2005). Interannual variability in the eddy activity may cause slight differences in the results north of the ACC. For example, altimetry shows 10 % increase in EKE

in the Agulhas Retroflection from 1993 to 2005. In addition, drifters converge towards the very diffusive regions (Davis, 1991), so the distribution of points will be biased toward these regions for the real drifter case compared to the experiment where we release virtual drifters on a regular grid.

Interestingly, the results computed with the same dataset but with and without the mean flow show substantial differences. For each simulated experiment on regular and real drifter grid, adding or removing mean flow change the resulting diffusion. South of the ACC where the mean flow is weak, the results with and without mean flow are in very good agreement. However, within the ACC, we observe different results. When the mean flow is included, the eddy diffusion is reduced. This result reinforces the finding of Bower et al. (1985) and Marshall et al. (2006) that the mean jet acts as a "barrier" to mixing. North of the ACC, the results with and without mean flow converge again. However, because there is a substantial mean flow induced by the western boundary current, the convergence is a bit less marked than south of the ACC.

We also simulated drifter trajectories using the Ekman currents at 15m in order to assess the contribution of Ekman in the diffusivity calculation. Following the method reviewed in section 4.1.3 from Van Meurs and Niiler (1997), we calculated Ekman virtual drifter trajectories using the wind stress field alone. We computed the diffusivity from these trajectories using the previous method (equations 4.2 and 4.3), and found a very different pattern of diffusion. The maxima are now found in the vicinity of the ACC front, in the Indian and Pacific basin, where the wind is the most powerful and variable (Trenberth et al., 1990 ; Luis and Pandey, 2004). The intensity of the diffusion is also much weaker, roughly one order of magnitude less than the geostrophic mesoscale eddy contribution. An along-stream average of the diffusion due to the Ekman velocities is shown on Figure 4.3. The Ekman contribution to the eddy diffusivity at 15m is negligible compare to the contribution of geostrophic mesoscale eddies.

Complementary statistical approach

In order to validate our calculation we have tested a number of different approaches for the estimating of κ. Firstly, we have calculated the probably density function (pdf) of the particle velocities and estimated κ with the explicit formulation (equation 4.1), in order to calculate the absolute dispersion of the flow particles (see equation 4.4). Figure 4.4 shows the results for the portion of the Southern Ocean between 30 and 50°E in two areas : north of the ACC in the very energetic Agulhas Retroflection between -45 and -35°S, and south of the ACC between -60°S and -50°S. This region is analysed because the intensity of the diffusion is greater in the Agulhas Retroflection, however the consistency between methods are quite similar around the circumpolar belt. Figure 4.4 also shows an estimate of the relative dispersion computed from the explicit formulation (equation 4.5). Since the calculation of relative dispersion requires pairs of drifters released close to each other at the same time, we perform this calculation using the idealized datasets, with drifters released at the same time on a half degree grid. Thus, Figure 4.4 compares different theoretical estimates based on the same dataset.

Figure 4.4a shows the very good agreement of the different methods. We note that the absolute dispersion, and consequently the absolute diffusion, computed with the explicit equation are very smooth since we fit an idealized function to the observed autocorrelation function before calculating these terms. These results are also in very good agreement with the coefficients found with the real drifter trajectory data. When the mean flow is removed (Figure 4.4c), the implicit calculation shows a slight increase, the

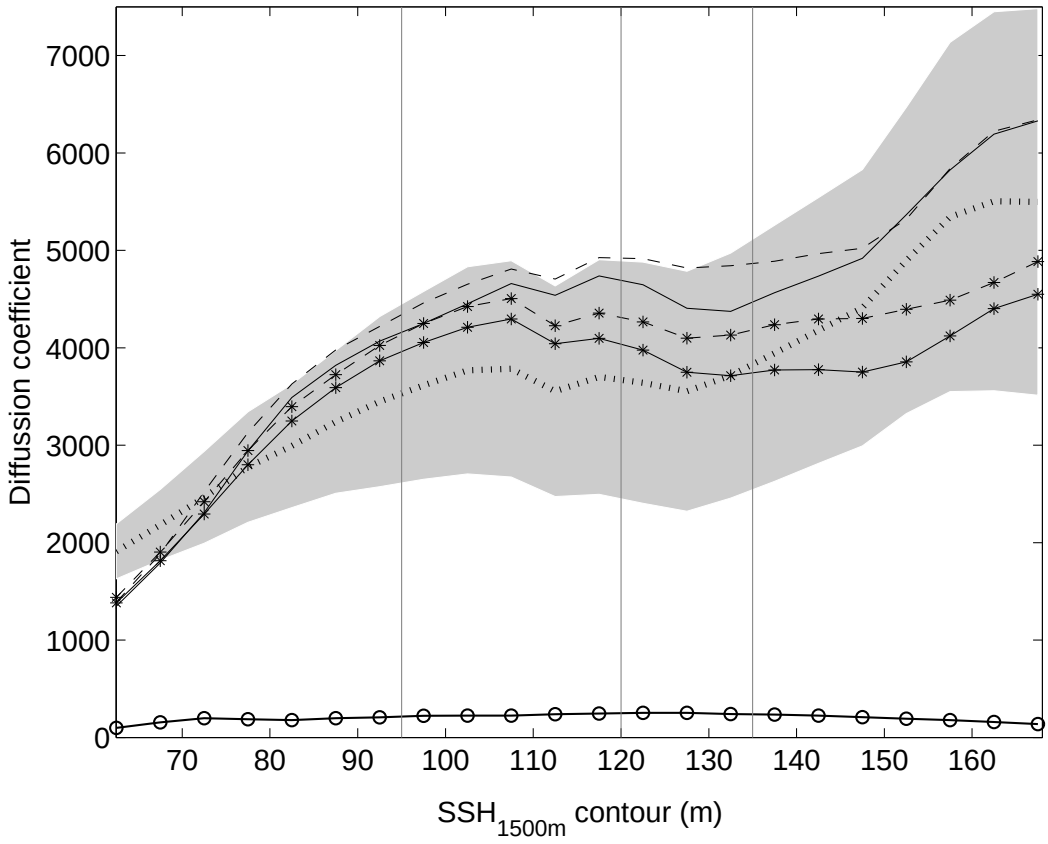

FIG. 4.3 – Along-stream average of the eddy diffusion coefficient for different drifter datasets. Dotted line shows the results when using the real in-situ drifters datasets. Solid line and dashed line represent respectively the results for the datasets released on the same grid as the real drifter with and without mean flow. Solid and dashed lines with star markers represent respectively the results for the datasets released on a half degree regular grid with and without mean flow. Solid line with circle markers represents the diffusion induced by virtual drifter trajectories released on the same grid as the real drifter but advecting only by the Ekman velocity. Vertical lines represents the PF ($SSH_{1500} = 95cm$), the SAF ($SSH_{1500} = 120cm$) and the Northern Branch of the SAF ($SSH_{1500} = 130cm$) ; see Sallée et al. (2007).

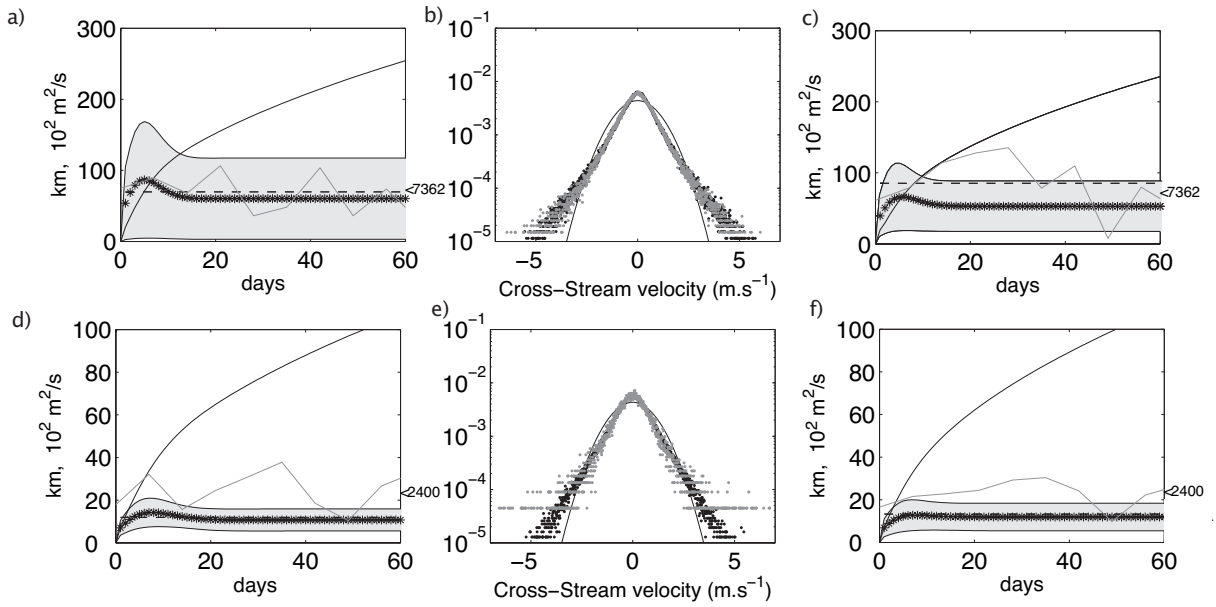

FIG. 4.4 – a) Absolute dispersion of particles (in km) in the Agulhas Retroflection north of the ACC between 30-50°E 35-45°S, calculated from the simulated drifters on a half degree regular grid with mean flow. The explicit absolute diffusion is given (stars) with its standard deviation (grey envelope). The limit at infinity of the implicit absolute diffusion ($\kappa_\infty^{(1)}$) is also marked (dashed line). The evolution of the relative diffusion divided by two is superimposed (grey line ; $1/2.\kappa^{(2)}$). b) Pdf of the velocities used in panel a (black points). Also shown is the pdf of the real in-situ drifter velocities over the same area (grey points). The black line represents a Gaussian envelope. Panel (c) is the same as panel (a) but for a simulation without the mean flow. Panels d, e and f correspond respectively to the panels a, b and c but for the area 30-50°E, 50-60°S, south of the ACC.

explicit calculation is decreased, and there is an increase in the relative dispersion. Since the pair statistic calculation is based on a description of the distortion of the flow whereas the single particle calculation provides the translation of the flow, comparing the two is a powerful way of representing the differences introduced by the shear of the strong jets. Once again, we find that within an intense current (the Agulhas Retroflection) the mean flow tends to reduce the value of the eddy diffusion coefficient.

Figure 4.4b shows the pdf of the (real) drifter velocities in this part of the ocean. There is a strong non-Gaussian shape to the pdf. Departures from the Gaussian shape are found at small and large velocities. Bracco et al. (2000) found similar pdf shapes in the Labrador Sea in the EUROFLOAT experiment, using subsurface floats. The departure from the expected Gaussian shapes are associated with the action of energetic coherent structures that introduce extreme velocities (Bracco et al., 2000). We note that the pdf from simulated drifters is exactly the same as the pdf found with real velocity data : the observed departure from Gaussian shape in the ocean is explained by quasi-geostrophic mesoscale eddies resolved by altimetry. Around the circumpolar belt, in bins of 5°longitude by 1°latitude, we found a sharp distribution of kurtosis centered on 5.5 (not shown), which reveals the departure from Gaussianity occurs nearly everywhere in the Southern Ocean.

South of the ACC the results are very similar. However, we note one interesting difference : the calculation with and without the mean flow are quite similar, even though the multiple particle calculation should be more sensitive to the action of a mean flow. As shown in Figure 4.3, this result supports the idea that the stronger mean jets in the ACC reduce the diffusivity.

Parameterization

The formulation of a climatological eddy diffusion map presented previously with its distinct geographical distribution is a first step in observing eddy mixing in the Southern Ocean. However, the calculation is difficult to replicate because of somewhat subjective averaging procedures, geographical bin size choices, etc. Of further interest would be to use these results to calibrate a simpler calculation directly from the altimetry observations themselves. In addition, we cannot use these results to study a time evolution of the diffusivity without waiting for many more drifter deployments. In this section we investigate whether a simple parameterization can be developed which relates the scales of motion of an altimetry-based random velocity field to the eddy diffusion in the Southern Ocean.

The eddy diffusion coefficient is basically the product of a typical eddy velocity, U_e multiplied by a typical eddy length scale, L_e. Since most ocean eddies are generated by baroclinic instabilities of the flow (Stammer, 1998), L_e is approximately equal to the baroclinic Rossby deformation radius, L_d. Finally, a measure of the typical eddy velocity is the square root of the eddy kinetic energy, $\sqrt{EKE}$. Then, we have :

$$\kappa^{(1)} = \langle u'd' \rangle = \alpha \sqrt{EKE} L_d, \tag{4.11}$$

where alpha is a proportionality constant. Stammer (1998) used this parameterization to calculate the diffusion in the Southern Ocean with altimetry, and applied a fixed coefficient $\alpha = 0.05$. In this study, we recalculated the coefficient α using our climatological eddy diffusion map from the Lagrangian drifters and compared it to EKE from altimetry over the same period.

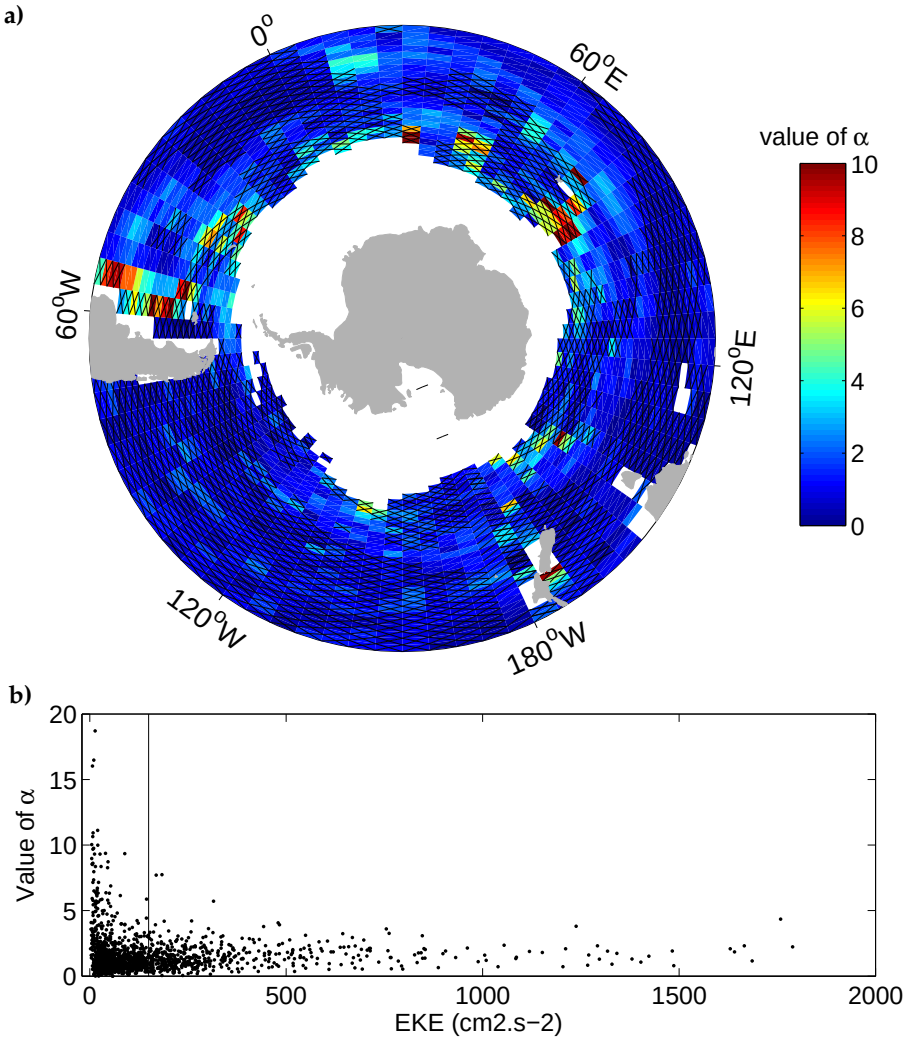

FIG. 4.5 – Result of the calibration of the proportionality coefficient α used in the parametrization of the eddy diffusion coefficient : $\kappa = \alpha.\sqrt{EKE}.L_d$. a) geographical distribution. Crosshatching indicates areas where EKE is less than 150 $cm^2.s^{-2}$. b) Value of the coefficient α as a function of the EKE. The vertical line represents EKE=150 $cm^2.s^{-2}$.

Figure 4.5a shows a map of the distribution of this coefficient α. We used the internal baroclinic Rossby radius L_d, calculated from climatological hydrographic data by Chelton et al. (1998). These values are made freely available by Chelton[4]. We found that values of α are quite stable in the energetic areas of the Southern Ocean (Figure 4.5b). A clear mode shows up in the histogram of α in the bins where EKE exceeds 150 $cm^2.s^{-2}$. The relatively sharp distribution of the α coefficient in these energetic regions justifies choosing a simple parameterization. In the lower energy regions we cannot apply a simple parameterization, revealing that Lagrangian integral length scale becomes uncorrelated with the Eulerian length scale given by altimetry. The regions where this simple parameterization holds are concentrated in the western boundary currents, and in the energetic ACC. An area of approximatively $2.10^7 km^2$ is concerned, which represents 30 % of the total area of the Southern Ocean studied here. Over the rest of the Southern Ocean, the eddy field is weaker and the mixing is fairly uniform and stable at about 1800+/-1000 $m^2.s^{-1}$. Finding a nearly constant α coefficient over the energetic ACC region implies that there is a proportional relationship between the Lagrangian and Eulerian length scales, i.e. that the energetic ACC region is in the *frozen field regime*. Thus, with respect to Lagrangian sampling, the ACC is similar to the highly energetic near-surface Gulf-Stream (Lumpkin et al., 2002). We chose the median value of this distribution for EKE$\geq$ 150 $cm^2.s^{-2}$ as the better estimate of the parameterization : α=1.35. This value is approximately 27 times greater than derived by Stammer (1998). We note, however, that our eddy diffusion values are of the same order in the Southern Ocean since Stammer (1998) uses a much greater baroclinic Rossby radius than ours. The L_d values given by Stammer (1998) are approximately 6 times greater than the internal Rossby radius values from Chelton et al. (1998). Hence our final eddy diffusion in the energetic areas is approximately four times greater than the diffusion found by Stammer (1998). However, we note that Stammer (1998) assumes a proportional relationship between the Lagrangian and Eulerian length scales everywhere in the Southern Ocean, which we have shown to be only true in the energetic areas along the ACC and in the western boundary currents. Outside these energetic regions, a constant value of α times $\sqrt{EKE}.L_d$ would give an overestimate of the diffusion. In the energetic areas, the simple parameterization using a recalibrated coefficient of proportionality allows one to map and monitor the eddy diffusion in the Southern Ocean using the time series of altimetric data maps.

We computed EOFs (Empirical Orthogonal Functions) of the EKE field from monthly filtered altimetry maps. A clear first mode shows up accounting for 97% of the total variance of EKE (see Figure 4.6b). The time series associated with this mode shows a slow variation over the 14 years of available altimetry data from 1993 to 2006 (Figure 4.6c). Over this period we observe an increase of approximatively 10% of the spatial pattern, corresponding to an increase of order of 100 $cm^2.s^{-2}$ in the turbulent western boundary current (Agulhas Retroflection and Brazil current). The mechanisms leading to this low frequency EKE variability have been studied before and could be a delayed response to atmospheric circulation (Meredith and Hogg, 2006). Hogg et al. (2007) had previously noted that this increase of EKE activity might be associated with an increase of the eddy heat diffusion in the Southern Ocean. Based on the parameterization above, we have deduced from the EKE analysis the first mode of variability of diffusion in the Southern Ocean (see Figure 4.6a). We observe an increase of more than 1000 $m^2.s^{-1}$ north of the ACC in the energetic western boundary current (Agulhas Retroflection and Brazil current), and of approximatively 400 $m^2.s^{-1}$ elsewhere north of the ACC in the energetic areas. This shows the tendency of the diffusion to increase at decadal scales and could be related to the warming of the Southern Ocean observed by Gille (2002) and Hogg et al. (2007).

[4] www.coas.oregonstate.edu/research/po/research/chelton/index.html

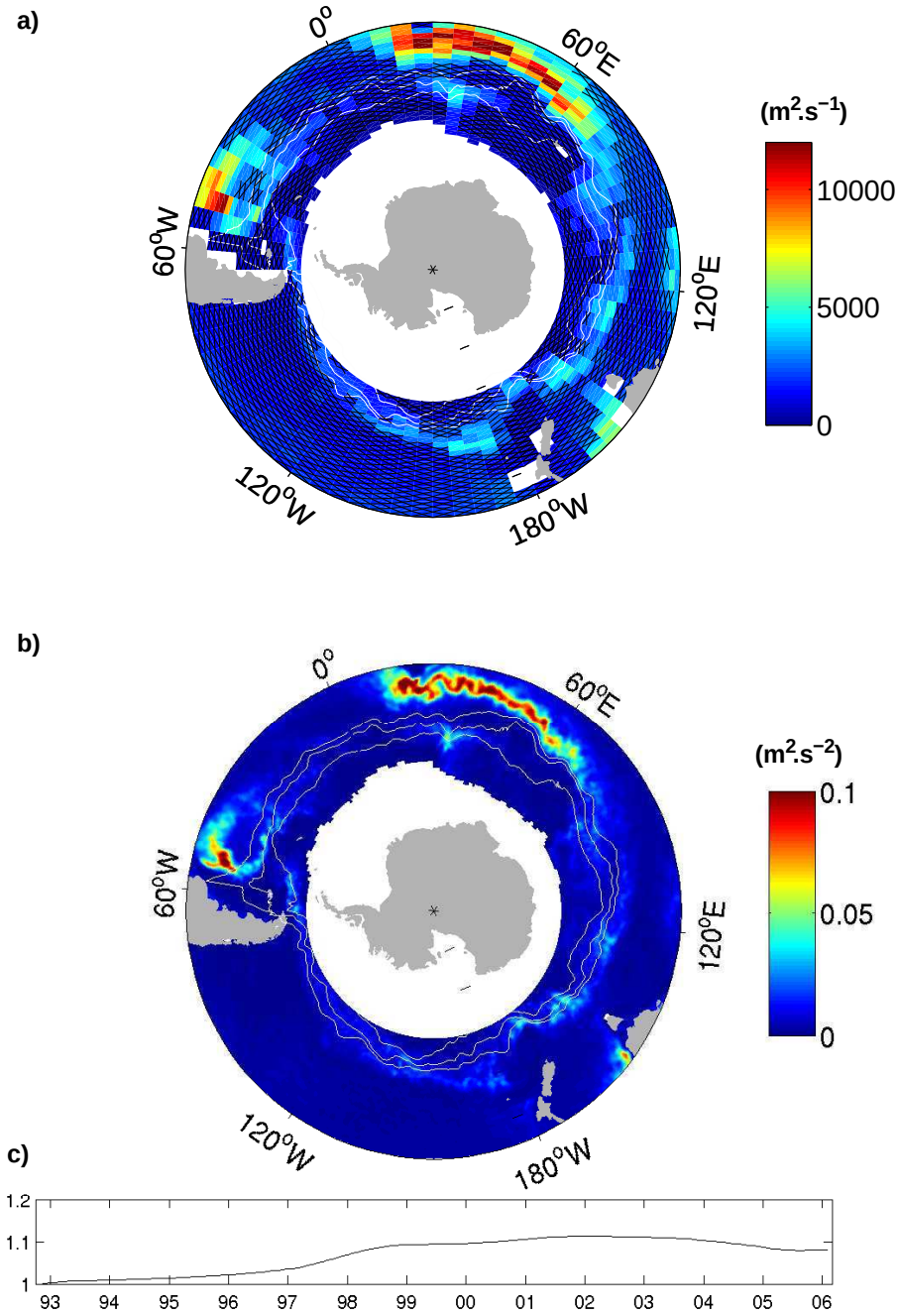

FIG. 4.6 – a) First mode of variability of diffusion over the 14 years 1993-2006 deduced from b) the first mode of variability of the EKE from altimetry. The associated times series is shown in (c). Crosshatching in (a) indicates areas where the eddy field is not in a "frozen field" regime (EKE less than 150 $cm^2.s^{-2}$). Note that values on the maps are divided by the minimum value of the time series. The interannual increase we want to emphasize in these plots is only 10% (time serie amplitude from 1 to 1.1) of the colorbar values.

4.1.5 Conclusion

The effective eddy diffusion coefficient κ has been determined using the newer, denser dataset of GDP drifters available in the Southern Ocean. We computed the statistics of drifter observations to find an estimate of this coefficient in different regions. We found that the Southern Ocean is significantly diffusive with maxima north of the main western boundary currents, such as the Agulhas Retroflection or the Brazil current, and also east of New Zealand.

We simulated drifter datasets using the altimetric-derived geostrophic currents and in some runs by adding a mean sea surface height field. These simulations allowed us to quantify some intrinsic errors when applying in-situ data to the statistical formalism, such as small scale aliasing or sampling error. In addition, the simulations showed the general characteristics of the diffusion, including the role of the mean flow, or the relative importance of the geostrophic flow in the diffusion or in the pdf shape. Complementary statistical computations, such as an explicit computation of the absolute statistics or a computation of the relative statistics, were used to support our results.

The general meridional shape of the eddy diffusion is an increase from a minimum at the Antarctica continent to the southern edge of the ACC, then a plateau in the vicinity of the strong ACC jets, then an increase of the coefficient north of the ACC with a further increase towards the energetic western boundary currents. We found that the geostrophic flow is the main contributor to the observed eddy diffusion at the scales we considered, specifically the geostrophic mesoscale eddies and the geostrophic mean flow. The mean flow tends to slightly decrease the diffusion. We investigated the sampling error and errors from aliased small scale processes, and found that neither caused significant errors in our calculations.

The high values of near surface diffusivity found here will strongly mix tracers in the surface mixed layer, but the strongest mixing is confined to relatively small regions of the Southern Ocean. A measure of this inhomogeneity is that the median values of κ in the ACC are approximatively 3000 $m^2.s^{-1}$, substantially lower than average values (around 3700 $m^2.s^{-1}$). These lower values are more representative of what a tracer experiences ; however, this does point to the fact that no single value represents tracer diffusion globally.

We found that the pdf of the Lagrangian velocities was not Gaussian, with elevated probabilities at small and large velocities. The non-Gaussian nature of these distributions have been related to the presence of vorticies and energetic coherent structures (Bracco et al., 2000), and we expect that this explanation is relevant in our study, where we have used both drifters and altimetric data to resolve the mesoscale eddies.

A simple parameterization based on the scales of motion resolved by altimetry may represent the explicit diffusion estimated from surface drifters in the energetic areas of the Southern Ocean. In these regions, we propose a parameterization similar to that of Stammer et al. (1998), but we recalibrated the proportionality coefficient based on our drifter results. We found that where EKE $\geq 150\ cm^2.s^{-2}$: $\kappa = 1.35\sqrt{EKE}.L_d$, where EKE is the eddy kinetic energy, and L_d the baroclinic Rossby radius given by Chelton et al. (1998). This formulation may be of use in coarse resolution models, or climate studies. As found by Lumpkin et al. (2002) in the high energetic surface Gulf Stream regions, we observed that in the

energetic ACC region the eddy field is in the "frozen field" regime. In this regime a simple parameterization can exist and implies a proportional relationship between Lagrangian and Eulerian length scales.

Chapitre 5

Vision circumpolaire de la formation des SAMW

L'étude introductive de cette thèse sur la formation des SAMW dans l'Océan Indien Sud-Est nous a beaucoup appris sur les principaux forçages mis en jeu dans le renouvellement de cette masse d'eau. Nous avons pour la première fois montré avec des données in situ qu'à grande échelle spatiale, la déstabilisation de la couche de mélange était due en premier ordre à l'association des actions du transport de chaleur d'Ekman et du flux de chaleur air-mer. Mais nous avons progressé dans la connaissance de ces phénomènes en montrant que par diffusion de chaleur, les tourbillons méso-échelle équilibrent ou même dominent les forçages d'Ekman et de flux air-mer dans la partie Ouest du bassin Indien. Ils empêchent ainsi la destratification de la colonne d'eau. Comme nous l'avons vu précédemment, ce premier travail nous a conduit à deux études complémentaires portant sur une meilleure définition, et sur la variabilité des forts jets de l'ACC d'une part (voir chapitre 3), et sur la quantification et la compréhension des causes de la diffusion tourbillonnaire dans l'Océan Austral d'autre part (voir chapitre 4).

Deux ans se sont écoulés et plusieurs dizaines de milliers de profils ARGO sont passés dans l'Océan Austral depuis cette première étude. Et c'est maintenant, forts de nos recherches intermédiaires et des nouvelles données disponibles, que nous reprenons, avec une vision cicumpolaire, ce qui faisait l'objet de notre étude introductive.

La question qui nous a taraudés pendant ces deux ans portait sur la possibilité d'étendre nos résultats à l'effet indirect de la diffusion tourbillonnaire. Existe-il d'autre endroits de la ceinture circumpolaire où cette contribution pourrait être décisive ? Des structures bathymétriques similaires à celle que l'on trouve au plateau de Kerguelen pourraient-elles provoquer ailleurs un pré-conditionnement à la formation des SAMW ? Ce chapitre expose la manière dont nous avons cherché à construire une vision circumpolaire de ces phénomènes à partir de cartes climatologiques des principaux forçages du budget de l'équation de la chaleur. Nous nous sommes efforcés de relier les structures de grande échelle des forçages climatologiques, à la circulation moyenne de l'ACC. Enfin, nous avons porté une attention particulière à la portion de l'ACC en aval du Plateau de Campbell (170°E). Cette région Ouest du bassin Pacifique semble présenter de fortes similarités avec le bassin Ouest de l'Océan Indien. Cette étude a fait l'objet

d'un article que nous avons très récemment soumis au journal *Geophysical Research Letter* et dont le contenu est présenté dans la prochaine section.

5.1 Subantarctic Mode Water formation around the circumpolar belt : The role of eddy diffusion (Sallée J.B., Morrow R. and Speer K., 2007)

abstract Subantarctic mode waters (SAMW) form in the deep winter mixed layers occuring north of the Subantarctic Front (SAF). The recent increase of hydrographic and surface drifter data in the Southern Ocean allows a better spatial representation of the distinct regions of SAMW formation. This study focuses on the thermodynamical processes acting on the winter mixed layer heat budget. Eddy heat diffusion play a substantial role in the local heat balance, whereas its action vanishes with large-scale averaging. South of the western boundary currents and north of the SAF, the eddy heating plays an important role in specific regions, counterbalancing the cooling of the mixed layer by Ekman advection and air-sea fluxes. Specifically, the eddy diffusion term reduces the tendency for mixed layer destabilisation north of the SAF in the Western Indian Ocean downstream of the Agulhas Retroflection and in the Western Pacific downstream of Campbell Plateau. This role for mixed layer eddy fluxes emphasizes a large-scale control of mixed layer properties by topography and mesoscale processes in the Southern Ocean.

5.1.1 Introduction

Subantarctic mode water (SAMW) is the water mass formed in the very deep winter mixed layers (MLs) found directly north of the Subantarctic Front (SAF) in the Southern Ocean. Mode waters are a primary result of air-sea interaction (Speer et al., 1995) and act to ventilate the interior of the upper ocean as they spread into gyres (McCartney, 1982 ; Hanawa and Talley, 2001). These oxygen-rich layers can persist to the tropics (McCartney, 1982). Since SAMW occupies a large area in direct contact with the atmosphere during winter, it is very sensitive to climate change (Sabine et al., 2004). A better understanding of the processes controlling the SAMW formation is a key requirement for climate studies.

Figure 5.1a shows the winter ML depth in the Southern Ocean deduced from 5 years of Argo and ship data superimposed on the mean Antarctic Circumpolar Current (ACC) fronts. It is striking how deep and inhomogenous the 5-year mean winter ML is north of the ACC. Previous studies have emphasized the substantial role of air-sea fluxes and Ekman fluxes in controlling the destabilisation of the winter ML in which SAMW is renewed (Speer et al., 1995 ; Rintoul and England, 2002). Recently, the new Argo dataset has allowed a more detailed vision of the water column evolution over all seasons (Sallée et al., 2006 ; hereafter SWMS06 ; Dong et al., 2007). These observational studies have supported the basic idea that the heat content variation of the ML can be explained to first order by the action of air-sea heat fluxes and Ekman heat transport.

However, although Ekman and air-sea fluxes are intense and relatively zonally distribted across the entire southern Indian Ocean, their action can be counterbalanced by eddy heat diffusion which can locally heat or cool the Subantarctic Zone where the SAMW forms (SWMS06). This could explain the observed non-zonal distrubution of deep MLs around the circumpolar belt (e.g. Figure 5.1a ; de Boyer Montégut et al., 2004). Indeed, eddy diffusion is very strong around the fronts in the western Indian sector

and contributes to warming and stratifying the Subantarctic Zone between 30 and 60°E, and cooling and destratifying the Subantarctic Zone around the Kerguelen Plateau (SWMS06).

New estimates of the eddy diffusion coefficient have now emerged from the Global Drifter Program (GDP) surface drifter dataset. Studies suggest that eddy diffusion in the Southern Ocean is strong north of the ACC, and especially in the western boundary currents (Zhurbas and Oh, 2004 ; Sallée et al., 2007b). These new estimates of surface eddy diffusivity are of the order of 10^4 $m^2.s^{-1}$ in the peak areas which would produce a strong impact on a local ML heat budget.

In this paper we aim to understand the cause of the sudden shallowing of the winter MLs in the Subantarctic Zone which occurs downstream of the Campbell Plateau near 170°E in the western South Pacific (see Figure 5.1a). We compute the different terms of the heat equation to compare their relative importance. Based on previous Southern Ocean heat budget studies (Jayne and Marotzke, 2002 ; Rintoul and England, 2002 ; SWMS06 ; Dong et al., 2007) we focus on three main forcing terms : air-sea fluxes, Ekman transport, and eddy diffusion. We will consider the winter climatological forcing over the Southern Ocean, and its impact on the winter MLs (Section 3 and 4). We will also investigate the ML evolution in the southwest Pacific using a time series of instantaneous Argo profiles (Section 5). Our aim is to establish whether or not the SW Pacific undergoes SAMW formation processes comparable to the SW Indian ocean (SWMS06).

5.1.2 Data and Methods

Heat Budget equation

Previous studies suggest that Ekman advection and air-sea fluxes are the dominant terms in destabilizing the winter water column to create the strong and deep convection observed (Rintoul and England, 2002 ; SWMS06 ; Dong et al., 2007). In the present study we focus on these two forcing terms as well as the eddy heat diffusion contribution. Therefore, we consider the simplified heat budget equation :

$$\frac{\partial T}{\partial t} = \frac{Q_0}{\rho C_p.h} - u_{ek}.\nabla T + \nabla(\kappa_h.\nabla T) \tag{5.1}$$

where h is the layer thickness, T the mean ML temperature, u_{ek} the Ekman velocity vector, Q_0 the total heat flux at the ocean surface, and κ_h the (annual mean) horizontal eddy diffusion coefficient in the ML. We estimated each term of the equation from the data presented below.

Data

To estimate the air-sea heat flux we use the JRA-25 reanalysis data (http ://jra.kishou.go.jp). This recent reanalysis includes more observational data than classical reanalysis product (Onogi et al., 2007), hence we believe it better represents synoptic and meso-scale features. We have compared the climatological mean air-sea fluxes from JRA-25 with those from ECMWF (ERA-40) and NCEP (V1). The colocated standard deviation of these 3 mean heat flux products ranges from 0 to 40 $W.m^{-2}$ with minimum differences around the ACC. The average standrad deviation of these climatological fluxes over the area studied here (-60/-35°S) was only 6 $W.m^{-2}$.

Wind stress are from the high-resolution monthly Quickscat data (http ://www.ifremer.fr/cersat/), with a given error of less than 7.10^{-3} Pa over the area studied. Surface temperature is from the global

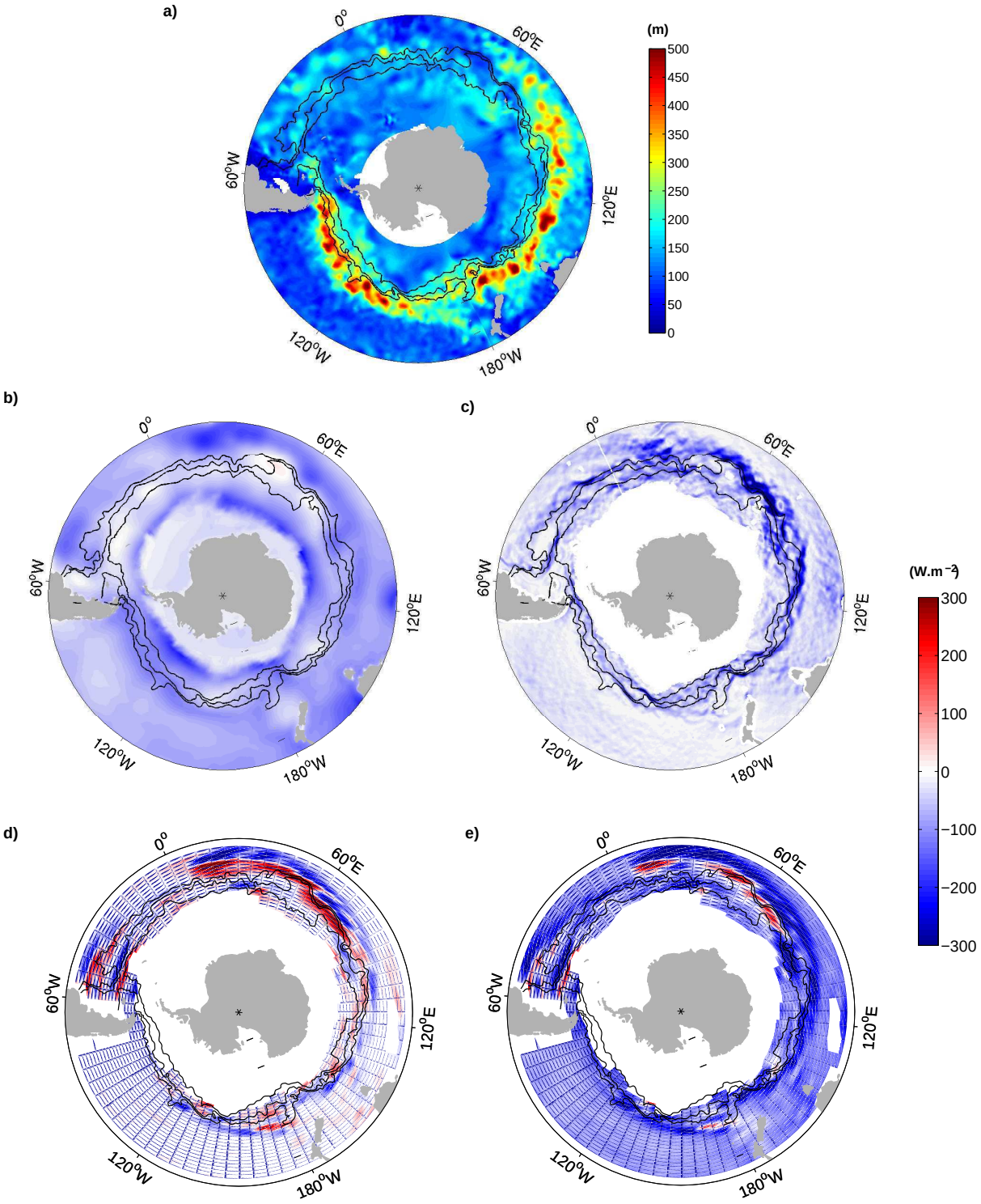

FIG. 5.1 – (a) Winter mixed layer depth in the Southern Ocean from Argo and ship data. b) Climatological winter air-Sea heat exchange, (c) Ekman heat advection, (d) Eddy heat Diffusion in the mixed layer and (e) the total of these three components. Contours represent the mean ACC fronts (PF, SAF and SAF-N)

satellite SST product from TMI and AMSR satellites (http ://www.ssmi.com/). Given that the area studied is mainly outside the boundary of TMI satellite, most of the data are from the AMSR-E satellite. When compared to MODIS or Reynolds OI SST, AMSR-E SST have less bias relative to in-situ observations. A comparison of AMSR-E SSTs with XBT repeated sections shows that the standard error is less than 0.1°C during winter (Dong et al., 2006). Combined with the wind stress error this results in an Ekman heat transport error of approximately 20 $W.m^{-2}$ over the studied area.

The annual mean climatological cross-stream eddy diffusivity coefficient has been estimated in bins of 5° longitude by 1° latitude for the Southern Ocean by Sallée et al. (2007b). This coefficient results from a statistical formulation, computed using 10 years (1995-2005) of surface drifter data. On average over the circumpolar belt, the diffusivity shows an increase from the Antarctic continent to the ACC, a stable plateau around $4000m^2.s^{-1}$ within the ACC and a further increase north of the ACC dominated by the western boundary current regions.

The mean circulation and fronts of the Southern Ocean are deduced from a climatology of Sea Surface Height (SSH) referenced to 1500m (SSH_{1500m}) following Sallée et al. (2007a). The Polar Front (PF) is associated with the 0.95m SSH_{1500m} contour ; the Subantarctic Front (SAF) with SSH_{1500m}=1.2m ; and the northern branch of the Subantarctic Front (SAF-N) with SSH_{1500m}=1.35m.

The ocean interior caracteristics are obtained using the Argo dataset (www.argo.ucsd.edu) and the Southern Ocean database (SODB) (http ://woceSO.atlas.tamu.edu). Databases of ML depth and SSH_{1500m} have been extracted from these datasets and then gridded using a loess fitting method. Following de Boyer Montégut (2004) and SWMS06, we used a density difference criteria of 0.03 $kg.m^{-3}$ to assess the ML depth of each profile.

5.1.3 SAMW formation pool

Figure 5.1a shows the winter (July to September) ML depth in the Southern Ocean. This maximum ML depth pattern is similar to previous studies (Talley, 1999 ; de Boyer Montégut et al., 2004). However, the Argo dataset provides a large amount of data in winter and in the middle of the gyres (Sallée et al., 2007a). Thus, for the first time, we have enough confidence in the winter climatology to confirm that the very deep MLs (up to 600m) shoals as the flow rounds the Campbell Plateau. Shallower winter MLs continue up to the Eltanin Fracture Zone in the mid-Pacific Ocean (220°E).

Deep winter MLs are clearly linked to the circulation, as they occur directly north of the SAF-N in the Indian basin and directly north of the SAF in the Pacific basin. Upstream of Drake Passage the deepest MLs occur further south, just north of the PF. In the southern Indian sector, SWMS06 have shown the role of the circulation and the eddy heat diffusion on the MLs. Can we infer a similar role in the Pacific basin ?

5.1.4 Climatological heat forcing and circulation

Based on the datasets presented in section 5.1.2, we computed the three climatological winter forcing terms on the right of the simplified heat budget equation (Equation 5.1). The winter air-sea fluxes in Figure 5.1b cool the Southern Ocean everywhere, with maximum cooling occurring north of the sea ice

and north of the SAF fronts. Stronger cooling occurs across the fronts downstream of Kerguelen around 90°E, around the Campbell Plateau at 170°E, and in the SE Pacific. The Ekman heat transport in Figure 5.1c is driven by the strong westerly winds, transporting cold water equatorward, resulting in a general loss of heat everywhere around the circumpolar belt. The eddy heat diffusion (Figure 5.1d) is the annual climatological mean, which should be similar to the winter mean. Eddies diffuse heat from the warm equatorward side of a temperature gradient to the cool poleward side ; hence, the eddy heat diffusion generally cools the northern side of the SAF and SAF-N and heats the southern side. However, departures from this general shape are locally observed when a powerful western boundary current associated with a substantial SST gradient interacts with the ACC or near topography. Thus, warming on the north side of the ACC is observed in the Southwestern Indian basin between the longitudes 30-60°E (SWMS06), downstream of the Campbell Plateau (170°E), and near the Brazil-Malvinas current (40°W).

Once the ACC rounds the Campbell Plateau, the flow divides into two branches. The Southern branch includes the PF and SAF, which flows southward hugging the Indo-Pacific Ridge. The northern branch includes the SAF-N, which turns sharply to the north following the southern flank of the Campbell Plateau until approximately 50°S.The two branches then merge to pass through the Eltanin Fracture Zone (220°E). As the SAF-N rounds the Campbell Plateau, it enters a region of weak winter air-sea cooling and positive eddy heat diffusion (Figure 5.1b,d). For the Southern branch, the eddy heat diffusion is negative, with stronger Ekman and air-sea fluxes, which cools the north side of the SAF and PF.

The general shape of the eddy heat transport agrees well with the studies of Jayne and Marotzke (2002). Although the diffusion can be strong locally, on a large scale average its contribution vanishes. Therefore, our results are not contradictory with previous large-scale heat budget estimation that succeeded in closing the heat budget while neglecting the eddy diffusion contribution (SWMS06 ; Dong et al., 2007).

Figure 5.2a,b shows the winter average of the sum of the three forcing terms (i.e. Figure 5.1e) and the winter ML depth, but now in alongstream coordinates relative to the position of the SAF-N. Also shown is the winter ML density for MLs greater than 200m depth (Figure 5.2c). Strong cooling north of the SAF-N coincides with the regions of deep winter MLs in the Subantarctic Zone. Strong cooling also occurs south of the SAF-N in three regions : downstream of Kerguelen around 90°-100°E, downstream of New Zealand near 170-190°E, and in the South Pacific from 240-260°E (100-120°W). These are the only regions with a deep winter MLs south of the SAF-N (Figure 5.2b), and have much denser MLs, exceeding 27.2 in the south Pacific (Figure 5.2c). The deep winter MLs continue north of the SAF-N in these zones, except for the region downstream of Campbell Plateau. Here, we observe an average winter warming of the area north of the SAF-N, related to stronger eddy diffusion and weaker air-sea cooling (Figure 5.1b,d). SWMS06 have shown that this warming prevents the formation of deep winter MLs north of the SAF in the western Indian basin. Figure 5.2 suggests that a similar process occurs downstream of Campbell Plateau. The substantial eddy diffusion of the region induces a strong cooling north of the Southern branch of the ACC composed of the SAF and PF. Consequently, diffusion tends to prevent deep ML formation north of the SAF-N, but enhances deep MLs north of the SAF. It results in a densification of SAMW downstream of Campbell Plateau (Figure 5.2c), where oxygen-rich deep MLs attain the density class of 27.1-27.2, usually associated with Antarctic Intermediate Water (AAIW).

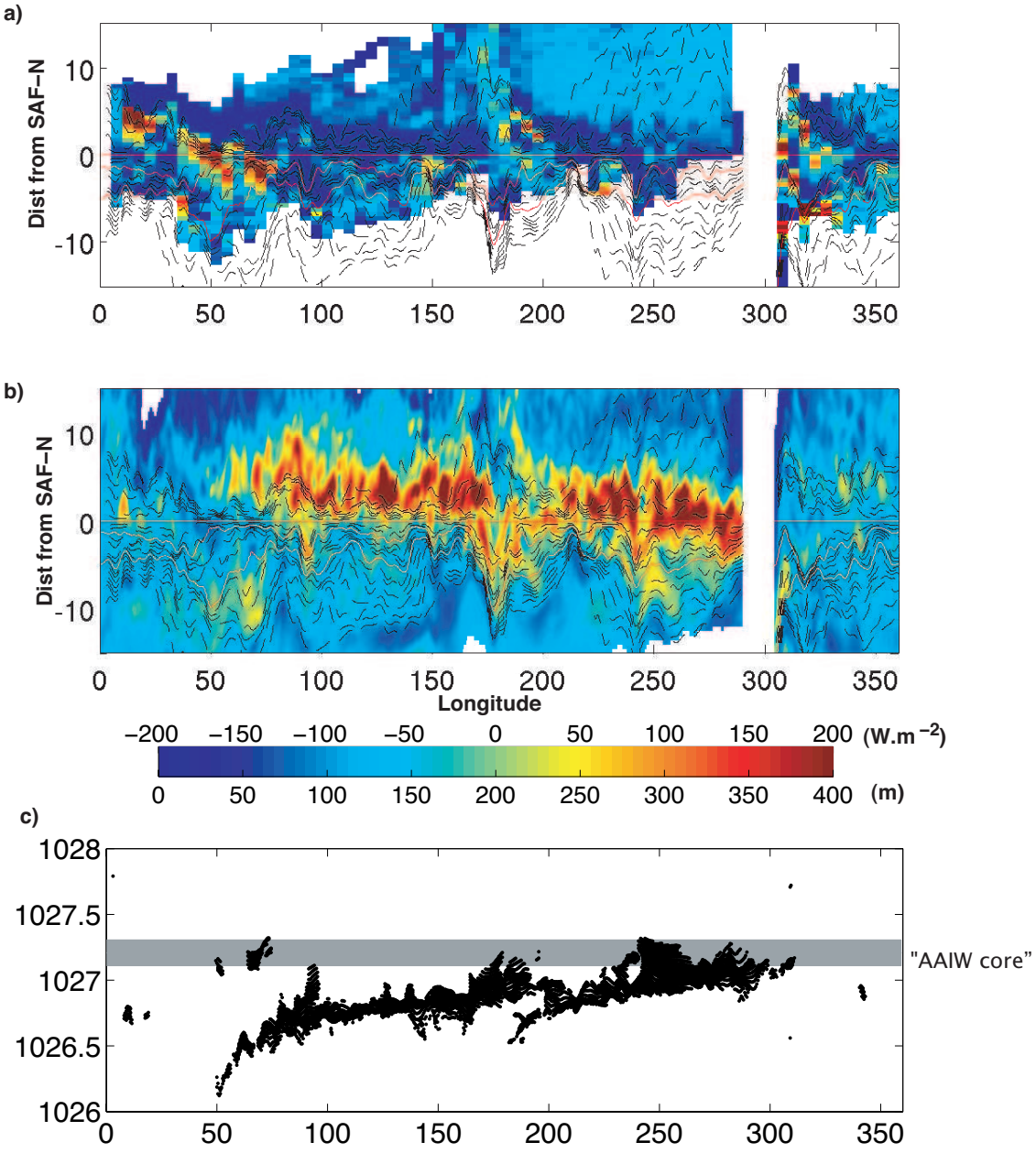

FIG. 5.2 – (a) Total of winter air-sea fluxes, Ekman fluxes and eddy diffusion, and (b) winter mixed layer depth in streamline coordinates following the SAF-N. Y-axis shows the distance in °latitude to the SAF-N. (c) Density class of the winter mixed layer deeper than 200m.

5.1.5 Water column evolution

By chance an Argo float drifted along the SAF-N downstream of the Campbell Plateau during the winter of 2006. The water column had undergone a typical seasonal cycle, with a minimum in ML depth of around 50m during summer and a deepening in winter (Figure 5.3c). The winter MLs reached a depth of approximately 250m and a potential density of around 26.9 $kg.m^{-3}$ during July which corresponds to the SAMW density class. Interestingly, the ML suddenly restratified in the middle of the winter, during the month of August, with the float still close to the front. We computed the terms on both sides of our simplified equation 5.1 to examine the evolution of the forcing terms, and determine the reason for this sudden and surprising stratification north of the SAF-N during winter. Figure 5.3d reveals that the water column restratified during the coldest month of winter with continued cooling by the Ekman transport. We note that one has to be careful when tracking water masses with Argo floats, since the float may drift at the surface and sample different water masses between two profiles. However, Figure 5.3c shows stable deep water masses, and Figure 5.3d shows that the heat content evolution is consistent with the forcing terms.

The local eddy heat diffusion estimate allows us to explain the observed warming of the water column. We observed two large departures from the balance between heat content variation and the cumulated contributions of Ekman and air-sea fluxes. Both of these departures are qualitatively explained by the sign of the eddy heat diffusion.

From April to July the float drifted in the vicinity of the SAF-N. The eddy diffusion term cooled the water column in this turbulent frontal area during this period (Figure 5.3a,b). In August, the float drifts east of New-Zealand, north of the SAF-N, in the region of inferred heating by eddy diffusion.

Figure 5.3b shows that the eddy diffusion heat gain is due to a coherent large scale feature that the float cross in late July and August. We note that the eddy heat diffusion calculated here appears strong compared to other terms. This may be an artefact of computing diffusion from a long term, large scale, climatological eddy diffusion coefficient and an instantenous high resolution SST. However, it does provide a first approximation and estimate of the tendency of the eddy heat diffusion in each region.

The Argo-derived ML shoals as the float drifts into this area, with a ML depth decrease consistent with the heating. Note that the strong heaving of isopycnals in September 2006 associated with a second cyclonic eddy are not enough to break the stratification, and the shallower ML remains into spring.

5.1.6 Concluding discussion

SAMWs form in the very deep ML occuring every winter north of the ACC (McCartney, 1982). This deep ML is not evenly distributed around the circumpolar belt. It is widely accepted that there is no subpolar mode water deepening from Drake Passage around to the Kerguelen Plateau (Talley, 1999; de Boyer Montégut et al., 2004). Mode waters have been detected in the retroflection region, but these are lower density subtropical mode waters. The growing new Argo dataset reveals that the winter MLs between 170 and 220°E in the Western Pacific Ocean are much shallower than those upstream or downstream. Moreover, MLs with density similar to AAIW is formed in the southwest Pacific.

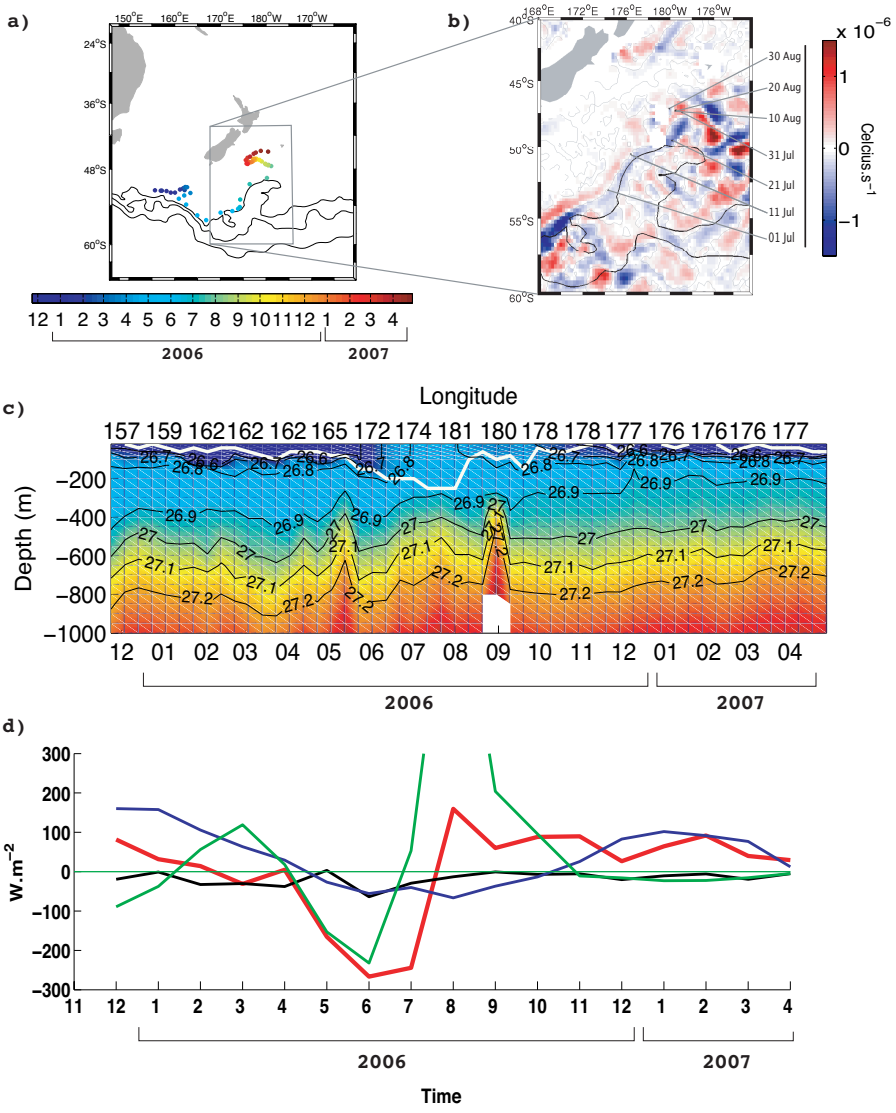

FIG. 5.3 – (a) Trajectory of the ARGO float WMO 5901106, with its date in color. (b) Vertical density section along its trajectory over time (bottom x-axis) and longitude (upper x-axis). (c) Monthly averaged simplified heat budget terms along the float trajectory. The red line is the heat content variation computed from the ARGO profiles. Also shown are local air-sea fluxes (blue), Ekman fluxes (black), and eddy heat diffusion (green) along the trajectory.

Consistent with previous work, we find that the eddy diffusion vanishes when taking a large scale averaging of the ML (Dong et al., 2007). However, locally its contribution is very important in the energetic western boundary currents and around topography. Winter climatological maps of the net heat forcing, simplified to its air-sea, Ekman and heat diffusion contributions, shows a strikingly similar spatial pattern to the winter ML depth. In the SW Pacific and north of the SAF-N, a region of shallow winter ML coincides with warming by the climatological eddy heat diffusion. A time-varying calculation of the ML depth, following the track of Argo float WMO 5901156, shows a surprising restratification during the coldest month of the year when arriving in this region. This restratification is qualitatively explained by an increase in the eddy heat diffusion.

The sudden change in the circulation of the ACC as it rounds the Campbell Plateau reduces the SAMW formation north of the SAF-N and enhances it on the southern side. Cooler and deeper winter MLs thus occur on the equatorward side of the SAF and PF in this area, which are associated with a denser class of SAMW. A similar jump in density also occurs in the SE Pacific, where AAIW is thought to form in winter (Hanawa and Talley, 2001). Sallée et al. (2007b) have suggested that an increase in the eddy diffusion coefficient occurred over the last decade. Such a change may have an impact on the SAMW properties and volume, for example a redistribution of AAIW relative to SAMW. These processes, in concert with the air-sea interaction could play a role in climate variability, and be fruitfully investigated with coupled climate models.

Conclusion générale

Les eaux modales Subantarctiques (SAMW) se forment dans l'épaisse couche de mélange hivernale qui se développe au Nord du front Subantarctique. Cette volumineuse couche d'eau de l'Océan Austral est un lien privilégié entre l'océan intérieur et l'atmosphère. Son étude est déterminante pour la compréhension et la prévision du climat. Cette thèse s'est donné pour but de mieux comprendre les processus de formation des SAMW. Les études autrefois consacrées à l'Océan Austral et basées sur son observation avaient toutes souffert du manque cruel de données in situ. Le présent travail a pu s'appuyer sur des jeux de données relativement récents, les flotteurs profilants ARGO et les dériveurs de surface GDP, éléments que nous avons complétés par des données hydrologiques de bateaux, ainsi que par des données satellitales. Pour la première fois, nous avons un jeu de d'observations in situ repartie équitablement sur toutes les saisons et tous les bassins au Nord de la zone de glace de mer.

L'étude des eaux modales qui a motivée l'écriture de cette thèse nous a poussé à élargir le spectre de nos investigations à l'Océan Austral. L'analyse de nos premiers résultats nous a suggéré que dans le cadre d'une étude des SAMW, il était nécessaire de clarifier au mieux la dynamique de l'Océan Austral. Aussi avons-nous laissé de côté un instant l'étude directe des SAMW pour nous concentrer sur la structure frontale de l'ACC et de ses tourbillons. A partir de l'association de données satellitales et de données in situ de la colonne d'eau, nous avons montré qu'un contour de hauteur de surface de la mer (SSH) définit la position des fronts PF et SAF de manière circumpolaire. Les données hydrologiques des bateaux et des flotteurs ARGO nous renseignent sur la circulation moyenne, et les données satellitales nous permettent un suivi hebdomadaires de la variabilité frontale sur les 13 années 1993-2005. Finalement, les dériveurs de surface GDP nous ont permis d'estimer statistiquement le coefficient de diffusion tourbillonnaire méso-échelle dans l'Océan Austral.

En associant les différents jeux de données à notre dispositions, nous avons pu calculer un bilan de chaleur dans la zone de formation des eaux modales dans le bassin Indien Est. En accord avec des études numériques précédentes (par exemple Ribbe, 1999 ; Rintoul et England, 2002), nous avons montré pour la première fois avec des données in situ que la variation du contenu de chaleur de la couche de mélange océanique est expliquée à grande échelle par les seules actions du transport d'Ekman et des flux air-mer. Plus largement, nous avons aussi pu comparé les importance relatives des forçage du bilan de chaleur le long de la ceinture circumpolaire. Nous avons ainsi mis en relief le rôle important de la diffusion tourbillonnaire dans le bilan de chaleur. Elément notable, ce rôle est localement très important mais, une fois moyenné sur une large zone, il devient négligeable.

Les bassins Ouest sont dominés par des courants de bord Ouest très energétiques. Notre travail a montré que diffusion est forte aux abords de ces courants. D'un point de vue méridional, la diffusion

s'intensifie entre le continent Antarctique et l'ACC, puis se stabilise dans le fort ACC, et finalement ré augmente au Nord de l'ACC dans les courants de bord Ouest. D'apres nos simulations la contribution principale à cette diffusion est la méso-échelle géostrophique. L'ACC domine généralement le gradient de temperature le long de la ceinture circumpolaire, résultant en une diffusion refroidissant la couche de mélange au Nord de l'ACC et réchauffant la partie Sud. Cependant, dans les bassins Ouest le gradient température dans la couche de mélange est dominé par le courant de bord Ouest. L'ACC, un peu plus au Sud, est alors associé à un gradient de température secondaire, plus faible. Ainsi s'opère un renversement du signe de la diffusion de chaleur dans la zone Subantarctique des bords Ouest. A chaque fois que l'ACC interagit avec des courants de bord Ouest, la diffusion de chaleur change de signe, vient réchauffer la couche de mélange en équilibrant et même en dominant les refroidissements hivernaux induits par le transport d'Ekman et les flux air-mer. On observe ce phénomène tant dans le bassin Ouest Indien (courant des Aiguilles) que dans l'Ouest Pacifique (Est de la Nouvelle Zélande), ou encore dans l'Ouest Atlantique (courant des Malouines).

Le SAF, fortement contraint par la bathymétrie tend à remonter vers le Nord dans les bassins Ouest, autour des Plateaux de Crozet et le Plateau Kerguelen (50-70°E), autour du Plateau de Campbell et la fracture d'Eltanin (170-220°E), et en aval du Plateau Sud-Américain (300°E). L'ACC transporte alors de l'eau froide vers des basses latitude ce qui implique des échanges air-mer hivernaux moins vigoureux. Ainsi en plus du réchauffement par diffusion toubillonaire, le refroidissement des flux air-mer est amoindrie car lorsque .

La bathymétrie fait ainsi ressortir des zones "cléfs" autour de la ceinture circumpolarire. Les structures topographiques très contraignantes dirigent la circulation autour de 40°S dans l'Atlantique et l'Indien, et bien plus au Sud, autour de 55°S dans le bassin Pacifique. Autour de chacune de ces imposantes structure bathymétriques, nous avons vu que les fronts sont associés à des transports plus importants et des faibles variabilités spatiales. Par exemple, le Plateau de Kerguelen oblige les différentes branches de l'ACC à se regrouper dans une enveloppe très fines. Cette convergence des fronts met en proche contact des masses d'eau de caractéristiques très différentes, augmentant ainsi les gradients de propriétés, et par conséquent l'intensité du refroidissement par transport de chaleur d'Ekman et par diffusion de chaleur. La diffusion, en réduisant la stratification, prend ici un rôle de pré-conditionnement de la colonne d'eau qui arrive dans l'Est du bassin Indien, moins stratifiée, prête à créer des SAMW sous les seules actions des flux d'Ekman et des flux air-mer. Le Plateau de Kerguelen marque ainsi le commencement de la profonde déstratification de la couche de mélange le long de la ceinture circumpolaire. De façon semblable, au niveau de la fracture d'Eltanin au milieu du Pacifique les deux principaux fronts se rejoignent. Nous n'avons pas étudié en détail ce qu'il se passe alors, mais nous soupçonnons une réaction proche de celle analysée dans l'Océan Indien Ouest lors du passage du Plateau de Kerguelen. Une exploitation des données ARGO dans cette région pourrait révéler d'intéressants mécanismes.

En aval du Plateau de Campbell, la remontée vers le Nord de la circulation enjendre un saut marqué de la densité des eaux modales. A cet endroit l'ACC se divise en deux : une branche Nord, dont le SAF-N se dirige vers le Nord en suivant le plateau de Campbell ; une branche Sud, composée notamment du SAF et du PF reste au Sud en suivant la dorsale Antarctique-Pacifique. La branche Nord, dans sa montée vers l'équateur, vient interagir avec le courant de bord Ouest longeant la côte de Nouvelle-Zélande. Comme dans l'Ouest du bassin Indien, cette interaction engendre un réchauffement par diffusion du côté Nord du SAF-N, se traduisant par une re-stratification de la couche de mélange. En parallèle, la branche Sud qui s'écoule loin du courant de bord Ouest subit un refroidissement intense sur son flanc Nord en rapport

avec l'activité tourbillonnaire. Ainsi, la diffusion tourbillonnaire de cette zone favorise le développement de SAMW denses associées au SAF, et bloque celui de SAMW moins denses associées au SAF-N. On observe un saut en densité des SAMW au passage du plateau de Campbell. Après ce passage très particulier, les branches Nord et Sud se rejoignent. La branche Nord recommence à être associée à une destratification, et la branche Sud se restratifie. Une variabilité interannuelle de la diffusion, comme suggérée dans notre étude du chapitre 4, induirait alors une sensible densification des SAMW dans le bassin Pacifique.

Les bassins Est sont des domaines beaucoup moins énergétiques. La diffusion au Nord de l'ACC y est bien plus faible qu'aux abords des courants Ouest. En parallèle, il s'avère que la bathymétrie y est beaucoup moins contraignante. On trouve des zones de fonds plats : Est Indien et Est Pacifique. La dynamique frontales y est donc très différente. On observe, par exemple, dans ces zones de fond plat une forte variabilité de la position méridienne des fronts. Dans ces zones, la variabilité haute fréquence des fronts est en partie liée au forçage atmosphérique. Notons que dans le bassin Sud Est Indien et Sud Est Pacifique, les mouvements des fronts à haute fréquence (inférieure à 3 mois) sont associés aux variations de l'indice climatique SAM. Un événement positif du SAM est associé à des fronts plus au Sud dans l'Indien et à des fronts plus au Nord dans le Pacifique Est. L'indice climatique ENSO est lui aussi associé aux mouvements de fronts dans le Pacifique. Cependant, la réponse à l'indice ENSO se situe sur des fréquences temporelles plus basses, de l'ordre de l'année.

Dans les bassins Est Indien et Est Pacifique, la colonne d'eau est faiblement stratifiée. Dans ces zones de profonde destratification de la couche de mélange, entre Kerguelen et le Passage de Drake, on observe une évolution circumpolaire de la densité des SAMW. Dans ces deux zones l'ACC qui est contraint à passé soit au Sud du Plateau de Campbell, soit à travers le Passage de Drake, tend à se déplacer vers le Sud. Cette tendance est associées à une densification des SAMW. Des excursions de refroidissement au Sud de la zone Subantarctique sont observées directement en aval du Plateau de Kerguelen et en aval de la fracture d'Eltanin. Des brusques densifications sont alors detectées, les SAMW atteignant les classes de densité des AAIW.

Notre travail à débouché sur des résultats portant sur large éventail de domaine de l'océanographie. Cependant tous les résultats de cette thèse se retrouvent autour d'une même constante : la non-zonalité des phénomènes. Cette non-zonalité est l'empreinte d'une part de la bathymétrie très saccadée de l'Océan Austral et d'autre part de la succession de courants de bord Ouest rencontrés le long de la ceinture circumpolaire. Elle est associée à des zone "clef", avec des sauts de propriétés ou des changements de régimes, et provoque une évolution circumpolaire des propriétés des SAMW.

Cette thèse laisse espérer de nombreuses pistes très captivantes pour le futur. Nous avons ouvert une voie à la compréhension de l'évolution longitudinale des propriétés des SAMW en invoquant le rôle de la diffusion de chaleur tourbillonnaire. Un travail sur la dynamique autour de la zone de fracture d'Eltanin serait très enrichissant et viendrait compléter les résultats de cette thèse. Comment la colonne d'eau réagit-elle à la traversée de cette fracture qui force deux branches de caractéristiques très différentes à entrer en proche contact dans une région océanique turbulente ? Ce scénario a été observé au niveau du Plateau de Kerguelen. Nous avons conclu à un pré-condionnement permettant la formation des SAMW en aval, dans le bassin Est Indien.

Un tel pré-conditionnement existerait-il dans le Pacifique ? Nous observons une forte densification des SAMW en aval de la fracture d'Eltanin. Les SAMW entrent dans des gammes de densité traditionnel-

lement associées aux AAIW. Il est légitime de se poser la question d'un lien entre un pré-conditionnement au niveau de la fracture d'Eltanin, la densification des SAMW, et la formation d'AAIW. Il se pourrait que les AAIW soient injectées depuis la couche de mélange en certains sites seulement (entre 60-80°E dans l'Océan Indien pour Wong, 2005 ; entre 120-150°W dans le Pacifique pour Iudicone, 2007). Dans ce cas le taux d'oxygène des AAIW serait important. En contraste, nos études en amont de Kerguelen ont mis en évidence d'important mélange et "interleaving" en subsurface entre des eaux subtropicales et polaires, jusqu'à des densité potentielle de 27.4 $kg.m^{-3}$ qui pourraient injecter des eaux peu salées, et probablement peu oxygènées au nord du SAF. Ces pistes sont à suivre dans les années à venir avec des données ARGO plus abondantes. L'idée de rajouter des capteurs d'oxygène sur certains flotteurs ARGO semble très prometteuse pour ce type d'étude (voir la page web du groupe "Friends of Oxygen on Argo" (FAO) : http ://ioc.unesco.org/IOCCP/FOA.htm ; et le projet FLOPS)

Dépassant le seul impact sur les SAMW, une nouvelle paramétrisation des effets tourbillonnaires peut potentiellement avoir un impact sur la représentation de la cellule méridienne de l'Océan Austral. Cette cellule hypothétique est associée à une remontée des eaux profondes circumpolaires supérieures (UCDW) et à une poussée de ces eaux vers le nord par transport d'Ekman. La branche Nord serait associée à la plongée des eaux AAIW et/ou SAMW, et un transport vers le sud à travers l'ACC bouclerait la circulation (Figure 1.3). Ce transport vers le sud est un transport ageostrophique induit par l'activité tourbillonnaire. L'idée d'un transport induit par les tourbillons (EIT) a été introduit par Gent et McWilliams (1990). A travers ces effets dynamiques des tourbillons, la diffusion tourbillonnaire méso-échelle peut avoir un impact sur la position et l'intensité de la convergence de masse associée à la coulée des eaux de la branche nord de la cellule de circulation supérieure de l'Océan Austral. La position de cette convergence est très importante pour savoir si elle est associée à l'enfoncement de SAMW ou de AAIW. Nous nous sommes rendu compte tout au long de cette thèse de la non-zonalité des phénomènes dans l'Océan Austral, notemment des effets tourbillonaires très différents dans l'Est et l'Ouest des bassins. Il est fortement probable que l'EIT et la circulation méridienne varient elles aussi fortement le long de la ceinture circumpolaire. Un premier travail nous a suggéré que la vue classique bidimensionnelle de ce problème n'est pas suffisante pour rendre compte de la complexité de cette cellule. Il serait en effet possible que la convergence de masse calculée soit en partie absorbée par la couche de mélange et transportée par l'ACC le long de la ceinture circumpolaire. Par endroits une puissante cellule pourrait être mise en route avec un export de masse d'eau dans l'intérieur de l'océan. Ce problème, très important dans le cadre d'une compréhension de la circulation océanique Australe, se doit d'être étendu tant que possible à une vue tridimensionnelle. Les modèles nous sont d'une aide précieuse pour l'étude de cette cellule (par exemple Marsh et al., 2000 ; Drijfhout, 2005 ; Hallberg et Gnanadesikan, 2006 ; Treguier, 2007). Mais, étant donné l'importance que nous conférons aux tourbillons, et le questionnement sur la justesse de leur représentation dans les modèles, il nous semble nécessaire d'également tenter d'aborder ces questions à partir d'observations de l'océan.

Les résultats de cette thèse posent également beaucoup de questions sur le lien entre la variabilité atmosphérique et les SAMW. Nous avons montré comment les conditions atmosphériques sont liées au mouvement méridional des fronts. Comment ce mouvement se traduit-il en terme de densité de la profonde couche de mélange associée ? Le problème étant vu sous un autre angle, ce mouvement influence-t-il la profondeur de la couche de mélange et ainsi le volume de SAMW renouvelé ? Hogg et al. (2007) ont montré le lien qui existe entre la variabilité atmosphérique et la diffusion tourbillonnaire. Nous avons documenté un possible lien entre la diffusion tourbillonnaire et la formation des SAMW, notamment leur

densité. Les variabilités climatiques influenceraient-elles alors les SAMW à travers la variabilité de la diffusion tourbillonnaire ? L'étude de phénomènes si complexes qui pourraient rétroagir sur l'atmosphère (Sen Gupta et England, 2007) nécessite au moins de longues séries temporelles des propriétés de la colonne d'eau et la possibilité d'effectuer des expériences "idéales". Pour tenter d'approcher au mieux le coeur de ces problématiques, il serait passionnant de pouvoir conduire une analyse de ces phénomènes basée sur un modèle de circulation réaliste couplé avec l'atmosphère.

Les études que nous avons menées pendant ces trois années documentent les phénomènes physiques à l'origine de la formation des SAMW dans les profondes couches de mélange. Cependant, nous n'avons pas quantifié le volume de ces eaux qui, une fois formées dans les fortes couches de mélange, sont effectivement injectées dans l'intérieur de l'océan. Cette information est primordiale pour comprendre ce que vont être les conséquences climatiques de nos résultats sur la formation et les forçages de la formation des SAMW. Si une masse d'eau reste dans la couche de mélange, sans entrer en interaction dans la circulation thermohaline globale (McCartney, 1977, 1982 ; Karstensen et Quadfasel, 2002), son étude a moins d'intérêt dans l'optique d'une analyse du climat à long terme. Il a été montré que les SAMW entrent dans ce processus de circulation thermohaline globale. Mais en quelle quantité ? Il serait très enrichissant d'exploiter les jeux de données in situ disponibles pour explorer cette question. Une analyse basée sur un modèle haute résolution résolvant les tourbillons pourrait sensiblement aider à la compréhension de cette subduction. Il nous reste également à aborder la problématique de la salinité. Nous avons surtout analysé la couche de mélange en invoquant des bilans de chaleur. A n'en pas douter, la salinité tient aussi une place importante dans la stratification de la colonne d'eau et la formation des SAMW. Mais le manque de données in situ de la salinité, en particulier un suivi de l'évolution de la salinité de surface à fine-échelle, nous a contraints à repousser à plus tard un travail consacré à cette question. L'emploi de modèles ou le prochain lancement de la mission SMOS pourrait aider à combler cette lacune.

En conclusion, nous avons dans cette thèse fait ressortir des résultats novateur à partir de l'analyse de données in-situ, et il serait très interessant de les confronter à une exploration de résultats d'un modèle haute résolution. Une telle étude permettrait de comprendre plus en détail la contribution des tourbillons aux transferts méridiens de chaleur et à la formation de masses d'eau associée. Elle pourrait notamment fournir des estimations précises de tous les termes nécessaires aux calculs de bilans couplés.

Bibliographie

Andrews, D. G., Holton, J. R., and Leovy, C. B. (1987). *Middle Atmosphere Dynamics*. Academic Press, 489 pp.

Aoki, S., Bindoff, N., and Church, J. (2005). Interdecadal water mass changes in the Southern Ocean between 30E and 160E. *Geophys. Research Letter*, 32 :L07607.

Arblaster, J. and Meehl, G. (2006). Contributions of external forcing to Southern Annular Mode (SAM) trends. *J. of Climat.*, 19 :2896–2905.

Argo Science Team (2000). Report of the argo science team 2nd meeting, 7-9 march 2000. Technical report, Southampton Oceanography Centre, Southampton, U.K.

Baker, D. J. (1982). A note on Sverdrup balance in the Southern Ocean. *J. Mar. Res.*, 40 (Suppl.) :21–26.

Batchelor, G. and Townsend, A. (1953). Turbulent diffusion. *surveys in Mechanics*, 23 :352–398.

Bauer, S., Swenson, M., and Griffa, A. (2002). Eddy mean flow decomosition and eddy diffusivity estimates in the tropical Pacific Ocean : 2. Results . *J. Geophys. Res.*, 107(C10) :3154.

Belkin, I. M. and Gordon, A. L. (1996). Southern Ocean fronts from the Greenwich Meridian to Tasmania. *J. Geophys. Res.*, 101 :3675–3696.

Bennett, A. (1984). Relative dispersion : local and nonlocal dynamics. *J. Atmos. Sci.*, 41 :1881–1886.

Bennett, A. (1987). A lagrangian analysis of turbulent diffusion. *Rev. of Geophys.*, 25(4) :799–822.

Bindoff, N. and Church, J. (1992). Warming of the water column in the southwest Pacific Ocean. *Nature*, 357 :59–62.

Bindoff, N. L. and McDougall, T. J. (2000). Decadal changes along an Indian Ocean Section at 32S and their interpretation. *J. Phys. Oceanog.*, 30 :1207–1222.

Bohme, L. and Send, U. (2005). Objective analyses of hydrographic data for referencing profiling float salinities in highly variable environments. *Deep-Sea Research*, 52/3-4 :651–664.

Bower, A. S., Rossby, H., and Lillibridge, J. (1985). The Gulf StreamÑBarrier or blender ? *J. Phys. Oceanog.*, 15 :24–32.

Bracco, A., LaCasce, J., and Provenzale, A. (2000). Velocity probability density functions for oceanic floats. *J. Phys. Oceanog.*, 30 :461–474.

Brainerd, K. and Gregg, M. (1995). Surface mixed and mixing layer depth. *Deep Sea Res., Part II*, 42(A) :1521–1543.

Bryden, H. (1979). Poleward heat flux and conversion of available potential energy in drake passage. *J. Mar. Res.*, 37 :1–22.

Bryden, H. and Heath, R. (1985). Energentic eddies at the northern edge of the Antarctic Circumolar Current in the South West Pacific. *Progress. Ocean.*, 14 :65–87.

Cai, W., Whetton, P., and Karoly, D. (2003). The response of the Antarctic Oscillation to increasing and stabilized atmospheric CO_2. *J. of Climat.*, 10 :1525–1538.

Caldeira, K. and Duffy, P. (2000). The role of the Southern Ocean in uptake and storage of anthropogenic carbon dioxide. *Science*, 287 :620–622.

Chaigneau, A. and R., M. (2002). Surface temperature and salinity variations between tasmania and antartica, 1993-1999. *jgr*, 107 :22–1–22–7.

Chelton, D., deSzoeke, R., Schlax, M., Naggar, K., and Siwertz, N. (1998). Geographical variability of the first baroclinic Rossby radius of deformation. *J. Phys. Oceanog.*, 28 :433–460.

Chelton, D., Schlax, M., Witter, D., and Richmann, J. (1990). Geosat altimeter observations of the circulation of the Southern Ocean. *J. Geophys. Res.*, 95 :17,877–17,903.

Chelton, D. B., Schlax, M., Freilich, M., and Millif, R. (2004). Satellite measurements reveal persistent small-scale features in ocean winds . *Science*, 303 :978–983.

Connoley, W. (2002). Long-term variation of the antarctic circumpolar wave. *J. Geophys. Res.*, 108(C4) :8076.

Daniault, N. and Ménard, Y. (1985). Eddy kinetic energy distribution in the Southern Ocean from altimetry and FGGE drifting buoys. *J. Geophys. Res.*, 90(C6) :11,877–11,889.

Davis, R. (1982). On relating Eulerian and Lagragian velocity statistics : single particles in homogeneous flows. *J. Fluid. Mech.*, 114 :1–26.

Davis, R. (1991a). Lagrangian ocean studies. *Annual Review of Fluid Mechanics*, 23 :43–64.

Davis, R. (1991b). Observing the general circulation with floats. *Deep Sea Res., Part II*, 38 :S531–S571.

Davis, R. (2005). Intermediate depth circulation of the Indian and South Pacific Oceans measured by autonomous floats. *J. Phys. Oceanog.*, 35(5) :683–707.

de Boyer Montégut, C., Madec, G., Fischer, A., Lazar, A., and Iudicone, D. (2004). Mixed layer depth over the global ocean : an examination of profile data and a profile-based climatology. *J. Geophys. Res.*, 109 :C12003.

de Szoeke, R. A. and Levine, M. D. (1981). The advective flux of heat by maen geostrophic motions in the southern ocean. *Deep Sea Res.*, 34 :33–44.

Deacon, G. (1933). A genereal account of the hydrology of the southern atlantic ocean. *Discovery Report*, 7 :171–238.

Deacon, G. (1937a). Note on the dynamics of the Southern Ocean. *Discovery Report*, XV :125–152.

Deacon, G. (1937b). The Hydrology of the Southern Ocean. *Discovery Report*, XV :1–124.

Dong, S., Gille, S., Sprintall, J., and Gentemann, C. (2006a). Validation of the Advanced Microwave Scanning Radiometer for the Earth Observing System (AMSR-E) sea surface temperature in the Southern Ocean. *J. Geophys. Res.*, 111 :C04002.

Dong, S., Sprintall, J., and Gille, S. (2006b). Location of the Polar Front from AMSR-E satellite sea surface temperature measurements. *J. Phys. Oceanog.*, 36 :2075–2089.

Dong, S., Sprintall, J., and Gille, S. (2007). An assessment of the Southern Ocean mixed layer heat budget. *J. of Climat.*, 20 :4425–4442.

Döös, K. and Webb, D. J. (1994). The Deacon cell and other meridional cells of the Southern Ocean. *J. Phys. Oceanog.*, 24 :429–442.

Drijfhout, S. (2005). What sets the surface eddy mass flux in the Southern Ocean ? *submitted to jpo.*

Drijfhout, S., DeVries, P., Doos, K., and Coward, A. (2003). Impact of eddy-induced trasnport on the Lagragian structure of the upper branch of the thermohaline circulation. *J. Phys. Oceanog.*, 33 :2141–2155.

Drijfhout, S., Maier-Reimer, E., and Mikolajewicz, U. (1996). Tracing the conveyor belt in the hamburg large-scale geostrophic ocean general circulation model. *J. Geophys. Res.*, 101 :22,563–22,575.

Ducet, N., Le Traon, P., and Reverdin, G. (2000). Global high-resolution mapping of ocean circulation from TOPEX/Poseidon and ERS-1 and -2. *J. Geophys. Res.*, 105 :19,477–19,498.

Eden, C. (2006). Thickness diffusivity in the Southern Ocean. *Geophys. Research Letter*, 33 :L11606.

Eden, C., Greatbatch, R., and Rahmstorf, S. (2006). A diagnosis of thickness fluxes in a eddy-resolving model. *J. Phys. Oceanog.*, in press.

England, M. (1993). Representing the global-scale water masses in ocean general circulation models. *J. Phys. Oceanog.*, 23 :1523–1552.

England, M., Godfrey, J., Hirst, A., and Tomczak, M. (1993). The mechanism for Antarctic Intermediate Water renewal in a World Ocean model. *J. Phys. Oceanog.*, 23 :1553–1560.

Fine, R. (1993). Circulation of Antarctic Intermediate Water in the South Indian Ocean. *Deep Sea Res., Part II*, 10 :2021–2042.

Fox-Kemper, B. and Ferrari, R. (submitted). Parameterization of mixed layer eddies. II : prognosis and Impact. *J. Phys. Oceanog.*

Freeland, H., Rhines, P., and Rossby, T. (1975). Statistical observations of the trajectories of neutrally buoyant floats in the North Atlantic. *J. Mar. Res.*, 33(3) :383–404.

Fu, L. (2003). Wind-forced intraseasonal sea level variability of the extratropical oceans. *J. Phys. Oceanog.*, 33 :436–449.

Fukumori, I., Raghunath, R., and Fu, L. (1998). Nature of the global large-scale sea level variability in relation to atmosheric forcing : a modeling study. *J. Geophys. Res.*, 103(C3) :5493–5512.

Fyfe, J., Boer, G., and Flato, G. (1999). The Arctic and Antarctic oscillations and their projected changes under global warming. *Geophys. Research Letter*, 26 :1601–1604.

Garraffo, Z., Mariano, A., Griffa, A., Veneziani, C., and Chassignet, E. (2001). Lagrangian data in a high-resolution numerical simulation of the north atlantic. i. comparison with in situ drifter data. *J. Mar. Sys.*, 29 :157–176.

Gent, P. R. and McWilliams, J. C. (1990). Isopycnal mixing in ocean circulation models. *J. Phys. Oceanog.*, 20 :150–155.

Gent, P. R., Willebrand, J., McDougall, T. J., and McWilliams, J. C. (1995). Paremeterizing eddy-induced tracer transports in ocean circulation models. *J. Phys. Oceanog.*, 25 :463–474.

Gill, A. E. (1982). *Atmosphere-Ocean Dynamics*. Academic Press, New York.

Gille, S. (2002). Warming of the southern ocean since 1950s. *Science*, 295 :1275–1277.

Gille, S. and Kelly, K. (1996). Scales of spatial and temporal variability in the Southern Ocean. *J. Geophys. Res.*, 101.

Gille, S. T. (1994). Mean sea-surface height of the Antarctic Circumpolar Current from GEOSAT data – method and application. *J. Geophys. Res.*, 99 :18,255–18,273.

Gille, S. T. (1997). The Southern Ocean Momentum Balance : Evidence for Topographic Effects from Numerical Model Output and Altimeter Data. *J. Phys. Oceanog.*, 27 :2219–2232.

Gille, S. T. (2003a). Float Observations of the Southern Ocean : Part 1, Estimating Mean Fields, Bottom Velocities, and Topographic Steering. *jpo*, 33 :1167–1181.

Gille, S. T. (2003b). Float Observations of the Southern Ocean : Part 2, Eddy fluxes. *jpo*, 33 :1182–1196.

Gille, S. T., Stevens, D. P., Tokmakian, R. T., and Heywood, K. J. (2001). Antarctic Circumpolar Current response to zonally-averaged winds. *J. Geophys. Res.*, 106 :2743–2759.

Gillett, N. and Thompson, D. (2003). Simulation of Recent Southern Hemisphere Climate Change. *Science*, 302 :273–275.

Goodman, J. and Marshall, J. (1999). A model of decadal middle-latitude atmosphere-ocean coupled modes. *J. Clim.*, 12 :621–641.

Gordon, A. (2001). *Ocean, Circulation and Climate*, chapter Interocean Exchange, pages 303–314. Academic Press.

Gordon, A. and Owens, W. (1987). Polar oceans. *Rev. Geophys.*, 25 :227–233.

Gordon, A. L. (1991). *Two stable modes of Southern Ocean winter stratification*, pages 17–35. Elsevier.

Gordon, A. L., Molinelli, E., and Baker, T. (1978). Large-scale relative topography of the Southern Ocean. *J. Geophys. Res.*, 83 :3023–3032.

Gordon, A. L. and Molinelli, E. J. (1982). *Southern Ocean Atlas*. 200 pp., Columbia Univ. Press, New York.

Hall, A. and Visbeck, M. (2002). Synchronous variability in the southern hemisphere atmosphere, sea ice, and ocean resulting from the annular mode. *J. of Climat.*, 15 :3043–3057.

Hallberg, R. and Gnanadesikan, A. (2006). The role of eddies in determining the structure of the wind driven southern hemisphere overturning : results from the modelling eddies in the southern ocean (meso) project. *J. Phys. Oceanog.*, 36 :2232–2252.

Hanawa, K. and Talley, L. (2001). *Ocean circulation and climate*. International Geophysics Series, Academic Press, New York.

Hansen, D. and Poulain, P. (1996). Quality control and interpolation of WOCE/TOGA drifter data. *J. Atm. Ocean. Tech.*, 13 :900–909.

Held, I. and Shneider, T. (1999). The surface branch of the zonally averaged mass transport circulation in the troposphere. *J. Atmos. Sci.*, 56 :1688–1697.

Hirst, A. C. and McDougall, T. J. (1998). Meridional overturning and dianeutral transport in a z-coordinate ocean model including eddy-induced advection . *J. Phys. Oceanog.*, 28 :1205–1223.

Hogg, A. and Blundell, J. (2006). Interdecadal variability of the Southern Ocean. *J. Phys. Oceanog.*, 36 :1626–1644.

Hogg, A., M.P., M., Blundell, J., and Wilson, C. (2007). Eddy heat flux in the Southern Ocean : response to variable wind forcing. *J. of Climat.*, in press.

Hoskins, B. and Karoly, D. (1981). The steady linear response of a sheprical atmosphere to thermal and orographic forcing. *J. Atm. Science*, 38 :1179–1196.

Hughes, C. (2002). Sverdrup-like theories of the Antarctic Cirumpolar Current. *J. Mar. Res.*, 60 :1–17.

Hughes, C. W. and Ash, E. (2001). Eddy forcing of the mean flow in the Southern Ocean. *J. Geophys. Res.*, 106 :2713–2722.

Hughes, C. W., Meredith, M., and Heywood, K. (1999). Wind driven transport fluctuations through Drake Passage : a southern mode. *J. Phys. Oceanog.*, 29 :1971–1992.

Ichikawa, Y. e. a. (2002). Estimation of drifting velocity and error at parking depth for the argo float. Technical report, Argo Technical Report, FY2001.

Iudicone, D., Rodgers, K., R., S., and Madec, G. (2007). An exchange window for the injection of Antarctic Intermediate Water into the South Pacific. *J. Phys. Oceanog.*, 37 :31–49.

Jayne, S. and Marotzke, J. (2002). The oceanic eddy heat transport. *J. Phys. Oceanog.*, 32 :3328–3345.

Johnson, G. C. and Bryden, H. L. (1989). On the size of the Antarctic Circumpolar Current. *Deep Sea Res., Part II*, 36 :39–53.

Johnson, G. C. and Orsi, A. H. (1997). Southwest pacific ocean water-mass changes between 1968/69 and 1990/91. *J Climate*, 10 :306–316.

Karoly, D. (1989). Southern Hemisphere circulation features associated with El-Nino-Southern Oscillation events. *J. of Climat.*, 2 :1239–1252.

Karsten, R. and Marshall, J. (2002). Constructing the residual circulation of the ACC from observations. *J. Phys. Oceanog.*, 32 :3315–3327.

Karstensen, J. and Quadfasel, D. (2002). Formation of Southern hemisphere thermocline waters : water mass conversion and subduction. *J. Phys. Oceanog.*, 32 :3020–3038.

Keffer, T. (1985). The ventilation of the world's oceans : maps of the potential vorticity field. *J. Phys. Oceanog.*, 15 :509–523.

Keffer, T. and Holloway, G. (1988). Estimating southern ocean eddy flux of heat and salt from satellite altimetry. *Nature*, 332 :624–626.

King, B. and Sudheer, J. (4-7 october 2006). Report on second argo delayed mode qc workshop (dmqc-2). Technical report, WHOI.

Kostianoy, A., Ginzburg, A., Frankignoulle, M., and Delille, B. (2004). Fronts in the Southern Indian Ocean as inferred from satellite sea surface sea temperature data. *J. Mar. Res.*, 45 :55–73.

Kox-Kemper, B. and Ferrari, R. (2007). Parametrization of mixed layer eddies. II : prognostic and impact. *J. Phys. Oceanog.*, submitted.

Kushner, P., Held, I., and Delworth, T. (2001). Southern Hemisphere atmospheric circulation response to global warming. *J. of Climat.*, 14 :2238–2249.

Kwok, R. and Comiso, J. (2002). Southern Ocean climate and sea ice anomalies associated with the Southern Oscillation. *J. of Climat.*, 15 :487–501.

LaCasce, J. (2000). Floats and f/h. *J. Mar. Res.*, 58(1).

LaCasce, J. (2007). Lagragian statistics from oceanic and atmospheric observations. *manuscript in preparation.*

LaCasce, J. and Bower, A. (2000). Relative dispersion in the subsurface North Atlantic. *J. Mar. Res.*, 58 :863–894.

Lachlan-Cope, T., Connoley, W., and Turner, J. (2001). The role of the non-axisymmetric Antarctic orography in forcing the observed pattern of variability of the Antarctic climate. *Geophys. Research Letter*, 28 :4111–4114.

Le Traon, P. and Morrow, R. (2001). *Satellite Altimetry and Earth Sciences*, chapter Ocean currents and eddies, pages 171–215. Academic Press.

Le Traon, P., Nadal, F., and Ducet, N. (1998). An improved mapping method of multisatellite altimeter data. *J. Atm. Ocean. Tech.*, 15 :522–534.

Lee, M. and Coward, A. (2003). Eddy mass transport for the southern ocean in an eddy-permittingglobal ocean model. *Ocean Modelling*, 5 :249–266.

Lee, M., Nurser, A., Coward, A., and de Cuevas, B. (2007). Eddy advective and diffusive transports of heat and salt in the Southern Ocean. *J. Phys. Oceanog.*, in press.

Levitus, S. and Boyer, T. (1994). World Ocean Atlas 1994. NOAA Professional Paper, U. S. Dept of Commerce, National Oceanic and Atmospheric Administration, 201 pp.

L'Heureux, M. and Thompson, D. (2005). Observed relationships between the El Nino-Southern Oscillation and the extratropical zonal-mean circulation. *J. of Climat.*, 19 :276–287.

Lombard, A., Cazenave, A., Le Traon, P., Guinehut, S., and Cabanes, C. (2006). Perspectives on present-day sea level change : a tribute to christian le provost. *Ocean Dynamics*, 56 :445–451.

Lovenduski, N. and Gruber, N. (2005). Impact of the Southern Annular Mode on the Southern Ocean circulation and biology. *Geophys. Research Letter*, 32 :1–4.

Luis, A. and Pandey, P. (2004). Seasonal variability of QSCAT-derived wind stress over the Southern Ocean. *Geophys. Research Letter*, 31 :L13304.

Lumpkin, R. and Flament, P. (2001). Lagragian Statistics in the central North Pacific. *J. Mar. Sys.*, 29 :141–155.

Lumpkin, R. and Garraffo, Z. (2005). Evaluating the decomposition of Tropical Atlantic Drifter observations. *J. Atm. Ocean. Tech.*, 22(9) :1403–1415.

Lumpkin, R. and Pazos, M. (2007). Measuring surface currents with Surface Velocity Program drifters : the instruments, its data and some recent results. In *Lagrangian analysis and prediction of coastal and ocean dynamics*. Cambridge University Press.

Lumpkin, R. and Speer, K. (in press). Global ocean meridional overturning. *J. Phys. Oceanog.*

Lumpkin, R., Treguier, A., and Speer, K. (2002). Lagragian Eddy Scales in the Northern Atlantic Ocean. *J. Phys. Oceanog.*, 32 :2425–2440.

MacCready, P. and Quay, P. (2001). Biological export flux in the Southern Ocean estimated from a climatological nitrate budget. *Deep Sea Res., Part II*, 49 :4299–4322.

Marsh, R., Nurser, A., Megann, A., and New, A. (2000). Water mass formation in the Southern Ocean in a global isopycnal coordinate GCM. *J. Phys. Oceanog.*, 30 :1013–1045.

Marshall, D. (1997). Subducting of water masses in an eddying ocean. *J. Mar. Res.*, 55 :201–222.

Marshall, G. (2003). Trends in the southern annular mode from observations and reanalyses. *J. of Climat.*, 16 :4134–4143.

Marshall, G., Stott, P., Turner, J., Connolley, W., King, J., and Lachlan-Cope, T. (2004). Causes of exceptional atmospheric circulation changes in the southern hemisphere. *Geophys. Research Letter*, 31 :L14205.

Marshall, J. and Radko, T. (2003). Residual mean solutions for the Antarctic Circumpolar Current and its associated overturning circulation. *J. Phys. Oceanog.*, 33(11) :2341–2354.

Marshall, J. and Radko, T. (2006). An model of the upper branch of the meridional overturning circulation of the Southern Ocean. *Prog. Ocean.*, 70 :331–345.

Marshall, J., Shuckburgh, E., Jones, H., and Hill, C. (2006). Estimates and implications of surface eddy diffusivity in the Southern ocean derived from tracer transport. *J. Phys. Oceanog.*, 36 :1806–1821.

Marshall, J. and Shutts, G. (1981). A note on rotational and divergent eddy fluxes. *J. Phys. Oceanog.*, 11 :1677–1680.

Masuzawa, J. (1969). Subtropical mode water. *Deep Sea Res., Part II*, 16 :463–472.

McCarthy, M. and Talley, L. (1999). Three-dimentional isoneutral potential vorticity structure in the Indian Ocean. *J. Geophys. Res.*, 104 :13,251–13,267.

McCartney, M. (1977). *Subantarctique Mode Water*. Pergamon Press, Oxford.

McCartney, M. (1982). The subtropical circulation of mode water. *J. Mar. Res.*, 40(suppl.) :427–464.

McCartney, M. and Talley, L. (1982). The subpolar mode water of the north atlantic ocean. *J. Phys. Oceanog.*, 12 :1169–1188.

Mcintosh, P. C. and McDougall, T. J. (1996). Isopycnal Averaging and the Residual Mean Circulation. *J. Phys. Oceanog.*, 26 :1655–1660.

McWilliams, J. C., Holland, W. R., and Chow, J. H. S. (1978). A description of numerical Antarctic Circumpolar Currents. 2 :213–291.

Metzl, N., Tilbrook, B., and Poisson, A. (1999). The annual fCO2 cycle and the air-sea CO2 flux in the sub-Antarctic Ocean. *Tellus*, 51B :849–861.

Molinelli, E. J. (1981). The antarctic influence on antarctic intermediate water. *J. Mar. Res.*, 39 :267–293.

Moore, J., Abbott, M., and Richman, J. (1999). Location and dynamics of the antartic polar front from satellite sea surface temperature data. *J. Geophys. Res.*, 104 :3059–3073.

Morrow, R., Brut, A., and Chaigneau, A. (2003). Seasonal and interannual variations of the upper ocean energetics between Tasmania and Antarctica. *Deep Sea Res., Part II*, 50 :339–356.

Morrow, R., Coleman, R., Church, J., and Chelton, D. (1994). Surface Eddy Momentum Flux and Velocity Variances in the Southern Ocean from GEOSAT Altimetry. *J. Phys. Oceanog.*, 24 :2050–2071.

Morrow, R., Valladeau, G., and Sallee, J. (2007). Observed subsurface signature of Southern Ocean decadal sea level rise. *Prog. Oceanogr.*, in press.

Munk, W. H. and Palmén, E. (1951). Note on dynamics of the Antarctic Circumpolar Current. *Tellus*, 3 :53–55.

Nagata, Y., Michida, Y., and Umimura, Y. (1988). Variations of positions and structures of the ocean fronts in the indian ocean sector of the southern ocean in period from 1965 to 1987. In Salirhage, D., editor, *Antarctic Ocean and Resources Variability*, pages 92–98. Springer-Verlag.

Naveira Garabato, A., Stevens, D., Watson, A., and Roether, W. (2007). Short-circuiting of the overturning circulation in the Antarctic Circumpolar Current. *Nature*, 447 :194–197.

Nowlin, W., Whitworth III, T., and Phillsbury, R. (1977). Structure and transport of the Antarctic Circumpolar Current at Drake Passage from short term measurements. *J. Phys. Oceanog.*, 7 :788–802.

Nowlin, Jr, W. D., Worley, S. J., and Whitworth, III, T. (1985). Methods for making point estimates of eddy heat flux as applied to the antarctic circumpolar current. *J. Geophys. Res.*, 90 :3305–3324.

Oh, I., Zhurbas, V., and Park, W. (2000). Estimating horizontal diffusivity in the east sea (sea of japan) and the northwest pacific from satellite-tracked drifter data. *J. Geophys. Res.*, 105 :6483–6492.

Olbers, D. and Ivchenko, V. (2001). On the meridional circulation and balance of momentum in the Southern Ocean of POP. *Ocean Dynamics*, 52 :79–93.

Olbers, D. (1998). Comment on 'On the obscurantist physics of 'form drag' in theorizing about the Circumpolar Current. *J. Phys. Oceanogr.*, 28 :1647–1654.

Onogi, K., Tsursui, J., Koide, H., Sakamoto, M., Kobayashi, S., Hatsushika, H., Matsumoto, T., Yamasaki, N., Kamahori, H., Takahashi, K., Kadokura, S., Wada, K., Kato, K., Oyama, R., Ose, T., Mannoji, N., and Taira, R. (2007). The JRA-25 reanalysis. *Journ. of Meteo. Soc. Jap.*, 85 :369–432.

Orsi, A., Whitworth III, T., and Nowlin Jr., W. (1995). On the meridional extent and fronts of the Antarctic Circumpolar Current. *Deep Sea Res., Part II*, 42 :641–673.

Owens, W. B. (1984). A synoptic and statistical description of the Gulf Stream and subtropical gyre using SOFAR floats. *J. Phys. Oceanog.*, 14 :104–113.

Park, Y.-H., Charriaud, E., and Fieux, M. (1998). Thermohaline structure of the Antarctic surface water/winter in the Indian sector of the Southern Ocean. *J. Mar. Res.*, 17 :5–23.

Patterson, S. L. (1985). Surface circulation and kinetic energy distribution in the Southern Hemisphere oceans from FGGE drifting buoys. *J. Phys. Oceanog.*, 15 :865–884.

Peterson, R. G. and Stramma, L. (1991). Upper-level circulation in the South Atlantic Ocean. *Progress in Oceanography*, 26 :1–73.

Peterson, R. G. and White, W. B. (1998). Slow oceanic teleconnections linking the Antarctic Circumpolar Wave with the tropical El Nino-Southern Oscillation. *J. Geophys. Res.*, 103 :24573–24583.

Phillips, H. E. and Rintoul, S. R. (2000). Eddy variability and energetics from direct current measurements in the Antarctic Circumpolar Current south of Australia. *J. Phys. Oceanog.*, 30 :3050–3076.

Pickard, G. and Emery, W. (1990). *Descriptive physical oceanography. An introduction.* Pergamon Press.

Piola, A. and Georgi, D. (1982). Circumpolar properties of antarctic intermediate water and subantarctic mode water. *Deep Sea Res., Part II*, 29 :687–711.

Poulain, P. and Niiler, P. (1989). Statistical analysis of the surface circulation in the Califfornian current system using satellite-tracked drifters. *J. Phys. Oceanog.*, 19 :1588–1603.

Qiu, B. (2002). Large scale variability in the midlatitude subtropical and subpolar north pacific ocean : observations and causes. *J. Phys. Oceanog.*, 32 :353–375.

Qiu, B. and Jin, F.-F. (1997). Antarctic circumpolar wave : an indication of ocean-atmosphere coupling in the extratropics. *Geophys. Res. Lett.*, 24 :2585–2588.

Qui, B. (2000). Interannual variability of the Kuroshio Extension system and its impact on the wintertime SST field. *J. Phys. Oceanog.*, 30 :1486–1502.

Reid, J. (1965). Intermediate water of pacific ocean. *John Hopkins Oceanographic Studies*, 2 :85.

Renwick, J. (2002). Southern Hemisphere circulation and relations with sea ice and sea surface temperature. *J. of Climat.*, 15 :3058–3068.

Ribbe, J. (1999). On wind-driven mid-latitude convection in ocean general circulation models. *Tellus*, 51A :505–516.

Ridgway, K., Dunn, J., and Wilkin, J. (2002). Ocean interpolation by four-dimensional weighted least squares : application to the waters around Australasia. *J. Atm. Ocean. Tech.*, 19 :1357–1375.

Rintoul, S. and England, M. (2002). Ekman transport dominates air-sea fluxes in driving variability of subantarctic mode water. *J. Phys. Oceanog.*, 32 :1308–1321.

Rintoul, S., Hughes, C., and Olbers, D. (2001). *Ocean, Circulation and Climate*, chapter The Antarctic Circumpolar Curent system, pages 271–302. Academic Press.

Rintoul, S. and Sokolov, S. (2001). Baroclinic transport variability of the Antarctic Circumpolar Current south of Australia (WOCE repeat section SR3). *J. Geophys. Res.*, 106 :2795–2814.

Rintoul, S. R. and Trull, T. W. (2001). Seasonal evolution of the mixed layer in the Subantarctic Zone south of Australia. *J. Geophys. Res.*, 106 :31,447–31,462.

Rio, M., Schaeffer, P., Hernandez, F., and Lemoine, J. (2005). The estimation of the ocean mean dynamic topography trough the combination of altimetric data, in-situ measurements and grace geoid : from global to regional studies. *Proceedings of the GOCINA international workshop, Luxembourg*.

Roemmich, D., J., G., Davis, R., Sutton, P., Wijffels, S., and Riser, S. (2005). Decadal spin-up of the South Pacific Subtropical gyre. *J. Phys. Oceanog.*, in press.

Rupolo (2007). A lagrangian-based approach for determining trajectories taxonomy and turbulence regimes. *J. Phys. Oceanog.*, 37 :1584–1609.

Sabine, C., Feely, R., Gruber, N., Key, R., Lee, K., Bulister, J., R., W., Wong, C., Wallace, D., Tilbrook, B., Mollinero, F., Peng, T., Kozry, A., Ono, T., and Rios, A. (2004). The oceanic sink for anthropogenic CO_2. *Science*, 305 :367–371.

Sallée, J. and Morrow, R. (2006). Delayed mode salinity quality control of Southern Ocean ARGO floats. Technical report, LEGOS technical report.

Sallée, J., Morrow, R., and Speer, K. (2007a). Response of the Antarctic Circumpolar Current to atmospheric variability. *J. of Climat.*, accepted.

Sallée, J., Morrow, R., and Speer, K. (2007b). Subantarctic Mode Water formation around the circumpolar belt : the role of eddy diffusion. *submitted to Geophys. Research Letter*.

Sallée, J., Morrow, R., Speer, K., and Lumpkin, R. (2007c). An estimate of Lagragian eddy statistics and diffusion in the mixed layer of the Southern Ocean. *submitted to J. Mar. Res.*

Sallée, J., Wienders, N., Morrow, R., and Speer, K. (2006). Formation of Subantarctic mode water in the Southeastern Indian Ocean. *Ocean Dynamics*, 56 :525–542.

Sandwell, D. T. and Zhang, B. (1989). Global mesoscale variability from the geosat exact repeat mission : correlation with ocean depth. *J. Geophys. Res.*, 94 :17971.

Sarmiento, J., Grubber, N., Brzezinski, M., and Dunne, J. (2004). High-latitude controls of thermocline nutrients and low latitude biological productivity. *Nature*, 427 :56–60.

Sarmiento, J. and Orr, J. (1991). Three-dimensional ocean model simulations of the impact of Southern Ocean nutrient depletion on atmospheric CO_2 and ocean chemistry. *Limnol. Oceanogr.*, 36 :1928–1950.

Schodlock, M. P., Tomczak, M., and White, N. (1997). Deep sections through the South Australian Basin and across the Australian–Antarctic Discordance. *Geophys. Res. Lett.*, 24 :2785–2788.

Sen Gupta, A. and England, M. (2006). Coupled Ocean-Atmopshere-Ice response to variations in the Southern Annular Mode. *J. of Climat.*, 19 :4457–4486.

Sen Gupta, A. and England, M. (2007). Coupled Ocean-Atmopshere-Ice feedback in the Southern Annular Mode. *J. of Climat.*, in press.

Shuckburgh, E. F. and Haynes, P. (2003). Diagnosing transport and mixing using a tracer-based coordinate system. *Phys. Fluids*, 15 :3342–3357.

Sinha, B. and Richards, K. (1999). Jet structure and scaling in the Southern Ocean. *J. Phys. Oceanog.*, 29(6) :1143–1155.

Sokolov, S. and Rintoul, S. R. (2002). Structure of Southern Ocean fronts at 140°E. *J. Mar. Syst.*, 37 :151–184.

Sokolov, S. and Rintoul, S. R. (2007). Synoptic mapping of the Southern Ocean fronts and filaments using sea surface height. *J. Phys. Oceanog.*, in press.

Sorensen, J., Ribbe, J., and Shaffer, G. (2001). On Antarctic Intermediate Water mass formation in general circulation models. *J. Phys. Oceanog.*, 31 :77–91.

Speer, K., Gould, J., and LaCasce, J. (1999). Year-long float trajectories in the Labrador Sea Water of the Eastern North Atlantic Ocean. *Deep Sea Res., Part II*, 46 :241–268.

Speer, K., Isemer, H., and Biastach, A. (1995). Water mass formation from revised COADS data. *J. Phys. Oceanog.*, 25 :2444–2457.

Speer, K. G., Rintoul, S. R., and Sloyan, B. M. (2000). The diabatic Deacon cell. *J. Phys. Oceanog.*, 30 :3212–3222.

Stammer, D. (1997). Steric and wind-induced changes in TOPEX/POSEIDON large-scale sea surface topography observations. *J. Geophys. Res.*, 102 :20987 – 21009.

Stammer, D. (1998). On eddy characteristics, eddy transports, and mean flow properties. *J. Phys. Oceanog.*, 28 :727–739.

Stevenson, J. and Niiler, P. (1983). Upper ocean heat budget during the Hawaii to Tahiti Shuttle Experiment. *J. Phys. Oceanog.*, 13 :1894–1907.

Stewart, R., Shum, C., Tapley, B., and Ji, L. (1996). Statistics of geostrophic turbulence in the southern ocean from satellite altimetry and numerical models. *Physica D.*, 98 :599–613.

Stramma, L. (1992). The South Indian Ocean Current. *J. Phys. Oceanog.*, 22 :421–430.

Sudre, J. and Morrow, R. (2007). Global surface currents : a high-resolution product for investigating ocean dynamics. *submitted to Ocean Dynamics.*

Sun, C. and Watts, D. R. (2001). A circumpolar gravest empirical mode for the Southern Ocean hydrography. *J. Geophys. Res.*, 106 :2833–2856.

Sverdrup, H. U. (1947). Wind driven currents in a baroclinic ocean, with application to the equatorial currents in the pacific. *Proc. Nat. Acad. Sci. U. S. A.*, 33 :318–326.

Sverdrup, H. U., Johnson, M. W., and Fleming, R. H. (1942). *The Oceans : their Physics, Chemistry and General Biology.* Prentice-Hall, Englewood Cliffs, N. J.

Sybrandy, A. and Niiler, P. (1991). WOCE/TOGA Lagrangian drifter construction manual. Technical report, Tech. Rep. University of California, San Diego, WOCE Report Number 63, 58 pp.

Taft, B. (1963). Distribution of salinity and disolved oxygen on surfaces of uniform potential specific volume in the South Atlantic, South Pacific and Indian Oceans. *J. Mar. Res.*, 21 :129–146.

Talley, L. (1999). Some aspects of ocean heat transport by the shallow, intermediate and deep overturning circulations. In *Mechanisms of Global Change at Millennial Time Scales*, volume 112, pages 1–22. American Geophysical Union.

Talley, L. D. (1996). Antarctic Intermediate Water in the South Atlantic. In Wefer, G., Berger, W. H., Siedler, G., and Webb, D. J., editors, *The South Atlantic : Present and Past Circulation*, pages 219–238. Springer.

Taylor, G. (1921). Diffusion by continuous movements. *Proc. Lond. Math. Soc.*, 20 :196–212.

Thompson, D. and Solomon, S. (2002). Interpretation of Recent Southern Hemisphere Climate Change. *Science*, 296 :895–899.

Thompson, D. and Wallace, J. (2000). Annular Mode in the Extratropical Circulation. Part I : Month-to-Month Variability. *J. of Climat.*, 13 :1000–1016.

Thompson, D., Wallace, J., and Hegerl, G. (2000). Annular Mode in the Extratropical Circulation. Part II : Trends. *J. of Climat.*, 13 :1018–1036.

Thomson, R. and Fine, I. (2003). Estimating mixed layer depth from oceanic profile data. *jaot*, 20(2) :319–329.

Treguier, A., England, M., and Rintoul, S. (2007). Upper ocean meridional circulation in a numerical model of the Antarctic Circumpolar Current. *submitted to Ocean Science.*

Treguier, A., Held, I., and Larichev, V. (1997). Parameterization of quasigeostrophic eddies in primitive equation ocean model. *J. Phys. Oceanog.*, 27 :567–580.

Treguier, A. M. and McWilliams, J. C. (1990). Topographic influences on wind-driven, stratified flow in a beta-plane channel : an idealized model for the Antarctic Circumpolar Current. *J. Phys. Oceanog.*, 20 :321–343.

Trenberth, K., Large, W., and Olson, J. (1990). The mean annual cycle in global wind stress. *J. Phys. Oceanog.*, 30 :1742–1760.

Tsuchiya, M. (1991). Flow path of the antarctic intermediate water in the western equatorial south pacific ocean. *Deep Sea Res., Part II*, 38(suppl.) :S273–S279.

Turner, J. (2004). The El-Nino Southern Oscillation and Antartica. *Intern. J. of Climat.*, 24 :1–31.

Van Meurs, P. and P.P., N. (1997). Temporal variability of the large-scale geostrophic surface velocity in the northeast pacific. *J. Phys. Oceanog.*, 27 :2288–2297.

Visbeck, M. and Hall, A. (2004). Reply of : Comments on "synchronous variability in the southern hemisphere atmosphere, sea ice, and ocean resulting from the annular mode". *J. of Climat.*, 17 :2255–2258.

Vivier, F., Kelly, K., and Harismendy, M. (2005). Causes of large scale sea level variations in the Southern Ocean : analyses of sea level and a barotropic model. *J. Geophys. Res.*, submitted.

Warren, B. A., J.H., L., and Robbins, P. E. (1996). On the obscurantist physics of 'form drag' in theorizing about the circumpolar current. *J. Phys. Oceanog.*, 26 :2297–2301.

Watts, D. R., Sun, C., and Rintoul, S. R. (2001). A two dimentional gravest empirical modes determined from hydrographic observations in the Subantarctic Front. *J. Phys. Oceanog.*, 31 :2186–2209.

Webb, D. and de Cuevas, B. (2002). An ocean reasonance in the Indian sector of the Southern Ocean. *Geophys. Research Letter*, 29 :1664.

Weisse, R., Mikolawejicz, U., Sterl, A., and Drijfhout, S. S. (1999). Stochastically forced variability in the Antarctic Circumpolar Current. *J. Geophys. Res.*, 104 :11049–11064.

White, W. (2000). Influence of the antarctic circumpolar wave on australia precipitation from 1958-1996. *J. of Climat.*, 13 :2125–2141.

White, W. B. and Cherry, N. J. (1998). Influence of the Antarctic Circumpolar Wave upon New Zealand temperature and precipitation during autumn-winter. *J. Clim.*, 12 :960–976.

White, W. B. and Peterson, R. (1996). An Antarctic Circumpolar Wave in surface pressure, wind, temperature and sea ice extent. *Nature*, 380 :699–702.

Whitworth, I. T. (1983). Monitoring the net transport of the Antarctic Circumpolar Current at Drake Passage. *J. Phys. Oceanog.*, 13 :2045–2057.

Whitworth, I. T. and Peterson, R. (1985). The volume transport of the Antarctic Circumpolar Current from three year bottom pressure measurements. *J. Phys. Oceanog.*, 15 :810–.

Wilkin, J. and Morrow, R. (1994). Eddy kinetic energy and momentum flux in the Southern Ocean : comparison of a global eddy-resolving model with altimeter, drifter, and current-meter data. *J. Geophys. Res.*, 99 :7903–7916.

Witter, D. L. and Chelton, D. B. (1998). Eddy-mean flow interactions induced by modulations of zonal ridge topography in a Quasi-Geostrophic Channel Model. *J. Phys. Oceanog.*, 28 :2019–2039.

Wong, A. (2005). Subantarctic mode water and Antarctic Intermediate Water in the South Indian Ocean based on profiling float data 2000-2004. *J. Mar. Res.*, 63 :789–812.

Wong, A., Bindoff, N., and Church, J. (1999). Large-scale freshening of intermediate waters in the pacific and indian oceans. *Nature*, 400 :440–443.

Wong, A., Johnson, G., and Owens, W. (2003). Delayed-mode calibration of autonomous ctd profiling float salinity data by theta-s climatology. *journal of atmospheric and oceanic technology*, 20 :308–318.

Wust, G. (1935). *The stratosphere of the Atlantic Ocean. Scientific Results of the German Atlantic Expedition of the Research Vessel 'Meteor'*, volume 6. W.J. Emery.

Yuan, X. J., D. G. M. and Dong, Z. Q. (2004). Upper ocean thermohaline structure and its temporal variability in the southeast indian ocean. *dsr2*, 51(2) :333–347.

Zhou, M., Niiler, P., and Hu, J. (2002). Surface currents in the Bransfield and Gerlache Straits, Antarctica. *Deep Sea Res., Part II*, 49 :267–280.

Zhurbas, V. and Oh, I. (2003). Lateral diffusivity and Lagrangian scales in the Pacific Ocean as derived from drifter data. *J. Geophys. Res.*, 108 :10–1/10–10.

Zhurbas, V. and Oh, I. (2004). Drifter-derived maps of lateral diffusivity in the Pacific and Atlantic Oceans in relation to surface ciculation patterns. *J. Geophys. Res.*, 109 :1–10.

Annexe 1 : Delayed mode salinity quality control of the Southern Ocean ARGO floats

Delayed mode salinity quality control of Southern Ocean ARGO floats.

J.B. Sallée*, and R. Morrow*

- LEGOS technical report - 01/2007

24 janvier 2007

*LEGOS, Toulouse, France

1 Introduction

In 1999, to combat the lack of in-situ data needed to monitor the ocean physics and its role in the global climate change, an innovative scientist program was launched by scientists to greatly improve the collection of observations within the ocean interior with better spatial and temporal coverage. This international program known as ARGO aimed to deploy 3,000 free-drifting profiling floats that measure the temperature and salinity over the upper 2000 m of the ocean, with a regular sampling every 10 days. Today, the program is almost reaching its objective and provides an unprecedented array of subsurface casts of the global ocean, which are freely available.

Argo floats are programmed to drift freely at a preset parking depth. They measure temperature, salinity and pressure profiles during each ascent to the sea surface every 10 days. At the sea surface they send their profile information by satellite, and return to their parking depth. The expected lifetime of a float in about 4 years (about 150 cycles due to battery capacity) during which it receives no maintenance. Therefore its very difficult to calibrate their CTD (Conductivity-Temperature-Depth) sensor once deployed in the ocean. The ARGO Science Team (2000) have set the ARGO accuracy target to be 5 dbar for pressure, 0.005 °C for temperature, and 0.01 psu for salinity. Pressure and temperature sensors are robust enough to reach the accuracy target during the whole float life with only an initial calibration before their deployment. However, the conductivity sensors are much more sensitive and reaching the accuracy target of 0.01 psu is a challenge for scientists. Salinity measurements are subject to drifts and offsets due to biofouling (Freeland, 1997), cell contamination (Oka and Ando, 2004 ; Oka, 2005), or other technical problems.

Several method have been attempted to evaluate the performance and correct the errors of the ARGO salinity sensors in the ocean. The only "direct" way is to recover the floats at sea and send them back to the laboratory to directly test their sensors. This method has given valuable results (Oka and Ando, 2004 ; Oka, 2005) but remains rare and costly, and cannot be generalized to the entire ARGO project due to the difficulty and the expensive cost of the recovery float operation.

Another possibility for calibrating the ARGO salinity measurement is to compare nearby measurements of different random ARGO floats. This has showed good results especially where historical data are rare (Durand and Reverdin, 2005 ; Bohme and Send, 2005). However, when differences are found it is difficult to affirm which of the floats are providing the "true" salinity (if one is "true"). Nevertheless, if an ARGO float has been calibrated by another technique, this method can then be applied using the calibrated float as the reference.

The more common method is to compare ARGO measurement with nearby shipboard CTD data. The problem is that shipboard CTD are not available around every ARGO profile. That's why a calibration method based on a local climatology are used. Feng and Wijffels (2001) or Kobayashi et al. (2002) have corrected float salinity using nearby CTD casts obtained in the World Ocean Circulation Experiment (WOCE). Wong et al. (2003 ; hereafter WJO) developed a calibration method that uses an objective mapping based on the World Ocean Database 1998 (WOD98). This method was the first proposed to the ARGO community during the Argo Science Team in 2001 (Argo Science, 2001). After testing the WJO method has been confirmed as effectively having the potential to reach the ARGO salinity target. It has therefore been adopted as the standard method for delayed mode calibration of ARGO salinity sensors at the third ARGO Data Management Meeting in 2002 (Argo Data Management Team, 2002).

Bohme and Send (2005 ; hereafter BS) found that the WJO method failed in highly variable environments and can be substantially improved in regions where the flow is bathymetrically controlled. For example, their new method, largely based on the WJO method, greatly improves the correction in the North Atlantic Ocean. Their method was presented for the first time to the ARGO community during the 4th meeting of the International ARGO Data Management in 2003 (Argo Data Management Team, 2003). Faced with the great improvement brought by the BS technique, in 2005, the ARGO community charged B.Owens and A.Wong with merging the two methods (WJO and BS) in a new correction product.

This merged correction method is now freely available[1] and provides good correction in the most parts of the world ocean (hereafter this method will be mentioned as BWC). However, the density of the reference database remains a key point of this method (Kobayashi and Minato, 2005). When these algorithms are applied to floats drifting in regions with very sparse historical CTD data such as the Southern Ocean, the existing methods give either large errors or no estimated correction. Errors are also increased when float data are close to strong hydrological fronts such as the Subantarctic Front (SAF) in the Southern Ocean. The SAF is associated with strong changes in hydrological characteristics and water mass structure. Since the salinity algorithms are compared to historical in-situ data within a certain radius (the basic influence bulb) it can choose historic profiles from each side of the SAF and mix them in the objective analysis, resulting in large salinity correction errors (see Figure 1). Since Lagrangian floats often converge towards hydrological fronts, this is a real issue for correcting Southern Ocean ARGO data.

Due to the specific problems in the Southern Ocean, we propose to improve the existing OWC calibration method. Our technique to improve the salinity correction in the Southern Ocean is based on a better choice of historical data profiles. The improvement are made in two ways : 1) by improving the number of historical data profiles available, and 2) by improving the choice of profiles close to the main polar fronts. We will finally test our calibration method on the 30 floats deployed during the FLOSTRAL program.

[1] http ://prelude.ocean.washington.edu/references.html

2 Original calibration algorithm

Since the beginning of the ARGO program the ARGO Data Management Team (ADMT) have promoted the homogenisation of the delayed-mode salinity correction. Wong et al (2003) (hereafter WJO) has provided to the community a robust correction based on statistics and easily adaptable to different region of the world. Thus, it has been being a reference calibration in the ARGO community on which PIs and regional experts have been adding their own algorithms developed more specifically for one part of the globe.

WJO 's algorithm use climatological potential temperature and salinity (θ /S) relationships and their variability to estimate errors on ARGO salinity measurements. Their algorithm can be summarized by several key points :

- Based on the regional hydrography, WJO start by choosing θ -levels which are evenly distributed in the water column.
- The mapping scheme is constrained by a set of spatial decorrelation scales and a temporal decorrelation scale. Anisotropic large spatial scales : Lx and Ly can be introduced, which reflect the regional water mass variability. To include the meso-scale variability of the basin they also define small-spatial scales. The temporal scale is representative of the ventilation time-scale.
- A set of 600 historic profiles are selected from the World Ocean Database (1998) (WOD98) for the mapping. The selection of these best historical points is based on three criteria : that they provide a good representation of the large scale mean around the profile, they include the closest profiles (in a spatial sense) and they include profiles with the best spatial-temporal separation factor relative to the small length scales and the temporal scale.
- At each level, WJO map the salinity from the historical set onto the ARGO float location. The mapping is done in a two-step manner based on Roemmich et al. (1983) and by assuming the covariance of the data to be Gaussian. It provides a first estimate of the mapping by considering the covariance function to be function of the large-scale spatial separation, and the Gaussian decay scale to be determinated by the large spatial scales. In the second stage, the residuals from the first stage are mapped using a covariance function based on the temporal separation and the small-scale spatial separation.
- Finally, they find a unique multiplicative correction for the entire profile by a weighted least square fit to all of the correction at each level. For this last point, they work with the potential conductivity instead of the salinity. This conversion has two great advantages. First, potential conductivity is not affected by pressure, hence all of the conductivity measurements at different level are easily comparable. The second advantage is that an error in salinity is represented by an additive correction, whereas the same error in potential conductivity is translated by a multiplicative correction, hence the problem is easier to solve by considering the potential conductivity.

In most part of the world ocean this method provides good calibration and allow us to reach the accuracy target of 0.01 psu. However, this reference algorithm does not provide well constrained salinities in regions where the water column is weakly stratified, highly variable, or exhibiting multiple temperature inversion. Bohme and Send (2005) (hereafter BS) have then developed an algorithm specifically adapted for these circumstances. Their algorithm is very close to the WJO technique. However, they introduced mainly two big differences :

- First, they change the selection of the θ -levels. In WJO the levels are a-priori chosen by considering the local hydrography. But in a highly variable environment the water mass structure can change, so that the best levels selected at one time can be different from the best levels that should have been selected at another time. BS resolved this problem by automatically selecting 10 "best" depth levels which are based on the float measurement. They then use the potential temperature at those 10 depth levels as the set of θ surfaces.
- They also defined a generalized distance following the idea of Davis (1998). The idea is introduce into the mapping the fact that in a bathymetrically constrained flow, two profiles with a closer planetary vorticity (f/H) are likely to have a more similar water mass structures. Thus they include planetary vorticity as a weighting factor in their covariance function to account for the cross-isobath separation in the bathymetrically constrained flows. This new scale is used in the same way as the spatial scales, hence BS have defined small and large cross-isobath scales.

This method yields strongly reduced errors compared to WJO for the mapped reference salinities in highly variable environments such as the North Atlantic Ocean. As such, this algorithm has quickly became a reference calibration process for ARGO PIs.

Recently Owens, Wong, and Campion (2006) (hereafter OWC) have developed a new algorithm which merge the objective mapping schemes of WJO, BS, and some new features. Potential vorticity has been added as an optional weighting function that can be switched on and off by users depending on which basin they work in. They have also updated the historical database from WOD98 to the WOCE Ocean Database 2001 (WOD01). The total number of reference stations used in the mapping has become variable, input as a user parameter. The selection of the θ -levels is made as in the BS technique. The 10 levels are : the shallowest and deepest P levels (2 levels), the minimum and maximum in θ and S on P levels (4 levels), the minimum θ and S variance on P levels (2 levels), and the minimum P and S variance on θ -levels (2 levels).
Finally, for each float, the correction is adjusted by an optimal piecewise linear fitting looking a-posteriori at the entire correction time-series to find consistent offsets and drifts. The method has been made freely available on http ://prelude.ocean.washington.edu/references.html. Further details on this algorithm can be found on the same website.

3 Historical data density

The calibration technique developed by B.Owens and A.Wong uses WOD01 for their historical data base, which includes 6646 profiles South of 25°S after processing. Our technique uses the WOCE Southern Ocean Data Base (SODB), which has been quality checked and made freely available by Orsi, A. H., and T. Whitworth III in 2005[2]. This dataset consists of about 93,000 hydrographic (bottle and ctd) stations south of 25S. We have applied to this dataset the same processing steps defined by B.Owens and A.Wong for the WOD2001 data, i.e :

1. We only used casts that sampled deeper than 900 dbar.

2. We weeded out all data points outside these ranges : $24 < S < 40$, $0.01 < P < 9999$, $0.01 < T < 40$, except for profiles located north of 60°N or south of 50°S, where $-2 < T < 40$ was used.

3. We eliminated nearby duplicates, i.e. profiles closer than 1 minute for latitude and longitude and 1 day for time. Stations with the most levels were kept.

After this processing, we have a final total of 31,582 historical profiles South of 25 °S. In addition to increasing the total number of profiles by more than 475 %, we note that the SODB also provides a broader spatial coverage of the Southern Ocean (see Figure 2).

Figure 3 shows the differences in the corrected salinity when either WOD or SODB is used in the objective analysis. The salinity corrected with the WOD dataset are completely unrealistic and so no correction would be performed. Applying the same correction method but using the SODB historical data provides a more acceptable corrected salinity.

[2]http ://wocesoatlas.tamu.edu/

4 Hydrological front issue

Improving the data density is not enough. Lets consider one profile from cycle 21 of the previous ARGO float (1900042) when it passes through the frontal interleaving region. Even when using the improved SODB database, we see that the automatic choice of selecting historical profiles within the influence bulb around the ARGO profile mixes data from very different water masses (see Figure 5a). In fact we recognize two different groups of profiles : warm, salty profiles typical from north of the SAF and fresh, cold profiles from south of the front. Since the ARGO profile (cycle 21) is typically from south of the SAF we choose to only select historic profiles from south of the SAF to improve the salinity correction.

How do we detect whether the historic profiles are north or south of a given front ? Sallée et al. (2006) have developed an automatic method to detect time evolution of the SAF positions, using contours of altimetric SSH. This allows us to calculate the distance of the ARGO float position with respect to the SAF localized by their method. This distance is then compared to the temperature at 300m depth from historic profiles (SODB and Argo) sampled during the altimetric years from 1992 to 2005. The two parameters provide a tight relation (see Figure 4a) and allow us to define a robust criterion to detect whether a profile is north or south of the SAF. This criterion is consistent around the circumpolar path. Hence we divided the Southern Ocean in three areas : (i) North of the SAF where $T_{300m} > 5°C$; (ii) South of SAF where $T_{300m} < 3°C$; and (iii) the "frontal zone" where 3 °C $\geq T_{300m} \geq 5°C$.

The frontal zone still needs particular processing, and we have added a second criterion for profiles localized in the "frontal zone" region.
Again, we use all of the WOCE historic data available during the altimetric years and localize these data with respect to the SAF, and then calculate a typical T/S profile envelope from south of the SAF, and a typical T/S profile envelope from north of the front (see Figure 4b). Hence all of the profiles which fall into the "frontal zone" in the first phase are then tested to see whether they lie inside the Southern or the Northern envelope (the envelope is defined by the mean T/S profile plus or minus the standard deviation). If the ARGO profile can't be localized after these two steps we use all of the historic profiles, as in the basic method.

This "front detection" is used as a pre-selection of the historical data in the OWC 's method. We select the best historical casts for the calibration from a subset of historical data that have passed the front criterion step.

An example of the results obtained by adding this step is given in Figure 5b. It shows the selection of historic profiles when we use the two step front criterion method. Clearly for profiles close to the SAF the two-step method provides a better representation of the water mass structure observed by ARGO.

Another striking example of the improvement made by the frontal criterion is given for the float WMO 1900314. This float flows in the Fawn Trough Current, south of the Kerguelen Plateau, in a very poorly sampled area and near the ACC frontal structure. Figure 6a show the uncalibrated profile of this float and a OISO/FLOSTRAL CTD profile sampled at the location and date of the

first cycle of the float. There is a net offset between the pack of initial ARGO profiles and the CTD profile. The classical OWC correction with the SAD2001 historical database proposes an unrealistic correction (Figure 6b). The mapped salinities are clearly affected by the lack of data in the region and give absurd results. When applying the same method with the denser database SODB2005, we obtain a much more coherent result (Figure 6c). However the result proposed by this method "spread" the hydrological characteristics in the bottom of the profile (saltiest and coldest part of the profiles). In the bottom of the water column the hydrological characteristics are very stable and we expect to observe the same characteristics for all of the bottom calibrated profiles, as measured by the uncalibrated data. This "spreading" is probably due to a comparison with historical data on the other side of the front. Even without this clue we would reject the proposed correction since it does not match the CTD control profile. We now apply the method with frontal criterion and the SODB2005 historical database. The result in Figure 6d clearly show an improvement of the correction. The stable characteristic at the bottom of the water column is respected and the first cycle perfectly match the WOCE control profile. We consider then to have reached a satisfying correction that detects the offset of the float.

5 FLOSTRAL project floats

We have tested this improved correction method for the 30 floats which were deployed as part of the FLOSTRAL project. The FLOSTRAL project is a french contribution to the ARGO project in the Southern Ocean. 30 PROVOR floats were deployed in 2003 and 2004. The first 20 sensors were FSI sensors with known problems of offset and drift. At the time of the first deployments of the program these problems were unknown. For the second series of deployments the scientific community were aware of the problems and more floats were equipped with SEABIRD sensors.
In this section we list remarks associated with the corrections made for each profile of the FLOSTRAL project. These corrections have been transferred to the CORIOLIS DAC and GDAC center and are thus available as the delayed-mode correction data on their website[3]. Table 1 summarizes information on these 30 floats. Figure 7 show the trajectories of each float.

WMO 1900123

The calibration method has detected a drift of the salinity sensor. Based on the knowledge of the area sampled we accept this drift as a sensor problem and then accept the calibration of the method.

WMO 1900124

No salinity profile passed the real time test (flag > 2).

WMO 1900125

The calibration method has detected a drift of the salinity sensor. Based on the knowledge of the area sampled we accept this drift as a sensor problem and then accept the calibration of the method.

WMO 1900126

The uncalibrated data are in good agreement with the historical knowledge of the area. We validate the sampled salinity of this float. The associated error is the typical instrumental (FSI) error : 0.01 psu.

WMO 1900127

No salinity profile passed the real time test (flag>2).

[3] www.coriolis.eu.org

WMO 1900128

The calibration method has detected an offset of approximately 0.1 psu. The proposition of correction is in good agreement with the hydrology of the area. We accepted then the calibration of the method. The associated error is approximately 0.04 psu.

WMO 1900129

The uncalibrated data are in good agreement with the historical knowledge of the area. However, profiles sampled after the 80th cycle are found to be wrong. We keep the original data and flag the profiles after the 80th cycle as wrong (flag 4). The associated error is the typical instrumental (FSI) error : 0.01 psu.

WMO 1900130

No salinity profile passed the real time test (flag>2).

WMO 1900131

Only 7 salinity profiles passed the real time test (flag>2). There is to few data to be able to correct the float with confidence. We don't provide delayed time quality control for this float.

WMO 1900132

No salinity profile passed the real time test (flag>2).

WMO 1900133

The calibration method has detected a drift which is well corrected. Considering the historical data and our knowledge of the sampled basin we considered this drift. We accepted then the calibration of the method. However profiles between the cycle 17 and 20 are very noisy in salinity and have been considered as wrong (flag 4).

WMO 1900224

The calibration method has detected an offset of approximately 0.1 psu. The proposition of correction is in good agreement with the hydrology of the area. We accepted then the calibration of the method. The associated error is approximately 0.03 psu.

WMO 1900312

The uncalibrated data are in good agreement with the historical knowledge of the area. However, some profiles around the cycle 42 are found to be very noisy in salinity. We keep the original data and flag the profiles around the cycle 42 as wrong (flag 4). The associated error is the typical instrumental (FSI) error : 0.01 psu.

WMO 1900313

The uncalibrated data are in good agreement with the historical knowledge of the area. We validate the sampled salinity as good. The associated error is the typical instrumental (FSI) error : 0.01 psu.

WMO 1900314

The calibration method shows an offset and corrects it. The WOCE control profile sampled at the location and date of the first cycle (by the OISO project team) confirm the coherence of the calibration proposed. We accept the calibration proposed by the method.

WMO 1900315

A strong offset is detected by the method. The offset is corrected by the method and has been validated as good by the P.I. who based his analysis on historical knowledge of the basin. However, the first 15 profiles are very noisy in salinity and thus are flagged as wrong data (flag 4). The error associated with the calibration of this float is approximately 0.027 psu.

WMO 1900316

The uncalibrated data are in good agreement with the historical knowledge of the area. No problem have been detected for this float. We validate the sampled salinity. The associated error is the typical instrumental (SEABIRD) error : 0.005 psu.

WMO 1900317

The uncalibrated data are in good agreement with the historical knowledge of the area. The calibration method proposed an offset considered as unreal by the experts of the area. We validate the sampled salinity. The associated error is the typical instrumental (SEABIRD) error : 0.005 psu.

WMO 1900318

The uncalibrated data are in good agreement with the historical knowledge of the area. The profiles show strong noise that have been interpreted as physically meaningful interleaving based

on the knowledge of the area. We validate the sampled salinity. The associated error is the typical instrumental (SEABIRD) error : 0.005 psu.

WMO 1900319

The calibration method proposes to correct a small drift in the salinity. This drift have been considered has a physically realistic salinity drift in the ocean based on the studies of Bryden et al. (2003) and Toole and Warren (1993). Thus the drift is not corrected and we validate the sampled salinity. The associated error is the typical instrumental (SEABIRD) error : 0.005 psu.

WMO 1900320-1900324

The uncalibrated data are in good agreement with the historical knowledge of the area. We validate the sampled salinity of these 5 floats. The associated error is the typical instrumental (SEABIRD) error : 0.005 psu.

WMO 1900325

The uncalibrated data are in good agreement with the historical knowledge of the area. We validate the sampled salinity except for the first profile which is extremely noisy. The first profile is flagged as a bad profile (flag 4). The associated error of the other profiles is the typical instrumental (SEABIRD) error : 0.005 psu.

WMO 1900134-1900137

A similar offset have been found in each of these 4 floats that sampled approximately the same area. The uncalibrated profiles show Intermediate Water (IW) at a salinity of approximately 34.3 psu although the historical data show them around a salinity of 34.4 psu. Previous studies (e.g. Toole and Warren, 1993) found also IW at a salinity of 34.4 psu in this area. We also compared this data with another float (WMO 1900321) sampling in the same period of time in the same basin. The uncalibrated profiles of this float have already been validated without any problem raised and show IW at 34.4 psu. This last test puts into question any possible freshening of the IW and give us confidence to correct the offset detected by the calibration method. We accept the correction of the method for each of these float.

5 FLOSTRAL project floats

WMO ID	Lat	Lon	Total Profiles (profiles that passes the RT test - qcflag¿2)	type of sensor	Controlled by the original algorithm	Controlled by the new algorithm
1900123	-27.7/-25.2	50.7/57.3	63(55)	CTF2	•	•
1900124	-28/-18.4	38.5/54.5	76(0)	CTF2	-	-
1900125	-30.1/-27.3	52.9/60.5	99(47)	CTF2	•	•
1900126	-36.6/-27.9	31.4/52.8	33(28)	CTF2	-	•
1900127	-38.9/-31.3	43.9/53.6	102(0)	CTF2	-	•
1900128	-42.9/-38.2	51.1/70.3	17(11)	CTF2	•	•
1900129	-44.3/-36.9	48.9/63.3	91(85)	CTF2	•	•
1900130	-43/-36.8	53.2/68.8	95(0)	CTF2	-	-
1900131	-47.9/-45.4	60.4/68.2	13(7)	CTF2	-	-
1900132	-44.1/-35.1	76.3/98.9	97(4)	CTF2	-	-
1900133	-41.6/-33.2	73/77.5	109(99)	CTF2	-	•
1900134	-35.9/-26.2	55.6/81.2	52(25)	CTF2	-	•
1900135	-36/-29.8	73.9/81.2	108(28)	CTF2	•	•
1900136	-37.2/-32.8	69.4/89.5	59(29)	CTF2	•	•
1900137	-37.2/-34.5	82/86.9	101(58)	CTF2	-	•
1900224	-33.8/-22.3	34.3/42.8	72(41)	CTF2-3.A	-	•
1900312	-36.9/-32.1	37.6/46.2	72(72)	CTF2-3.A	-	•
1900313	-45.1/-38.4	42.6/60.8	41(41)	CTF2-3.A	-	•
1900314	-57.6/-50.9	62.3/86.8	67(66)	CTF2-3.A	-	•
1900315	-40.8/-36.6	50.6/65.6	66(64)	CTF2-3.A	-	•
1900316	-38.1/-31.7	17.9/62.3	71(67)	CTS2-4.1	-	•
1900317	-37.4/-33.3	59.7/64.5	70(66)	CTS2-4.1	•	•
1900318	-33.2/-26.4	40.8/59.4	71(68)	CTS2-4.1	-	•
1900319	-31/-27.7	54.7/59.4	55(51)	CTS2-4.1	•	•
1900320	-27.3/-24	48.7/57.6	71(68)	CTS2-4.1	-	•
1900321	-46/-35	69.1/119.5	65(65)	CTS2-4.1	-	•
1900322	-39.7/-35.6	67.3/74.1	65(65)	CTS2-4.1	•	•
1900323	-36.7/-29.1	41.3/66.4	57(56)	CTS2-4.1	-	•
1900324	-31.3/-29.7	65/66.9	35(34)	CTS2-4.1	-	•
1900325	-24.5/-21.3	57.2/60.3	65(65)	CTS2-4.1	•	•

Tab. 1 – FLOSTRAL floats

6 Conclusion

These new salinity correction techniques are giving promising results for correcting Southern Ocean ARGO profiles. The technique can also be applied in other regions with strong frontal conditions, as long as reliable frontal criteria can be derived based on the temperature structure. Work is underway to continue validating the technique in different circumpolar regions, with the aim of making the algorithms available for the international community.

Références

Argo Data Management Team (2002). Report of the argo data management meeting. argo data management 3rd meeting, 18-20 september 2002. Technical report, Marine Environmental Data Service, Ottawa, Canada.

Argo Data Management Team (2003). Report of the argo data management meeting. argo data management 4th meeting, 5-7 november 2003. Technical report, Monterey, California, USA.

Argo Science Team (2000). Report of the argo science team 2nd meeting, 7-9 march 2000. Technical report, Southampton Oceanography Centre, Southampton, U.K.

Argo Science Team (2001). Report of the argo science team 3rd meeting, 20-22 march 2001. Technical report, Institute of Ocean Sciences, Sidney, B.C., Canada.

Bohme, L. and Send, U. (2005). Objective analyses of hydrographic data for referencing profiling float salinities in highly variable environments. *Deep-Sea Research*, 52/3-4 :651–664.

Bryden, H., McDonagh, A., and A., K. B. (2003). Changes in ocean water mass properties : oscillations or trends ? *Science*, 300 :2086–2088.

Davis, R. (1998). Preliminary results from directly measured mid depth circulation in the tropical and South Pacific. *J. Geophys. Res.*, 103 :24619–24639.

Durand, F. and Reverdin, G. (2004). A statistical method for correcting salinity observations from autonomous profiling floats : an argo perspective. *journal of atmospheric and oceanic technology*, 22 :292–301.

Feng, M. and Wijffels, S. (2001). Results from a pilot argo float program in the southeastern indian ocean.the scientific and technical workshop of the data buoy cooperation panel. Technical report, Perth, Australia.

Freeland, H. (1997). Calibration of the conductivity cells on P-ALACE floats. *US WOCE Implementation Report, No.9, 37-38.*, No.9 :37–38.

Kobayashi, T., Ichikawa, Y., Takatsuki, Y., Suga, T., Iwasaka, N., Ando, K., Mizuno, K., Shikama, N., and Takeuchi, K. (2002). Quality control of argo data based on high quality climatological dataset (hydrobase). Technical report, ARGO Technical Report FY2001, Japan Marine Science and Technology Center.

Kobayashi, T. and Minato, S. (2005). Importance of reference dataset improvements for argo delayed-mode quality control. *J. of Oceanog.*, revised.

Oka, E. (2005). Long-term sensor drift found in recovered ARGO profiling floats. *J. of Oceanog.*, 61 :775–781.

Oka, E. and Ando, K. (2004). Stability of temperature and condictivity sensors of ARGO profiling floats. *J. of Oceanog.*, 60 :253–258.

Roemmich, D. (1983). Optimal estimation of hydrographic station data and derived fields. *J. Phys. Oceanog.*, 13 :1544–1549.

Sallée, J., Morrow, R., and Speer, K. (2006). Southern ocean fronts and their variability to climate modes. *submitted to J. of Climat.*

Toole, J. and Warren, B. (1993). A hydrographic section across the subtropical south indian ocean. *DSR*, 40 :1973–2019.

Wong, A., Johnson, G., and Owens, W. (2003). Delayed-mode calibration of autonomous ctd profiling float salinity data by theta-s climatology. *journal of atmospheric and oceanic technology*, 20 :308–318.

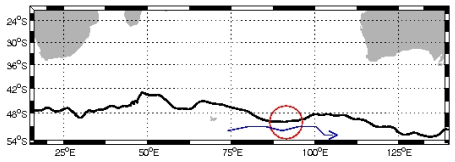

FIG. 1 – Mean position of the SAF in the Southern Indian Ocean (black line) from Sallée et al. (2006). The basic influence bulb (red circle) for a drifting ARGO float (blue line) which is close to the SAF can include historic profiles from either side of the front.

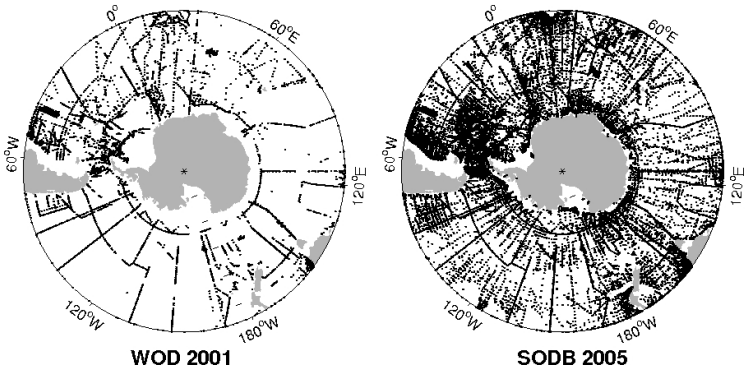

FIG. 2 – Spatial distribution of historical data from WOD2001 (left) and SODB2005 (right) in the Southern Ocean after the same database treatment is applied following Wong et al (2006)

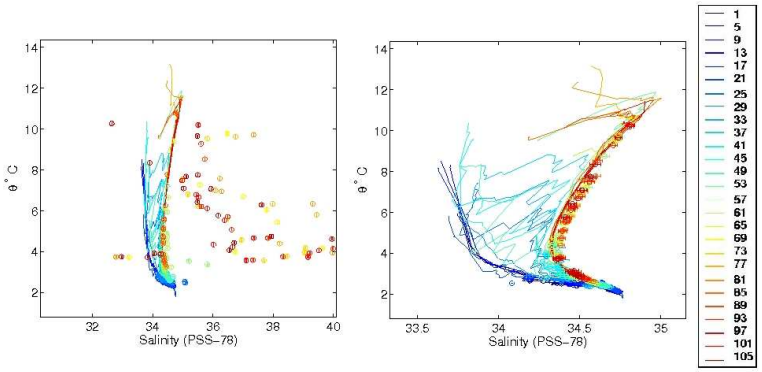

FIG. 3 – Uncalibrated $\theta - S$ profiles for float $n\circ$ 1900042 (solid lines) compared with the estimated salinity correction from the objective analysis along theta levels for each profile (circles). Left panel : correction based on WOD2001 historical database ; right panel : SODB2005 historical database. The colours show the time evolution from cycle 1 (blue) to cycle 108 (red) three years later. The float starts south of the SAF (cold fresh profiles) and moves north of the front (warm, salty profiles) passing through the frontal region with strong interleaving.

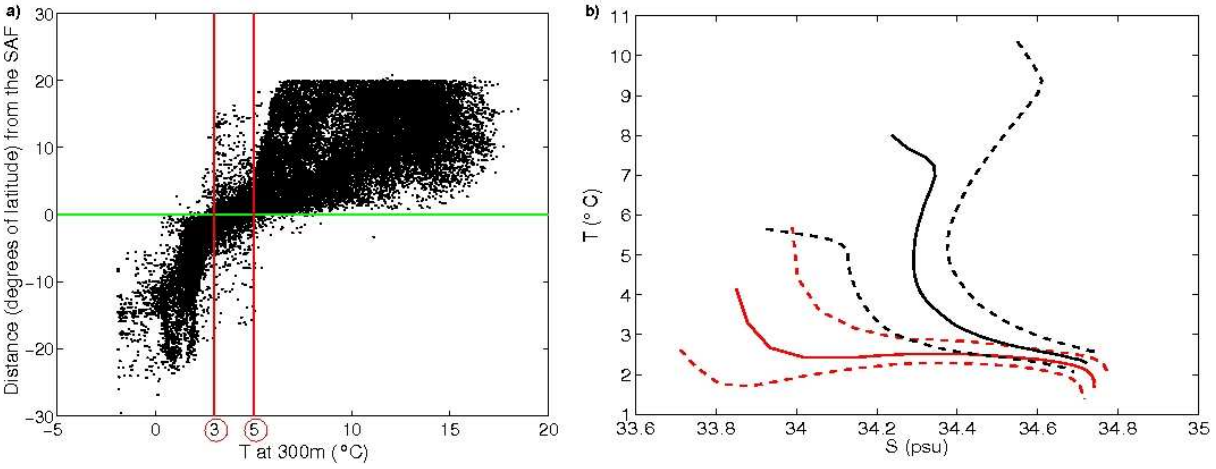

FIG. 4 – (a) Temperature at 300m depth versus the distance from the SAF. Temperature data are from all of the SODB2005 and ARGO profiles available during the altimetric years (1992-2005). The SAF location is found following the Sallée et al. (2006)'s altimetric method. A positive (negative) distance means the profile is north (south) of the SAF.
(b) Mean T/S profile from south of the SAF (solid red line) with its standard deviation (dashed red line) ; mean T/S profile from north of the SAF (solid black line) plus standard deviation (dashed black line), derived from all SODB2005 profiles available during the altimetric years. The SAF location is found following the Sallée et al. (2006) altimetric method.

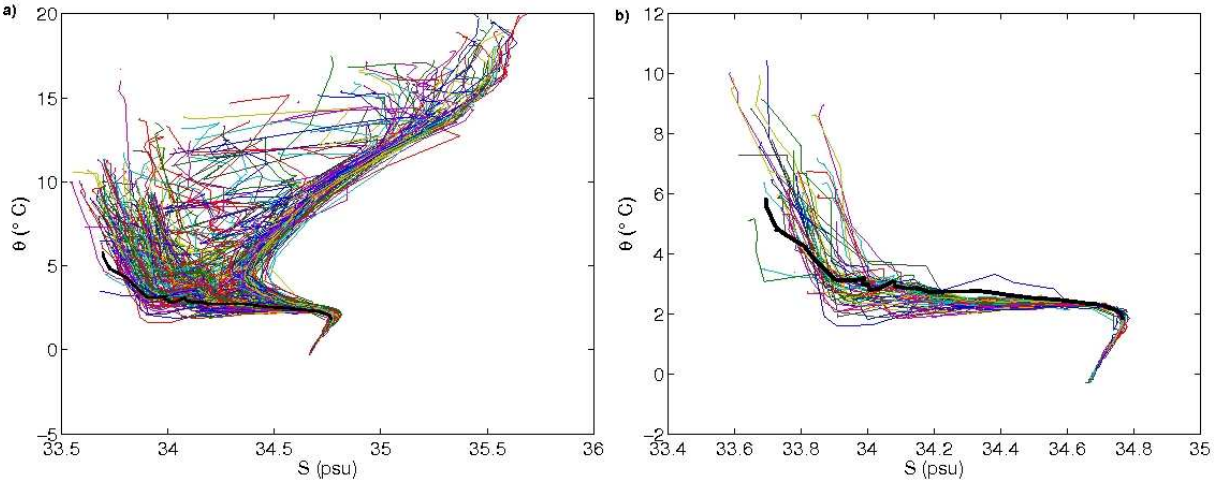

FIG. 5 – Choice of historical profiles used to calibrate cycle 21 of float 1900042. The 21th $\theta - S$ profile sampled by the Argo float 1900042 is superimposed (bold black). (a) SODB2005 historic profiles selected without using the front criterion method. (b) SODB2005 historic profiles selected using the front criterion method

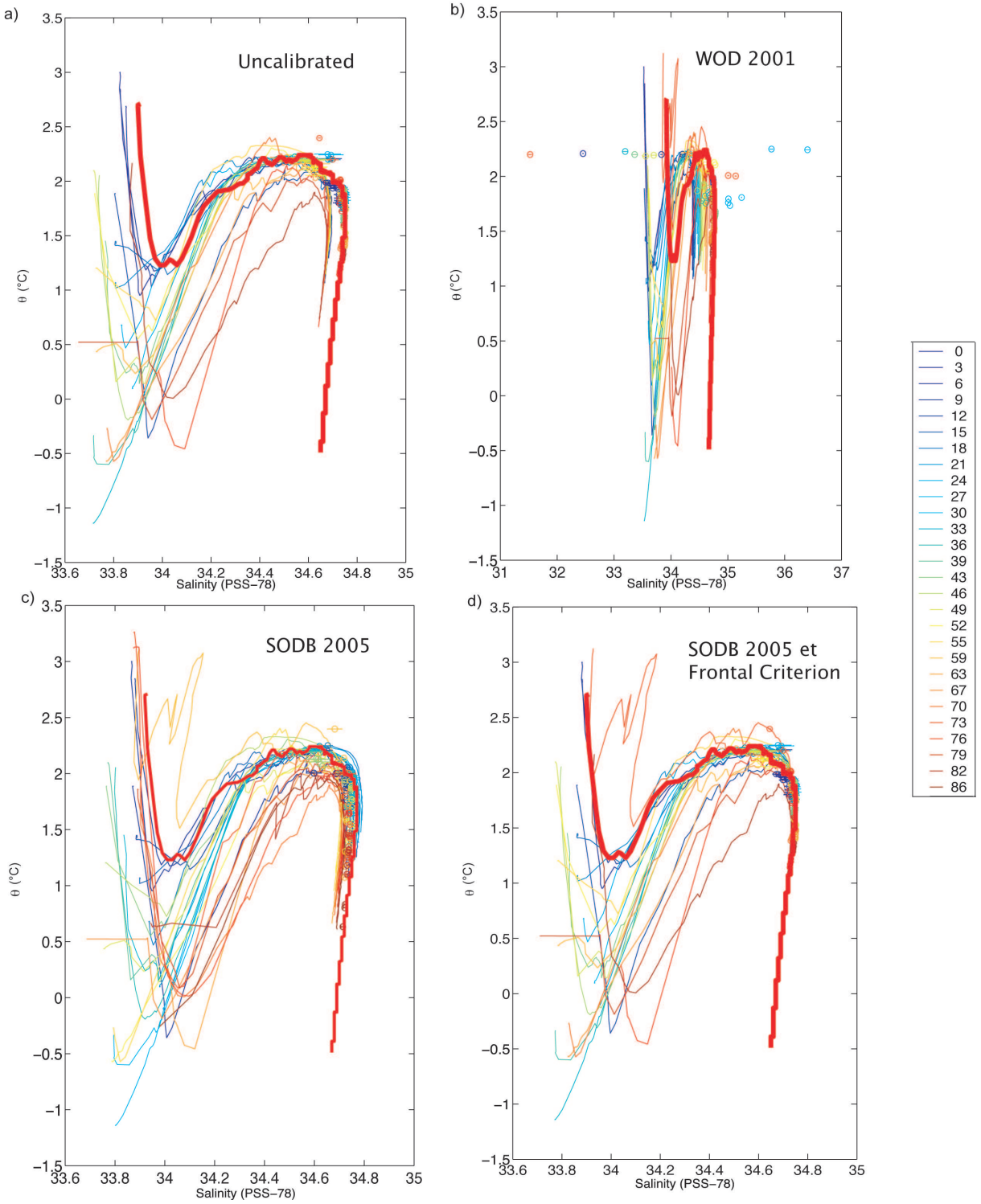

FIG. 6 – $\theta - S$ profiles for float $n\circ$ 1900314 (solid lines) compared with the estimated salinity correction from the objective analysis along theta levels for each profile (circles). The number of cycle of each profile is showned by color. The red bold line represents the CTD profiles sampled at the location and date of the first cycle of the float.**a)** show the uncalibrated profiles.**b)** show the calibrated profiles when using the WOD2001 historical database without the frontal criterion.**c)** show the calibrated profiles when using the SODB2005 historical database without the frontal criterion.**d)** show the calibrated profiles when using the SODB2005 historical database with the frontal criterion.

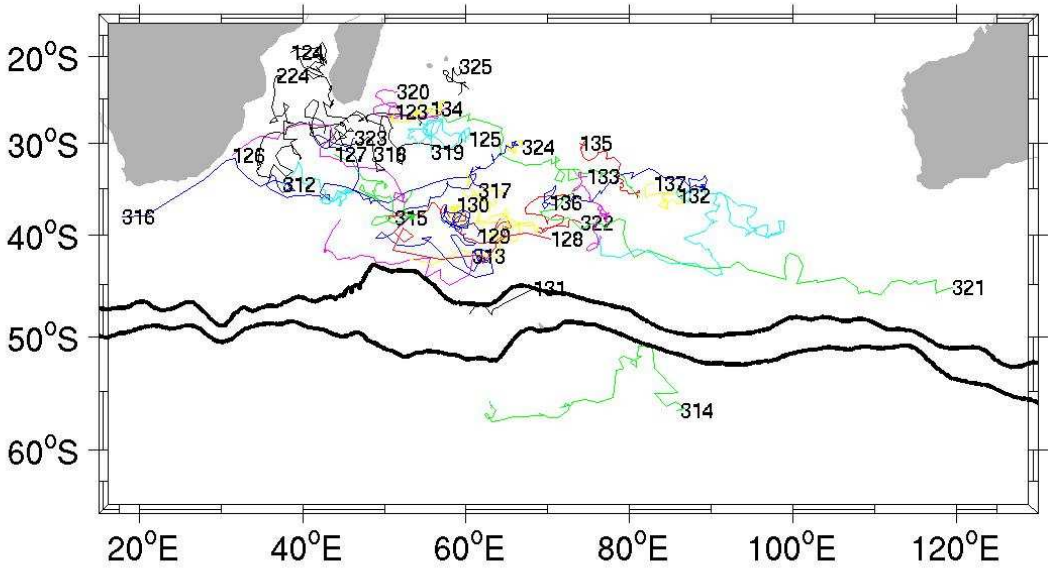

FIG. 7 – Flostral floats trajectories

Annexe 2 :

Observed subsurface signature of Southern Ocean sea level rise

Rosemary Morrow, Guillaume Valladeau and Jean-Baptiste Sallee

LEGOS/OMP, 18 av. Edouard Belin, 31401 Toulouse Cedex 9 FRANCE

Corresponding author : Rosemary.Morrow@cnes.fr

Version : Jan 2007
Revised version for Progress in Oceanography

Abstract

Satellite altimetry data show a strong increase in sea level in various parts of the Southern Ocean over the 1990s. In this paper we examine the causes of the observed sea level rise in the region south of Australia, using 13 years of repeat hydrographic data from the WOCE-SR3 sections, and the SURVOSTRAL XBT and surface salinity data. The hydrographic data show a poleward shift in the position of the Subtropical and the Subantarctic Fronts over the period. In the Antarctic Zone, the Antarctic Surface Water has become warmer and fresher, and the Winter Water tongue has become warmer, fresher, thinner and shallower. Increased freshening south of the Polar Front is linked to increased precipitation over the 1990s. Temperature changes over the upper 500 m account for only part of the altimetric sea level rise. The CTD sections show that the deeper layers are also warmer and slightly saltier and the observed sea level can be explained by steric expansion over the upper 2000 m. ENSO variability impacts on the northern part of the section, and a simple Sverdrup transport model shows how large-scale changes in the wind-forcing, related to the Southern Annular Mode, may contribute to the deeper warming to the south.

Keywords : Southern Ocean, fronts, sea level, climate modes.

Table of Contents

1. Introduction

Recent studies on global sea level rise based on Topex-Poseidon satellite altimetry data have noted a strong increase in sea level in various parts of the Southern Ocean (Figure 1a) over the period 1993-2003 (Lombard et al., 2005, Willis et al., 2004). The dynamical processes governing the sea level rise are not well understood. Different authors have calculated the steric expansion in the upper 700 m from global in-situ data (Guinehut et al., 2004; Willis et al., 2004; Ishii et al., 2005) and found that it explains only 50-60% of the observed global sea level rise (Figure 1b). They attribute the other 40-50% to ocean mass changes.

The difference between the TOPEX altimetric sea level rise and the steric expansion over the upper 700 m depth is shown in Figure 1c. The largest differences occur in the Southern Ocean. The difference is sea level rise could be due to the barotropic response to variations in the wind forcing (e.g. Vivier et al., 1999), or to warming or freshening at deeper levels.

Roemmich et al. (2006) have studied the dynamical processes which cause the strong sea level rise over the last decade in the South Pacific subtropical gyre, using altimetric data, ARGO floats and a repeat WOCE hydrographic transect along 170°W. Altimetry shows that sea level rises by 12 cm in the subtropical gyre, centred around 40°S 170°W, between 1993 and 2004. The difference map (Figure 1c) indicates that the steric expansion in the upper 700 m explains only part of the observed signal. The analysis of subsurface hydrographic data indicates a deepening of the isopycnals to ~1800 m, and the WOCE and ARGO float trajectories confirm the gyre spin-up during the 1990s. Roemmich et al. (2006) suggest that the gyre spin-up is related to the decadal intensification of wind-stress curl east of New Zealand associated with the decadal increase in the atmosphere's Southern Annular Mode (SAM).

The principal mode of atmospheric forcing in the Southern Ocean is the Southern Annular Mode. Positive values of the SAM index correspond to a poleward shift and increase in the westerly winds, which strengthens the sub-polar westerly winds and weakens the subtropical westerlies (Thompson and Wallace, 2000). A positive trend in SAM has been noted since 1979 (Thompson et al. 2000), which tend to increase the wind-stress curl and Ekman pumping over the midlatitude ocean gyres, raising sea level as noted by Roemmich et al. (2006). There is also stronger upwelling at higher latitudes in the Antarctic Divergence, leading to a decrease in sea level here. Hall and Visbeck (2002) have used a coupled model to investigate the Southern Ocean's response to changes in SAM. They find that the strengthened westerlies around 60°S increase the northward Ekman transport leading to anomalous upwelling of cold water along the Antarctic margins (which decreases the sea level) and anomalous downwelling around 45°S (increasing sea level). This anomalous flow also increases the vertical tilt of the isopycnals over the Southern Ocean, so that a positive SAM is associated with a stronger Antarctic Circumpolar Current (ACC).

As well as its long-term trend, the SAM index also shows higher frequency variability including distinct interannual changes. During the 1990s, the SAM index was mainly positive with stronger events occurring during 1993-94 and 1998-2000. After 2000, the index oscillates around zero, with two negative events occurring during 2000-2001 and 2002. These interannual changes in the strength of the SAM may also modify the strength of the convergence and divergence in the different years, leading to interannual variations in sea level.

The second mode of atmospheric variability affecting the Southern Ocean is the El Nino Southern Oscillation (ENSO). The largest impact of ENSO is predominantly felt in the South Pacific and South Atlantic (Karoly, 1989), although an oceanic response to ENSO is also noted in the SW Pacific (Holbrook and Bindoff, 1996) and in the southern Indian (Park and Gamberoni, 1995). Sallee et al. (2006) have shown that the Southern Ocean's sea level anomaly response is strongly linked to both the SAM and ENSO modes during the period 1992-2005. However, rather than a zonal response to SAM around the circumpolar belt as predicted by the coupled models, the observed sea level responds in a different way in each Southern Ocean basin. Sallee et al. (2006) find that the regional response depends on the relative strength of the ENSO and SAM modes in the different basins, the bathymetry, and the latitudinal variations in the path of the circumpolar current.

The higher latitudes of the Southern Ocean are characterised by weaker stratification and strong air-sea interactions. This means that interannual changes in the climate forcing at the surface can drive an energetic, deep-reaching thermohaline circulation (Speer et al., 2000). This will be detected by altimetric sea level observations, which respond to the vertically integrated mass and density changes. Observing and quantifying these deep ocean changes is difficult in the Southern Ocean due to the lack of long-term repeat in-situ data. This situation is being improved with the vast deployment of Argo floats in the Southern Ocean since 2002 (http://www.argo.ucsd.edu). However, ARGO floats cannot solve the problem of the lack of long-term in-situ observations. Two long-term monitoring sites do exist in the Southern Ocean with high-density repeat CTDs and XBTs since the 1990s : at the WOCE SR1 site in Drake Passage (Cunningham et al., 2003; Sprintall, 2003) and at the WOCE SR3 site south of Tasmania (Rintoul and Sokolov, 2001; Morrow et al., 2003).

The present paper aims to use the repeat hydrographic observations in the sector south of Australia to investigate the reasons behind the sea level rise and its interannual variations in this part of the Southern Ocean. Since 1992, in the region between Tasmania and Terre Adèlie in Antarctica, we have available concurrent high-resolution satellite altimetry and sea surface temperature (SST) data, 7 WOCE SR3 repeat hydrographic transects and 76 high-resolution repeat XBT sections and 103 surface salinity sections from the SURVOSTRAL programme (Figure 2). The satellite data and surface meteorological forcing data allows us to look at the basin-scale structure of the sea level rise and its possible forcing. The subsurface data allow us to investigate whether the surface changes are responding to variations in the surface mixed layer or to deeper temperature and salinity changes, and whether meridional frontal movements can contribute to the observed sea level rise. The relation between the SAM and ENSO climate forcing and the deeper hydrographic changes will also be explored.

2. Data Sets

2.1 Altimetric sea level anomaly data

The altimeter products were produced by Ssalto/Duacs and distributed by AVISO, with support from CNES. The data set spans 12 years from January 1993 to December 2004 and corresponds to sea level anomaly (SLA) relative to a seven year mean (January 1993 to December 1999). Details of the mapping technique used to derive the 1/3° gridded data are given by Le Traon and Dibarboure (1999), and a discussion of the aliased high-frequency errors is given by Morrow et al. (2003). Globally, this data set resolves wavelengths greater than 150 km, with a temporal resolution of 20 days (Ducet et al., 2000). In the Southern Ocean where the groundtracks converge, we can resolve 100 km wavelengths, and variations at 50 km wavelength are present but reduced by 50% in energy.

2.2 CTD, XBT and thermosalinograph data

Five full depth repeat CTD sections are available from the WOCE (World Ocean Circulation Experiment) SR3 line, collected between Tasmania and Terre Adélie (Antarctica) during voyages of the research vessel R/V *Aurora Australis*. These sections were made in March 1993; January 1994; January 1995; July 1995; September 1996. An additional CTD section along the SR3 line was made in November 2001 as a contribution to the CLIVAR Repeat Hydrography and Carbon Program (Rintoul and Sokolov, 2001). The station spacing for these CTD sections is around 55km with more tightly grouped measurements in the frontal regions. The data processing steps are described in Rosenberg *et al.* (1995). These data are precious since they provide the only information on deep temperature and salinity changes between Australia and Antarctica over the 1990s.

As part of the SURVOSTRAL program (SURVeillance de l'Océan auSTRAL), high-density XBT and thermosalinograph measurements are obtained between Tasmania and Terre Adélie in Antarctica every austral summer. The French Antarctic supply ship "*l'Astrolabe*" was used to obtain 6 XBT and 10 thermosalinograph (TSG) sections per year along the nearly-repeating line from Hobart, Tasmania (43°S 147°E) to the French Antarctic base Dumont D'Urville (66°S, 140°E) (Figure 2). The first XBT and TSG section for each austral summer occurs at the end of October, the final section is in mid March. The time series starts in late 1992. We are able to maintain high density XBT sampling due to the presence of an onboard observer: weather and faulty probes permitting, XBT measurements are made every 35 km, and every 18 km in the frontal zone from 48°S-54°S (see Figure 2). Most observations attained 800 m depth, but nearly all reached at least 500 m. All XBT data are carefully quality controlled by the CSIRO Marine and Atmospheric Research (CMAR), Hobart, Australia. The October transects are not exactly repeating south of 60°S, as the ship searches for clear sea routes through the ice. So in the following analysis, our "summer mean" calculations are based on the available December to March exactly repeating sections.

Continuous surface temperature and surface salinity measurements are available from the thermosalinograph, with an average measurement every 1-5 minutes (at least one per nautical mile). Salinity data processing is described in Chaigneau and Morrow (2001).

2.3 Surface Forcing data sets

Winds. Two different wind products will be used in the following analysis : monthly averaged winds computed from ERS gridded scatterometer winds are available on a 1.0° grid for the period 1992-1999, and higher resolution monthly Quickscat gridded winds on a 0.5° grid for the period 1999-2005. Both wind data sets are available from the IFREMER Cersat (French Satellite Processing and Archiving Facility) website (http://www.ifremer.fr/cersat).

Heat Flux. We use the monthly NCEP reanalysis on a 2° grid to estimate the air–sea heat flux. These data are made available by the NOAA-CIRES Climate Diagnostic Center (http://www.cdc.noaa.gov/).

Evaporation and Precipitation. Following Reverdin et al., (2006) who compared different surface forcing products in the North Atlantic, we have taken the evaporation fields from the monthly reanalysis product ERA40 of ECMWF (Simmons, A.J. and J.K. Gibson, 2000, unpublished document available on www.ecmwf.int/research/era). The precipitation field comes from the 1° gridded CMAP blended satellite and in-situ product, available to August 2002 (Xie and Arkin, 1997).

Reynolds Sea Surface Temperature. 1° resolution, weekly, optimally interpolated maps of satellite and in-situ SST observations were used (http://podaac.jpl.nasa.gov/reynolds/). An analysis of this product is provided by Reynolds et al. (2002).

3. Temporal Evolution of the Surface Characteristics

The temporal evolution in sea level rise is of course more complex than the simple trend depicted in Figure 1a. Figure 3a shows altimetric sea level anomalies along the SURVOSTRAL line from Tasmania (44°S) to Dumont D'Urville (66°S) from January 1993 to December 2004. The data have been low-pass filtered to remove signals less than 90 day period.

Three main zones are apparent on this map:
1) A region of high mesoscale variability between 49°S and 54°S associated with eddies and meanders of the main dynamical fronts: the Subantarctic Front (SAF) between 49-52°S and the Polar Front (PF) between 51-54°S. This band is the Inter Polar Frontal Zone. Although the data have been filtered at 90-days, the annual and interannual variations of the mesoscale field are still apparent. This region shows a strong increase in sea level in 2000 and 2001 which is associated with a large increase in eddy kinetic energy (Morrow et al., 2003).
2) North of the SAF is the Subantarctic Zone (SAZ), a region of deep winter mixed layers where Subantarctic Mode waters form (Rintoul and Trull, 2001).
3) South of the PF is the Antarctic Zone (AZ), a region with fairly homogenous surface properties characterised by a low salinity (~33.9) due to sea ice melt and a subsurface temperature minimum layer of "Winter Water" (Chaigneau et al., 2004).

The boundaries between the different zones are delimited by the variable front positions. The SAF can be defined as the maximum temperature gradient between 3 and 8°C at 300 m depth (Belkin and Gordon, 1996). The 3 and 8° isotherms limits are shown in bold in Figure 3b. The maximum temperature gradient occurring within this limit is deep-reaching, and coincides with a maximum meridional sea level gradient (Sokolov and Rintoul, 2002; 2006). Recent studies have shown that the frontal positions can also be monitored using absolute sea surface height contours (Sokolov and Rintoul, 2002; 2006; Sallee et al. (2006)). In the present study we use the SAF definition of Sallee et al (2006) (red line, Figure 3b). This corresponds to the southern and most energetic branch of the SAF, and is defined as the 1.20 m contour of sea surface height relative to 1500 dB (SSH_{1500dB}). In Figure 3b, we note that our SAF definition is relatively stable over time, whereas the 8°C isotherm varies over a much larger latitudinal extent. The 8°C isotherm is frequently pushed north of cold-core eddies which detach just north of the SAF within the SAZ (Rintoul et al., 1997; Morrow et al. 2004). The main frontal gradient remains to the south, as depicted by the red line.

The PF is defined as the northern limit of the winter water tongue, with temperatures cooler than 2°C at 200 m depth (Belkin and Gordon, 1996), as shown in Figure 3c. Again, we use the Sallee et al (2006) definition for the PF, which is the 1.0 m contour of SSH_{1500dB}, which corresponds to the northern PF position as defined by Sokolov and Rintoul (2006). We note the good correspondence between the 2°C contour at 200 m depth and the altimetric definition of the PF in Figure 3c.

This satellite-derived technique allows us to monitor every week the time-varying positions of the SAF and PF, and the SAZ and AZ limits, during the altimetric period 1992-2005. This is even possible for periods with no subsurface hydrographic data. In the following section, we

will examine the surface forcing and the ocean response along the SURVOSTRAL line, using these variable zone limits. The SAZ is defined between 47°S and the Sallee et al. (2006) SAF position. The AZ is defined between Sallee et al. (2006) PF position and 58°S. Annual and summer means are presented where available. Summer mean values are calculated from mid December to mid March.

In the SAZ

Sea level rises to a maximum in 2000 in the SAZ (Figure 3a, Figure 4a), and falls thereafter in both the summer mean and annual mean values. The summer mean wind stress curl is mainly positive during the 10-year period (Figure 4b), generating downwelling in the SAZ. The annual mean wind stress curl is near zero, strengthens to positive values in 1997-1999 and shows a larger negative anomaly in 2004. The increase in downwelling favourable annual winds during 1997-1999 preceedes, and may contribute to, the peak in SLA in 2000.

The sea surface temperature (SST) and salinity (SSS) evolution is shown in Figures 4c and 4e, respectively. The summer mean values of SST are from the combined SURVOSTRAL XBT data, and the summer WOCE SR3 sections (blue line). The summer (red) and annual mean SST (cyan) values are also shown, based on the Reynolds SST product. The summer mean SSS values are from the TSG data and available WOCE SR3 sections. The SST and SSS values are highly correlated (r=0.75), with cooler, fresher surface waters in the summers of 1993, 1998-99 and 2003-2004 with warmer, saltier waters in 2001-2002. There is no apparent correlation (r=-0.2) between the SST signature and the NCEP surface heat flux on a summer or annual mean (Figure 4d), nor between the SSS signal and the biannual variations in evaporation – precipitation (E-P) data (Figure 4f).

The periods with cooler SST in the SAZ (during 1998-1999 and 2003-2004) are periods with more summertime cold-core eddies just north of the SAF, and consistent cool temperatures over the upper 300 m (see Figures 3b and c). If we extract the altimetric sea level anomalies at the exact space-time location as the XBT measurements, we find a good correlation between the warm/cold eddies and positive/negative sea level anomalies, as expected. However, the summer-mean averages do not always coincide, and the differences are mainly due to the in-situ data sampling which is not evenly distributed each summer. For example, the peak in sea level during the summer of 2000 is due to the large positive anomaly in the north of the SAZ, which is poorly sampled by the XBTs during December 1999 – January 2000. The mesoscale variations are reduced in amplitude in the summer mean calculated from the Reynolds data, and absent from the annual mean SST from Reynolds. This reinforces that the SURVOSTRAL SST and SSS data in the SAZ can be dominated by mesoscale events, such as persistent eddies or front meandering.

In the AZ

A tighter relation exists between the local atmospheric forcing and the surface characteristics in the AZ, where the mesoscale eddy energy is weaker. SLA rises over the decade (Figure 5a), with sharper increases in 1995-1997 and 2001-2002. These interannual sea level variations appear out of phase with the SAZ, which has also been noted from a 7-year time series at the same location by Sokolov and Rintoul (2003).

Although there is no net trend in wind stress curl at these latitudes, there is a weak but significant correlation (r=0.25) between interannual SLA variations and local wind stress curl changes (Figure 5b). Sea level rise occurs during periods with weaker Ekman suction. Periods

of stronger Ekman suction during 1998-2000 and 2004 increases upwelling of denser water to the surface, leading to a decrease in sea level. Summer SST is also in phase with this interannual cycle in SLA and Ekman suction, and higher SLA is associated with higher SST (Figure 5c). There is also a minor trend of increasing SST. There is no apparent interannual variation in the mean heat flux (Figure 5d), suggesting that the SST may reflect a dynamical ocean response or remote forcing.

Interestingly, the SSS shows a net decrease of ~0.1 psu over the period, which is accompanied by an increase in precipitation of ~20 mm/month. If we assume this increase in freshwater flux is completely mixed into the surface mixed layer (which has an average depth of 55 m in the AZ in summer, Chaigneau et al., 2004), then the precipitation increase is sufficient to explain the drop in salinity.

4. Subsurface structure

WOCE SR3 subsurface temperature and salinity data are available over the entire water column and will be used to provide information on the deep temperature and salinity changes over the 1990s. However, we will start by an analysis of the summer mean SURVOSTRAL repeat XBT data from mid December to mid March, which are statistically more robust with 4-6 sections per year over the 13 years.

4.1 XBT temperature structure in the SAZ

Sokolov and Rintoul (2003) have shown that there is a strong temperature correlation over the upper 500 m in the SAZ due to the deep winter mixed layers and the fact that the region is often subject to deep-reaching meandering fronts and detached eddies. We can see the impact of these deep reaching mesoscale eddies and meanders when we plot the temporal evolution of the summer temperature structure at different depths in the SAZ (Figure 6). From the surface down to 500 m depth, the summer temperature structure shows evidence of heaving isotherms which are coherent over the upper 500 m, this heaving occurs even within one summer period (eg. January 1998). Part of the interannual change is due to the XBT sampling, with incomplete coverage in the SAZ during the summers of 1998, 2000 and 2001. Despite these sampling anomalies, there is also a background trend with temperatures increasing over the upper 400 m. The maximum increase occurs at 80 m with 0.047°C per year, yielding a 0.6°C temperature increase over the 13 years at this level. We note that the error bars on the trend calculation are large, due to the strong mesoscale signal in our summer observations, and only the trend at 80 m depth is statistically significant.

The background trend over the upper 500 m is equivalent to a 0.02°C increase per year, leading to a steric sea level rise of 1.6 mm/year (assuming a constant salinity of 34.5 over the upper ocean). This is in the right sense to explain the SL rise in the SAZ but explains only one third of the total observed sea level rise of 5 mm/ year from 1993-2003 (Figures 1a, 4a).

4.2 XBT temperature structure in the AZ

Figure 7 shows the summer mean temperature evolution in the AZ, along different depth levels from 0 to 500 m depth for the period 1992 - 2004. Linear temperature trends are superimposed at each depth level. During this period of decadal sea level rise, temperatures increase in the surface summer mixed layer (0-40 m depth) by 0.8 °C over 12 years. Below the summer mixed layer we have the “Winter Water” (WW) layer characterised by a tongue

of low temperature water < 2°C. Within this winter water layer, temperatures show a slight decrease from 80-120m, and then increase again from 150-250 m depth. Below 300 m we are in the upper circumpolar deep water layer, and the temperatures show minor warming to ~400 m depth then cooling by < 0.05° in the deepest layers. The warming trend in the surface mixed layer, and at 150 m depth is statistically significant, although the smaller temperature changes in the winter water layer and deeper than 250 m are not significant with the precision and sampling of the XBT data.

The temperature signals at 80 m and 150 m depth are mostly out of phase … the large increase in temperatures at 80 m in January 1998 is accompanied by a rapid drop in temperature at 150 m depth, whereas the temperature difference is minimal around January 2001. A large temperature gradient occurs between 80 – 150 m depth when there is a thinner core winter water layer, and vice versa.

This vision of alternative layers warming and cooling can be more clearly explained if we consider how the mean temperature structure over the section has changed between the later high sea level years (2000-2004) and the earlier years (1992-1996). Figure 8 shows the mean temperature structure averaged a) over 1992-1996, b) over 2000-2004 and c) their difference. Firstly we note that the STF, which is defined as the position of the 11°C isotherm at 150 m depth (Nagata et al. 1988) has shifted southward from 46° to 47°S during this period, introducing a large warming over the upper 500 m in the northern part of the section. Similarly, the northern branch of the SAF has also shifted southward from 50.5° to 51.5°S again introducing a warming to depths greater than 500 m. So part of the observed warming and sea level rise in the SAZ may be due to a southward shift in these fronts. The southward shift in the PF has also been observed at this location by Sallee et al. (2006) in a circumpolar analysis of the frontal positions (Figure 3c).

In the AZ the story is more complicated. There is indeed net warming in the surface mixed layer, and we have seen from the SSS data that this is accompanied by a net freshening. It is therefore unlikely that this layer is influenced by a stronger Ekman transport which would bring a larger volume of fresher but cooler water from the south. The summer wind stress curl is slightly stronger during 2000-2004 than during 1992-1996, which should introduce cooler water into the surface layer. In the absence of a net heat flux trend, the reason for the surface heating in the mixed layer is not yet understood.

The subsurface cooling and warming may be explained by the fact that the tongue of Winter Water is shallower and not as thick at the end of the period. This shift to shallower levels has the effect of cooling the layers from 80-120 m on the top of the tongue, and warming the layers from 150-250 m at the base of the tongue, although we note that only the deeper warming is statistically significant. The reason for the shallower winter water tongue may be twofold. Firstly, both the summer mean and the annual mean SST have warmed between the two periods, meaning warmer winter conditions which could reduce the winter mixed layer depth. The stronger Ekman suction in summer at the end of the period (2000, 2001, 2004) may also "lift" the winter water tongue. Finally, close to the Antarctic continent, we also observe a net cooling by nearly 1°C as the Southern Boundary front appears to have shifted northward, perhaps as a response to stronger upwelling along the Antarctic Continent.

4.3 CTD T-S structure

The adjacent WOCE SR3 CTD data provides valuable information on the deeper water mass changes, including the salinity changes. However, we have fewer sections available. It is a

delicate task to interpret net T-S changes over a decadal period based on a limited number of sections, when seasonal modifications in the surface mixed layer and the strong mesoscale eddy signal can have a big impact on the observed variations. Bearing this in mind, we have averaged together the 3 summer CTD sections available in the 1992-1996 period (March 1993, January 1994, January 1995), and compared this summer mean to the only transect available in the period 2000-2004 (November 2001).

Figure 9 shows the evolution of temperature and salinity from these 4 WOCE SR3 sections calculated in a similar way to Figure 8. The CTD section of Nov 2001 shows strong mesoscale eddy structures, including a very strong cold-core eddy at 49.5°S which completely perturbs the mean position of the SAF. Despite this, the CTD difference maps (Figure 9c) show similar features to the better-sampled XBT difference maps (Figure 8c). There is a clear southward shift in the STF, with maximum amplitude near 100-200 m depth which tapers away near 500 m depth. The CTD sections reveal that there is additional sub-surface warming between 700-1300 m, and the water is also saltier over the upper 1500 m. This suggests a southward meander or shift of the STF, probably associated with an increase in the Tasman Sea outflow, which brings with it warmer, saltier Tasman Sea waters over the upper 1500 m (Rintoul and Sokolov, 2001). This replaces the cooler, lower salinity mode and intermediate waters which extended north of 46°S during the early 1990s (Figure 9a).

Altimetry maps confirm the presence of two cold-core eddies at 47°S and 49°S in November 2001; the CTD sections show these eddies have cooler water over the upper 1500 m which is fresher than the surrounding waters in the upper 1000 m, and saltier from 1000-2000 m depth. This T-S structure is characteristic of the water mass structure south of the SAF (Figure 9). The detachment of cyclonic eddies from the SAF, transporting Polar Frontal Zone waters into the SAZ south of Tasmania, has been documented by Morrow et al. (2004).

The surface mixed layer shows cooling in the CTD difference maps whereas the XBT difference maps show a net warming. This is because we are comparing different seasons … the Nov 2001 section is in late spring at the start of the summer heating cycle, and the seasonal warming is only just reaching 58°S. This seasonal heating cycle is much stronger than the trend in surface temperature. The surface mixed layer extends down to ~100 m depth in the AZ in the Nov 2001 section.

The CTD sections do help us understand the dynamics of the evolving Winter Water tongue in the AZ. The CTD sections confirm that the Winter Water tongue appears to have diminished … the low salinity surface water still extends down to ~200 m depth in the AZ, but the water between 100 – 200 m depth shows a warmer band … as seen in the XBT profiles. This follows the tendency towards warmer, fresher winter conditions suggested earlier. There is a pronounced mesoscale signal in the AZ, evident in the November 2001 section. Warm anomalies, for example at 56°S, heave the isotherms and isohalines downward, inducing warm fresh anomalies from 300-1000 m depth. At the base of the winter water layer near 200 m depth there are patches of warmer, higher salinity waters where the winter water layer thickness has been locally reduced.

We have also repeated our difference calculation on isopycnal surfaces to separate the effects of eddy "heaving" from real warming/freshening at depth. In the AZ, the same structure of subsurface warming is present, although on isopycnal surfaces the anomalies are warmer and slightly saltier. The southward movement of the STF remains both warmer and saltier. The strong subsurface warming at the base of the Winter Water tongue and lesser warming

extending down to 1500 – 2000 m are also present in the winter SR3 sections made during August 1995 and September 1996 (not shown).

The CTD sections allow us to make more precise estimates of the steric height changes across the ACC during this period. Figure 10 shows the steric height calculated from the mean 1993-1995 summer period, the November 2001 section, and their difference. Steric height is calculated over the upper 500 dB, similar to the XBT data analysis, and also relative to 2000 dB. The mesoscale structure, in particular from November 2001, is evident in the difference plot. Despite this, there is a net increase in the 0/2000 dB steric height in the AZ between 54-63°S of 1-4 cm. Leaving aside the two cyclonic eddies in the SAZ, the southward movement of the STF also increases 0/2000 dB steric height by ~4-5 cm.

Unfortunately, November 2001 was an anomalous month in the AZ. Figure 3a shows the temporal evolution of altimetric SLA at SURVOSTRAL, just downstream of the SR3 line, and we note the strong mesoscale activity in the AZ during November 2001. Given the strong mesoscale positive sea level anomalies, it is difficult to draw firm conclusions on the net sea level rise over the period using these 4 CTD sections. However, the CTD sections clearly show that the warming is not limited to the upper 700 m, and deeper warming does occur down to 1500 – 2000 m depth. This deep warming increases the steric height rise over 0/2000 dB by a factor of 2-3, compared with the steric height calculated from 0/500 dB. This reinforces that the steric height estimates calculated over 0/700 dB for the global sea level rise studies (Lombard et al., 2005; Willis et al., 2004, Ishii et al., 2005) will be underestimating the real steric sea level rise by at least a factor of 2-3 in this part of the Southern Ocean.

5. Relation with climate mode forcing : ENSO and SAM

How might changes in the atmospheric forcing contribute to the observed sea level rise? The two main climate modes which effect the ocean circulation south of Tasmania are the Southern Annular Mode (SAM) and the El Niño Southern Oscillation (ENSO). Figure 11a shows the MEI ENSO Index based on a weighted average of the main ENSO features (for details see http://www.cdc.noaa.gov/ENSO/enso.mei_index.html). Positive values of the MEI Index represent the El Niño phase of ENSO, with warming in the central and eastern Pacific, and cool and dry conditions in the western Pacific. Although ENSO is a tropical coupled system, its impact can be felt in the entire southwest Pacific, carried by the East Australian Current (Holbrook and Bindoff, 1996). In our study region, the positive MEI ENSO index corresponds to cooler ocean conditions in the South Tasman Sea during 1997, the negative MEI index corresponds to warming, which occurs during the austral summers of 1996-1997 and 1999-2000.

The Southern Annular Mode (SAM) is defined as the leading principal component of the 850 mb height anomaly in the region south of 20°S (Thomson and Wallace, 2000). The SAM index is shown for the period 1992-2005 in Figure 11b, with a 3-month running average applied. The SAM has been essentially positive during the 1990s, with stronger events during in 1993, 1998-1999, and 2001. The SAM had more negative events in the 2000s, with negative indices during 2000 and 2002-2003.

Studies over the circumpolar region have found that the ENSO and SAM indices are often anti-correlated (L'Heureux and Thompson, 2005). This is certainly the case for the strong 1999 La Nina event (Figure 11). When negative ENSO is associated with a positive SAM index, there is also a southward shift in the winds and in the position of zero wind stress curl. Rintoul and Sokolov (2001) have demonstrated that a poleward shift in the zero wind stress

curl is associated with a stronger Tasman outflow, bringing warmer, saltier water into the northern part of the section. This would increase the sea level, as observed in 1999-2000.

We have regressed the SAM index and the ENSO index onto altimetric sea level anomalies in the Southern Ocean (Figure 12). Negative ENSO events lead to a positive sea level rise in the SAZ, with a lesser impact in the AZ south of the Polar Front. Positive SAM events during the 1990s increased downwelling in the SAZ which increased sea level, whereas there was stronger upwelling in the Antarctic divergence which tends to decrease sea level in the AZ. After 2000, when the SAM index becomes negative, the reverse occurs, with sea level falling in the SAZ and increasing in the AZ. Sallee et al (2006) find that in the sector south of Australia, ENSO dominates the sea level response north of the SAF, and SAM dominates south of the SAF.

Consider the impact of these two climate modes in the SAZ. The SAM tendency for sea level rise during the 1990s and a weak decrease after 2000 is evident in the sea level anomaly and SST fields (Figure 4a, c). In addition, the positive ENSO forcing tends to reduce the sea level at the beginning and end of the 13-year period, and enhances the sea level rise during 1999-2000. Interestingly, the strong positive El Nino event of 1997-1998 is associated with weaker subsurface temperatures (Figure 6) and a northward movement of the 8°C isotherm at 300 m depth around the dominant cold-core eddies (Figure 3b), with a minor drop in SST (Figure 4c), but no influence on the mean SAZ sea level (Figures 3a, 4a). It is possible that the shift to a strong positive SAM index during this period may counteract the negative sea level anomalies induced by the El Nino signal. The interplay between the ENSO and SAM forcing, and its impact on the SAZ sea level, merits further study. Unfortunately, the strong mesoscale eddy signal, particularly in the period 1998-2000, confuses the climate mode response.

In the AZ where the SAM forcing dominates, positive SAM events during the 1990s are associated with stronger negative wind stress curl (upwelling – Figure 5b) which effectively reduces the sea level during these years, with increasing sea level during the negative SAM years 2000-2003.

In addition to the sea level response, Sallee et al (2006) have also examined how the mean front positions (SAF and PF) respond to the westerly wind anomalies induced by positive or negative SAM events. In the SURVOSTRAL region, positive SAM events paradoxically tend to generate a minor northward movement of the fronts. Along the SURVOSTRAL line, the position of the Southeast Indian Ridge partially inhibits the SAF frontal movement (Figure 3b). The fact that the SAM index changes from being positive in the 1990s to mainly negative after 2000, means that the front positions shift from their northern, positive SAM position to the south. This is observed in our in-situ hydrographic sections for the PF (Figure 3c), and the northern branch of the SAF, indicated by the 8°C isotherm in Figure 3b.

Although direct SAM forcing, shifting the wind stress curl field, has an impact on the observed interannual sea level changes, there is only a weak trend in wind stress curl over the period 1992-2005 (Figure 4b), yet there is a strong sea level rise. Why is this so? If we consider the integrated response of the wind forcing we get a more complete picture. We have calculated the Sverdrup transport based on the mean satellite winds of ERS-1 (1991-1995) and Quikscat (1999-2005), integrated over the Southern Ocean basins deeper than 2000 m. Our model integrates the wind stress curl from east to west, starting from the 2000 m depth contour along an eastern continental boundary or submerged ridge (black points), up to the western boundary (red points). Figure 13 shows the integrated Sverdrup transport for the ERS

period (top panel) and the Quikscat period (bottom panel), with a zoom over our region 70°-170°E. In the northern section of our zoom, the eastern boundary is along the New Zealand - Campbell Plateau or the coast of Tasmania. South of 55°S, the eastern boundary lies along the Falkland Ridge east of Drake Passage, or the Antarctic Peninsula further south.

During the ERS period (1991-1995) when the SAM index is mostly positive (Figure 11b), there is an intense eastward circulation around 60°S imposed by the poleward shift and intensification of the westerly winds. There is also a noticeable westward current along the Antarctic continent. This forms a cyclonic recirculation gyre, including a westward coastal current, and an eastward recirculation further north. A much weaker cyclonic gyre has been observed with CTD sections, ADCP currents and floating buoys during the BROKE campaign in the summer of 1996 (Bindoff et al., 2000) – a period when the SAM index was close to zero. Clearly during most of the 1990s, this cyclonic gyre is more intense, implying a lower sea level. More importantly, the western boundary of this basin lies along the Kerguelen Plateau around 80°E, and this cyclonic recirculation draws in cold, fresh Antarctic Slope Current waters into the northward flowing western boundary current (Bindoff et al., 2000; Speer and Forbes, 1994). Part of this flow originates in the Weddell–Enderby Basin, passing south of the Kerguelen Plateau via the Princess Elizabeth Trough (Wong et al., 1998). These cool, fresh western boundary current waters are then transported eastward from 55-60°S by the integrated Sverdrup flow in the upper 2000 m (Figure 13). Numerical model results suggest that thes waters reach the SURVOSTRAL line some 12-18 months later (S. Speich, pers. comm.). Stronger cool-fresh flow implies a lower sea level in the early 1990s.

During the Quikscat period (1999-2005) when more negative SAM events occurred, the integrated Sverdrup flow has weakened across the SURVOSTRAL line around 47°S. The negative Sverdrup circulation in the SAZ during this period recirculates water from further south in the Tasman Sea, and may contribute to the lower subsurface temperatures in the later years (Figure 3b, Figure 6) and lower sea level (Figure 3a, 4a). More strikingly, the cyclonic circulation south of the fronts from 55-65°S has weakened across the whole basin. This implies a reduced transport of cool, fresh water south of the fronts, which is warmer and saltier at depth, which would raise sea level during the early 2000s, as observed (Figure 5a, Figure 8, Figure 9).

6. Discussion and Conclusion

This study has investigated the causes of the observed sea level rise in the Southern Ocean south of Australia over the 1990s, by examining the vertical temperature structure in the upper ocean from available repeat in-situ data.

Fronts

One clear result of this work is that the position of the main fronts (STF, SAF, PF) show a net shift to the south over the 10 year period. This is despite the fact that the SAF is bounded to the south by the Southeast Indian Ridge. Sallee et al (2006) have monitored the position of the SAF and PF from 1992-2005 using a combination of altimetry and in-situ data, and considered the effect of the main climate modes (ENSO, SAM) on the frontal position. In the region south of Tasmania, they find that the SAF is constrained by bathymetry, but the PF shows a net southward shift over the 13 years. Their SAF/PF definition corresponds to the SAF-S/N-PF-S definitions of Sokolov and Rintoul (2002) in the same region. The Sallee et al. (2006) SAF-S and N-PF-S frontal positions are shown in Figures 3b, c over the period 1992-2005. We can see that during 1992-1996 the fronts were slightly north of their mean position,

and during 2000-2004 there is a minor shift to the south. Thus the in-situ observations and the altimetry-derived fronts are coherent.

Salinity in the AZ

Our observations suggest that salinity has decreased in the Winter Water tongue during this decade, although salinity has slightly increased on isopycnal surfaces in the deeper layers. The few subsurface CTD salinity data over the decade and our few spring SURVOSTRAL SSS observations all show a decline in the AASW and WW salinity. In addition, the annual E-P trend follows the summer mean E-P trend (Figure 5) with increasing precipitation over the decade. The decrease in sea surface salinity in this zone can be explained by the increased precipitation. However, the near constant value of around 33.85 over the 10° latitude band south of the PF is also due to its long advection time. Lagrangian studies of upper ocean currents show that the WW along the SURVOSTRAL line is formed by winter convection in a source region south of 60°S and near 80-100°E. The AASW and WW layers then undergo ~12-18 months of ENE advection before they arrive in the SURVOSTRAL region (ie. at least one complete seasonal heating/cooling cycle – S. Speich, pers. comm.). The increase in precipitation at the SURVOSTRAL line (Figure 5) is also representative of a larger pattern south of the PF in the Indo-Pacific sector (not shown). So the freshening may be related to increased precipitation which occurred along the 12-18 month lagrangian drift (warmer and fresher). We cannot rule out that increased sea-ice melt may also contribute to the observed salinity decrease, but that would imply cooler and fresher anomalies. Modelling studies would help to elucidate this point.

Steric contribution to sea level rise

A trend of increasing XBT temperature in the SAZ is quite coherent over the upper 500 m during the 1990s, with a maximum in temperature increase around 80-150 m and dropping to near zero at 500 m. Assuming a constant salinity of 34.5 over the upper ocean, we have estimated that the steric sea level rise due to these temperature trends in the upper 500 m would account for 1.6 mm/yr in sea level rise over the 12 years. This is only 1/3 of the observed sea level rise from the altimeter data (see Figure 1a), but is in line with recent analyses of global 0-700 m in-situ data products (Figure 1b; Lombard et al., 2005; Ishii et al., 2005). Our CTD sections show that even deeper warming (500-1500 m) may also contribute to the observed sea level rise. The deeper signal may be due to an increased Tasman Sea outflow, bringing warmer, saltier intermediate water across the northern part of the section, which can extend to the sea floor (Rintoul and Sokolov, 2001). Clearly, our XBT sampling to 500 m depth will not be capturing all of this signal.

The Antarctic Zone is where the difference between the altimeter sea level trend and the in-situ steric trend is the largest (Figure 1c). We find distinct changes in the AASW and Winter Water characteristics, as well as deeper warming evident in the CTD sections. The XBT time series show that the surface layer of Antarctic Surface water (AASW) has become warmer and fresher over the last decade. This summer surface mixed layer is shallow, around 55 m +/- 10 m (Chaigneau et al., 2004), and so has a limited impact on the observed sea level rise. We estimate that the observed warming by 0.067°C/yr, and freshening by -0.0077 psu/yr would contribute to a 0.6 mm/yr sea level rise, only a fraction of the observed 4 mm/yr sea level rise in Figure 5a. The subsurface temperature minimum Winter Water layer has also become thinner and shallower, stocking less cold water in the period 2000-2004. The northern limit of the winter water tongue, defined by the PF position, has also shifted south (Figure 3c). The mean winter water depth from 8 years of XBT observations (1992-2000) was 177 +/- 11 m (Chaigneau et al., 2004), whereas in the 2000-2004 sections, the Winter Water layer is only

150 m deep (Figure 8). If we consider that the AASW and the WW layers have decreased in salinity by -0.0077 psu/yr, and that the subsurface layers have followed the temperature trends in Figure 7, then the upper ocean heat and salinity changes would lead to a 1.5 mm/yr sea level rise. Our CTD difference plots show a 4 cm rise over the AZ, calculated relative to 2000 dB, over the period to November 2001, roughly equivalent to the 4 mm/yr observed with altimetry. Thus it is the deeper changes in the AZ temperature-salinity structure which are mainly contributing to the observed sea level rise.

Our CTD results are only indicative south of Tasmania, since only one recent SR3 CTD section is available. However, the steric height calculated over 0-2000 dB is 2-3 times greater than the 0/500 dB steric height, in the SAZ and the AZ. This suggests that deeper ocean warming below 500-700 m depth can explain the observed altimetric sea level rise, at least south of Tasmania. Part of this warming is clearly associated with the southward frontal movements and water mass redistribution, but whether the water mass characteristics themselves have also changed requires a separate study.

Response to climate modes

In the AZ, where the SAM forcing dominates, there is a direct relation between the interannual sea level response and the wind stress curl variations. In the SAZ, the interannual variations in sea level rise appear to respond to both the SAM forcing and the negative ENSO (La Nina) events. As the seat of SAMW formation, it is important to understand the relation between the climate forcing and the subsurface water mass characteristics. Unfortunately, it is difficult to extract a subsurface large-scale climate signal from the in-situ measurements, when their sampling is dominated by the intense mesoscale eddy field in the SAZ, which itself has strong interannual variability (Morrow et al., 2003). Until we have better subsurface observational coverage (e.g., ARGO), the spatial-temporal variability in the SAZ can only captured by altimetry and numerical models.

Our simple Sverdrup transport model suggests that the vertically-integrated wind-driven flow may be partly responsible for the deeper warming trend in the AZ, and may also act to reduce the thickness of the Winter Water tongue. This simple model shows gyre-scale circulation changes, in the right sense to explain the observed sea level rise south of the polar front. Our simple model does not include bathymetry, which is a major constraint in the Southern Ocean, and is also based on two different wind products which may contribute to the differences. More sophisticated models are needed to provide a more precise estimate of the circulation changes over these 15 years.

The CTD sections, and the Sverdrup model results, both underscore how important the deeper ocean changes are in the Southern Ocean, and that calculating sea-level trends using only data to 500-700 m will largely underestimate the ocean's response to climate changes.

Acknowledgements

We thank the captain and crew onboard l'*Astrolabe* and the *Aurora Australis*, as well as our numerous volunteer observers, for helping us obtain the in-situ measurements in the frequently inhospitable weather conditions. Thanks to Ann Gronell and Mark Rosenberg for their help with quality control of the XBT and CTD data, respectively. We all appreciated the frequent discussions with Kevin Speer during his stay at LEGOS, including his constructive comments on the manuscript. The SURVOSTRAL program receives support from the Institut Polaire – Emile Victor (IPEV) and the Programme Nationale d'Etudes Dynamique du Climat (PNEDC) in France, the Australian Greenhouse Office and the Cooperative Research Centre

Program in Australia, and the National Oceanic and Atmospheric Administration (NOAA – USA) through a cooperative agreement NA37GP0518.

References

Belkin, I. M., and Gordon, A. L., 1996. Southern Ocean fronts from the Greenwich Meridian to Tasmania. *J. Geophys. Res*. **101**, 3675-3696.

Bindoff, N.L., M.A. Rosenberg and M.J. Warner, 2000. On the circulation and water masses over the Antarctic continental slope and rise between 80 and 150°E. *Deep Sea Res. II.,* **47**, 2299-2326.

Chaigneau , A. and R.A. Morrow, 2001. Surface temperature and salinity variations between Tasmania and Antarctica, 1993-1999. *J.Geophys. Res.,*107 (C12), 8020, doi:10.1029/2001JC000808.

Chaigneau, A., R.A. Morrow and S.R. Rintoul, 2004. Seasonal and interannual evolution of the mixed layer in the Antarctic Zone south of Tasmania. *Deep-Sea Research* I, **51**, 2047-2072.

Cunningham S. A., S. G. Alderson, B. A. King, and M. A. Brandon, 2003. Transport and variability of the Antarctic Circumpolar Current in Drake Passage, *J. Geophys. Res.,* **108** (C5), 8084, doi:10.1029/2001JC001147.

Ducet N., P.-Y. Le Traon, and G. Reverdin, 2000. Global high resolution mapping of ocean circulation from TOPEX/POSEIDON and ERS-1/2, *J. Geophys. Res*. **105**, 19477-19498.

Guinehut, S., P.Y. Le Traon, G. Larnicol and S. Philipps. Combining Argo and remote-sensing data to estimate the ocean three-dimensional temperature fields – a first approach based on simulated observations. *J. Mar. Sys.,* 46, 85-98, 2004.

Hall, A. and M. Visbeck, 2002. Synchronous variability in the Southern Hemisphere atmosphere, sea ice and ocean resulting from the annular mode, *J. Clim*, 15, 3043-3057.

Holbrook, N. and N. Bindoff, 1996. Interannual and Decadal Temperature Variability in the Southwest Pacific Ocean between 1955 and 1988. *J. Climate*. **10**, No. 5, pp. 1035–1049.

Ishii, M., M. Kimoto, K. Sakamoto and S.I. Iwasaki, 2005. Steric sea level changes estimated from historical ocean subsurface temperature and salinity analyses, *J. Oceanography,* submitted.

Le Traon, P.Y. and G. Dibarboure, 1999: Mesoscale mapping capabilities from multiple altimeter missions. *J. Atmos. Oceanic Tech.*, **16,** 1208-1223.

Lombard A., Cazenave A, Le Traon P.Y. and M. Ishii, 2005. Contribution of thermal expansion to present-day sea level change revisited, *Global and Planetary Change*, **47**, 1-16.

Morrow, R., Brut, A. and Chaigneau, A., 2003. Seasonal and interannual variations of the upper ocean energetics between Tasmania and Antarctica, *Deep Sea Research, I*, **50**, 339-356.

Morrow R., J.-R. Donguy, A. Chaigneau and S. R. Rintoul, 2004. Cold-core Anomalies at the Subantarctic Front, south of Tasmania, *Deep Sea Res., I*, **51**, 1417-1440**.**

Nagata Y., Y. Michida and Y. Umimura, 1988. Variations of positions and structures of the ocean fronts in the Indian Ocean sector of the Southern Ocean in the period from 1965 to 1987, *Antarctic Ocean and Resources Variability,* ed. D Salirhage. Springer-Verlag, Berlin, 92-98.

Park, Y.H. and L. Gamberoni, 1995. Large-scale circulation and its variability in the South Indian Ocean from Topex/POSEIDON altimetry. *J. Geophys. Res*., **100,** 24911-29929.

Reverdin, G. E. Kestenare, C. Frankignoul, and T. Delcroix, 2006. Surface salinity in the Atlantic Ocean (30°S – 50°N). *Prog. In Oceanogr.* (in press).

Reynolds, R. W., N. A. Rayner, T. M. Smith, D. C. Stokes and W. Wang, 2002: An improved in situ and satellite SST analysis for climate. *J. Climate,* **15**, 1609-1625.

Rintoul, S. R. and Sokolov, S., 2001. Baroclinic transport variability of the Antarctic Circumpolar Current south of Australia (WOCE repeat section SR3). *J. Geophys. Res*., **106**, 2795-2814.

Rintoul, S. R. and Trull, T. W., 2001. Seasonal evolution of the mixed layer in the Subantarctic Zone south of Australia. *J. Geophys. Res*., **106**, 31.477-31.462.

Roemmich, D., J. Gilson, R. Davis, P. Sutton, S. Wijffels and S. Riser, 2006. Decadal Spin-up of the South Pacific Subtropical Gyre, *J. Phys. Oceanogr*. (submitted).

Rosenberg, M. A.**,** Eriksen, R., Bell, S., Bindoff, N. and Rintoul, S. R., 1995. Aurora Australis marine science cruise AU9407: Oceanographic field measurements and analysis. *Res. Rep. 6*, 97pp., Antarctic Coop. Res. Cent., Hobart, Tasmania, Australia.

Sallee, J.B., K. Speer, and R.A. Morrow, 2006. Response of the Antarctic Circumpolar Current to the atmospheric variability. *J. Climate*, (submitted).

Sokolov, S., Rintoul, S. R., 2002. Structure of Southern Ocean fronts at 140°E. *J. Mar. Systems,* **37**, 151-184.

Sokolov, S. and S.R. Rintoul, Subsurface structure of interannual temperature anomalies in the Australian sector of the Southern Ocean, *J. Geophys. Res*., **108 (C9),** 3285, doi:10.1029/2002JC001494, 2003.

Sokolov, S. and S.R. Rintoul, 2006. Synoptic mapping of Southern Ocean fronts and filaments using sea surface height, (manuscript in preparation).

Speer, K., and A. Forbes, 1994. A deep western boundary current in the South Indian Basin. *Deep-Sea Research I*, **41** (9), 1289-1303.

Sprintall, J. Seasonal and interannual upper-ocean variability in the Drake Passage. *J. Mar. Res.*, **61**, 27-57, 2003.

Thompson, D and J. Wallace, Annular modes in the extratropical circulation. Part I. Month-to-month variability. *J. Climate*, **13**, 1000-1016, 2000.

Thompson, D.C., J. Wallace, and G. C. Hegerl, Annular Modes in the Extratropical Circulation. Part II: Trends. *J. Climate*, **13**, 1018–1036, 2000.

Vivier, F., K.A. Kelly and M. Harismendy,2005. Causes of large-scale sea level variations in the Southern Ocean: Analyses of sea level and a barotropic model. *J. Geophys. Res.,* **110**, C09014, doi:10.1029/2004JC002773, 2005

Willis, J.K., D. Roemmich, and B. Cornuelle, 2004. Interannual variability in upper-ocean heat content, temperature and thermosteric expansion on global scales*, J. Geophys. Res*., **109**, C12036, doi:10.1029/2003JC002260.

Wong, P.S., Bindoff, N.L., and A. Forbes, 1998. Ocean-ice shelf interaction and possible bottom water formation in Prydz Bay, Antarctica. In: Jacobs, S., Weiss, R. (Eds.), *Ocean, Ice, and Atmosphere: Interactions at the Antarctic Continental Margin, Antarctic Research* Series 75. American Geophysical Union, Washington, pp. 173-187.

Xie, P., and P.A. Arkin, 1997. Global precipitation : a 17-year monthly analysis based on gauge observations, satellite estimates and numerical model outputs. Bull. Amer. Meteorolog. Soc., 78, 2539-2558.

Figure Captions

Figure 1. Global distribution of sea level rise (in mm/yr) from (top panel) Topex-Poseidon altimetric observations over 1993-2003; (middle panel) sea level rise over the upper 700 m calculated from the ARMOR in-situ data projection of Guinehut et al (2004); (bottom panel) difference map Topex – ARMOR (after Lombard et al., 2005). The study region is outlined in black.

Figure 2. (left panel) Position of the WOCE SR3 CTD transects (*) and SURVOSTRAL XBT and TSG transects (x) between Tasmania and Antarctica, overlaid on the bathymetry. The 3000 m isobath is marked. The zoom represents the mean frontal positions defined by altimetry (Sokolov and Rintoul, 2002). The abbreviations used are: SAF : Subantarctic Front; N-PF : Northern Polar Front; S-PF : Southern Polar Front; N-SACCF and S-SACCF: Northern and Southern branch of the Southern ACC Front; SB : Southern Boundary of the ACC.

Figure 3. (a) Hovmöller diagram of altimetric sea level anomalies along the SURVOSTRAL line from Tasmania (44°S) to Dumont D'Urville (66°S) from January 1993 to December 2004. Altimetry data are low-pass filtered to remove signals less than 90 days. (b) SURVOSTRAL XBT temperature at 300 m depth, with the 3°C and 8°C isotherms in bold. The SAF position is marked in red, after Sallee et al. (2006). (c) XBT temperature at 200 m depth, with the 11°C and 2°C isotherms in bold. The PF position from Sallee et al. (2006) is in red.

Figure 4. Temporal evolution of the surface characteristics in the Subantarctic Zone, averaged between 47°S and the SAF position from Sallee et al (2006), for the period 1992-2005. In all plots, the annual mean is in green (with diamonds) and the summer mean in blue (with stars). a) altimetric sea level anomalies, b) wind stress curl from the ERS and Quickscat scatterometers; c) summer mean SST from SURVOSTRAL XBTs and WOCE SR3 summer sections (blue). Also shown, Reynolds summer mean SST (red), Reynolds annual mean SST (cyan). d) NCEP surface heat flux; e) summer mean SSS from SURVOSTRAL TSG data and WOCE SR3 summer sections; f) surface E-P : evaporation from ECMWF and precipitation from Xie and Arkin monthly climatology.

Figure 5. As for Figure 4, but for the Antarctic Zone averaged between the Sallee et al (2006) PF position and 58°S.

Figure 6. Temperature trends (°C/yr) in the SAZ, with a linear fit to the summer mean temperature data, along different depth levels from 0 to 500 m depth for the period 1992 - 2004.

Figure 7. Temperature trends (°C/yr) in the AZ, with a linear fit to the summer mean temperature data, along different depth levels from 0 to 500 m depth for the period 1992 - 2004. (top panel) temperature in the summer mixed layer from 0 – 50 m depth; (second panel) winter water layer from 80 – 250 m depth; (third panel) deep water layer from 300 – 500 m depth.

Figure 8. Mean XBT temperature structure over 0-500 m depth averaged over the summertime SURVOSTRAL sections for the period a) 1992-1996, b) 2000-2004 and c) the

temperature difference between these two mean summer periods. The SAZ and AZ discussed in the text are delimited by the vertical black lines. The position of the STF and SAF are marked.

Figure 9. Left panels: a) Mean CTD temperature structure over 0-2000 m depth averaged over the summertime WOCE SR3 sections of Mar 1993, Jan 1994, Jan 1995, c) temperature structure for the Nov 2001 section e) the temperature difference between these two periods. Right panels: b), d), f) : same for salinity.

Figure 10. a) Steric height calculated from 0/500 dB and 0/2000 dB based on the mean of the WOCE SR3 CTD sections from March 1993, January 1994, and January 1995, and compared to the November 2001 section. B) Steric height difference (Nov 2001 – Mean 93-94-95) for 0/500 dB and 0/2000 dB.

Figure 11. Temporal evolution of the a) MEI ENSO Index, based on a weighted average of the main ENSO features, and b) the SAM Index, for the period 1992-2005.

Figure 12. Altimetric SLA regressed onto a) the ENSO index and b) the SAM index for the period 1993-2005 in the Southern Ocean. Only values greater than the 95% confidence level are shown. The approx. position of the SURVOSTRAL measurements is shown by the bold line.

Figure 13. Sverdrup transport (10^{-4} Sv/m) based on the a) mean ERS-1 winds (1991-1995) and b) the mean Quikscat winds (1999-2005), integrated over the Southern Ocean basins deeper than 2000 m. Within each basin, the model integrates wind stress curl from east to west, starting from the 2000 m depth contour along an eastern continental boundary or submarine ridge, up to the western boundary or ridge.

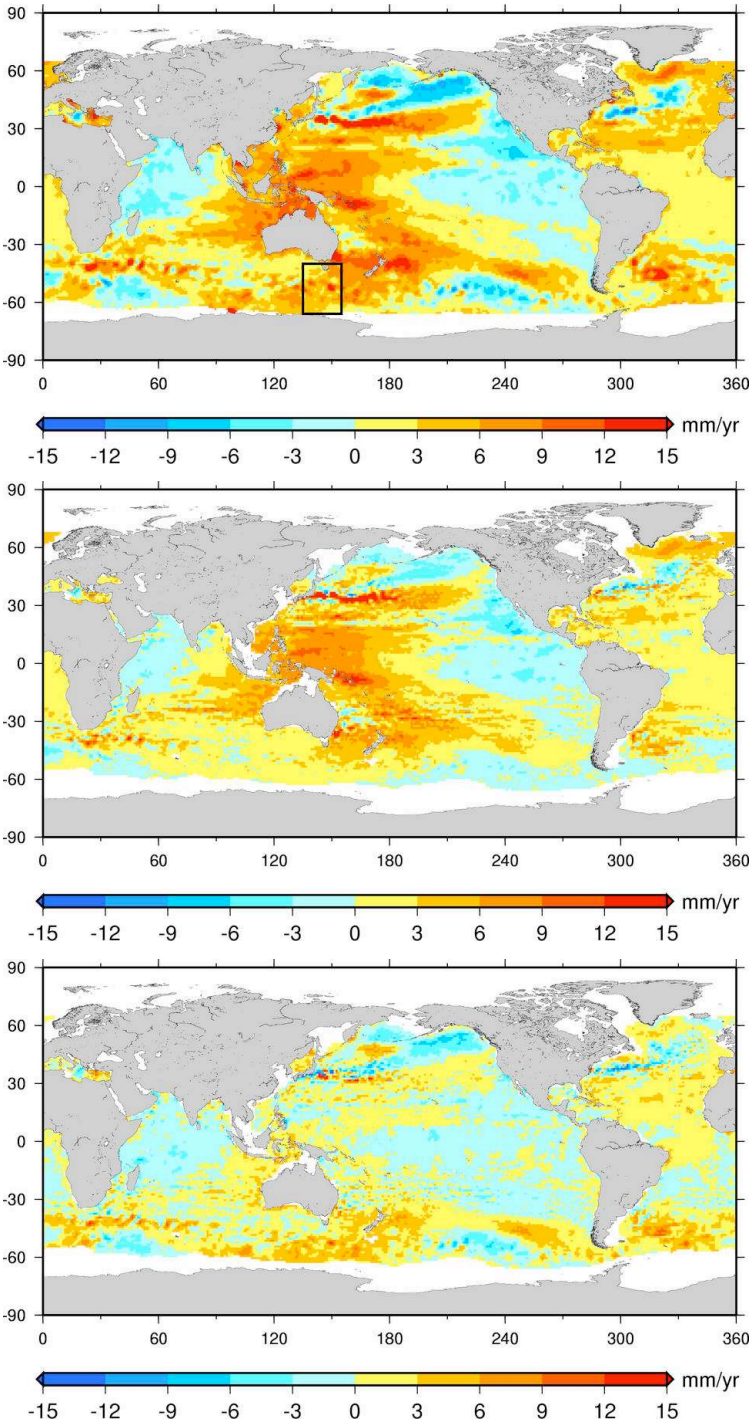

Figure 1. Global distribution of sea level rise (in mm/yr) from (top panel) Topex-Poseidon altimetric observations over 1993-2003; (middle panel) sea level rise over the upper 700 m calculated from the ARMOR in-situ data projection of Guinehut et al (2004); (bottom panel) difference map Topex – ARMOR (after Lombard et al., 2005). The study region is outlined in black.

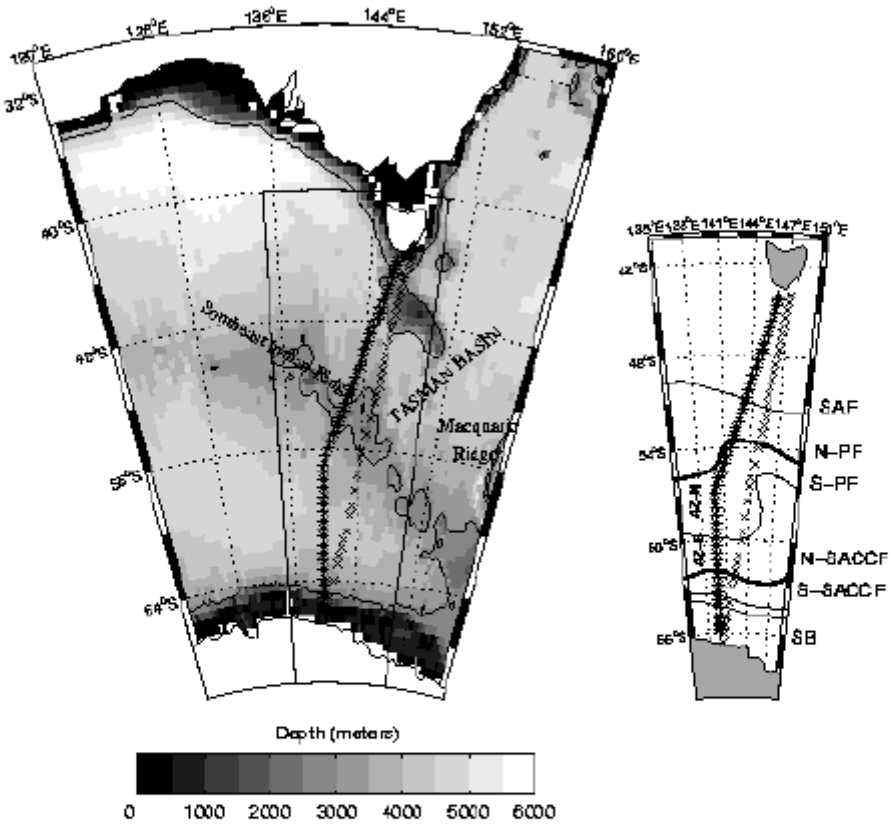

Figure 2. (left panel) Position of the WOCE SR3 CTD transects (*) and SURVOSTRAL XBT and TSG transects (x) between Tasmania and Antarctica, overlaid on the bathymetry. The 3000 m isobath is marked. The zoom represents the mean frontal positions defined by altimetry (Sokolov and Rintoul, 2002). The abbreviations used are: SAF : Subantarctic Front; N-PF : Northern Polar Front; S-PF : Southern Polar Front; N-SACCF and S-SACCF: Northern and Southern branch of the Southern ACC Front; SB : Southern Boundary of the ACC.

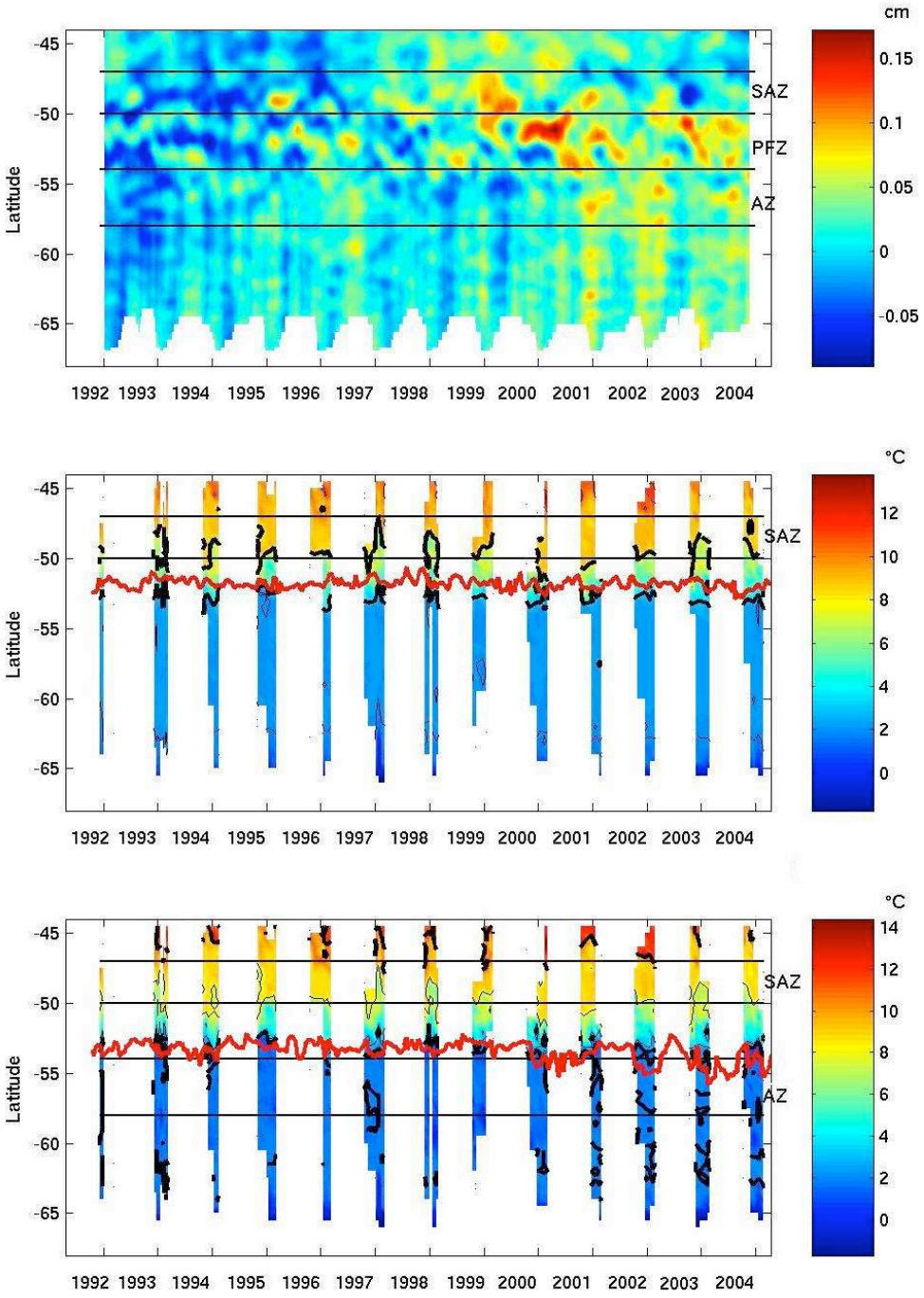

Figure 3. (a) Hovmöller diagram of altimetric sea level anomalies along the SURVOSTRAL line from Tasmania (44°S) to Dumont D'Urville (66°S) from January 1993 to December 2004. Altimetry data are low-pass filtered to remove signals less than 90 days. (b) SURVOSTRAL XBT temperature at 300 m depth, with the 3°C and 8°C isotherms in bold. The SAF position is marked in red, after Sallee et al. (2006). (c) XBT temperature at 200 m depth, with the 11°C and 2°C isotherms in bold. The PF position from Sallee et al. (2006) is in red.

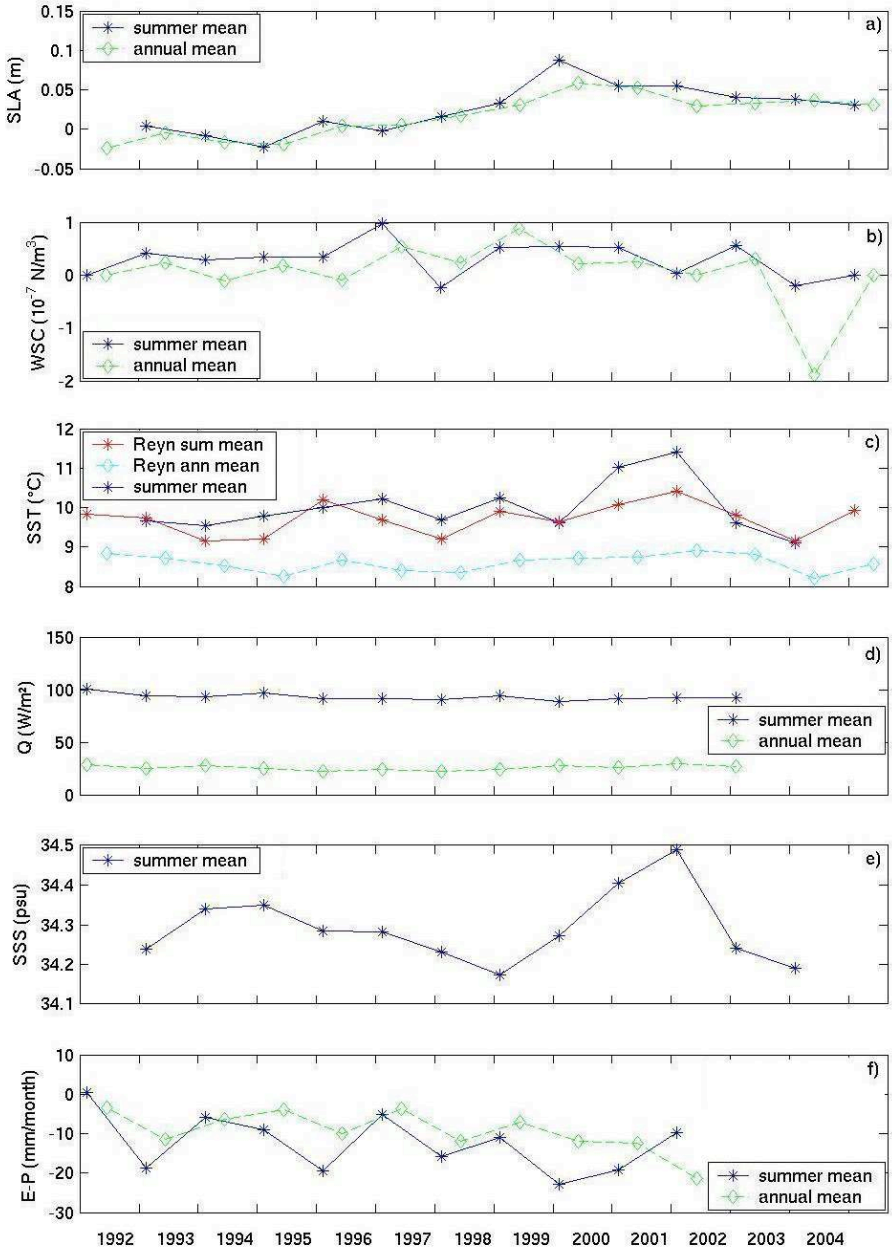

Figure 4. Temporal evolution of the surface characteristics in the Subantarctic Zone, averaged between 47°S and the SAF position from Sallee et al (2006), for the period 1992-2005. In all plots, the annual mean is in green (with diamonds) and the summer mean in blue (with stars). a) altimetric sea level anomalies, b) wind stress curl from the ERS and Quickscat scatterometers; c) summer mean SST from SURVOSTRAL XBTs and WOCE SR3 summer sections (blue). Also shown, Reynolds summer mean SST (red), Reynolds annual mean SST (cyan). d) NCEP surface heat flux; e) summer mean SSS from SURVOSTRAL TSG data and WOCE SR3 summer sections; f) surface E-P : evaporation from ECMWF and precipitation from Xie and Arkin monthly climatology.

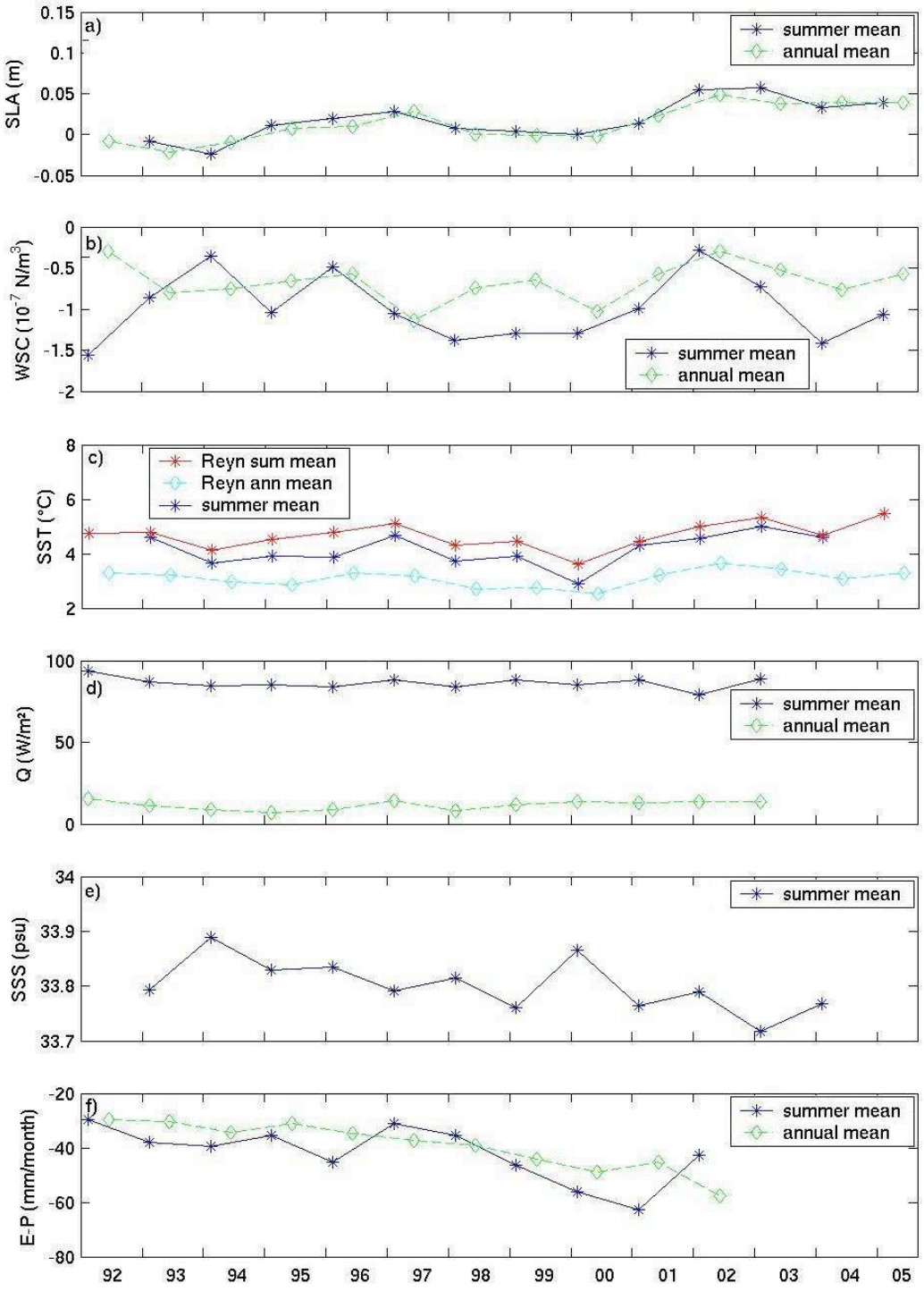

Figure 5. As for Figure 4, but for the Antarctic Zone averaged between the Sallee et al (2006) PF position and 58°S.

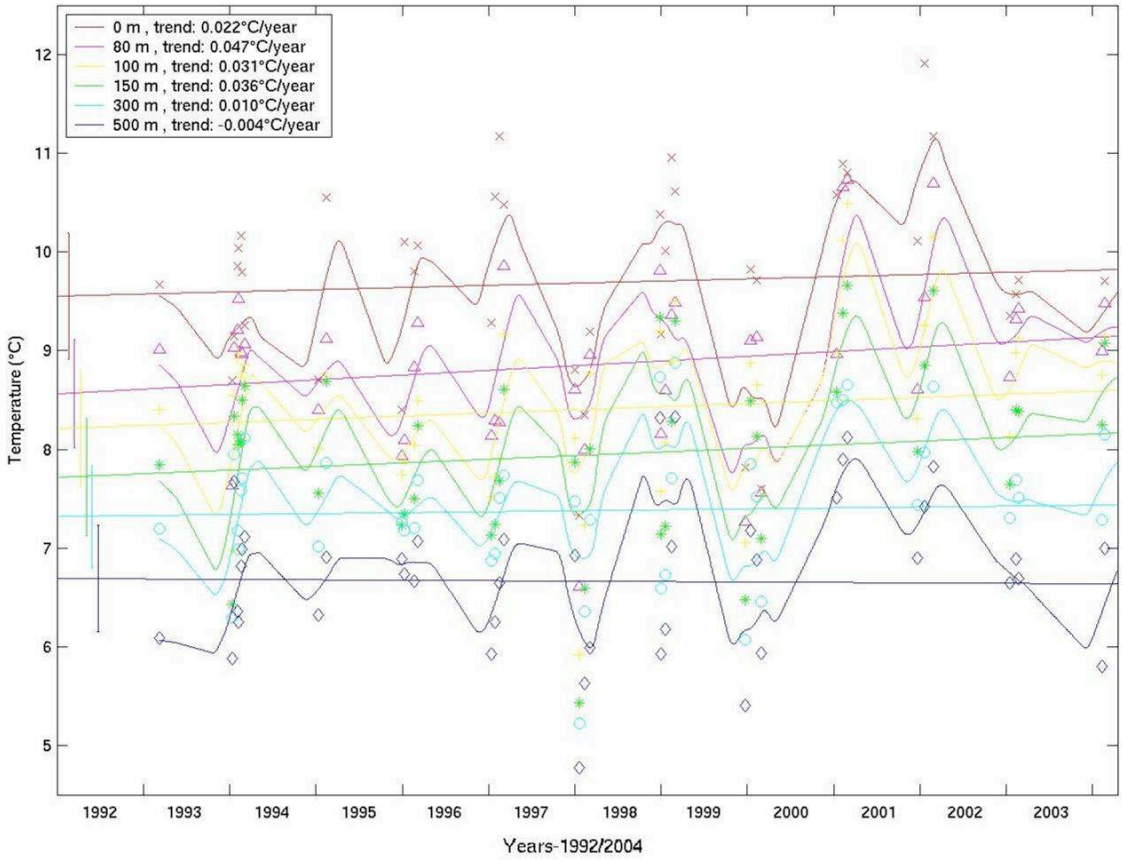

Figure 6. Temperature trends (°C/yr) in the SAZ, with a linear fit to the summer mean temperature data, along different depth levels from 0 to 500 m depth for the period 1992 - 2004.

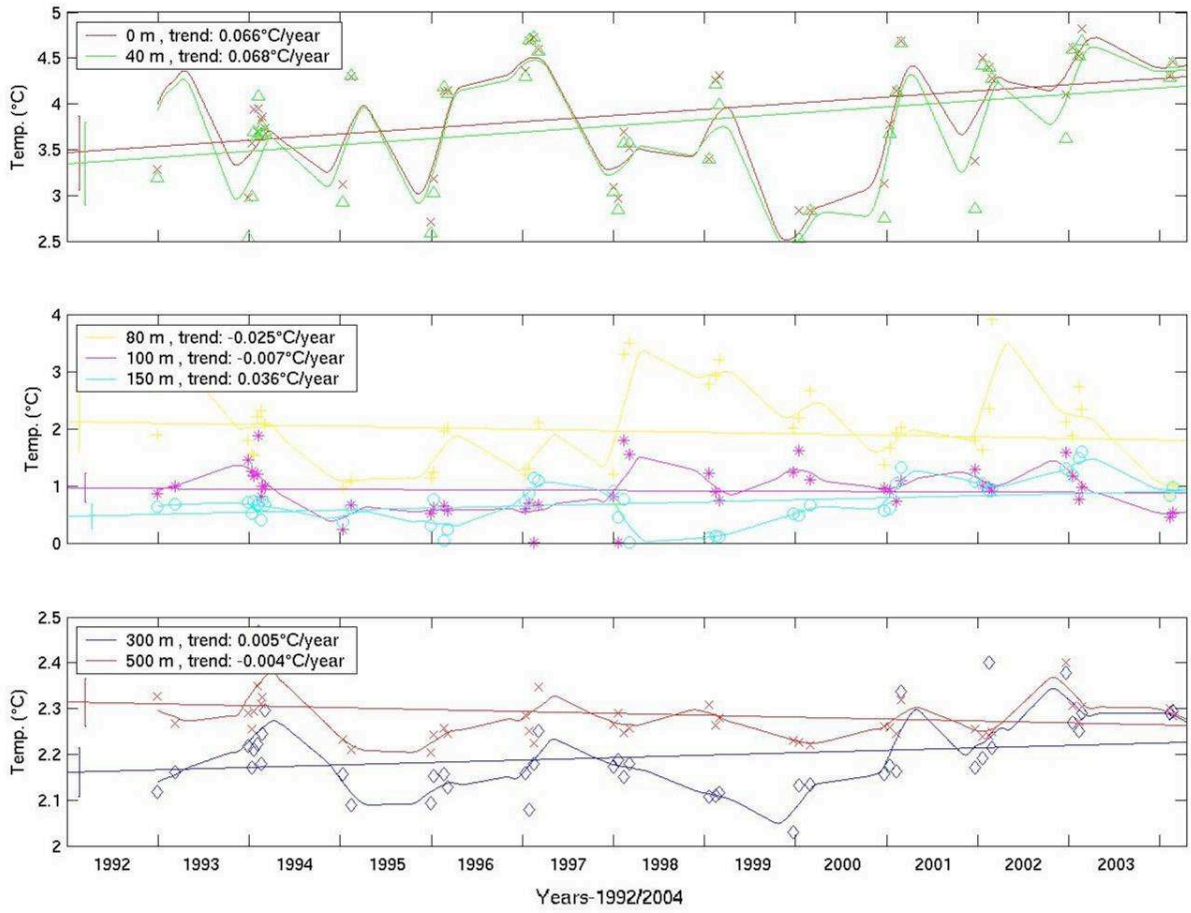

Figure 7. Temperature trends (°C/yr) in the AZ, with a linear fit to the summer mean temperature data, along different depth levels from 0 to 500 m depth for the period 1992 - 2004. (top panel) temperature in the summer mixed layer from 0 – 50 m depth; (second panel) winter water layer from 80 – 250 m depth; (third panel) deep water layer from 300 – 500 m depth.

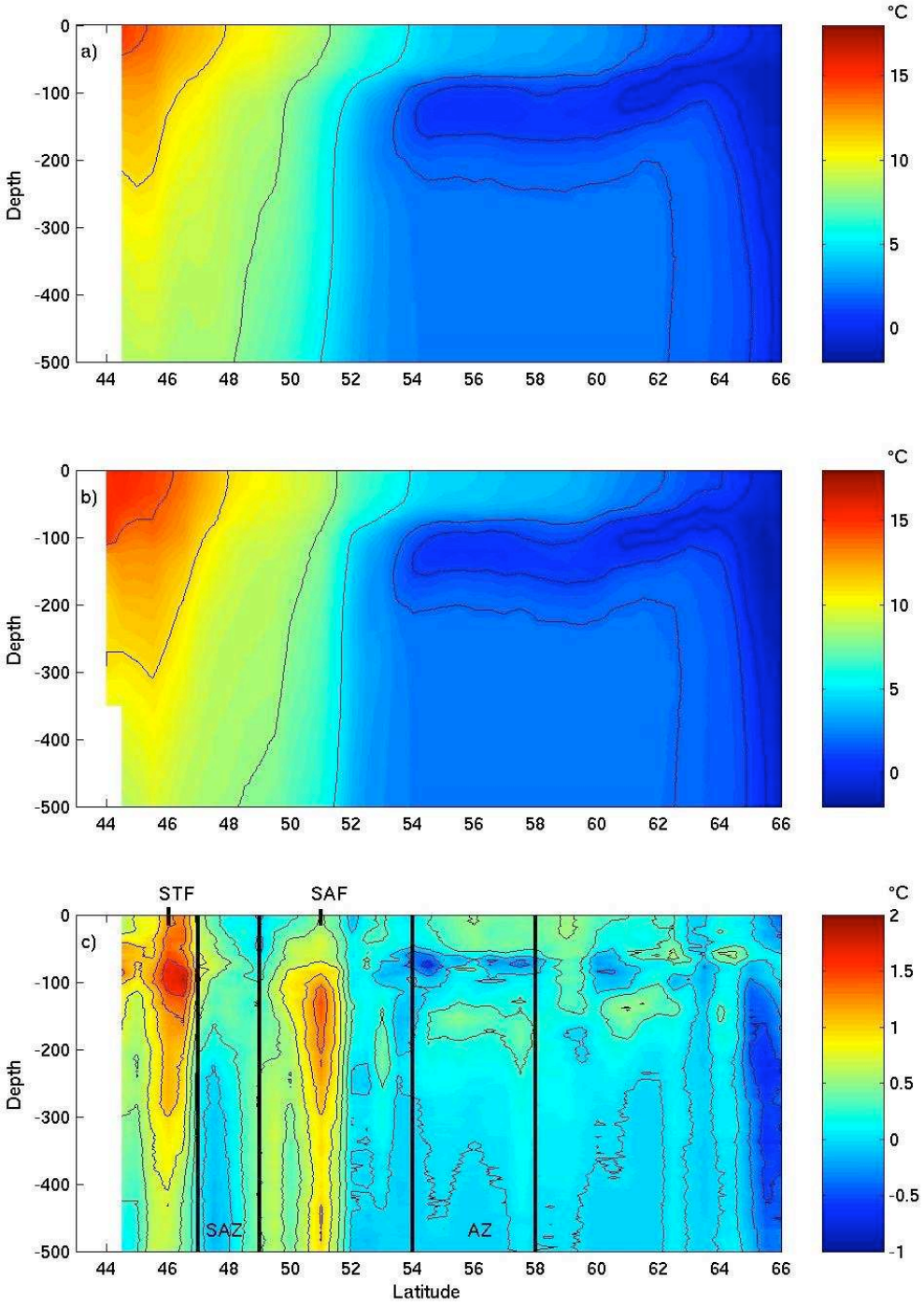

Figure 8. Mean XBT temperature structure over 0-500 m depth averaged over the summertime SURVOSTRAL sections for the period a) 1992-1996, b) 2000-2004 and c) the temperature difference between these two mean summer periods. The SAZ and AZ discussed in the text are delimited by the vertical black lines. The position of the STF and SAF are marked.

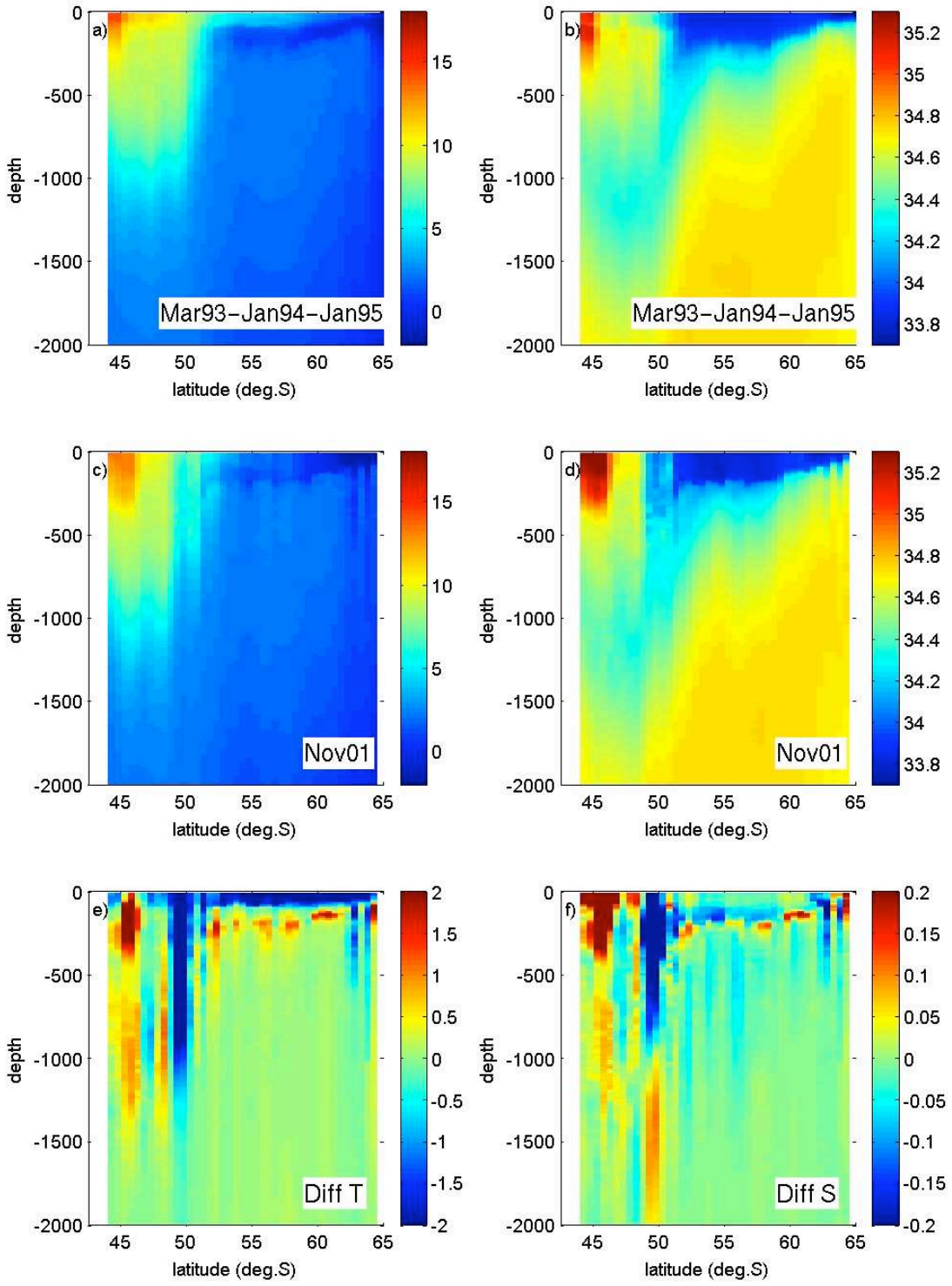

Figure 9. Left panels: a) Mean CTD temperature structure over 0-2000 m depth averaged over the summertime WOCE SR3 sections of Mar 1993, Jan 1994, Jan 1995, c) temperature structure for the Nov 2001 section e) the temperature difference between these two periods. Right panels: b), d), f) : same for salinity.

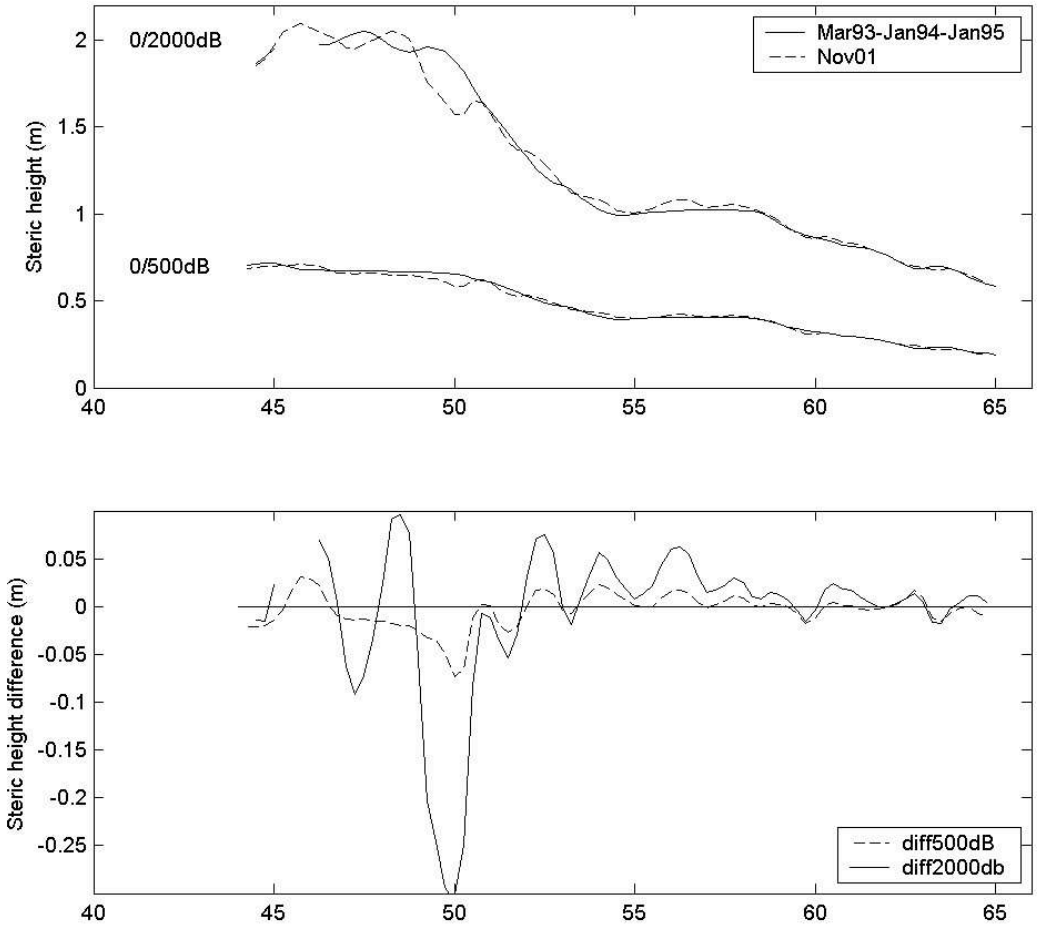

Figure 10. a) Steric height calculated from 0/500 dB and 0/2000 dB based on the mean of the WOCE SR3 CTD sections from March 1993, January 1994, and January 1995, and compared to the November 2001 section. B) Steric height difference (Nov 2001 – Mean 93-94-95) for 0/500 dB and 0/2000 dB.

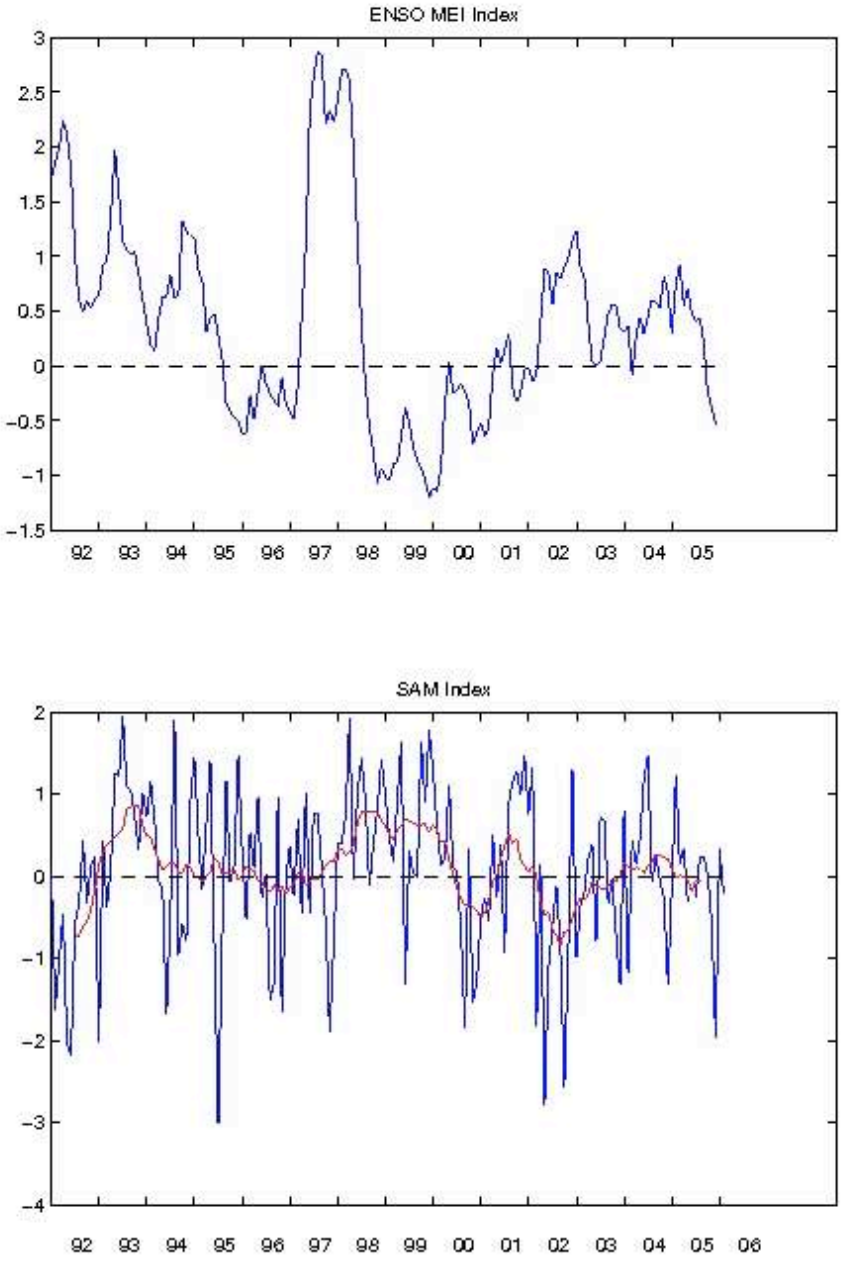

Figure 11. Temporal evolution of the a) MEI ENSO Index, based on a weighted average of the main ENSO features, and b) the SAM Index, for the period 1992-2005.

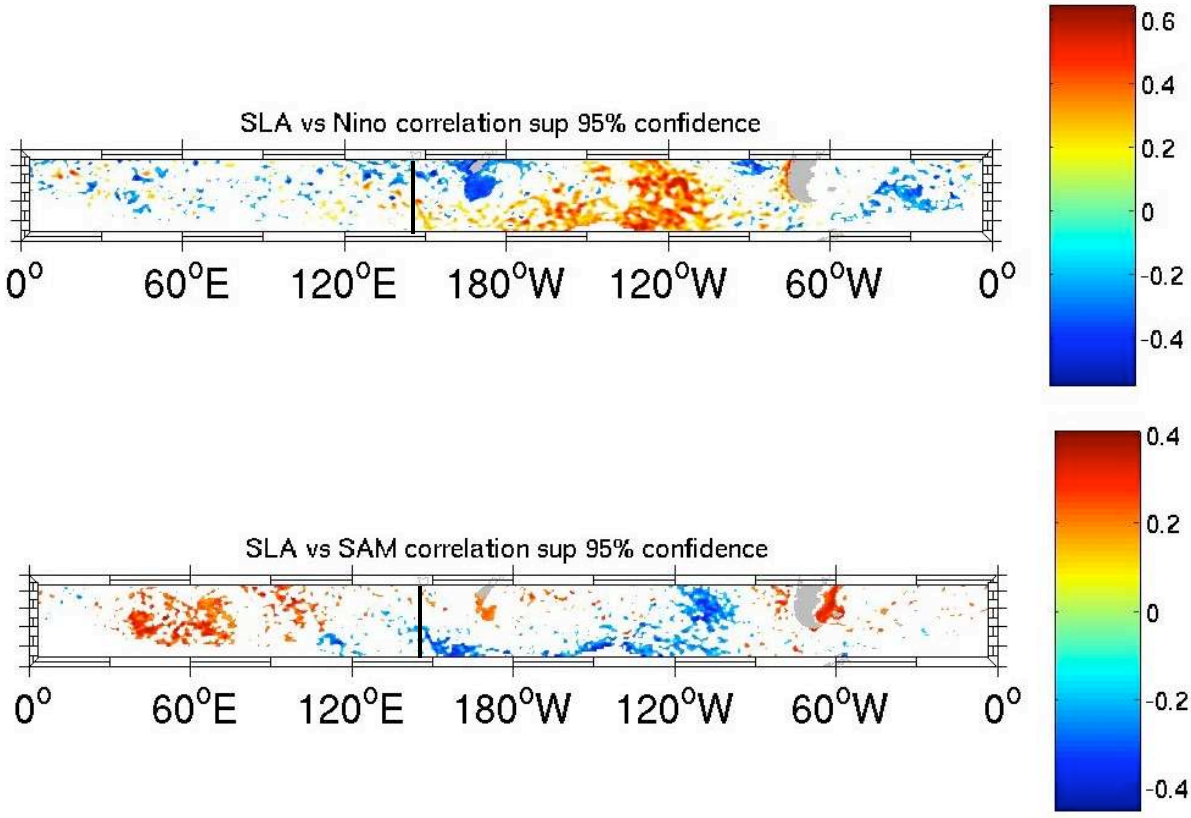

Figure 12. Altimetric SLA regressed onto a) the ENSO index and b) the SAM index for the period 1993-2005 in the Southern Ocean. Only values greater than the 95% confidence level are shown. The approx. position of the SURVOSTRAL measurements is shown by the bold line.

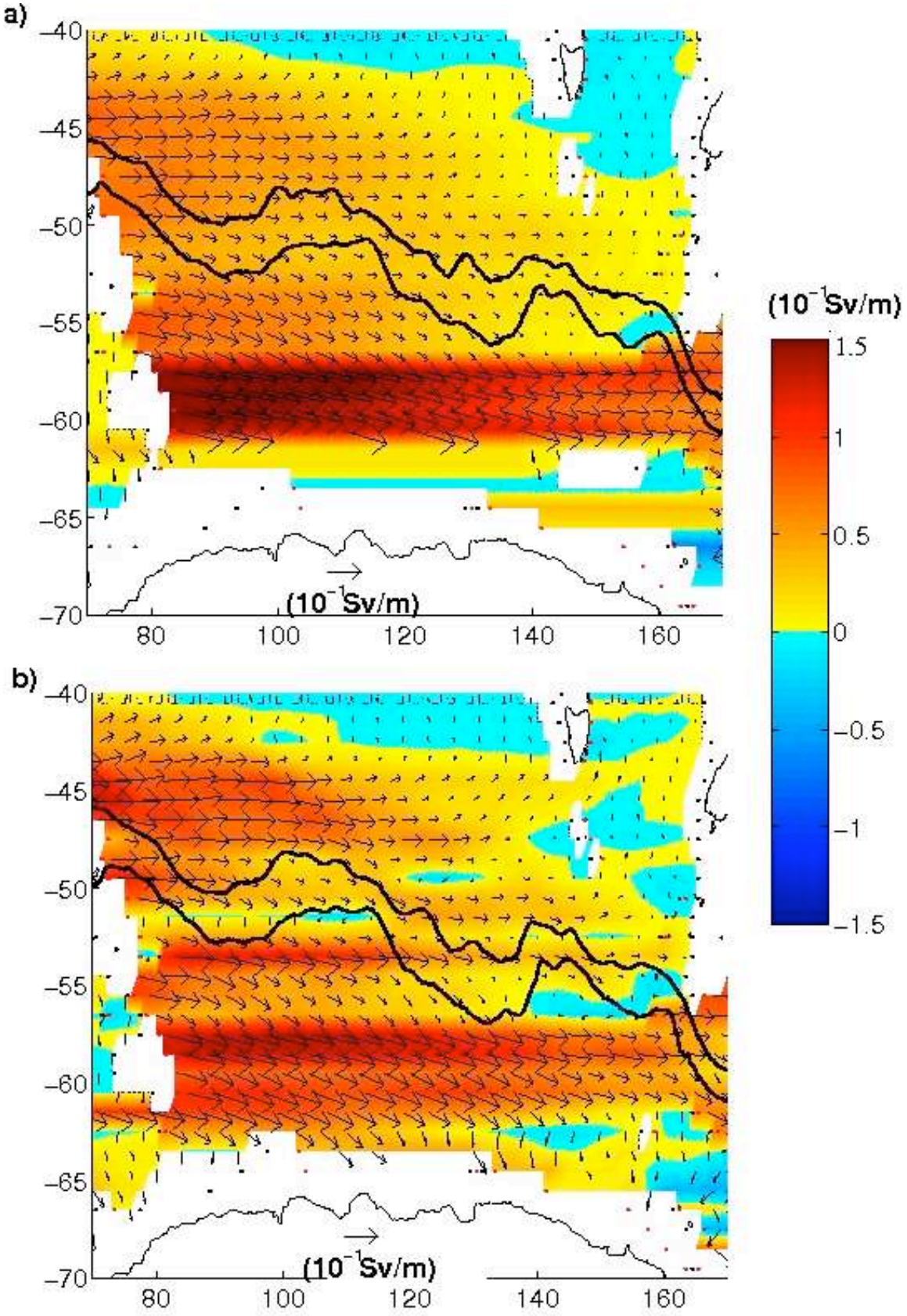

Figure 13. Sverdrup transport (10^{-4} Sv/m) based on the a) mean ERS-1 winds (1991-1995) and b) the mean Quikscat winds (1999-2005), integrated over the Southern Ocean basins deeper than 2000 m. Within each basin, the model integrates wind stress curl from east to west, starting from the 2000 m depth contour along an eastern continental boundary or submarine ridge, up to the western boundary or ridge.